NATIONAL AERONAUTICS AND SPACE ADMINISTRATION

Technical Report 32-1096

Investigation of Supersonic Shock Phenomena in a Two-Phase (Liquid-Gas) Tunnel

Robert B. Eddington
Major, USAF

JET PROPULSION LABORATORY
CALIFORNIA INSTITUTE OF TECHNOLOGY
PASADENA, CALIFORNIA

March 15, 1967

NATIONAL AERONAUTICS AND SPACE ADMINISTRATION

Technical Report 32-1096

Investigation of Supersonic Shock Phenomena in a Two-Phase (Liquid-Gas) Tunnel

Robert B. Eddington
Major, USAF

Approved by:

D. R. Bartz, Manager
Research and Advanced Concepts Section

JET PROPULSION LABORATORY
CALIFORNIA INSTITUTE OF TECHNOLOGY
PASADENA, CALIFORNIA

March 15, 1967

JPL TECHNICAL REPORT 32-1096

Prepared Under Contract No. NAS 7-100
National Aeronautics & Space Administration

This document, JPL Technical Report 32-1096, is partial fulfillment of the requirement for admission to candidacy for the degree of Aeronautical Engineer at the California Institute of Technology.

Preface

Homogeneous flows of liquid and gas are currently used in two-phase, magnetohydrodynamic nuclear-electric power conversion systems for space, and, in addition, are common in devices employing the boiling, condensing, and pumping of saturated gases or liquid sprays. Flow velocities in such processes have reached levels at which compressible effects in the mixture are significant, particularly near the gas-to-liquid volume ratio of 1:1, the ratio at which the velocity of sound propagation theoretically becomes a minimum.

Pressure discontinuities of the nature normally associated with shock phenomena have been reported in studies of two-phase-fluid diffusers by Elliott, et al., (Ref. II-1), and Muir and Eichhorn (Ref. I-15) at flow velocities exceeding the velocity of sound propagation in the mixture. However, because no facility existed in which a supersonic two-phase flow could be generated and analyzed in a precise manner analogous to the single-phase gas media, virtually no experimental study and little theoretical study have been made of the potential shock phenomena in two-phase mixtures.

Heretofore, relatively simple devices have been used in two-phase media investigations. These devices limited measurements to such flow characteristics as the propagation velocity of weak pressure pulses, the propagation and attenuation of weak sound waves, thrust and pressure in subsonic compressible flow devices, and void fraction distributions in bubbly mixtures. Consequently, a valid need existed for a more sophisticated research device.

The primary objective of this investigation, then, was the design, fabrication, and operation of both a tunnel for supersonic liquid-gas flow, and associated instrumentation with sufficient versatility and precision to permit spatial measurements of flow characteristics, phase interrelationships, and any shock phenomena that might occur. The relatively opaque nature of two-phase mixtures near a volume ratio of 1:1, the unknown boundary-layer development, and the very high pressures to be expected with shock phenomena placed special demands on the design of such a tunnel.

Upon fabrication, the tunnel and instrumentation for supersonic two-phase flow was placed in operation in late 1963. During the initial tunnel operation, the presence of shock-type phenomena in supersonic two-phase gas-liquid flows was verified, and the structure was defined sufficiently to permit relatively precise measurements of the associated flow characteristics.

In contrast to the very formidable system of equations applicable to two-phase flow that account for such phase interrelations as surface tension, gas dissolution, bubble dynamics, and heat transfer between phases, actual flow measurements confirmed the use of the relatively simple isothermal equation of state. In conjunction with the continuity and momentum equations that use average continuum properties upstream and downstream of the shock structure, the isothermal equation provides a very close representation of the more interesting continuum properties of pressure, velocity, Mach number, and volume ratio. Applicability of these equations was found to extend over a wide range of Mach numbers, and well into hypersonic flow.

Preface (contd)

Analytical extension of the flow relationships was made for a relatively wide range of gas-liquid volume ratios centered about 1:1 and within the analytically suggested applicability of the isothermal continuum theory. In addition, the isothermal theory was analytically extended to oblique shock phenomena for similar ranges of applicability to provide angular, pressure, velocity, and volume-ratio relationships. Examination of oblique shock structures over variously angled double wedges in the tunnel further confirmed the validity of the isothermal continuum theory.

Other information fundamental to the flow model (velocity profiles, boundary-layer development, void distribution, and total pressure head) was obtained in auxiliary flow devices. It was found, for instance, that the development of a boundary layer along the duct walls had a significant effect on pressure, void ratio, and relative phase velocity.

Thus, achievement of the objective provided fundamental empirical and analytical information relative to supersonic two-phase liquid gas flows.

The author is currently Assistant Professor, Department of Mechanical Engineering, Air Force Institute of Technology, Wright-Patterson Air Force Base, Ohio.

Acknowledgment

This investigation into the phenomena of supersonic two-phase liquid-gas flow was possible through the joint support of the Department of Aeronautics at the California Institute of Technology and the Research and Advanced Concepts Section of the Caltech Jet Propulsion Laboratory. By this cooperative arrangement, the author, assigned to Caltech by the United States Air Force for graduate study in Aeronautics, was able to develop and operate successfully a supersonic two-phase test facility at the Jet Propulsion Laboratory.

At the suggestion of Dr. David G. Elliott of the Research and Advanced Concepts Section, JPL, the investigation was initiated to provide basic information about supersonic two-phase liquid-gas flow in support of the development of a two-phase nuclear-electric power conversion system for use in space.

Dr. Homer J. Stewart of the Department of Aeronautics, Caltech, and the Advanced Technical Studies Section, JPL, provided overall supervision of the investigation, contributed timely suggestions, and performed a critical review of the results.

The relatively rapid development of this unique, two-phase test facility was due to the strong support of Dr. Elliott and his group, and other supporting facilities at the Jet Propulsion Laboratory.

Considerable credit is due to the personnel of the Fabrication Shop Section for the difficult job of producing the many unusual assemblies used in the tunnel, and particularly to Mr. David L. Perkins who was responsible for assembly of the various tunnel components into a finished, precision research tool.

The severe photographic requirements imposed by the need for high-speed motion pictures of the relatively opaque supersonic two-phase flows were met by the patience and ingenuity of the personnel of the Photographic Section, Mr. Donald R. Maxeiner and Mr. Robert L. Hansen in particular.

Charles Dame assisted the author in operating equipment associated with the tunnel.

Thanks are extended to Mrs. Lois Bush who assisted in the extensive computer analysis required to produce the numerical extensions of the isothermal normal and oblique shock theories.

Thanks are also due to Mrs. Grace Molen, AFIT, Detachment No. 5, Malmstrom AFB, Montana, and Mrs. Edna M. Uhl, AFROTC, Caltech, for their secretarial assistance in the preparation of the original manuscript.

Contents

Contents (contd)

Contents (contd)

Figures

Contents (contd)

Figures (contd)

Contents (contd)

Figures (contd)

Contents (contd)

Figures (contd)

Contents (contd)

Figures (contd)

Contents (contd)

Figures (contd)

Contents (contd)

Figures (contd)

Contents (contd)

Figures (contd)

Contents (contd)

Figures (contd)

Contents (contd)

Figures (contd)

Contents (contd)

Figures (contd)

Contents (contd)

Figures (contd)

Abstract

Homogeneous two-phase flows of dispersed liquid and gas having gas-to-liquid volume ratios around 1:1 exhibit the characteristics of a continuum flow with a greatly reduced sound propagational velocity that approaches 66 ft/sec at atmospheric pressure, and that is reduced further in value as the square root of the pressure. Flows of such mixtures at velocities in excess of the local velocity of sound can produce shock phenomena similar to that experienced in supersonic gaseous media. A supersonic two-phase tunnel was designed and built with such versatility and precision that normal and oblique shock structures can be photographed and analyzed in the absence of boundary-layer interference. The applicability of the isothermal continuum theory to such flows is confirmed empirically for volume ratios near 1:1, and the theory is mathematically extended for both normal and oblique shocks over a wide range of volume ratios centered about the 1:1 value. Auxiliary flow devices were constructed for the measurement of such difficult flow parameters as the relative phase velocity, local void ratio, coefficient of friction, and stagnation pressure. A general change in the flow model matrix was found at volume ratios approaching 1:1. Pressure gradients and relative phase velocities were correlated with the proposed flow models with generally good agreement. The coefficient of friction measured for supersonic flow was found to be a simple function of the local void ratio. Stagnation pressures measured for a wide range of flow conditions approximate an isentropic relation for a substantial part of the lower velocity spectrum. At higher velocities, the stagnation pressure closely approaches the normal shock plus isentropic slowdown theory. Considerable photographic information pertaining to shock structure and phase movement is obtained over the spectrum of flow conditions with Mach numbers ranging from 2 to 20.

I. Introduction and Approach to Isothermal Two-Phase Flow Relationships

A. Introduction

Systems exist in both nature and engineering that involve multiphase flow conditions; "phase" implies a solid, gaseous, or liquid state in which one or more species of molecules can be identified, and their states and motions characterized by single-phase, thermodynamic and hydrodynamic equations. Flows of a liquid or gas in which solid particles are suspended are referred to as "suspensions"; these flows are often used in the pneumatic transport of solids. Flows containing one or more distinguishable elements having both liquid and gas phases are known generally as "two-phase flows"; these flows constitute the broad category under which the work described in this paper was organized.

Figure I-1 identifies a large number of classifications of multiphase systems, and indicates the specific areas of this investigation. Within any of the two-phase liquid-gas systems, flows have been historically categorized as shown in Fig. I-1, in the horizontal line labeled "Flow Categorization." These flows may be present as functions of position and time. The vertical flow of a liquid in a flash-type boiler header-tube, for example, contains many of these categories from the initiation of boiling nucleation to the final single-phase vapor. The variable time and space categorization of the flow makes the formulation of the fundamental hydrodynamic equations extremely difficult because the probability relationships governing multi-element systems must also be applied. To date, the majority of the multiphase analytical and experimental investigations have been in this difficult area. Their individual successes have been primarily dependent upon the proper analytical description of an applicable flow model.

With the advent of the high-flow velocities and heat transfer rates found in certain nuclear reactors, flash boilers, rocket propulsion systems with cryogenic fluids, two-phase flow power generating equipment (Ref. I-1), and two-phase particle flows in solid rockets, the time-stable (in a broad sense) homogeneous bubble and spray flows have appeared as principle characteristics of the systems. The spray- or particle-type two-phase flows in which the volumetric ratio of gas to particles or droplets is greater than 10 have been analytically treated by Marble (Ref. I-2). Flows with a volumetric ratio of gas-to-liquid between 0.1 and 10, and that are sufficiently homogeneous to be described as continuum flows can be treated by considerably simplified hydrodynamical equations.

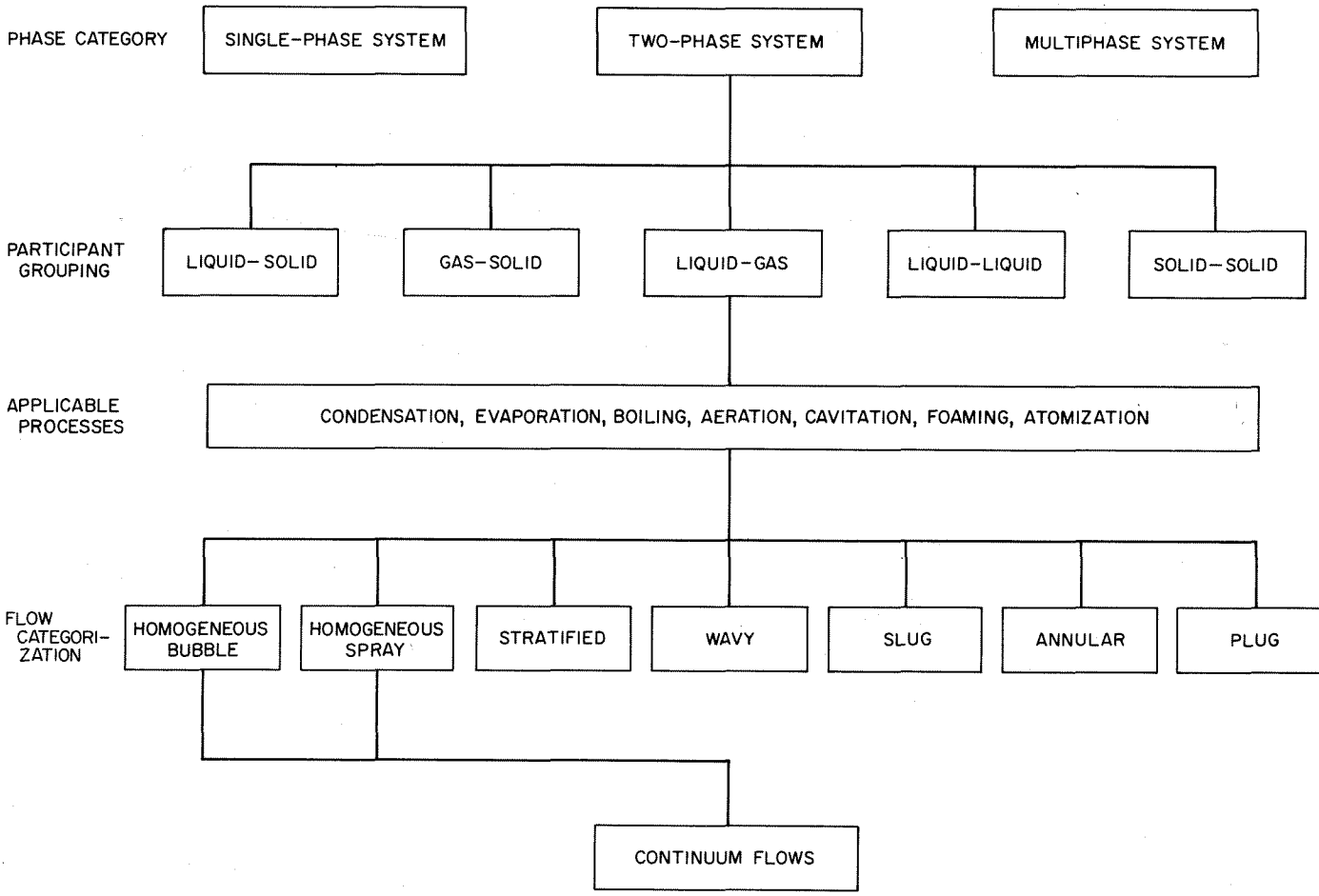

Fig. I-1. Categorization of multiphase systems according to grouping and mechanism

B. Speed of Sound in Two-Phase Continuum Flows

The very small droplets of liquid or bubbles of gas in most two-phase flows still contain a number of molecules sufficient to make them subject to such static concepts as temperature, pressure, viscosity, and density. At standard conditions, bubbles 10^{-4} cm in diameter contain on the order of 10^{7} molecules; therefore, considering the bubbles and droplets large compared with the molecules contained within them, the fundamental principles of hydrodynamics may be applied to such combined flows.

The propagation of a pressure disturbance in a bubble-liquid mixture or froth was first investigated by Mallock (Ref. I-3). He assumed that the gas in the bubbles obeyed Boyles law and that the mixture could be characterized by an average bulk density and modulus. An interesting result of these assumptions was that the velocity of a pressure protuberance in the mixture is reduced by more than an order of magnitude from that velocity in either pure species; this is true for a relatively wide range of gas-to-liquid volume ratios. Ackeret (Ref. I-4), Wood (Ref. I-5), and Spitzer (Ref. I-6) further derived formulas for the propagation and attenuation of pressure disturbances in bubbly mixtures. Silberman (Ref. I-7) investigated experimentally the propagation and attenuation of oscillatory pressure waves in bubbly mixtures. Campbell (Ref. I-8), and Campbell and Pitcher (Ref. I-9) investigated the velocity and attenuation of single pressure pulses in bubbly mixtures.

One general conclusion from the investigations to date is that a two-phase medium can be treated as an isothermal continuum for the propagation of pressure waves if the distance between bubble centers is less than ½ wave length, and if the bubble radii are less than 0.004 in., unless the sound frequency is less than 100 cps (Ref. I-8). The sonic velocity in the continuum (c) depends upon the

pressure (P) and the density (ρ) through the well-known ratio,

$$c = \left(\frac{dP}{d\rho}\right)^{1/2}. \tag{I-1}$$

If the gas-to-liquid mass ratio is designated by r_m, and the gas-to-liquid (static) volume ratio by r_v, then

$$r_m = \frac{m_g}{m_l} \text{ per unit volume}, \qquad r_v = \frac{V_g}{V_l} \text{ per unit volume} \tag{I-2}$$

and the average density of the continuum can be written as

$$\rho = \rho_l \frac{1 + r_m}{1 + r_v} \tag{I-3}$$

where ρ_l is the liquid density.

For pressures less than 1000 psi, a liquid such as water can be considered incompressible. For volume ratios less than 10, the temperature changes in the continuum can be considered negligible so that, from Boyles law, the pressure times the volume is a constant that gives an isothermal equation of state:

$$P(r_v) = \text{constant}. \tag{I-4}$$

Combining Eqs. (I-3) and (I-4), and obtaining the derivatives P and ρ as in Eq. (I-1), the velocity of sound in an isothermal continuum becomes:

$$c = (1 + r_v)\left[\frac{P}{\rho_l r_v (1 + r_m)}\right]^{1/2}. \tag{I-5}$$

The density of the gas can be ignored in the formulation of Eq. (I-5) with an error in c of less than 0.5% over an r_v of 0.01 to 4.0 (Ref. I-8). In analyzing a heterogeneous elastic model of gas and liquid components, Campbell found that the resultant propagational velocity for pressure disturbance was within 1% of the isothermal model just considered.

Not only have the effects of water compressibility been neglected in the foregoing analysis, but the effects of surface tension as well. Campbell found that the effects of surface tension are negligible unless the bubble diameters are less than 0.004 in. according to the relation:

$$c = (1 + r_v)\left[\frac{P + \frac{8\sigma}{3D}}{\rho_l r_v (1 + r_m)}\right]^{1/2} \tag{I-6}$$

where σ is the surface tension of the liquid, and D the diameter of the bubble. In the vicinity of $D = 0.004$ in., the difference between c determined from Eq. (I-5), and c determined from Eq. (I-6) is on the order of only 1%.

Figure (I-2) shows the isothermal speed of sound (c) as a function of r_v according to Eq. (I-5). A definite minimum can be seen for an $r_v = 1.0$ corresponding to $c \cong 65$ ft/sec. Further, it should be noted that c remains at less than 100 ft/sec over a wide range of r_v from about 0.2 to 6.2. The dotted line in the figure shows, for the purpose of comparison, the velocity of sound in pure water.

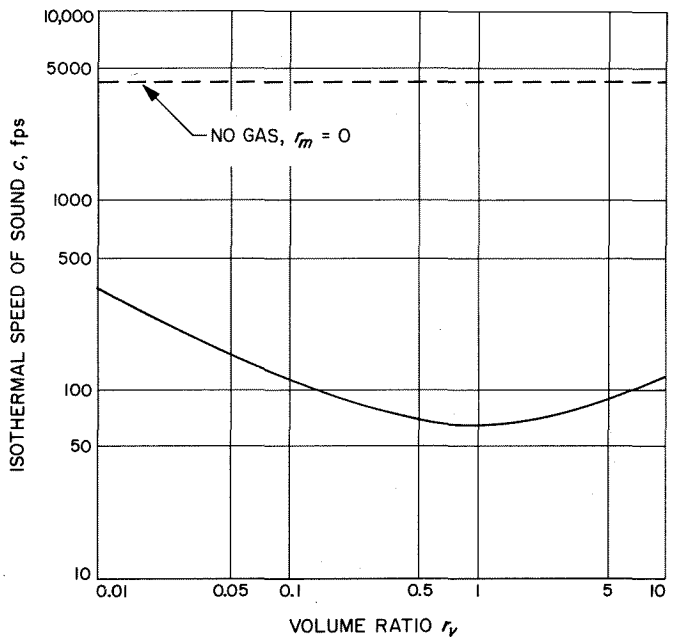

Fig. I-2. Isothermal speed of sound in an air-water mixture at 530°R

C. Considerations for Shock Wave Propagation in Two-Phase Continuum Flows

Mathematical studies on the compressibility and dynamics of two-phase liquid-gas mixtures have been conducted by Heinrich (Ref. I-10), Charyk (Ref. I-11), Zwicky (Ref. I-12), Tangren, Dodge, and Seifert (Ref. I-13),

Campbell and Pitcher (Ref. I-9), Parkin, Gilmore, and Brode (Ref. I-14), and Muir and Eichhorn (Ref. I-15). The experimental work prior to 1958 was concentrated in the area of underwater propulsive devices in which a compressible, two-phase mixture was ejected from a convergent or convergent-divergent nozzle to obtain thrust. In some of these tests, choked flow with limited supersonic expansion was achieved. Campbell and Pitcher's experiments were a departure from those devoted to propulsive devices. They constructed a small shock tube containing a bubbly mixture through which weak shock waves were propagated upon the rupturing of a diaphragm. The results supported the isothermal continuum approach to the propagation of sound waves and weak shock waves through a bubbly gas-liquid mixture. Muir and Eichhorn analyzed two-phase compressible choked flow with bubbly mixtures in a small, convergent-divergent tunnel. Pressure jumps obtained in the divergent section suggested normal shock-type phenomena.

The fundamental principles of hydrodynamics can be applied to two-phase liquid-gas flows as well as a single-phase flow. The basic conservation equations form a fifth order set of partial differential equations where applied to a single-phase flow. For a two-phase flow, however, a minimum of one additional variable is present in the form of the volume ratio (r_v). If state and change information of the individual species is desired, the set must be expanded. A continuity equation is required for each phase and, if both species are allowed to exist in each phase, appropriate relationships between the mass fractions of species in the phases are required. In addition,

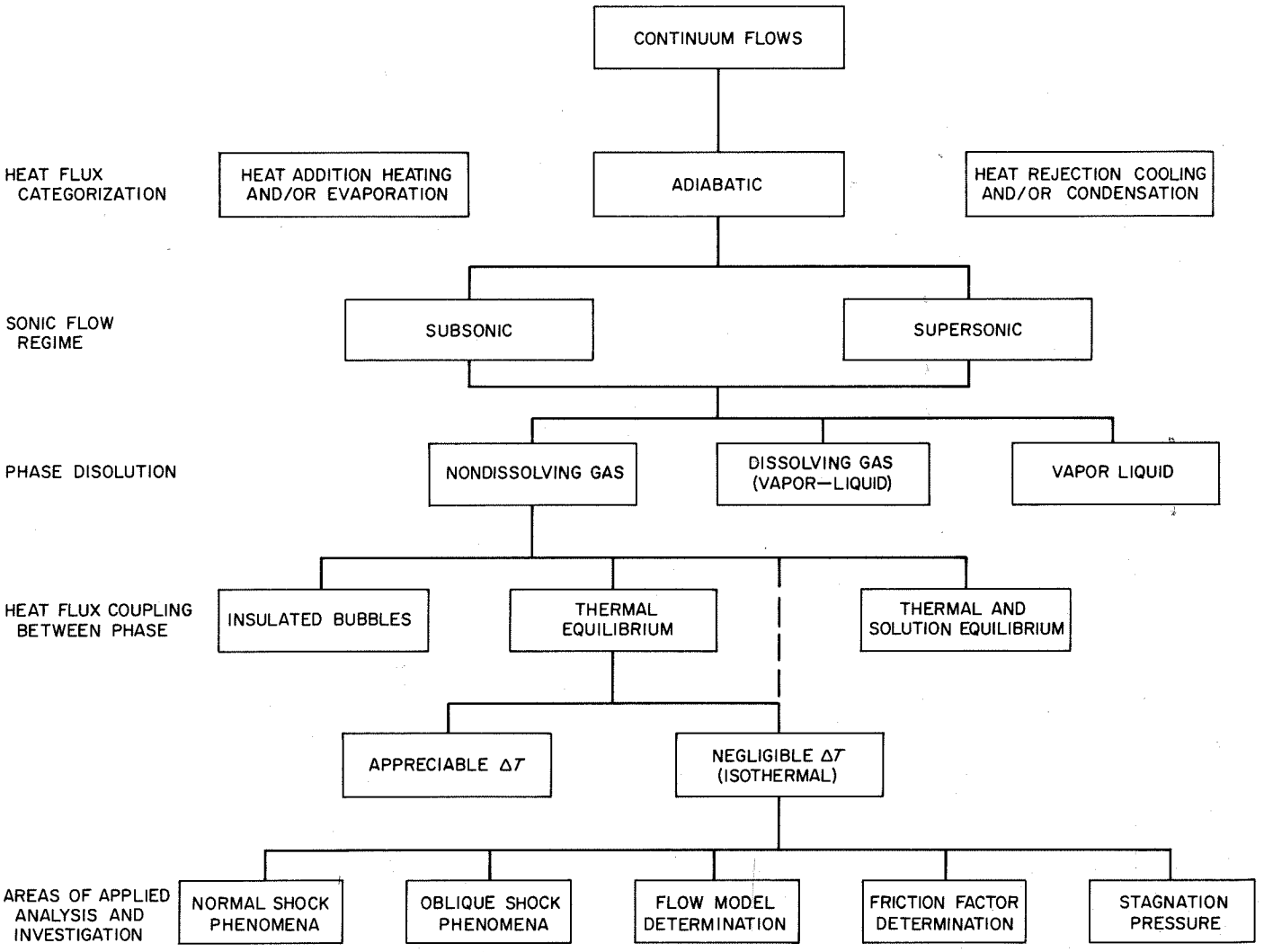

Fig. I-3. Categorization of continuum flows

the energy and momentum equations must be modified to allow for coupling between heat, mass, and momentum transfer between phases. Further, both static and flow qualities can be derived for the numerous ratios between the phases when a difference in phase velocity is allowed.

Figure I-3 shows further considerations relating to a more complete description of the flow regime. Most of the work referenced above relates to adiabatic flow in the subsonic and supersonic regimes, and constitutes, therefore, a significant departure from previous experimental efforts. Either computations can be made for the specific species of the mixture, or assumptions can be made about the phase dissolution. The error in assuming a nondissolution case will be treated later in more detail.

Campbell and Pitcher's analytical investigation of the propagation of shock structure through a gas-liquid mixture assumed thermal equilibrium of the phases and no velocity relative to each other. The conservation equations were used to derive an expression for the temperature rise across a shock structure. Extrapolating their results to pressure ratios across the shock of 40:1 results in a less than 1-°F rise in temperature for the mixture. Thus, while pressure effects are significant, temperature changes for the mixture at equilibrium conditions are practically negligible for a wide range of shock strengths.

Further, the entropy change for the shock structure was derived with the form:

$$\Delta S = \frac{r_m R}{(1 + r_m) W}\left(\frac{P_2^2/P_1^2 - 1}{2P_2/P_1} - \ln\frac{P_2}{P_1}\right) \qquad \text{(I-7)}$$

in which R is the universal gas constant, W the gas molecular weight, and P_2/P_1 the ratio of pressure across the shock. The expression is positive only if $P_2 > P_1$; consequently, a rarefaction cannot be propagated without a change of form. It was shown that the derivative of the velocity of sound with respect to density is greater than zero ($dc/d\rho > 0$), implying that a gently sloping compression wave can be expected to steepen into a shock wave. For a pressure ratio of $(P_2/P_1) = 40$, ΔS for a nitrogen-water mixture of $r_v = 1.0$ has a value of less than 1.0. It is obvious that ΔT cannot be considered zero for the derivation of ΔS, although both ΔT and ΔS are, for reasonably strong shocks, small enough to make an isothermal approach to the development of the shock relationships entirely reasonable.

It was further concluded by Campbell and Pitcher that energy dissipation is confined primarily to the shock front, and negligibly little dissipation, such as that known from studies of acoustic propagation, is included.

Parkin, Gilmore, and Brode (Ref. I-14) assumed that shock dissipation dominates all other types of dissipation for a large range of shock propagation, and extended the analysis of Campbell and Pitcher to more intense shocks involving downstream pressures approaching 10,000 psi. They evaluated the errors involved in neglecting the interphase relationships summarized here.

1. Surface Tension

Considering that the pressure in a gas bubble due solely to surface tension is

$$P = \frac{2\sigma}{R} \qquad \text{(I-8)}$$

where R = bubble radius, and σ = surface tension of the liquid, and that the internal pressure increases as $1/R_3$ for isothermal air compression, or even faster for insulated bubbles, the pressure increment of compression will exceed that of surface tension by at least a factor of $1/R^2$. Consequently, if surface tension, which contributes only a few percent of atmospheric pressure for bubbles of $R > 10^{-3}$ in., is initially negligible, it will continue negligible from a pressure consideration.

2. Dynamic Bubble Behavior

The dynamic bubble behavior of spherical bubbles was investigated with Lamb's equation of motion for a spherical gas-liquid interface. The liquid was assumed inviscid and incompressible, and at equilibrium with the gas under standard conditions when a pressure increase was imposed at time $t = 0$. A solution of the differential equation was

$$t_c \approx \tau_c R_1 (\rho_l/P_2)^{1/2} \qquad \text{(I-9)}$$

where t_c is the time to the first minimum bubble radius R, and P_2 is the overpressure. Considering that the bubble will overshoot its equilibrium size during collapse and oscillate about that size, t_c is less than the total time to reach equilibrium. However, observation was cited that suggests that the subsequent oscillations are highly damped. For an overpressure range from 30 psia to 10,000 psia, τ_c was determined to be 1.0 ± 0.1 sec. Thus, for an

initial bubble size of $R = 0.010$ in. at atmospheric pressure with an overpressure of 100 psia applied, the resulting value of the time to the first minimum (t_c) is 14 μsec. Radii from 0.1 to 0.01 in. have values of t_c from 140 μsec to 14 μsec, respectively.

3. Heat Conduction

A heat flow analysis made between phases of a two-phase mixture of air and water at overpressures up to 10,000 psi showed relatively small temperature changes in the water because of its small compressibility and large specific heat. Temperature changes in the gas phase, however, depend upon how rapidly compression is accomplished, and these changes can be large. In the immediate vicinity of the bubble, temperature change in the gas compared with that in the liquid was shown to be on the order of $\Delta T_g/\Delta T_l > 10$.

Neglecting variations in the thermal diffusivity of the air, the average temperature in the bubble at any later time (t) was found to be

$$T = T_1 + \frac{6(T_2 - T_1)}{\pi^2} \sum_{n=1}^{\infty} \frac{1}{n^2} \exp\left[- D_a t \left(\frac{n\pi}{R}\right)^2 \right] \tag{I-10}$$

where D_a is the thermal diffusivity of air. Assuming a variation of D_a with pressure, and a compression adiabatic to pressure P_2 with $\gamma = 4/3$ followed by cooling at a constant P_2 while the radius R approaches its equilibrium value, the time to reach 90% of the thermal equilibrium temperature was determined to have the relationship:

$$t\,(90\%) \approx 800\, R_1^2\, (P_2/P_1)^{1/3}. \tag{I-11}$$

For a bubble having an initial radius of 0.040 in. with an applied pressure ratio $P_2/P_1 = 40$, a cooling time of a few milliseconds is required. Figure I-4 reproduced from Ref. I-14 shows both 10% and 90% cooling times, and times to reach the first bubble minimum (t_c) for various initial bubble diameters. It is quickly seen that this cooling time is significantly longer than that involved with bubble dynamics; therefore, the thermal equilibria process will spread out the shock structure far beyond the considerations for bubble dynamic equilibria. Even then, thermal equilibrium occurs within a few milliseconds.

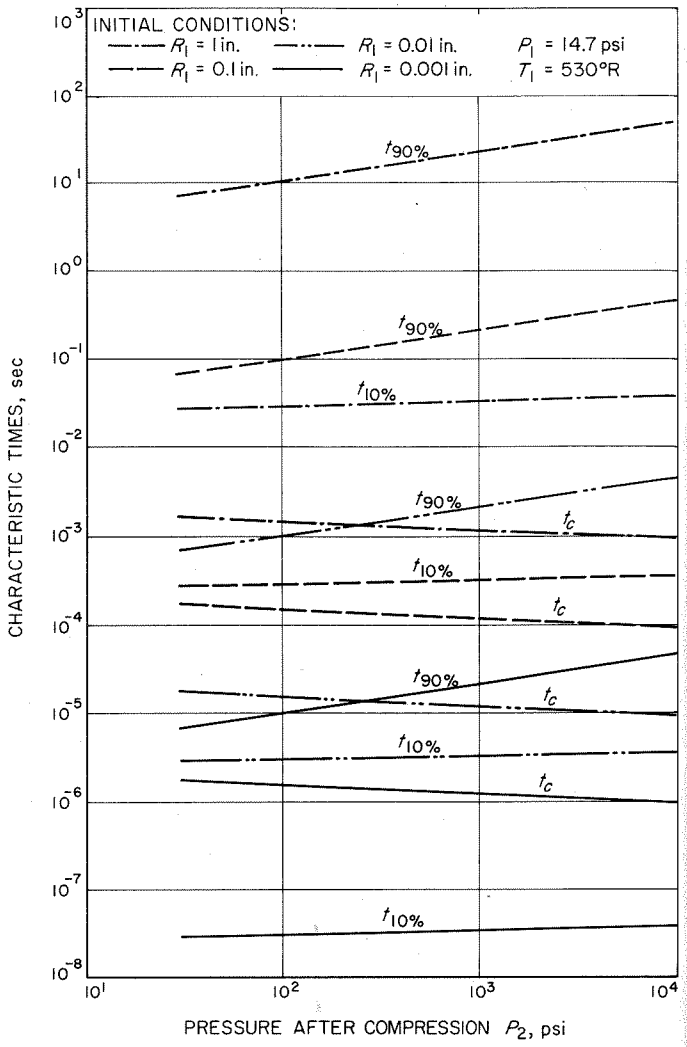

Fig. I-4. Collapse and cooling times for air bubbles of different sizes

4. Dissolving of the Gas Phase into the Liquid

For the problem of a spherical gas bubble dissolving in an unsaturated liquid, Ref. I-14 referred to the work of Epstein and Plesset (Ref. I-16), who had solved this problem for air dissolving in water at 532°R under a constant pressure. For a bubble initially at radius R, pressure P_1, and subsequently compressed to pressure P_2, the time to dissolve is given by the following relationship:

$$t_d = 1.5 \times 10^8\, R_1^2\, (P_2/P_1)^{-2/3}. \tag{I-12}$$

Considering a pressure ratio $P_2/P_1 = 40$, and an initial radius $R = 0.010$ in., the value for t_d is 8.9 sec. With respect to the thermal equilibria time, t_d is much larger by a factor

of 10^2 to 10^3. However, for flow lengths much longer than the shock structure, the dissolution of the gas phase must be considered.

The consideration of whether the bubbles are insulated or at thermal equilibrium is effectively bypassed by considering regions just beyond the shock structure. The consideration for solution equilibrium depends upon the phase constituents, but, for species such as air and water, the dissolution of phases can be considered negligible on a shock structure scale.

In summary, for an atmospheric to 10^4 psia range of pressures over a 0.1 to 10 range of volume ratios, the flow can be considered isothermal through normal shock structure, and the relationships for the most important flow parameters such as pressure, velocity, density, and volume ratio can be derived directly from the conservation relations of mass and momentum and the isothermal equation of state applying on both sides of the shock structure, but ignoring the relaxation processes within. The experimental work done in the following sections will demonstrate how well this approach approximates the actual flow characteristics over a wide range of shock strengths. Only in the discussion of the actual flow model in Section II will consideration of the relative velocity between phases be necessary.

5. Mach Number

Based on Eq. (I-5), a Mach number can be defined in the usual form for the two-phase continuum flow:

$$M = \frac{V}{C} = \frac{V}{(1 + r_v)} \left[\frac{\rho_l r_v (1 + r_m)}{P} \right]^{1/2} \qquad \text{(I-13)}$$

This relationship is plotted in Figs. I-5 through I-10 for volume ratios of 0.5, 1.0, and 5.0, respectively. The most

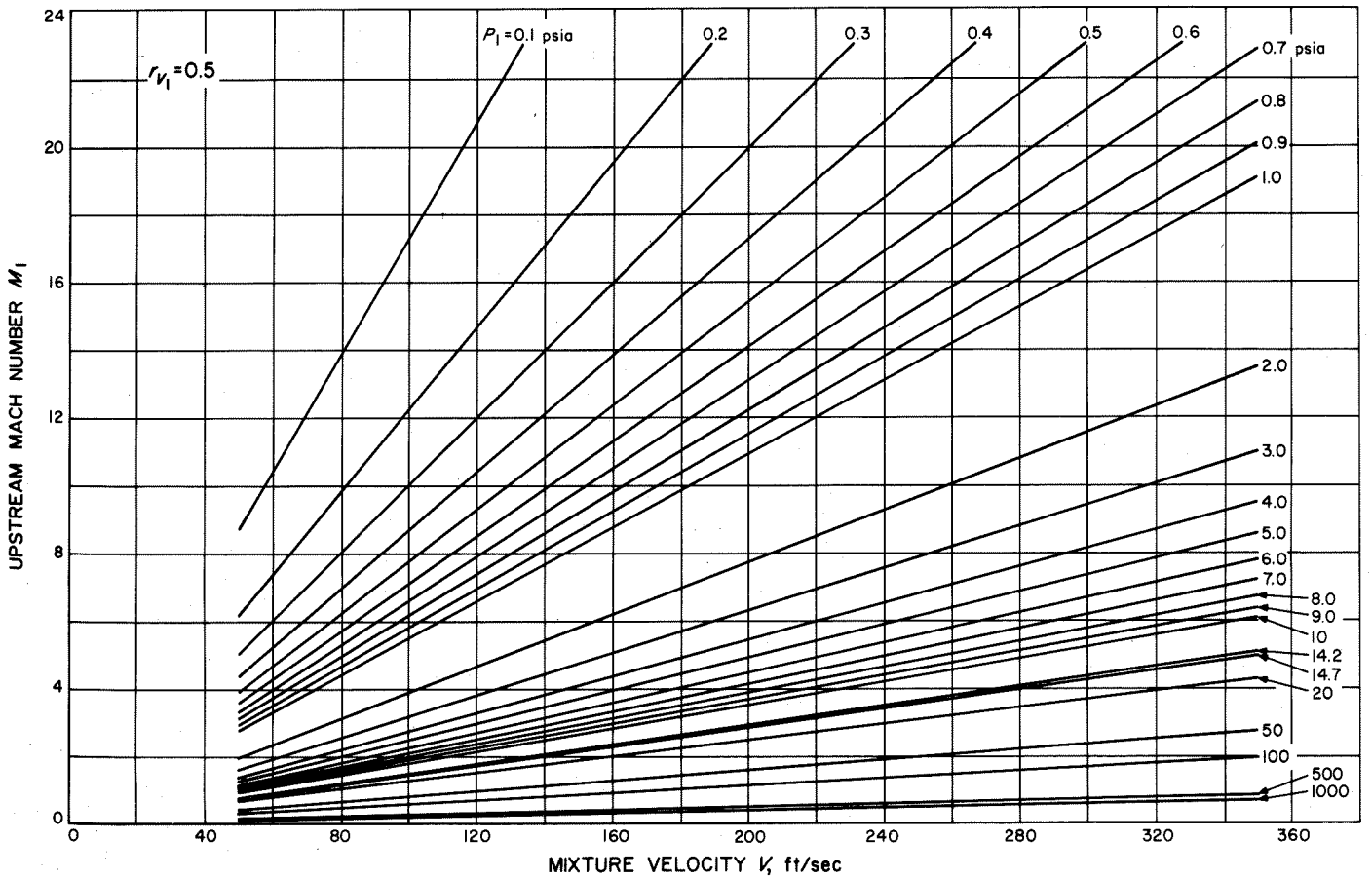

Fig. I-5. Upstream Mach number as a function of mixture velocity for various values of static pressure ($0 \leq M \leq 24$, $r_v = 0.5$)

striking feature of these figures is the Mach number in the two-phase flow, which is a strong function of both pressure and velocity, and a weak function of volume ratio in the range considered. A reduction in upstream pressure causes a rapid rise in Mach number particularly as the pressures reach the vicinity of the vapor pressure of water at standard temperature. For the supersonic tunnel described in Section II, a theoretical maximum Mach number approaching a value of 100 exists near the vapor pressure of water at standard temperature.

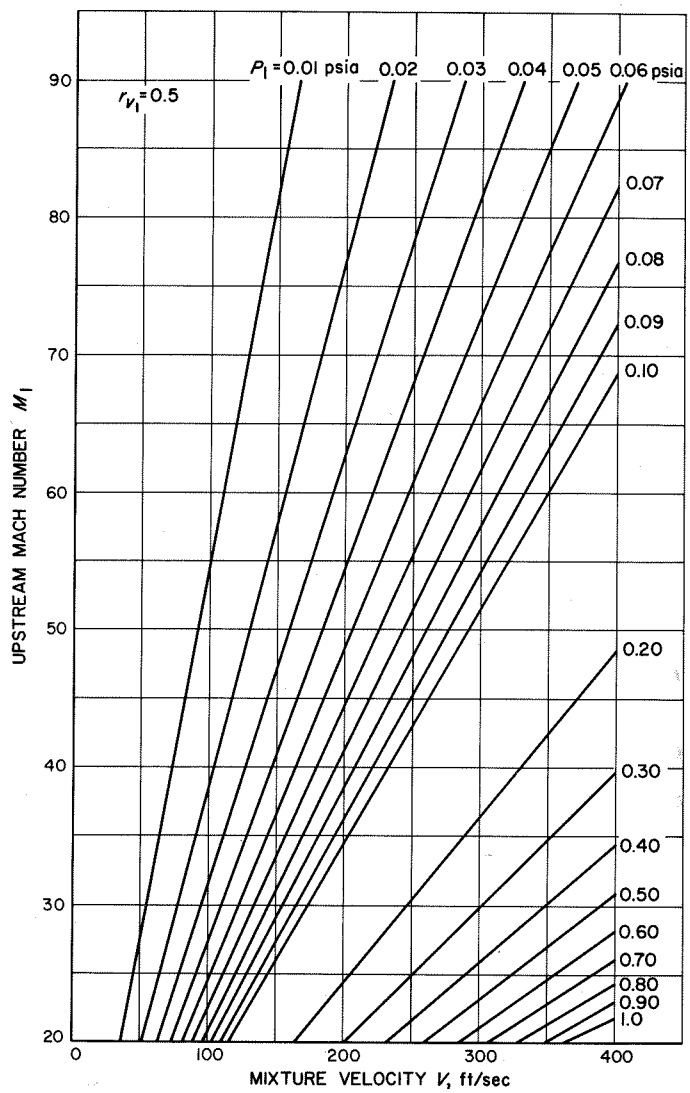

Fig. I-6. Upstream Mach number as a function of mixture velocity for various values of static pressure ($20 \leq M \leq 90$, $r_{V_1} = 0.5$)

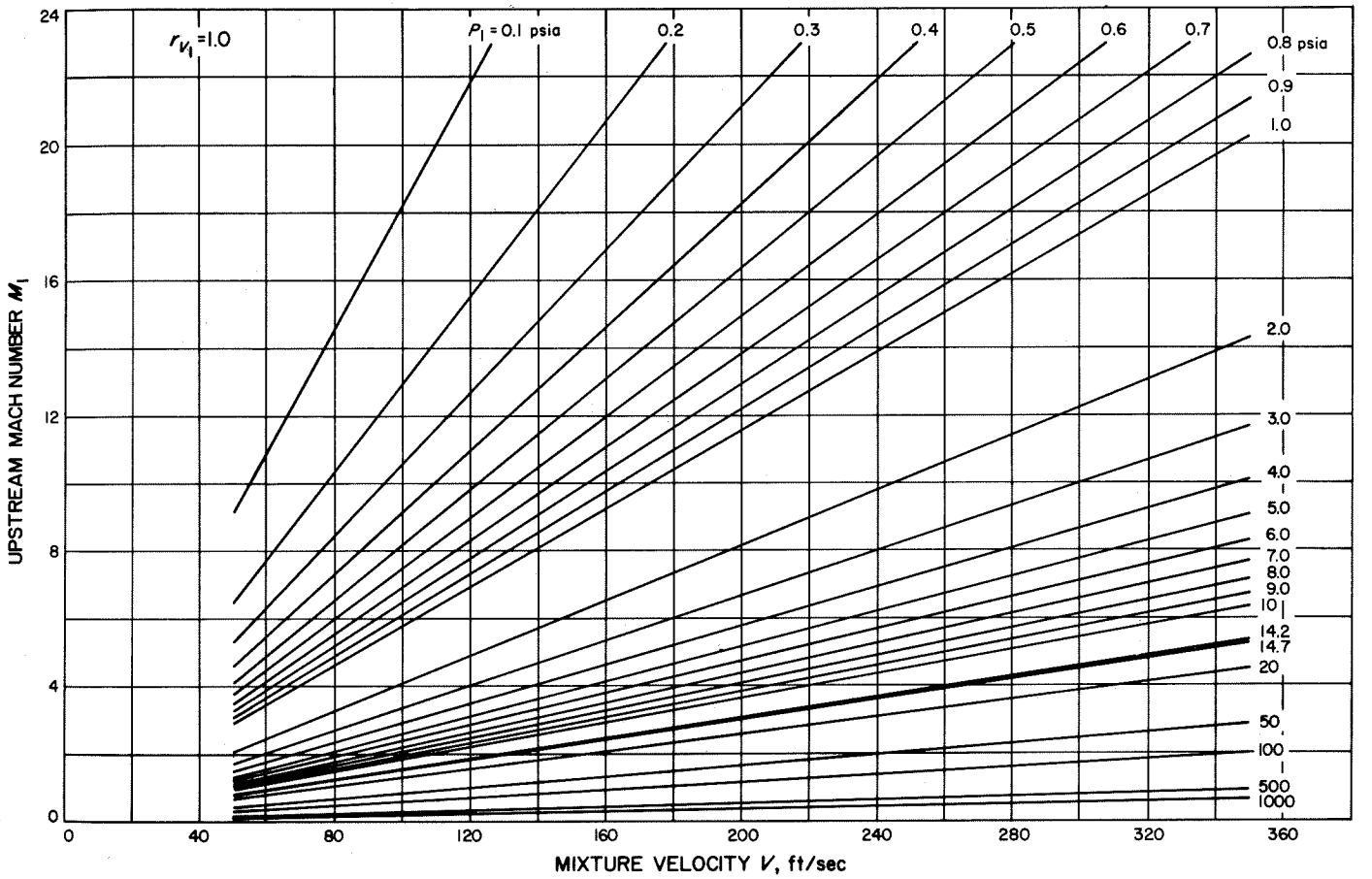

Fig. I-7. Upstream Mach number as a function of mixture velocity for various values of static pressure ($0 \leq M \leq 24$, $r_v = 1.0$)

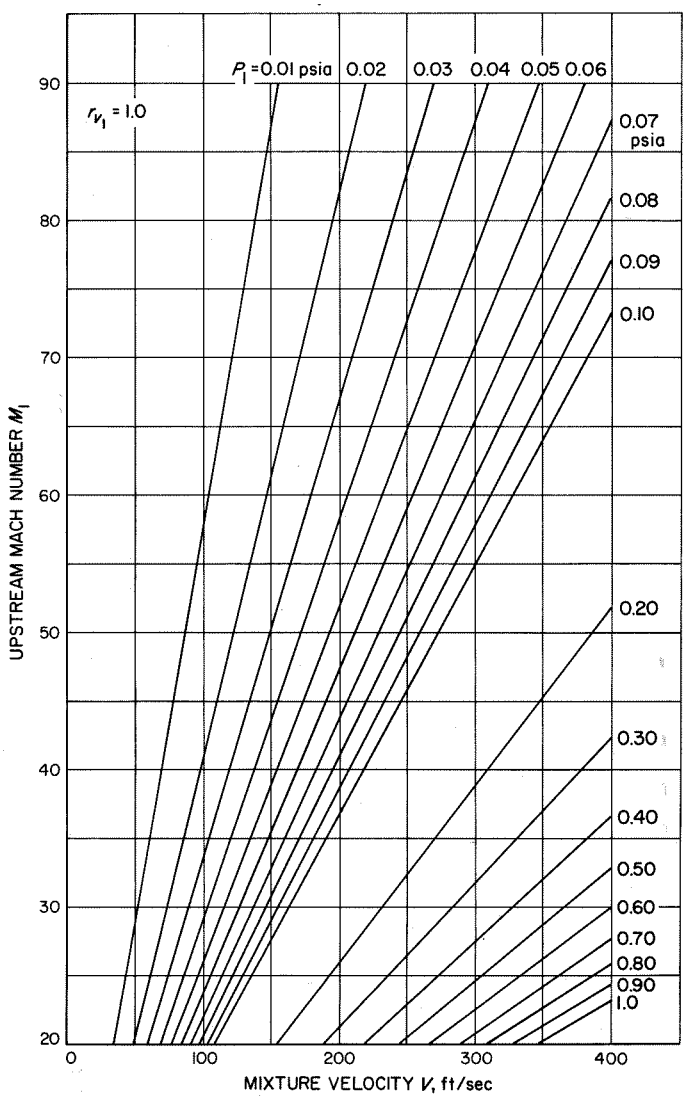

Fig. I-8. Upstream Mach number as a function of mixture velocity for various values of static pressure ($20 \leqq M \leqq 90$, $r_v = 1.0$)

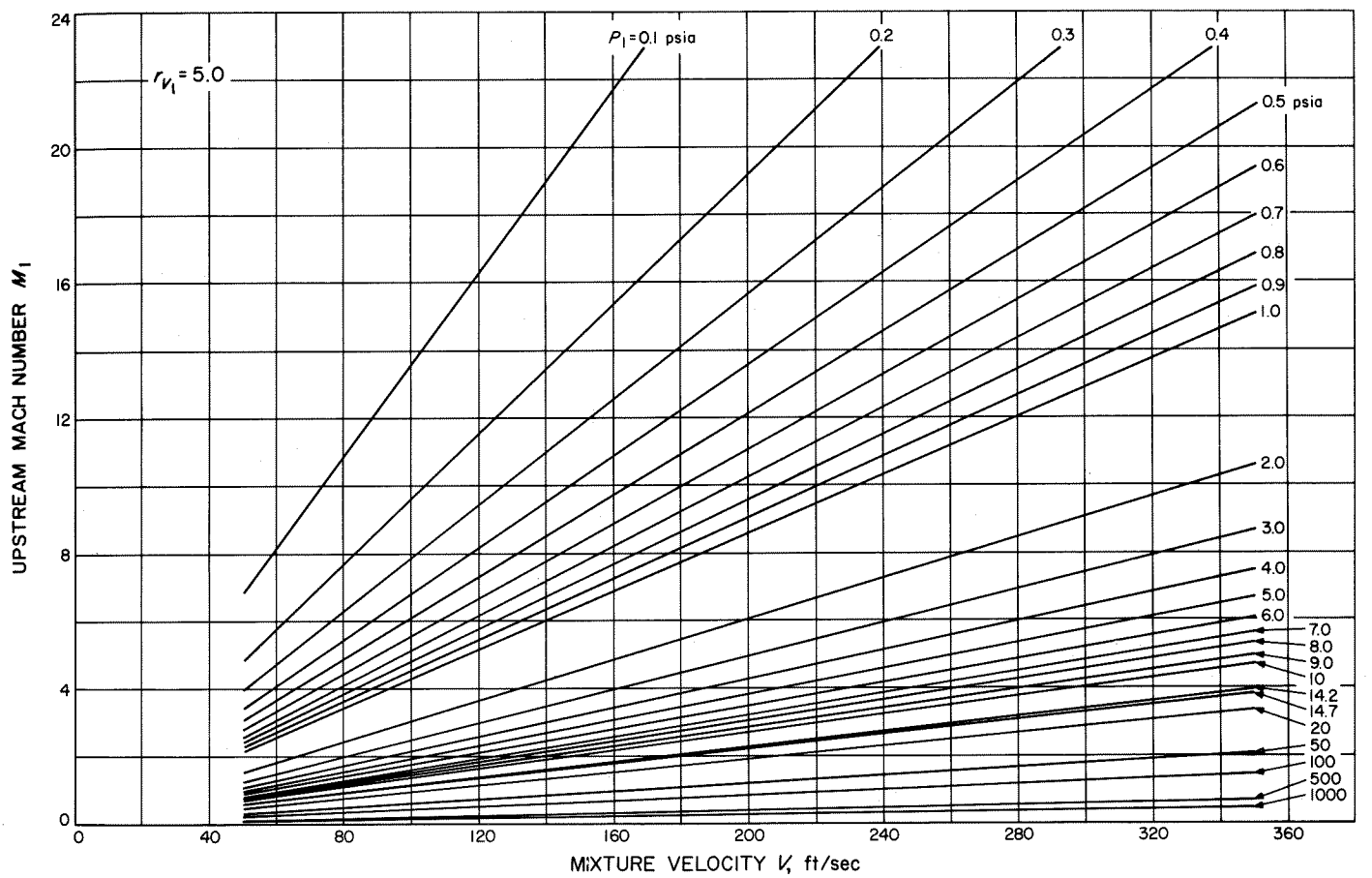

Fig. I-9. Upstream Mach number as a function of mixture velocity for various values of static pressure ($0 \leq M \leq 24$, $r_v = 5.0$)

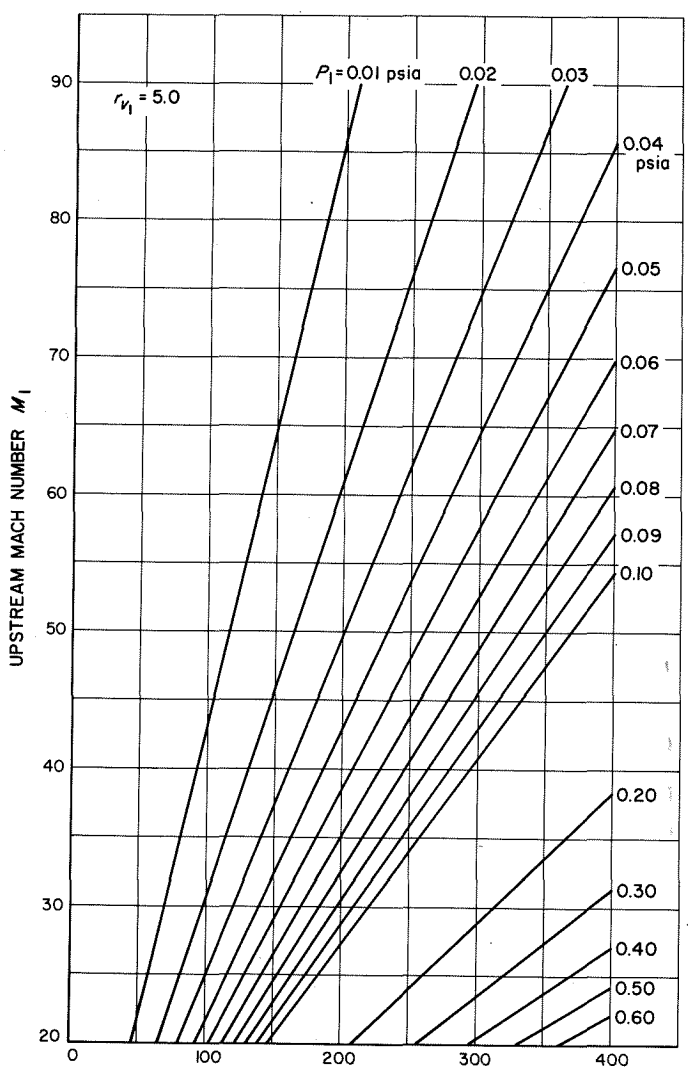

Fig. I-10. Upstream Mach number as a function of mixture velocity for various values of static pressure ($0 \leq M \leq 24$, $r_v = 5.0$)

Nomenclature

c	velocity of sound (ft/sec)
D	bubble diameter (ft)
D_a	thermal diffusivity of air (ft²/sec)
M	Mach number
m_g	mass of gas (slug/ft³)
m_l	mass of liquid (slug/ft³)
n	summation number
P	mixture pressure (lb/ft²)
R	bubble radius (ft)
R	universal gas constant (ft²/sec²-°F)
r_m	gas-to-liquid mass ratio
r_v	gas-to-liquid volume ratio
S	entropy (BTU/lb-°R)
t_c	time to first minimum bubble radius (sec)
t_d	time for gas to dissolve (sec)
T	mixture temperature (°R)
T_g	gas phase temperature (°R)
T_l	liquid phase temperature (°R)
$\mathcal{V}_g$	volume of gas (ft³)
$\mathcal{V}_l$	volume of liquid (ft³)
V	velocity of mixture (ft/sec)
V_g	velocity of gas phase (ft/sec)
V_l	velocity of liquid phase (ft/sec)
W	molecular gas weight
γ	ratio of gas specific heats (C_p/C_v)
Δ	increment
ρ	mixture density (slug/ft³)
ρ_g	gas density (slug/ft³)
ρ_l	liquid density (slug/ft³)
Σ	summation
σ	surface tension (lb/ft)
τ_c	time to first minimum of bubble radius (sec)

References

I-1. Elliott, D. G., "Two-Fluid Magnetic Hydrodynamic Cycle for Nuclear-Electric Power Conversion," *ARS Journal*, vol. 32, no. 6, pp. 924–928, June 1962.

I-2. Marble, F. E., "Dynamics of a Gas Containing Small Solid Particles," *5th AGARDograph Colloquium*, pp. 175–213, Pergamon Press, N. Y., 1963.

I-3. Mallock, A., "The Damping of Sound in Frothy Liquids," *Proceedings of the Royal Society*, series A, vol. 84, pp. 391–395, 1910.

I-4. Ackeret, J., "Experimental and Theoretical Investigations on Cavitation in Water," *Techmische Mechanik and Thermodynamic (Forschung)*, vol. 1, no. 1, Berlin, 1930.

I-5. Wood, A. B., *A Textbook of Sound*, p. 361, The Macmillan Company, New York, 1941.

I-6. Spitzer, Jr., NDRC Report No. 6, 1 - sr 20-918, 1943.

References (contd)

I-7. Silberman, E., "Sound Velocity and Attenuation in Bubbly Mixtures Measured in Standing Wave Tubes," *Journal of the Acoustical Society of America,* vol. 29, no. 8, pp. 925–933, August 1957.

I-8. Campbell, I. J., "Note on Sound Propagation in a Gas-Liquid Mixture," A.R.L. /NI/G/H7/17/0, August 1957.

I-9. Campbell, I. J., and Pitcher, A. S., "Shock Waves in a Liquid Containing Gas Bubbles," *Proceedings of the Royal Society,* series A, vol. 243, p. 534, February 11, 1958.

I-10. Heinrich, G., "Uber Stromungen von Schaumen," Zeits, f, angew. Math. Mech., vol. 22, pp. 117–118, 1942.

I-11. Charyk, J., Progress Report 2-2, Jet Propulsion Laboratory, Pasadena, Calif., November 1943.

I-12. Zwicky, F., Aerojet Engineering Corporation Report R-10, Aerojet-General Corporation, Azusa, Calif., January 1944.

I-13. Tangren, R. F., Dodge, C. H., and Seifert, H. S., "Compressibility Effects in Two Phase Flow," *Journal of Applied Physics,* vol. 20, no. 7, p. 637, July 1949.

I-14. Parkin, B. R., Gilmore, F. R., and Brode, H. L., *Shock Waves in Bubbly Water,* Memorandum RM-2795-PR (unclassified), the Rand Corporation, Santa Monica, Calif., October 1961.

I-15. Muir, J. F., and Eichhorn, R., "Compressible Flow of an Air Water Mixture through a Vertical, Two-Dimensional, Converging-Diverging Nozzle," *Proceedings of the 1963 Heat Transfer and Fluid Mechanics Institute,* Stanford University Press, 1963.

I-16. Epstein, P. S., and Plesset, M. S., "On the Stability of Gas Bubbles in Liquid-Gas Solutions," *Journal of Chemical Physics,* vol. 18, no. 11, November 1950.

II. Supersonic Two-Phase Tunnel

A. Design Requirements and Considerations

The proposed investigation of supersonic phenomena in a two-phase water-gas flow implied a tunnel having considerable flexibility in many of its basic construction and measurement parameters. No previous investigations into the completely supersonic regime of two-phase flow had been performed prior to the present effort, and such flow characteristics as boundary-layer buildup, shock thickness, shock visibility, flow stability, and total head pressure were uncertain. Furthermore, limited time for tunnel construction and operation made accommodation of variations in these parameters by adjustments of the tunnel during actual operation desirable.

Mach numbers of three or greater in the tunnel test section were needed to provide information applicable to the two-phase MHD Power Generator being developed at JPL by Elliott and others. Thus, for a test section having a transverse cross section of 1 in.^{2} at volume ratio (r_v) near 1.0, a water pump capable of about 600 psi at 500 gal/min was required. A water pump in the hydrodynamic laboratory at JPL having a capacity of 720 gal/min at 1100 psi made possible a design point of Mach 5 at atmospheric pressure with a 1½-in.^{2} test section.

Water and gas mixing for volume ratios near 1:1 could be accomplished by introducing gas into a water flow, or introducing a water spray into a gas flow. Most previous studies of the various types of two-phase liquid-gas flows used a water flow with gas injected through perforated or porous tubes lying crosswise in the flow. To prevent cavitation and excessive drag, the cross section at the injection point must be large relative to the throat of the test section. The distribution of the bubbles is difficult to control, however, and the bubbles tend to be larger than desired for such high-capacity flows. Further, shock waves could be unpredictable and uncontrollable, if the arrangement were designed to reach Mach 5.

To reach the necessary water velocities (exceeding 300 ft/sec in the test section) and have reasonably homogeneous distribution of gas and water, a mixer of small water tubes about which gas would be injected seemed very desirable. Elliott, et al., Ref. II-1, used such devices in prior experiments with reasonably good results, although two problems were immediately inherent: the increased surface area of such small tubes presented considerable frictional drag, and there was a significant pressure drop in the gas flowing transversely toward the center of the tube bundle. Preliminary calculations indicated that water velocities of approximately 320 ft/sec with a pressure drop of 1000 psi could be expected in commercially available stainless steel tubes having an inside diameter of 0.070 in. and a length/diameter not exceeding 18.

The problem of gas pressure drop was solved previously in the design of an injector of this latter type that regularly increased the angle of the tubes to the plane of the outlet face in each row of tubes beginning with the row next to the center. This solution, however, tends toward an excess concentration of liquid at the center line where the liquid velocity vectors converge. If each row of tubes were bent in a smooth curve to make their outlets parallel at the outlet face and their inlets separate according to the bending angle, sufficient clearance could be allowed

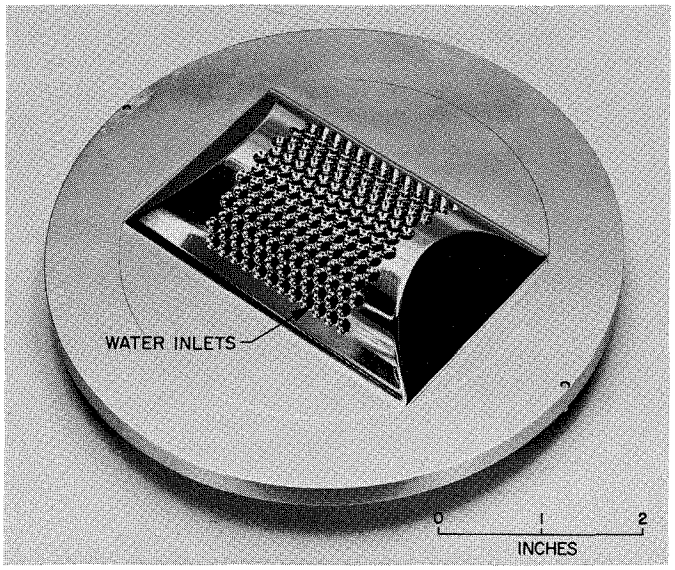

Fig. II-1. Two-phase injector showing water entrant ports

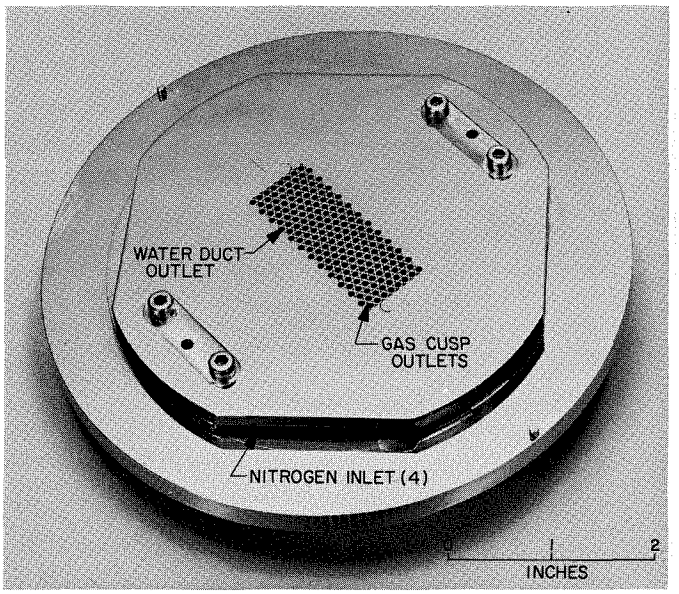

Fig. II-2. Downstream face of two-phase injector

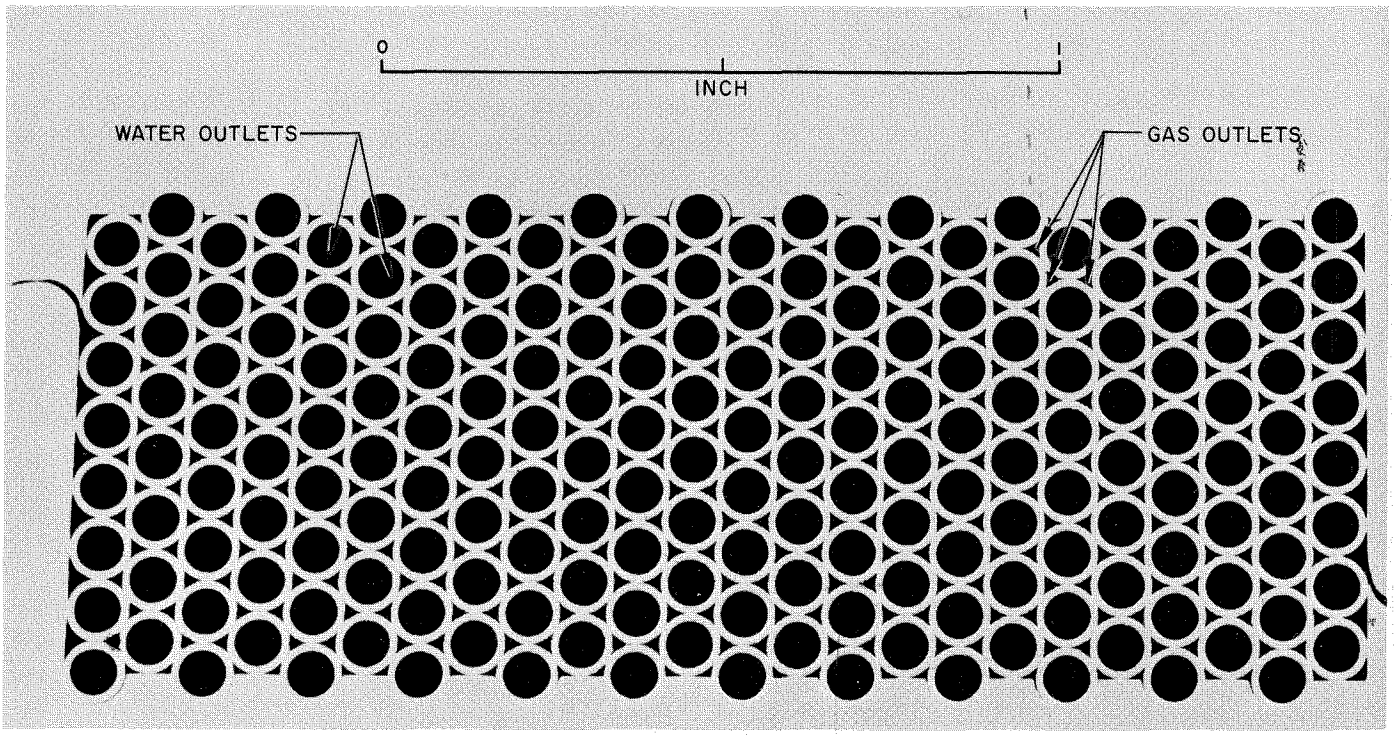

Fig. II-3. Enlargement of two-phase injector showing water tube and nitrogen cusp exits

near the tube inlet to preclude a significant pressure loss toward the center of the bundle. An injector of this type was designed for the two-phase tunnel as a replaceable element to permit use of injectors of varying volume ratios, if necessary.

B. Details of Construction

Figure II-1 shows the upstream face of the injector in which each tube has a polished and contoured entry channel. Figure II-2 shows the downstream face at which all tubes form a parallel outlet pattern. The gas inlet to the area surrounding the tubes is located between the outlet face clamps and the upstream diaphram plate. Figure II-3 shows the small triangular cusps between the tubes through which the gas is ejected and subsequently mixed with the emerging water streams.

Tests were conducted with the finished injector, a rectangular duct, and a total head probe to determine the length required for homogeneous mixing of the water and gas. Beyond 7.0 in. from the injector, individual liquid jets could not be detected; therefore, a length of 8.5 in. was used as the length of the tunnel input to the test section. A minimum length is desirable to minimize boundary-layer buildup and water-gas separation.

A seat for the injector was provided between the upstream flange of the tunnel test section and the main water inlet flange, as shown in Figs. II-4 and II-5. A gas plenum chamber can be seen about the periphery of the seat with the eight symmetric holes from the nitrogen harness leading to it. O-ring seals on the downstream faces contain the water and gas, and prevent their mixing prior to the discharge plane.

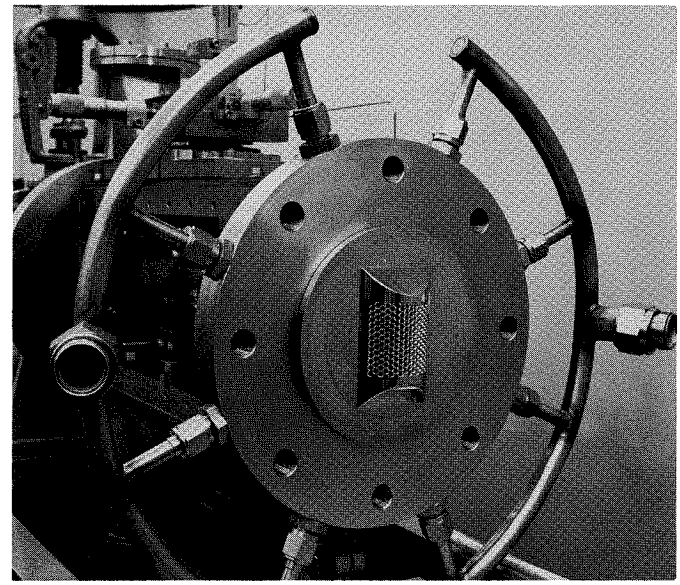

Fig. II-5. Injector in position on leading tunnel flange

Flow straightening vanes were installed in the main water inlet pipe (Fig. II-6) to prevent asymmetrical water velocities at the tube inlets.

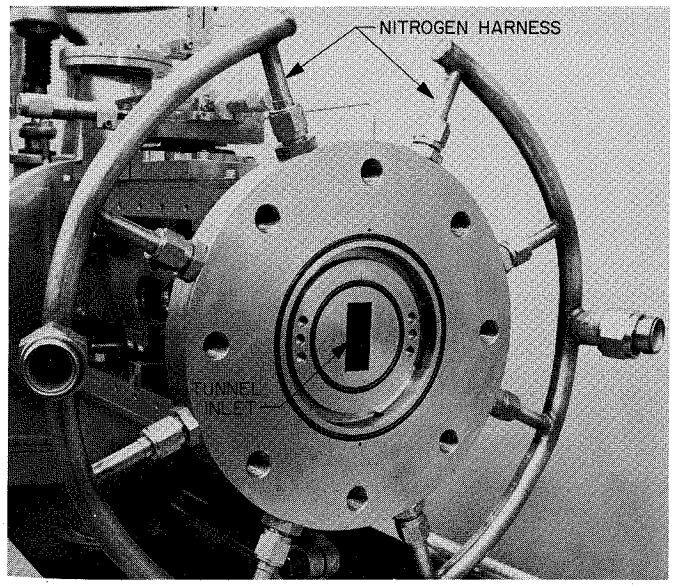

Fig. II-4. Injector seat and nitrogen harness arrangement

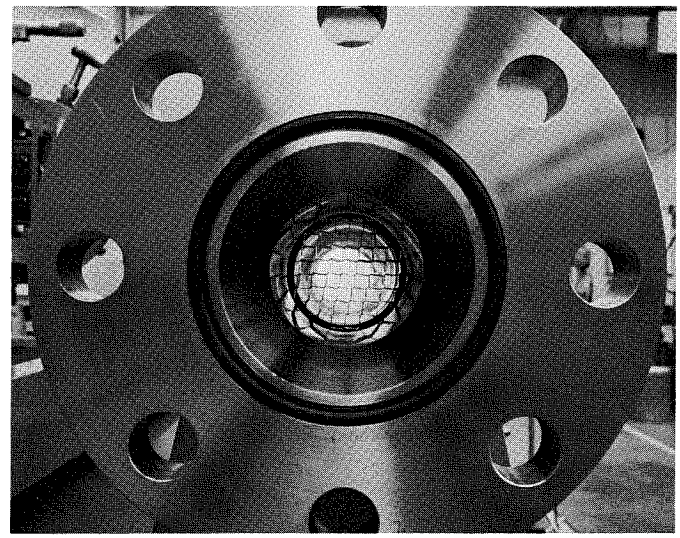

Fig. II-6. Flow straightening honeycomb in water inlet header

A filter bank of six filters provides full-flow filtering of the water for all particles larger than 50 μ. Flexible 1½-in. hoses lead from the filters into the inlet head in a plane perpendicular to the axis of the tunnel.

A rectangular test section and rectangular ducting were required to minimize gas pressure loss in the injector tube bundle and minimize the light requirements for high-speed photography in the test section. Cerini's prior experience suggested that such mixtures would be relatively opaque to transmitted light photography. Therefore, one dimension of the two-dimension flow needed to be relatively small.

The opaqueness of the flow led to another requirement: if the photography were to reveal significant characteristics of the uniform flow core, any boundary-layer whose velocity or composition or both had changed from the basic core flow should be removed just prior to the test section. Because the boundary-layer buildup rate was unknown, variable depth boundary-layer removal was necessary for at least the narrow dimension, through which all photography would be accomplished. For the long dimension, fixed removal blades were incorporated with a setting expected to be in excess of the boundary-layer thickness at the test position (Fig. II-7). In addition, the fixed blades would be a convenient holding point for a normal shock assuming that the tunnel test section could be back pressured sufficiently to produce the shock.

Containment of pressures approaching 1000 psi in a test section containing variable position walls posed a problem. Because boundary-layer removal must occur just ahead of the test section, and because the removal knife must be flush with the test section wall to preclude changes in the photographable flow, a complete O-ring seal of the side wall could not be made. Also, the horizontal boundary-layer blade edges had to appear in a portion of the transparent side wall that would permit photographs of normal shocks. Therefore, O-ring channels were cut from a point just behind the lower leading edge of the boundary layer knife to pass toward the rear of the test section, then up and around a circular junction with

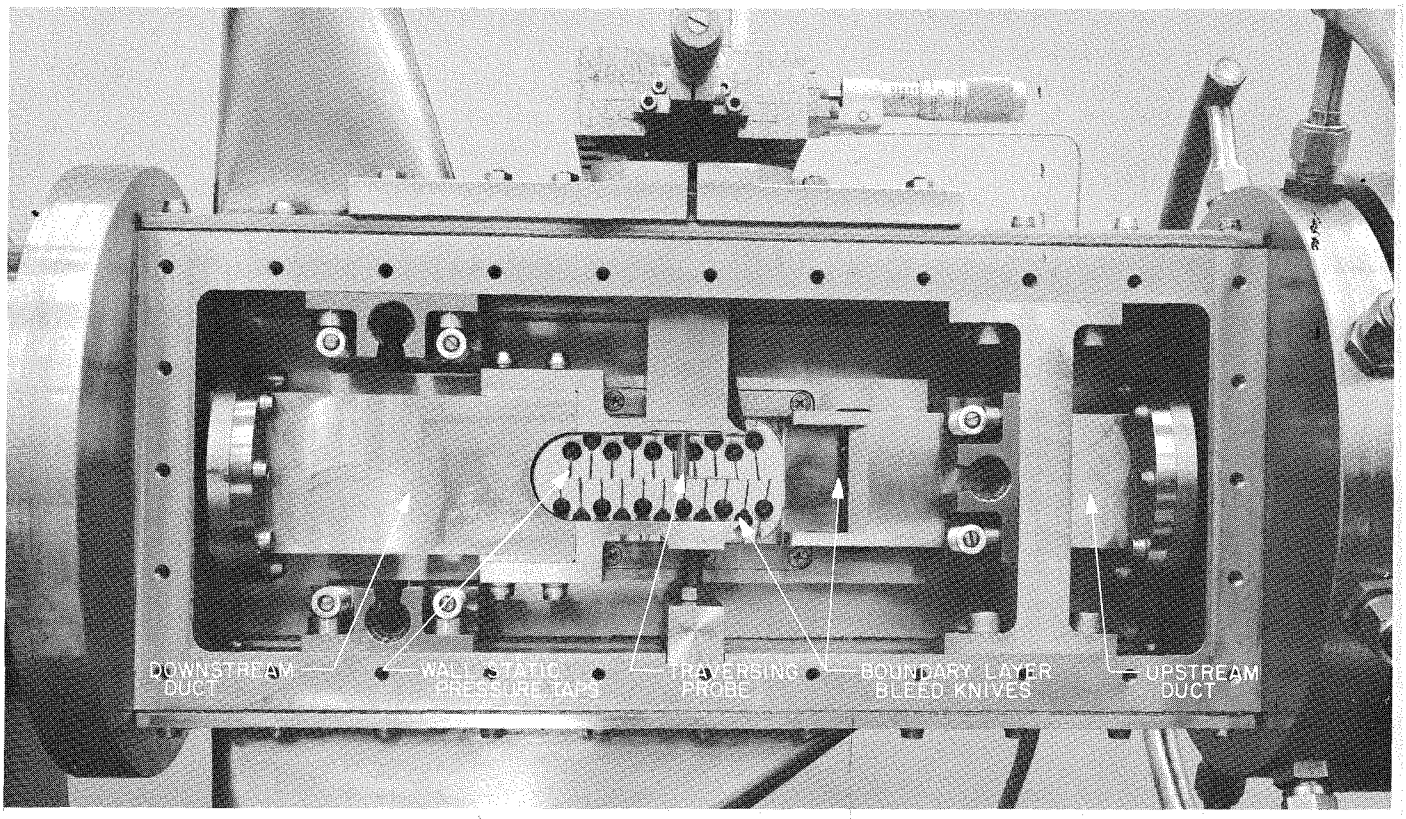

Fig. II-7. Tunnel assembly with side plate and carriage removed

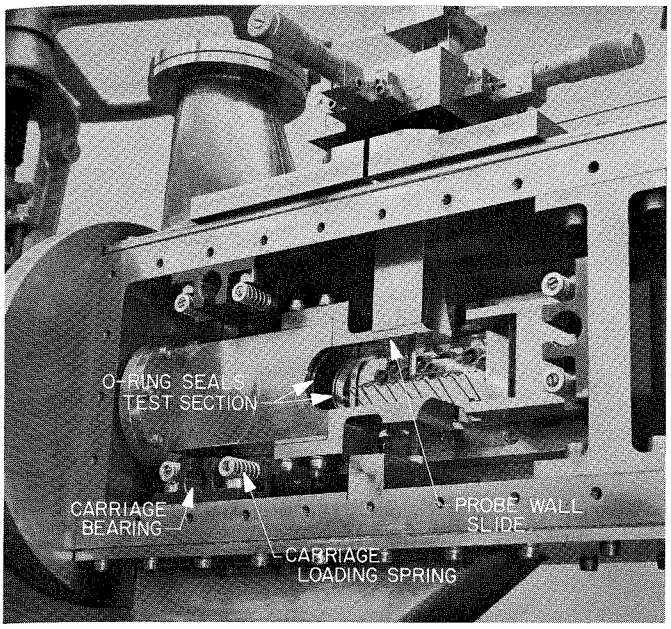

Fig. II-8. Three-quarter view showing boundary layer knives, O-ring seals and sliding probe plate

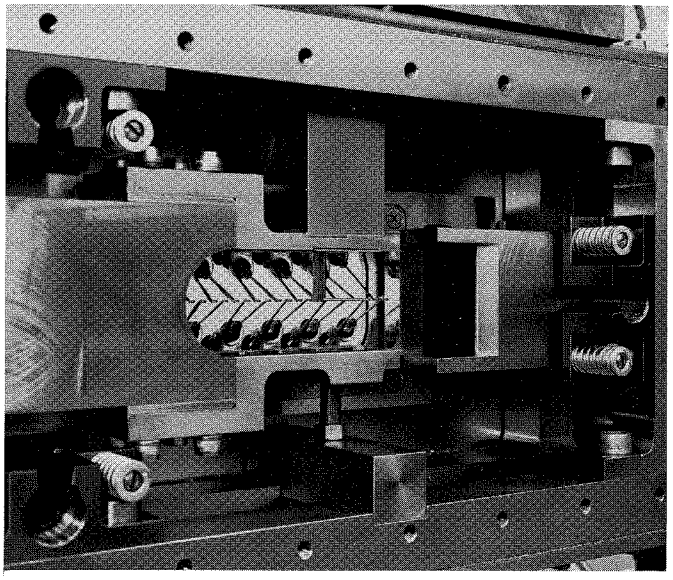

Fig. II-9. Tunnel test section showing forward duct and carriage bearing block details

the rear portion of the tunnel, and, finally, forward along the upper boundary-layer knife to the smoothing plate for the total head probe, as shown in Fig. II-8. The transparent side walls, then, fit between the upper and lower boundary-layer knives, and were sealed along most of this junction by the O ring.

A second containment jacket was required to collect the high-speed (300 ft/sec) water-gas spray removed by the boundary-layer knives to prevent it from interfering with the photographic equipment. Therefore, an outer case was designed through which the transparent side wall outer face could protrude. An O-ring seal between the transparent side-wall protrusion and the outer case provided the necessary sealing.

Side-wall movement with the inner and outer O-ring restrictions is accomplished by a carriage in three bearings. The bearings are ball extensions from the carriage; they rest in a matching seat on the end of a screw; the screw passes out through an O-ring-sealed gland in the side wall. The screw load is borne by split bearings with a ball-guide channel and matching threads; each bearing is mounted on the main tunnel structural members (Figs. II-7, II-8, and II-9). Three bearings were used to permit adjustment from the outside of the side walls to their various convergent, divergent, or flush positions while the walls were under a load. To allow some degree of convergent-divergent settings and minimize the length of the light path, side-wall thickness was limited to approximately 3 in.; this, however, constricted the carriage and bearing size. With full stoppage of the downstream tunnel, approximately 10 in.^{2} of side wall would be subjected to ultimate pressures of 1000 psi, producing a thrust of 5 tons on the three bearings.

For resistance to water corrosion and in possible later use of sodium in the tunnel, all metal parts were fabricated from stainless steel. Load requirements for the carriage made necessary processing of the stainless steel bearings on the carriage to an ultimate tensile capability near 220,000 psi. This was done with a "Tuftriding" process on basic 17-7 material.

Figure II-10 shows the carriage on the inside face, and Fig. II-11, the outside face. In both figures, the bearing stubs are shown in place between the spring seats; it is the spring pressure on the spring seats that keeps the assembly in the outermost position against the bearing adjusting screws. Figure II-12 shows the carriage in place in the tunnel with the outer casing removed. Figures II-13 and II-14 show the upstream tunnel extension that will be used at pressures below atmospheric for investigations at high Mach numbers. The extensions prevent oblique shock waves from forming upstream of the horizontal boundary-layer blades. Figures II-13 and II-14 also show

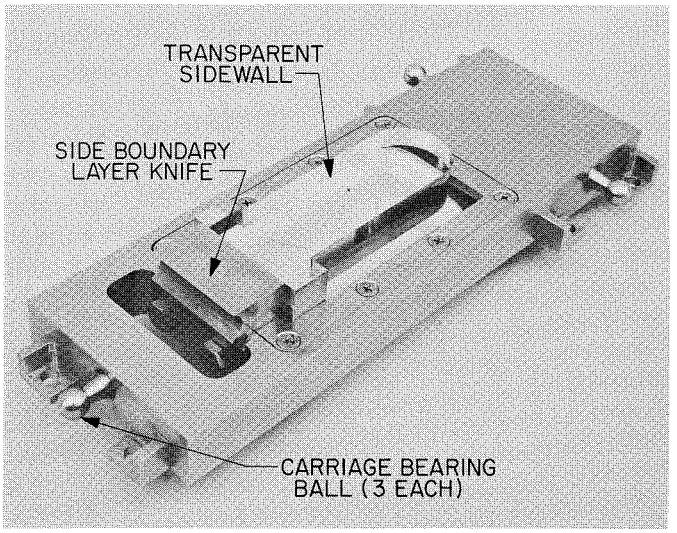

Fig. II-10. Side wall carriage assembly showing inner face and side boundary layer knife assembly

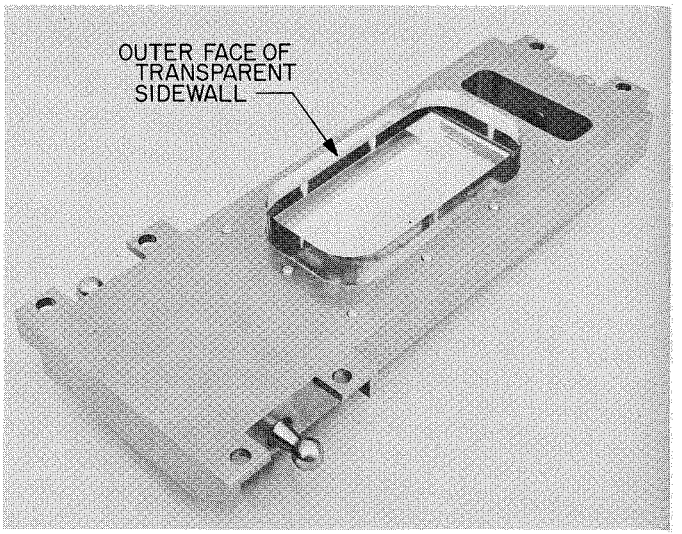

Fig. II-11. Carriage assembly showing outer face of transparent side wall

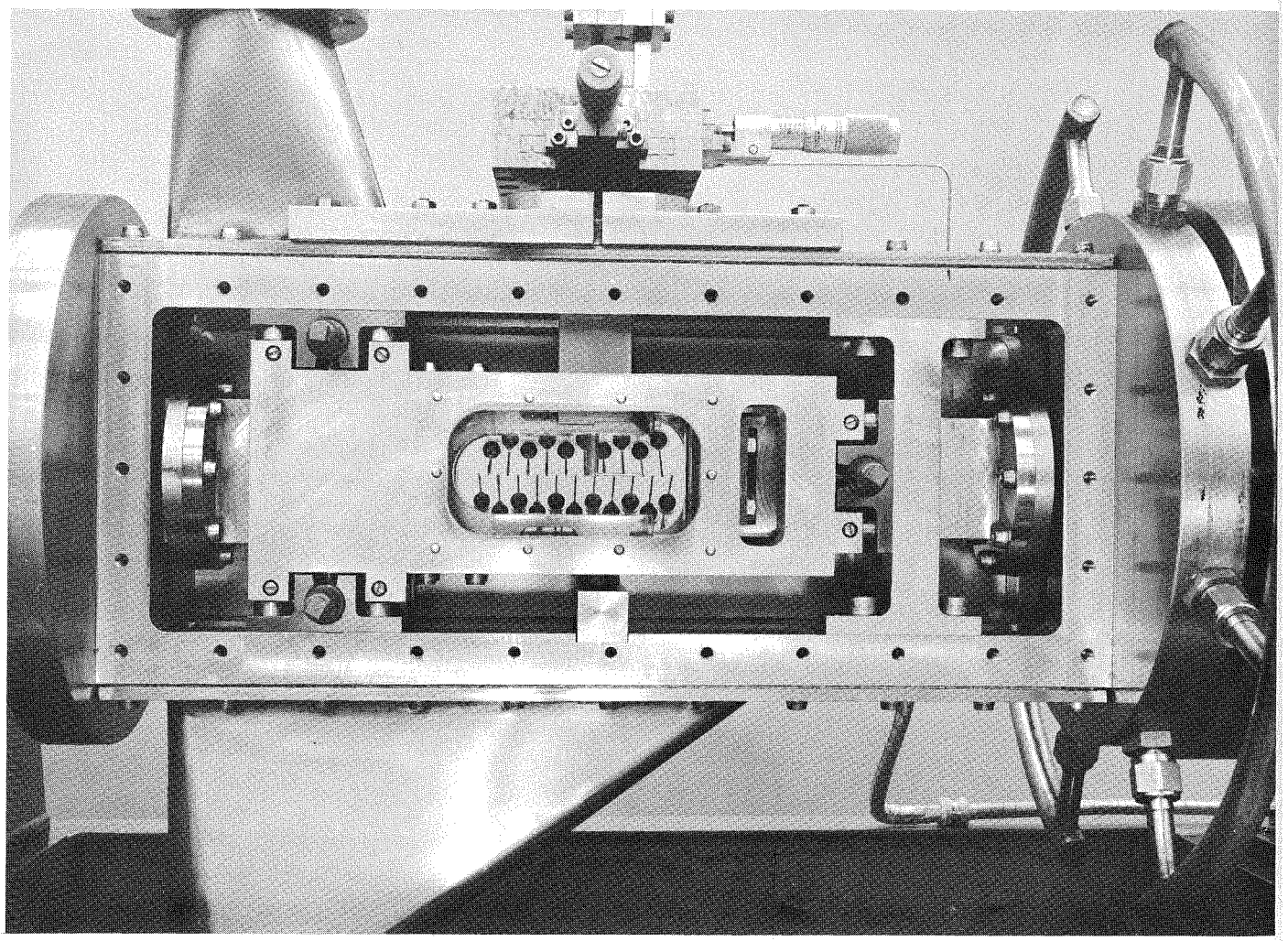

Fig. II-12. Carriage assembly installed in tunnel

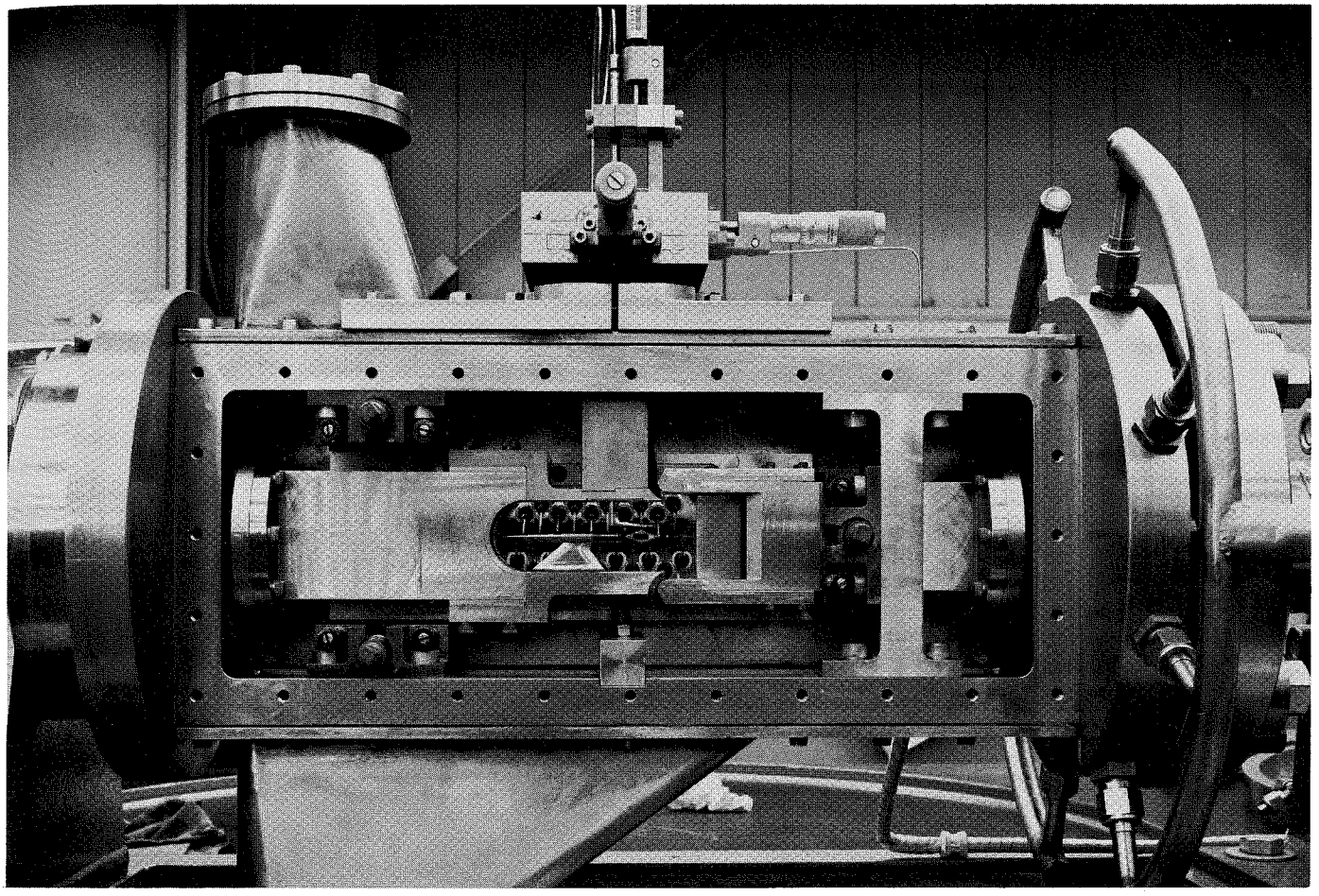

Fig. II-13. Tunnel side view showing forward duct extensions

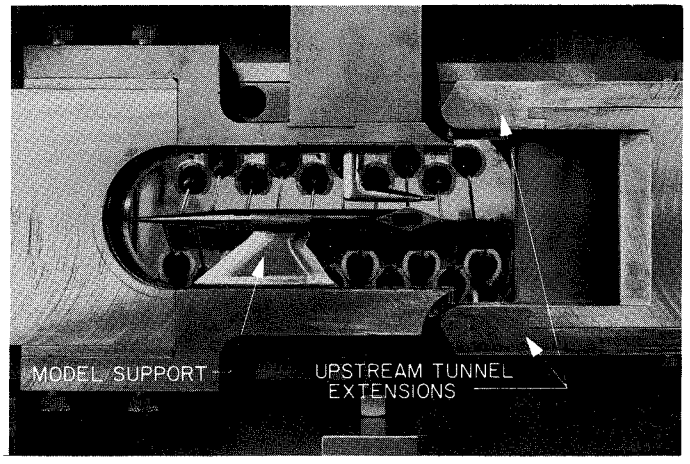

Fig. II-14. Closeup of test section showing typical model placement and forward duct extensions

an alternate lower boundary-layer blade that was constructed with a model support. Models of double wedges, cones, and balls were constructed for mounting on this support.

For protection of an observer in case of failure of the plexiglass, a 5/16-in. tempered glass window was installed over the outer face of the plexiglass (Figs. II-15 and II-16). Thus, failure of the sidewall under high pressure would not result in the ejection of the plexiglass from the side of the tunnel; the water and gas mixture in such a failure would be safely dumped between the inner and outer walls, and ejected out of the lower discharge tube into the water sump.

The fiducial marks shown in Fig. II-16(b) were etched on the internal surface of the transparent sidewall facing the camera as an aid in measuring flow velocities and in fixing the position of shock structures.

Variable back pressure on the inner downstream tunnel is provided by a 3-in. ball seat union valve, which can be seen in Fig. (II-17). A short, straight, 3-in. duct carries the core discharge to a 90° deflector that returns the water to the under floor sump.

C. Instrumentation

1. Pressure and Flow Measurement

Static pressure taps for the test section are drilled along the center line of the lighted transparent face on 0.2 in. centers. Angled ducts leading from the 0.2-in.-deep holes to fittings threaded into the outer face of

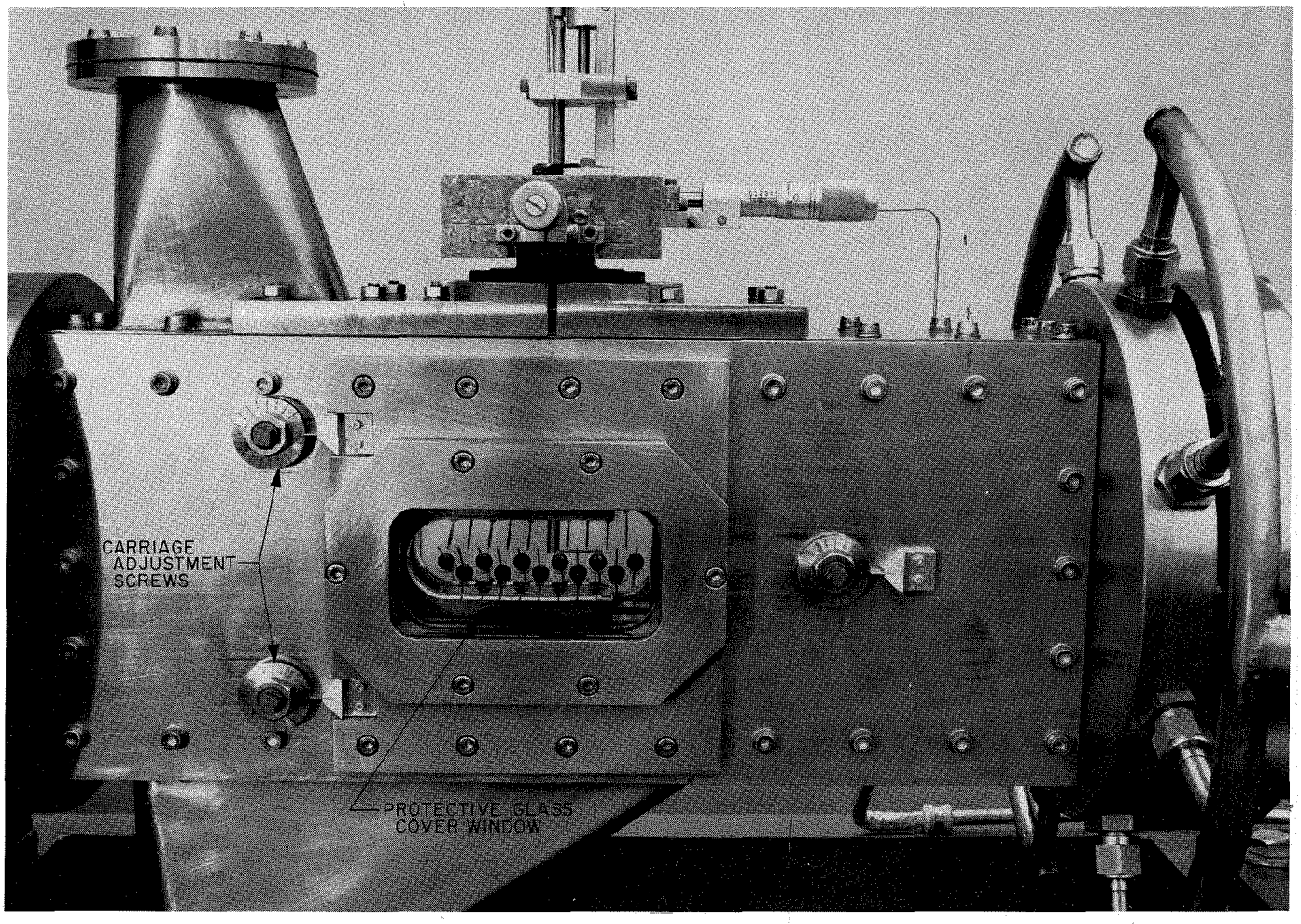

Fig. II-15. Tunnel side view showing protective tempered glass cover plate and carriage adjustment screws

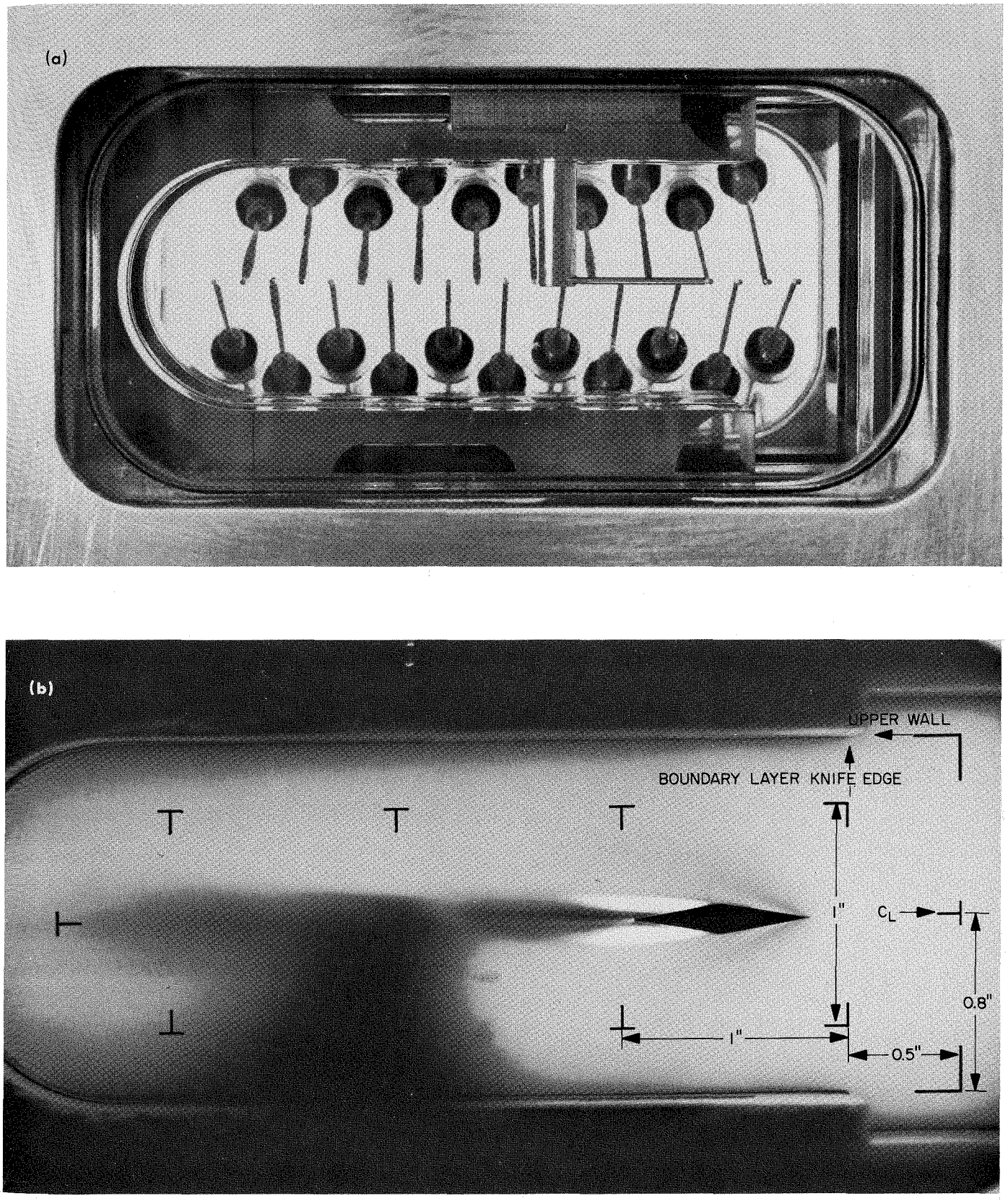

Fig. II-16. Test section view for all photographic work done during tunnel tests

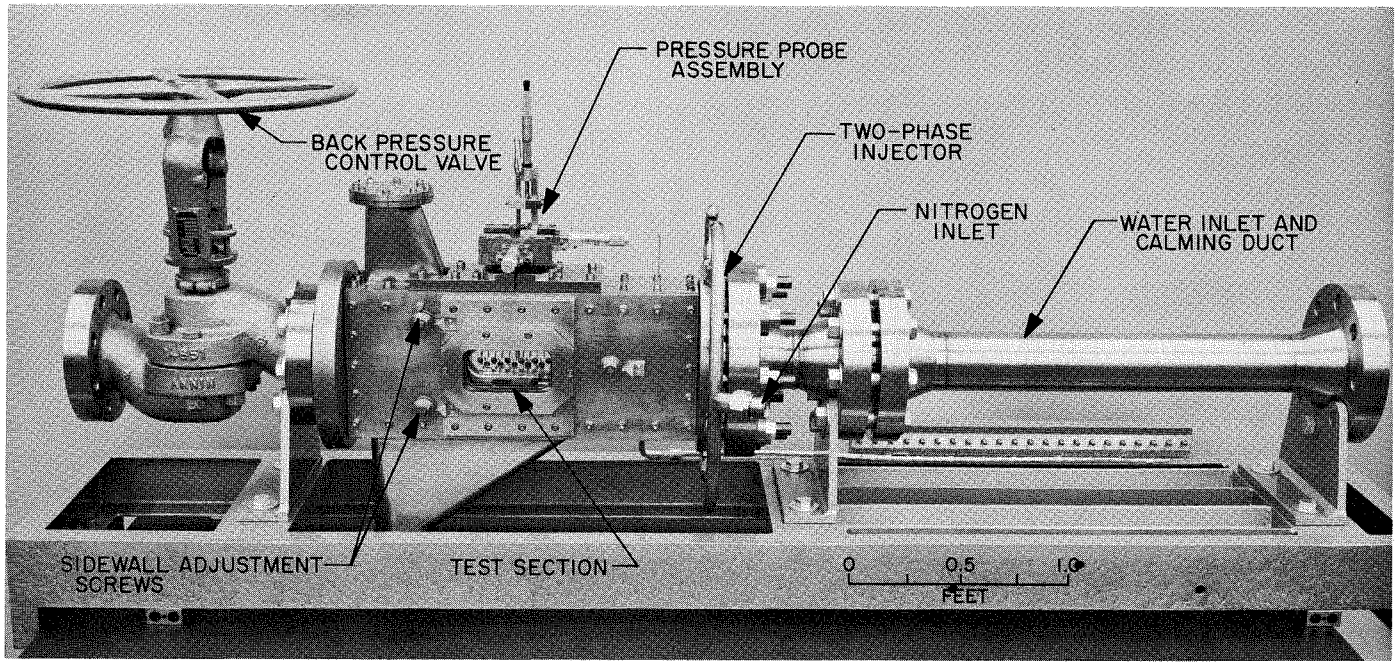

Fig. II-17. Side view of complete tunnel assembly

the transparent wall (Fig. II-18 and II-19) allow light to pass through the face with minimum obstruction, and allow simultaneous measurement of the static pressure along 21 points of the test section. Stainless steel tubing 1/16-in. in diameter leads from the transparent wall through flexible loops to a pressure tap connection fixture.

Pressure taps were also placed in the upstream and downstream ducts to monitor and measure any pressure phenomena occurring in either, and in the high pressure water line before and after the filters, and at various points prior to the injector face to monitor water pressure and detect any obstructions that develop.

Water flow was determined by a 6-in. Waugh internal vane meter that was connected to an electronic counter; nitrogen flow was determined by a Fisher-Porter tapered flow rater and associated pressure instrumentation.

2. The Probe Assembly

Because of the uncertain consistency of the flow in the upstream duct and uncertainties in any shock waves that may be formed, a total head probe providing three-dimensional positioning was designed for the test section. A duct leading to a three-dimensional gland assembly was attached to the upper boundary-layer knife. The lower end of the duct was covered by a sliding plate with a longitudinal slit 0.080 in. wide through which the probe could protrude into the flow, as shown in Fig. II-8. The upper surface of the sliding plate was backed by a Teflon seal, the edges of which continued over the plexiglass side walls to maintain an effective seal in the test section.

Two-dimensional movement of the upper gland assembly was accomplished by sandwiching stainless steel plates between clamps and linear rows of ball bearings. O-ring seals were installed between the plates to contain the 1000-psi design pressure. Vertical movement of the probe was provided through an O-ring gland in the uppermost plate. Micrometers were attached in all three axes to provide precise positioning of the probe. The gland assembly is shown in Fig. II-20.

The probe assembly consists of a tungsten rod for maximum stiffness and a stainless steel double wedge with a probe tip; the assembly was passed through the slot in the covering plate and into the tunnel. A single channel ran from the probe tip to a fitting on the outside from which the pressure could be sensed. Various probes for both total pressure and static pressure were constructed and used in the many tests performed.

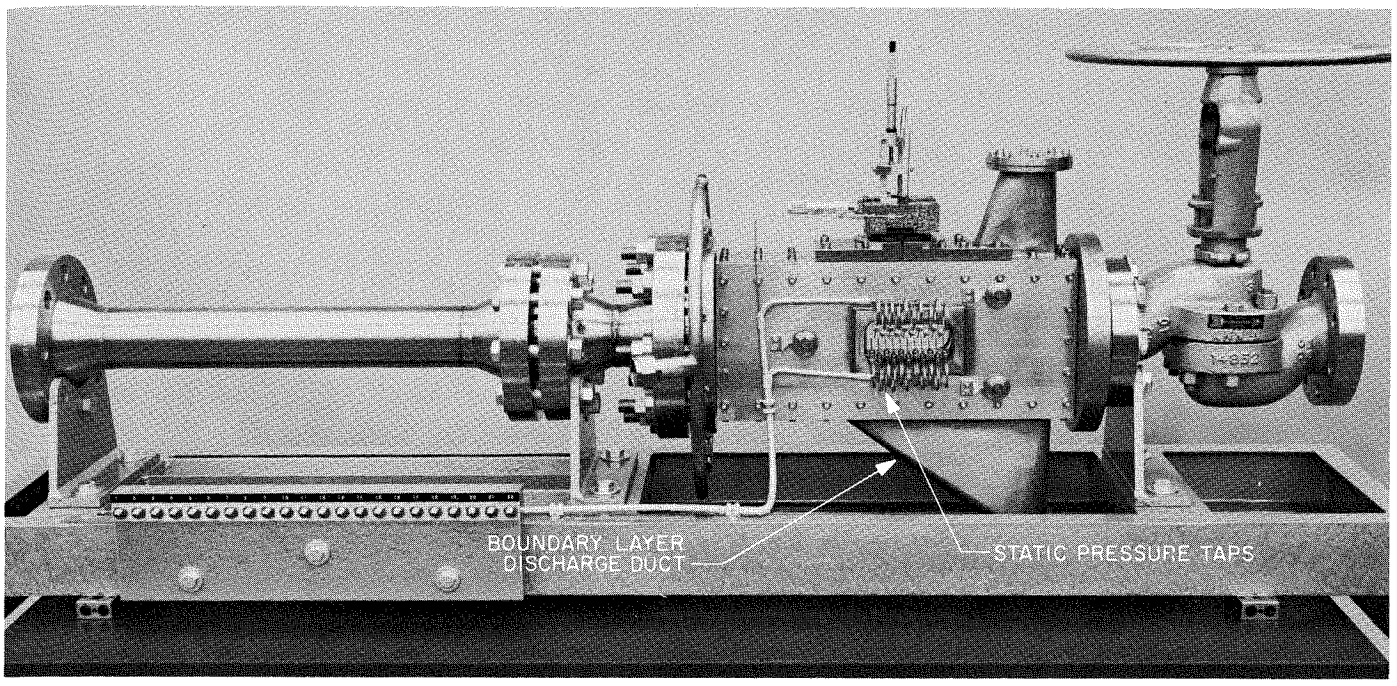

Fig. II-18. Reverse view of complete tunnel assembly

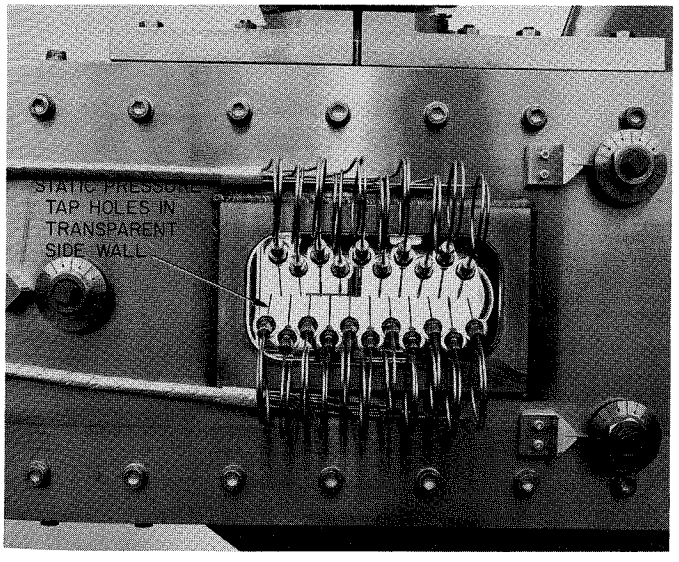

Fig. II-19. Closeup view of test section static pressure instrumentation

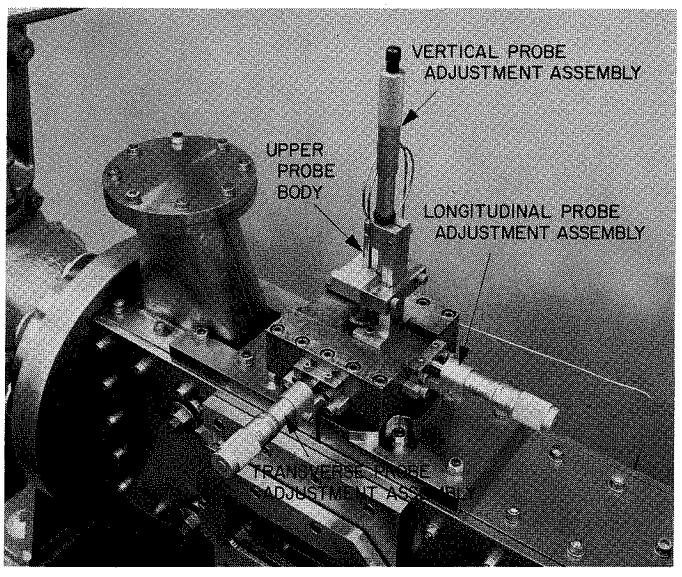

Fig. II-20. Positioning platform assembly for total head probe

3. Calibration Procedures

All pressure gauges were calibrated on secondary standards at the hydraulics laboratory. Further, calibration was made on the test stand with the lines filled with water as they would be during a test measurement; movements were zeroed for this condition.

The nitrogen-flow rater was calibrated by measuring the change in weight and the corresponding time of flow of nitrogen at various rates of flow from a high pressure tank mounted on scales. The gaseous nitrogen was passed through a heat exchanger that provided a constant temperature input to the flow meter.

The main water flow meter was calibrated periodically by an outside contractor using full-range flow tests.

D. Photography

1. Slow-Speed Still Photography

A standard 4 x 5 Speed Graphic camera was mounted on a tripod in front of the protective glass cover to photograph quasi-steady phenomena. Lighting through the test section was provided by a 500-w photo spot lamp mounted on the side of the tunnel opposite the camera, and shining through the static-pressure instrumented transparent wall. The intensity of the photo spot was controlled by an autotransformer. Figure II-21 shows the camera and lighting arrangement for free flow and tunnel flow.

Shutter speeds of $\frac{1}{50}$ to $\frac{1}{150}$ sec were adequate to freeze slight relative motion between the tunnel and the camera. Such a phenomenon as the oblique shock waves from the upper knife body and probe tip, for example, can be seen in the supersonic flow of Fig. II-22. Figure II-23 shows a normal shock positioned at the knife edges; Fig. II-24 shows a normal shock positioned just downstream of the probe tip. The intersection of the normal shock and the conical shock from the probe tip is clearly visible in Fig. II-24.

Polaroid Type 52 color and Type 413 infrared films were used to proof camera and light settings. Negative films such as Royal Pan and Plus-X were used for permanent reproducible records. Figures II-22 through II-24 were recorded on Royal Pan negative film.

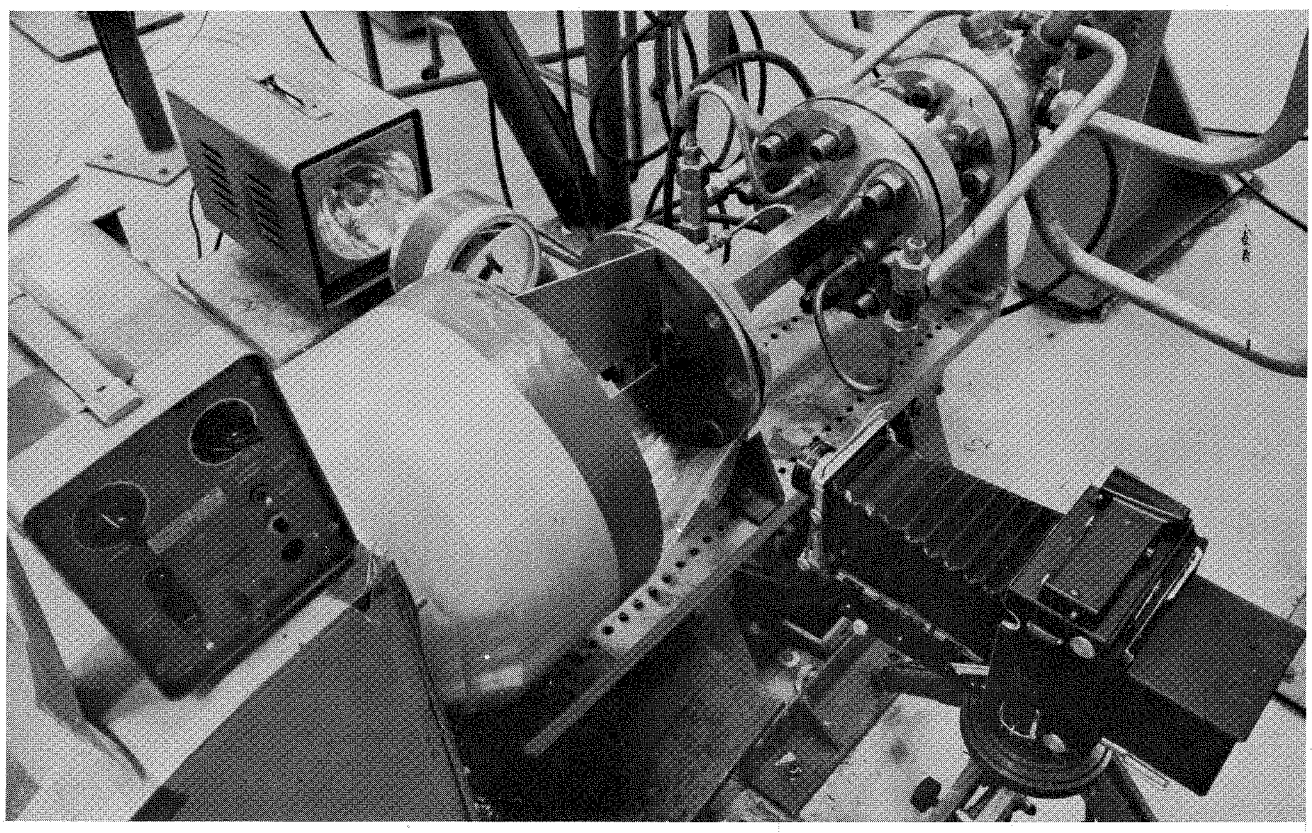

Fig. II-21. Camera and light arrangement for high-speed (½ μsec) free-flow pictures

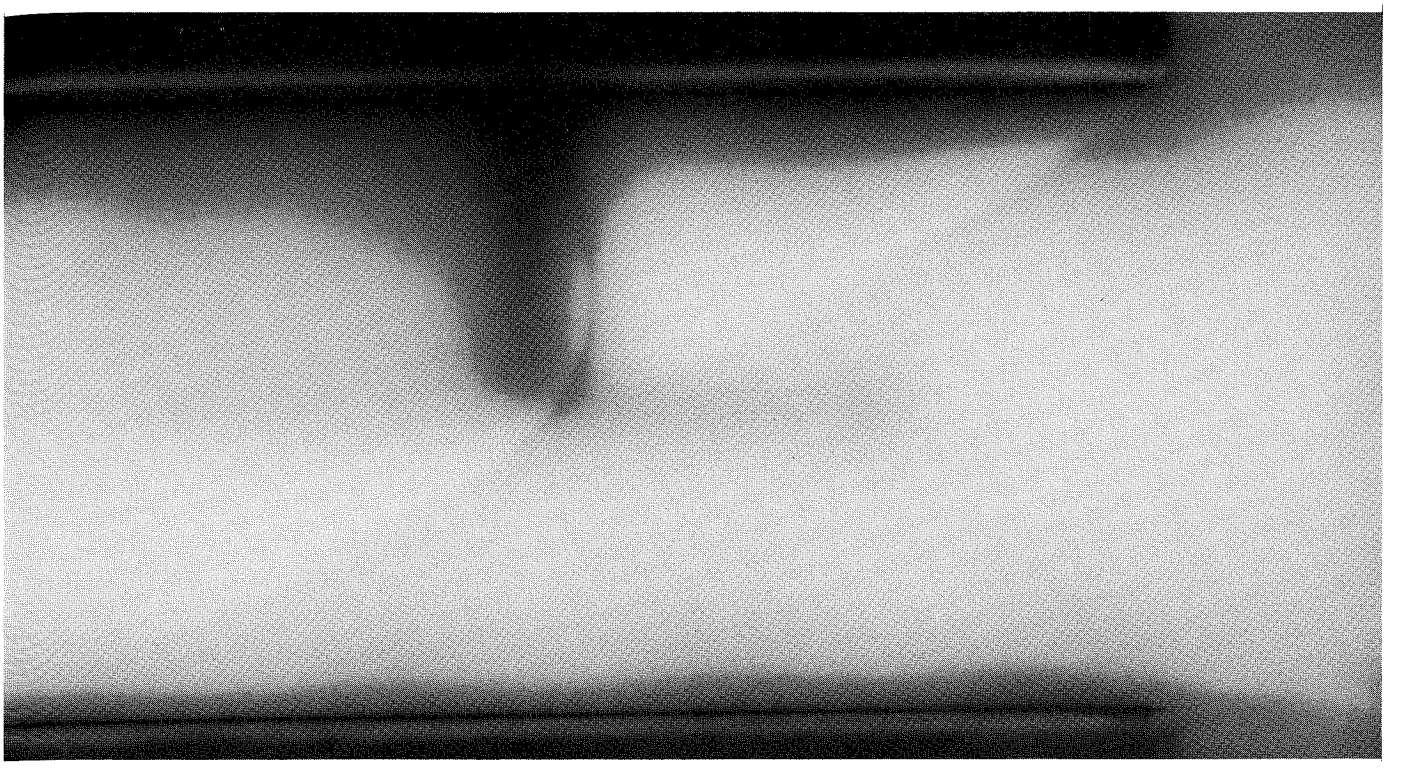

Fig. II-22. Oblique shocks from inlet and probe body at 275 ft/sec ($M = 4.2$)

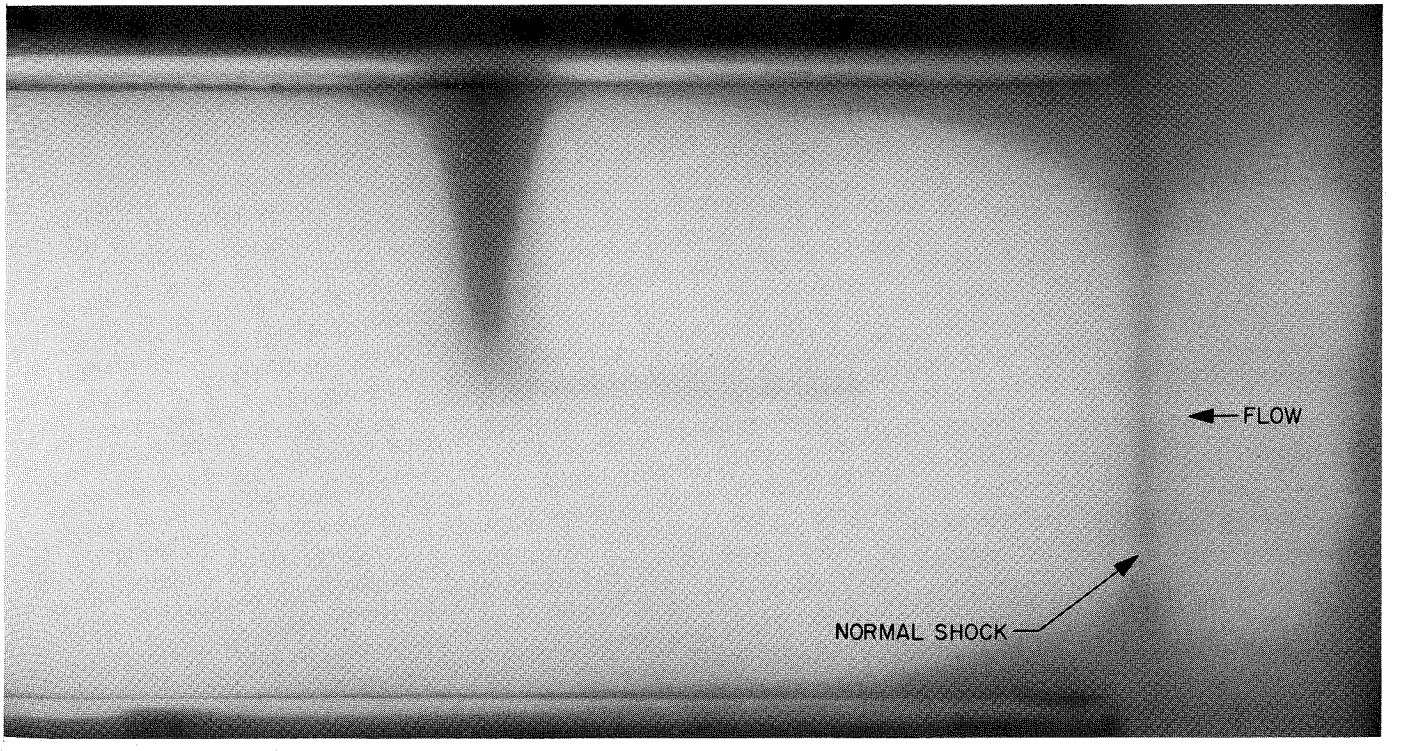

Fig. II-23. Normal shock at inlet at 275 ft/sec

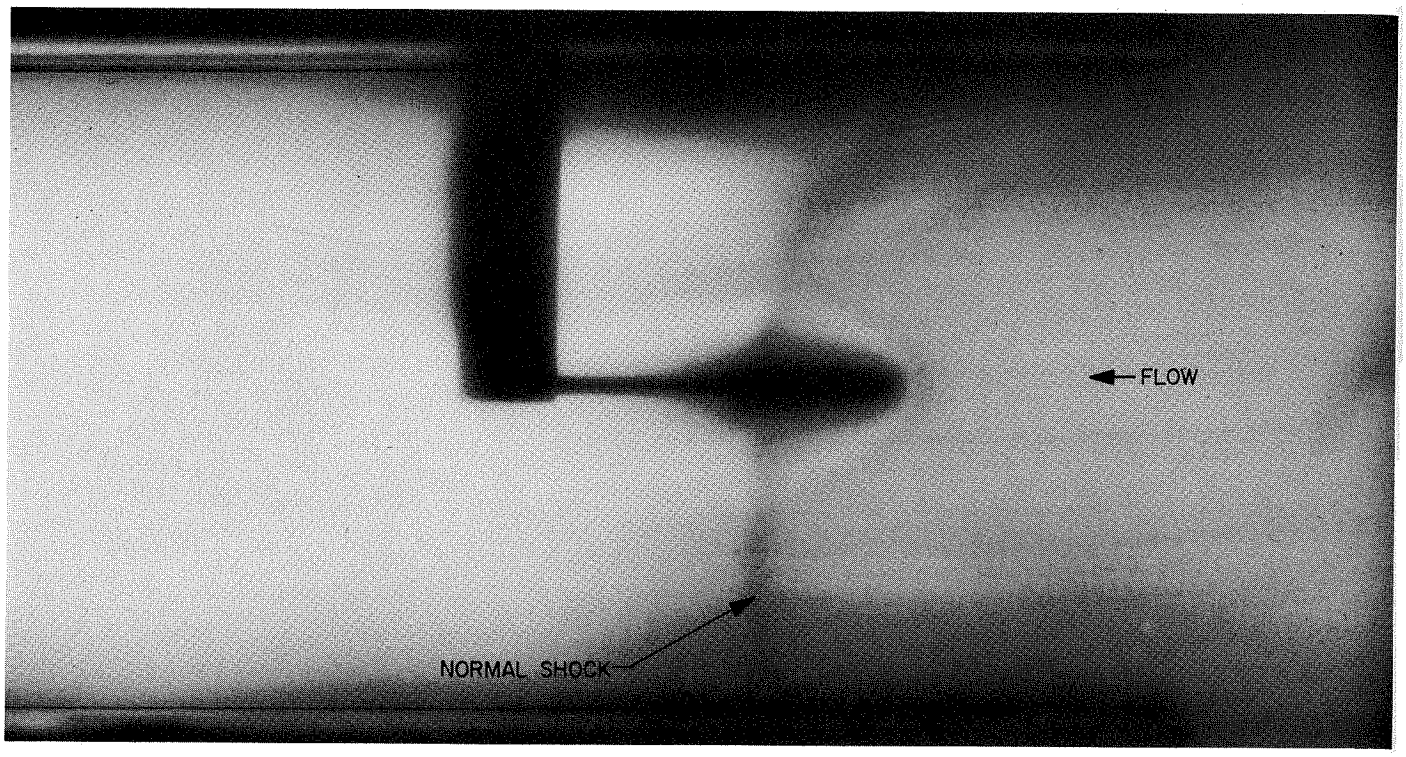

Fig. II-24. Intersection of normal and conical shocks from probe at 275 ft/sec

2. High-Speed Still Photography

Exceptionally short exposure times are necessary to resolve water–gas fine structure in the tunnel. At a velocity of 350 ft/sec, movement of 0.0042 in. occurs during a 1-μsec exposure. Thus, for bubbles of a cross section of approximately 0.020 in., an exposure of not more than 1-3 μsec can be allowed.

A model 500 Biplaner Image Converter Camera System[1] was used to obtain exposure times down to 5 nsec (Fig. II-25). From an analysis of these pictures, an exposure between 1 and 3 μsec is sufficient to resolve observable detail in the two-phase flows. Consequently, for all single-frame, high-speed still pictures subsequently taken with the Speed Graphic Camera, Plus-X or Tri-X film was used on open shutter with an Edgerton, Germeshausen, and Grier Micro flash unit, as light conditions permitted. The flash unit was placed about 24 in. from the center line of the tunnel with a 6-in. condenser lens between the flash and the transparent wall. Exposure times of ½ and 1 μsec were used. Figure II-21 shows the camera, light source, and lens arrangement.

[1]Camera system courtesy of Beckman and Whitley, Mountain View, California.

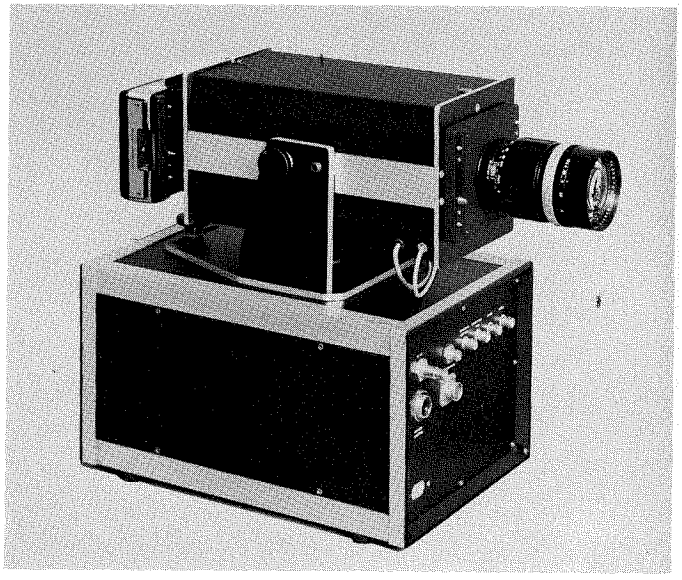

Fig. II-25. Model 500 Biplanar Image Converter Camera System (courtesy of Beckman and Whitley)

Figure II-26 shows a free flow at 275 ft/sec taken at an exposure time of ½ μsec. Structural details down to 0.020 in. are clearly visible. Figure II-27 shows the

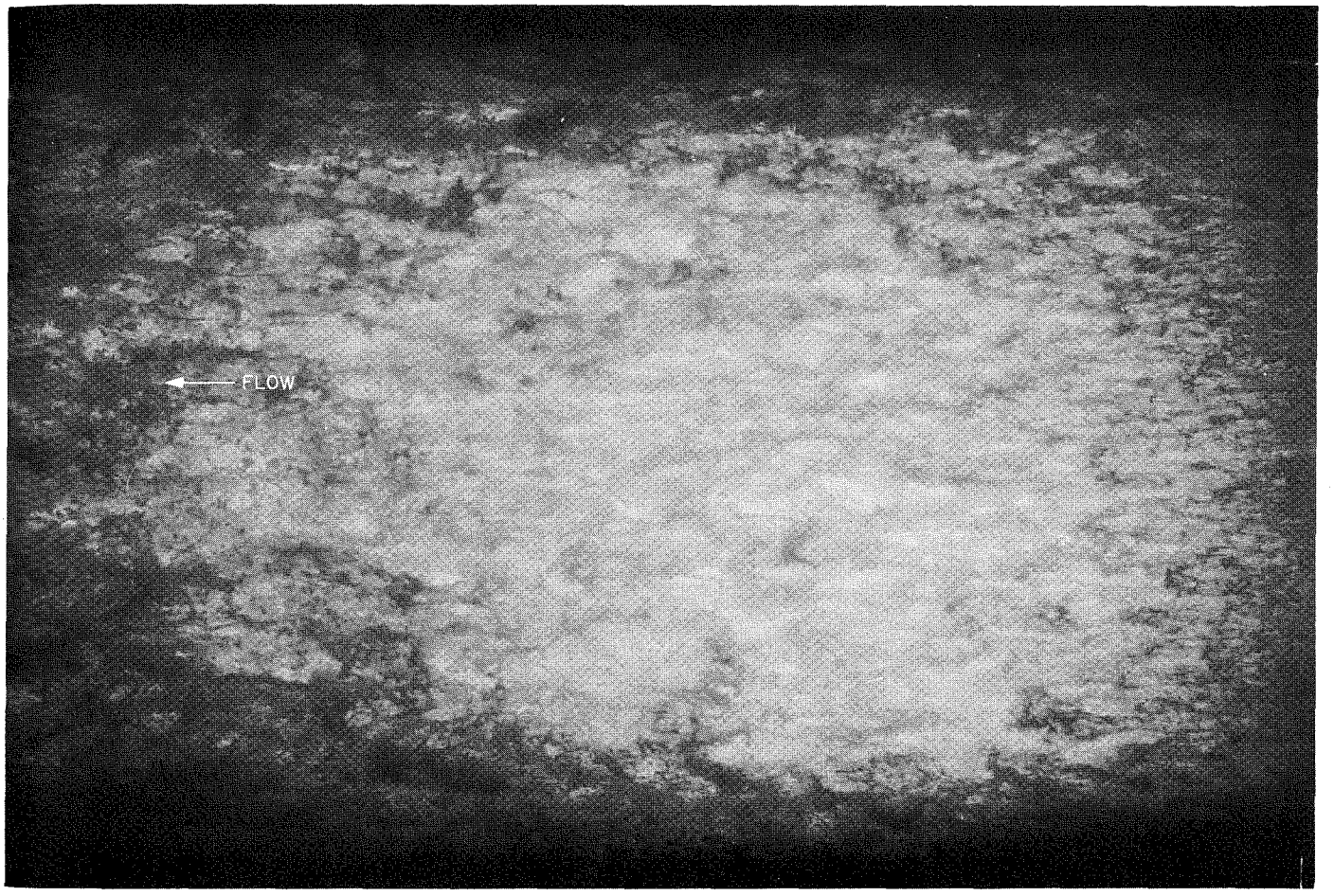

Fig. II-26. Two-phase free-stream flow at 275 ft/sec, ½-μsec exposure

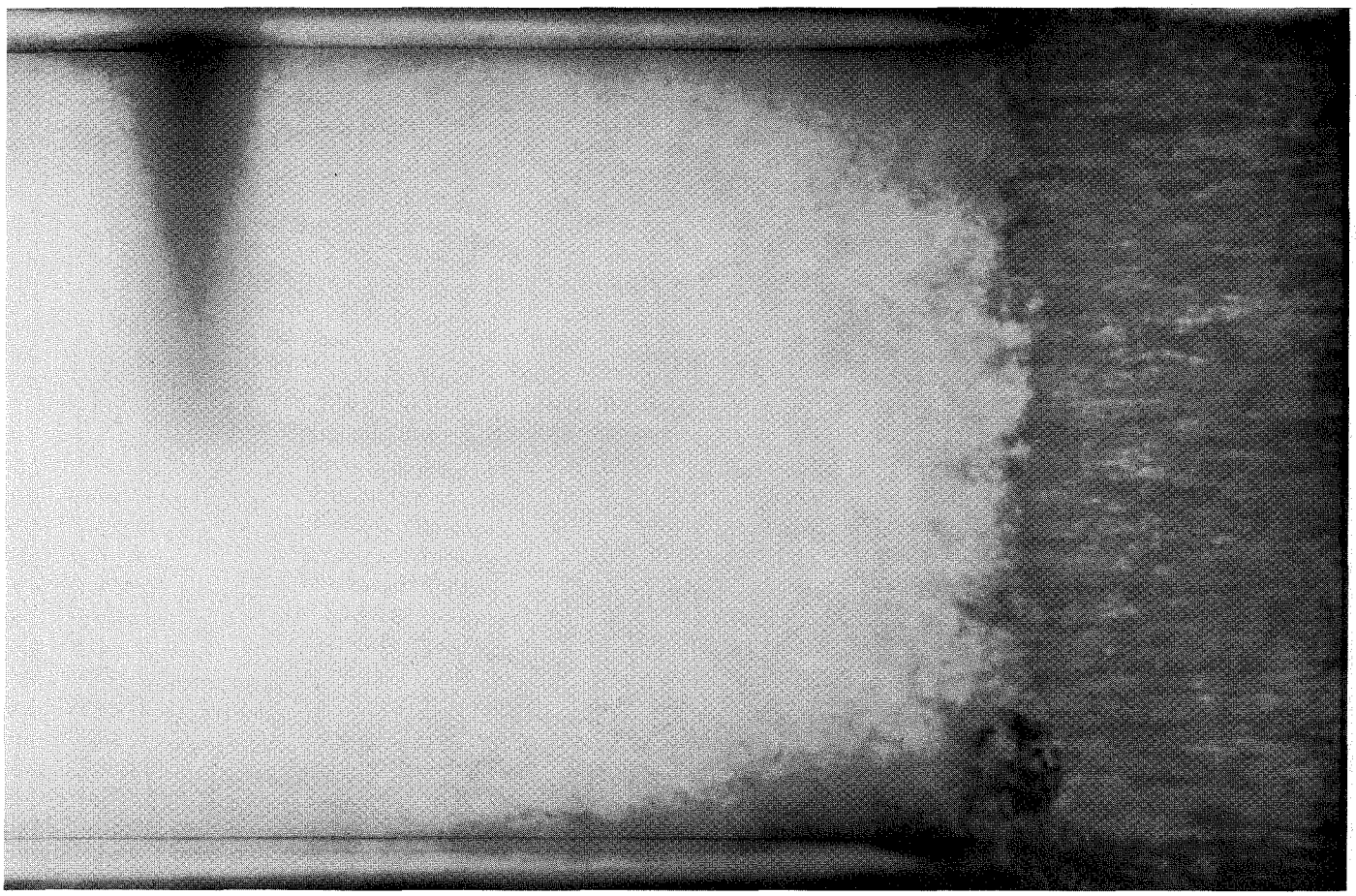

Fig. II-27. Normal shock at 275 ft/sec, ½-μsec exposure

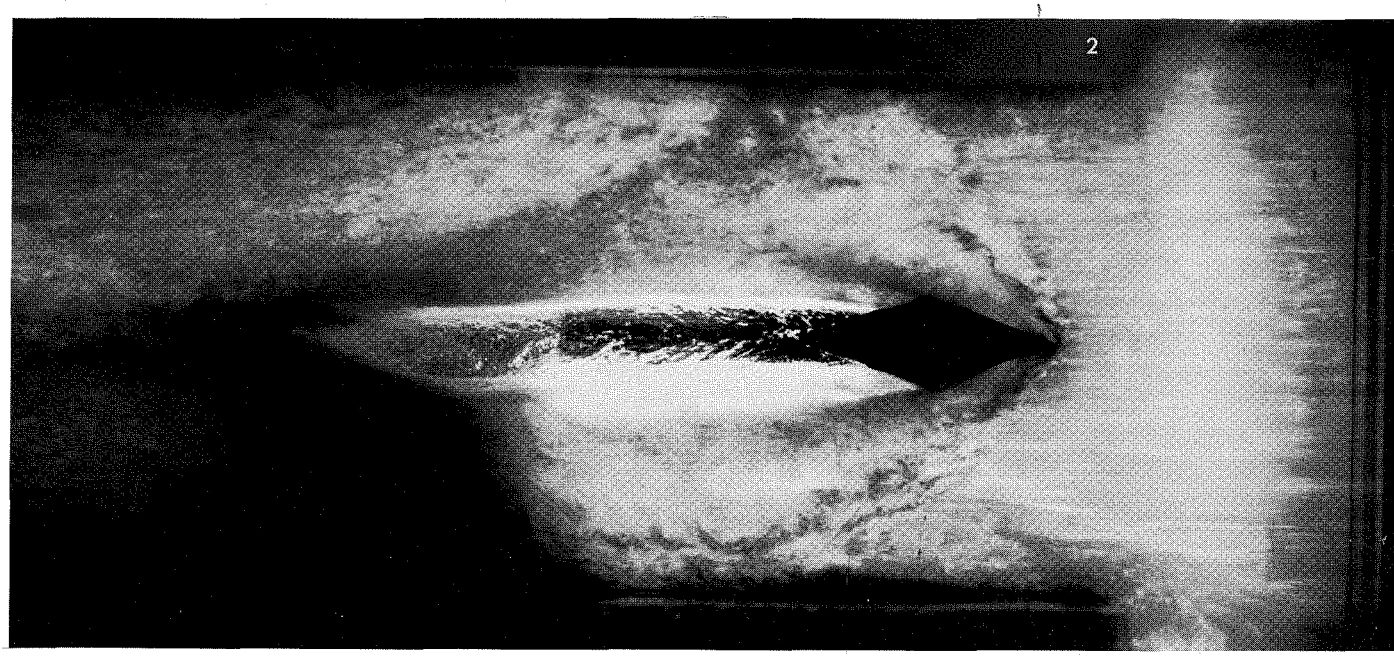

Fig. II-28. The 20° deflection wedge, flow at 300 ft/sec, ½-μsec exposure

difference in the gas-bubble-connected phase upstream of a normal shock, and the liquid connected phase downstream. Flow deflection by oblique shock waves from a double wedge is clearly evident in the ½-μsec exposure of Fig. II-28.

3. Slow-Speed Motion Pictures

Relatively slow transient phenomena discernible to the eye were recorded in front of the tunnel on 16-mm color film using a Milliken Instrumentation Camera mounted on a tripod. Shutter speeds of $\frac{1}{50}$ sec at frame speeds of 24 frames/sec were quite adequate. The 500-w photo spot light with autotransformer control was used for lighting. It was generally found that color film provided the most accurate record of all phenomena visible to the observer.

4. Medium-Speed Motion Pictures

A Fastax Camera with a frame speed of 5000 frames/sec at a shutter speed of $\frac{1}{1500}$ sec also was used to explore the area of observable transient phenomena. Generally, fine structure was completely blurred, and there was no improvement over the slow-speed motion pictures. Figures II-29 and II-30 show typical positions of the camera and light source for the Fastax and higher-speed motion picture equipment.

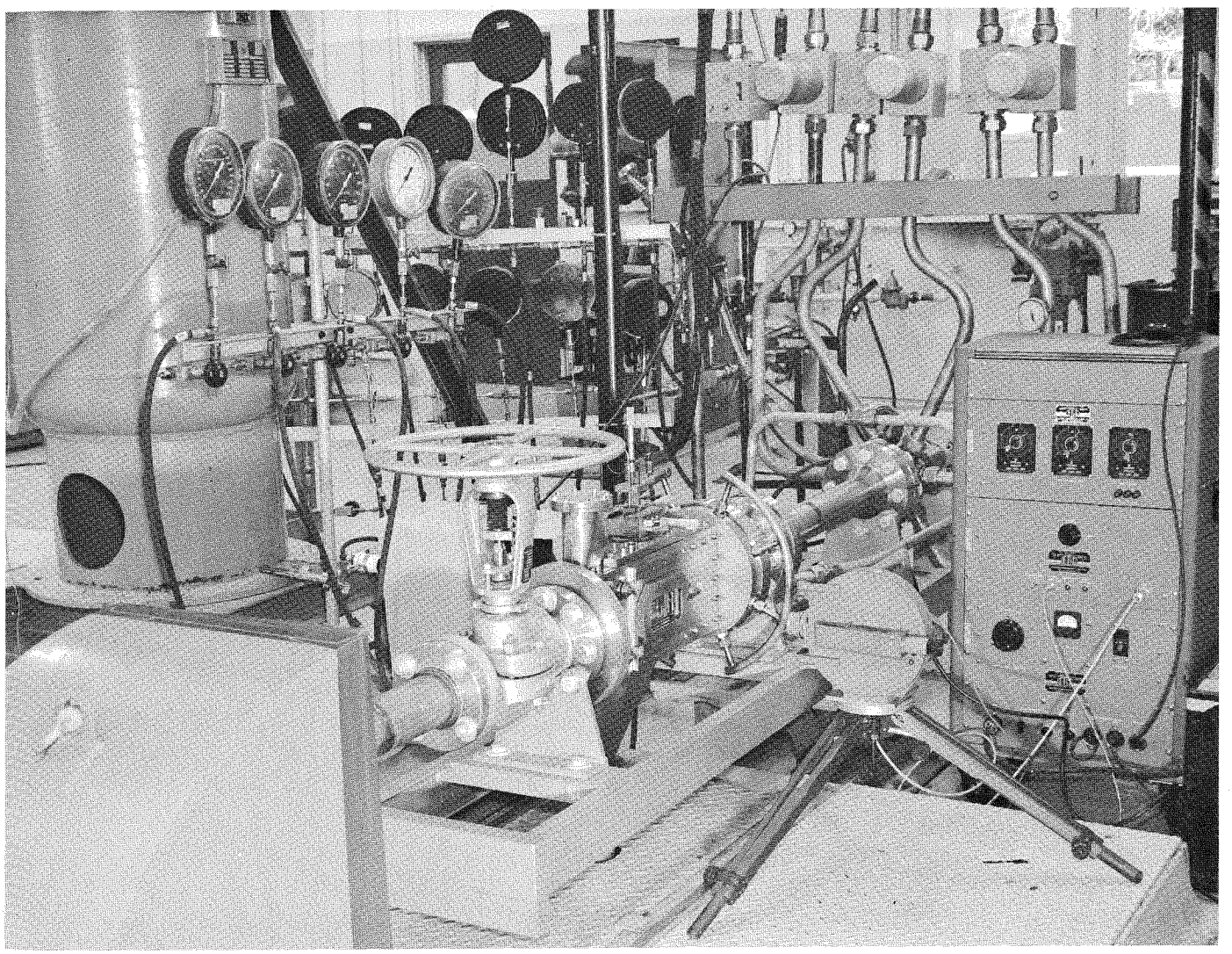

Fig. II-29. Fastax camera setup at tunnel

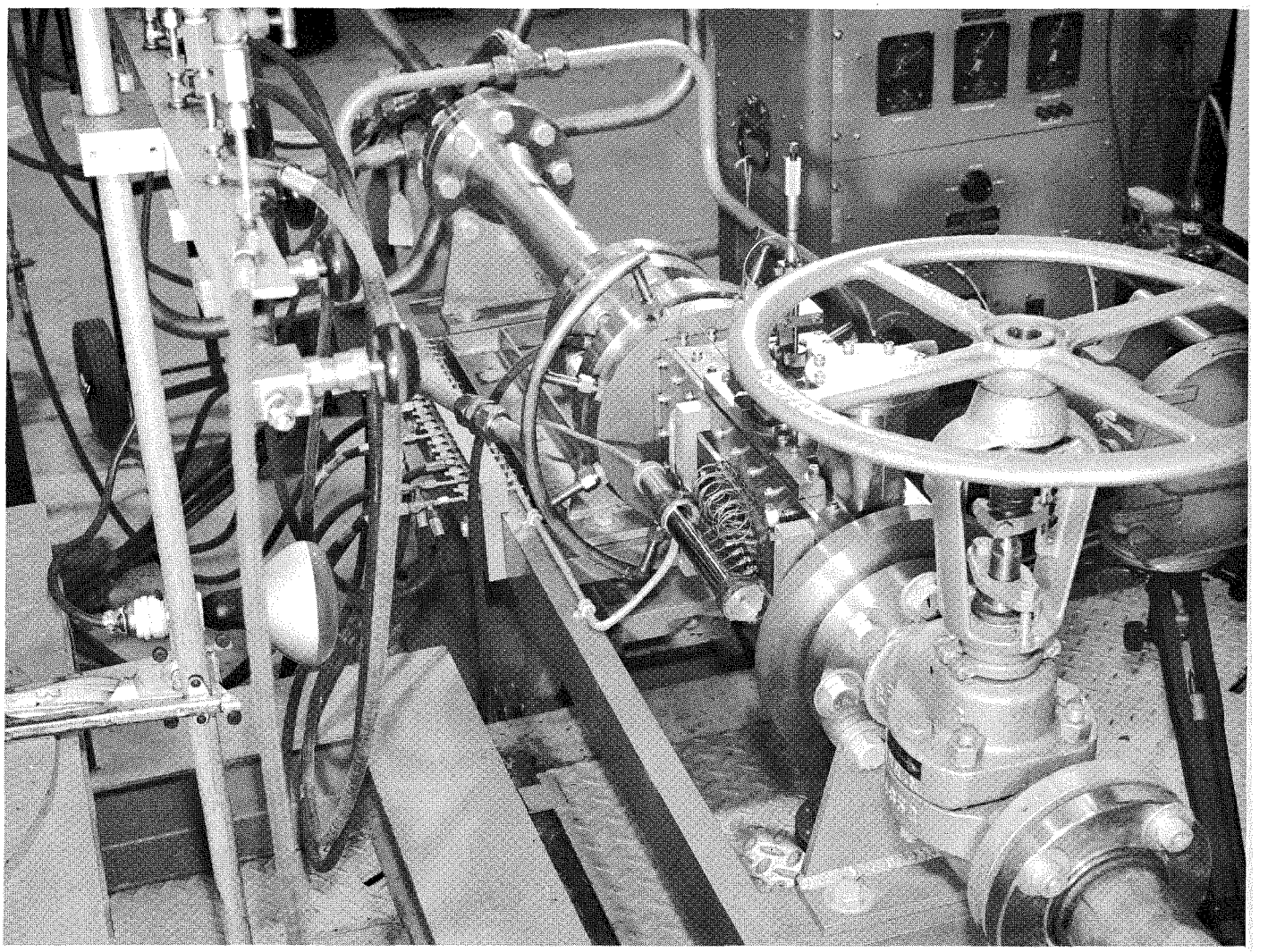

Fig. II-30. Location of flash tube for Fastax camera setup

5. High-Speed Motion Pictures

A Dynafax Camera with a maximum frame rate of 26,000 frames/sec and a shutter speed of 2.5 μsec recorded the fine-structure movements on both sides of normal and oblique shocks. Such light sources as high intensity flash bulbs and electronic strobe lights were tested. Because of the high shutter speed, a peak light intensity of 1.5 million cp was necessary when using Plus-X film. A Model 358 Beckman and Whitley electronic flash unit gave good results in this speed range. Figure II-31 shows the Dynafax camera, and Fig. II-32 the light source. Position with respect to the tunnel was the same as that for the Fastax-type equipment.

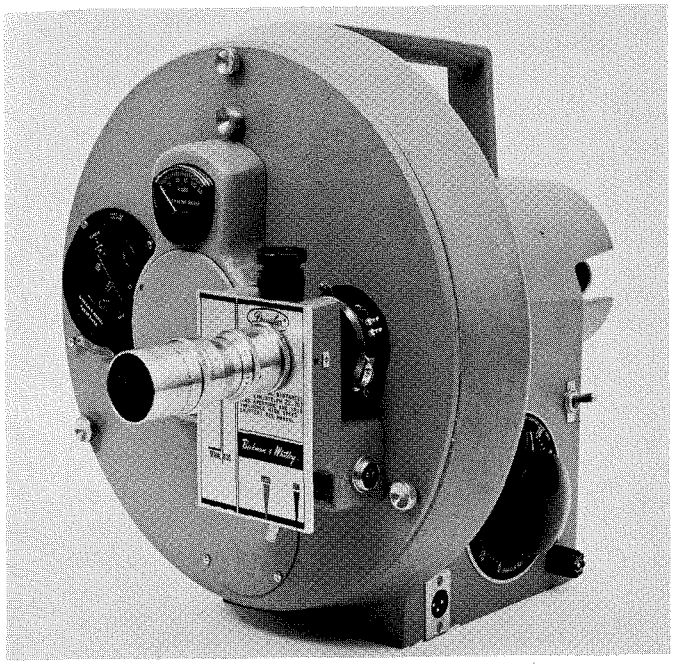

Fig. II-31. Dynafax camera (courtesy of Beckman and Whitley)

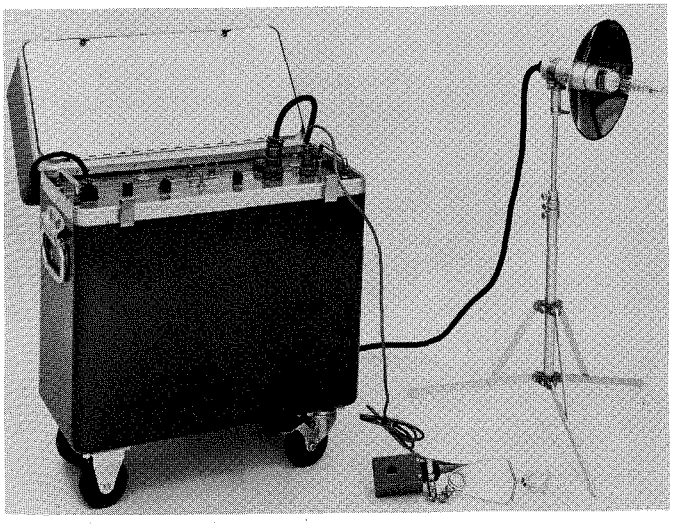

Fig. II-32. The 1.5-million-cp flash unit, Beckman and Whitley Model 358 used with Dynafax camera

Sequential projection of the resultant pictures, however, is difficult. The Dynafax camera exposes two rows of 16-mm frames on 35-mm film. A print must be made of each frame and the print rephotographed in sequence by an animation camera to obtain the full 224 frames in sequence on 16-mm film. It took considerable effort to obtain sufficient contrast on the large negatives, prints, and the final 16-mm film. Dupont #936A negative film provided the sharpest contrast in this area.

6. Ultra-High-Speed Motion Pictures

In an attempt to observe bubble dynamics in the fine structure while passing through shock waves, a Model 200 Simultaneous Streak and Framing Camera[2] was used (Fig. II-33). A frame speed of 800,000 frames/sec was

[2]Camera courtesy of Beckman and Whitley, Mountain View, California.

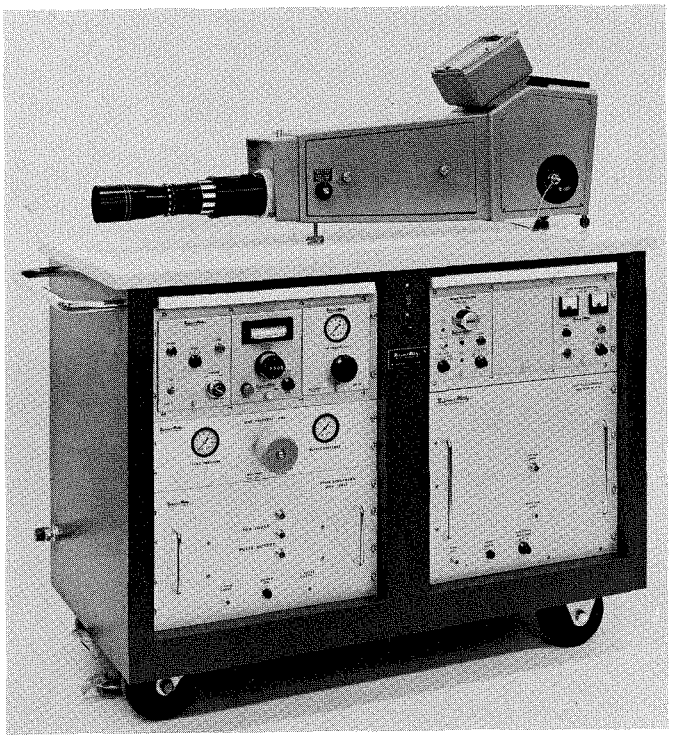

Fig. II-33. Model 200 Simultaneous Streak and Framing Camera (courtesy of Beckman and Whitley)

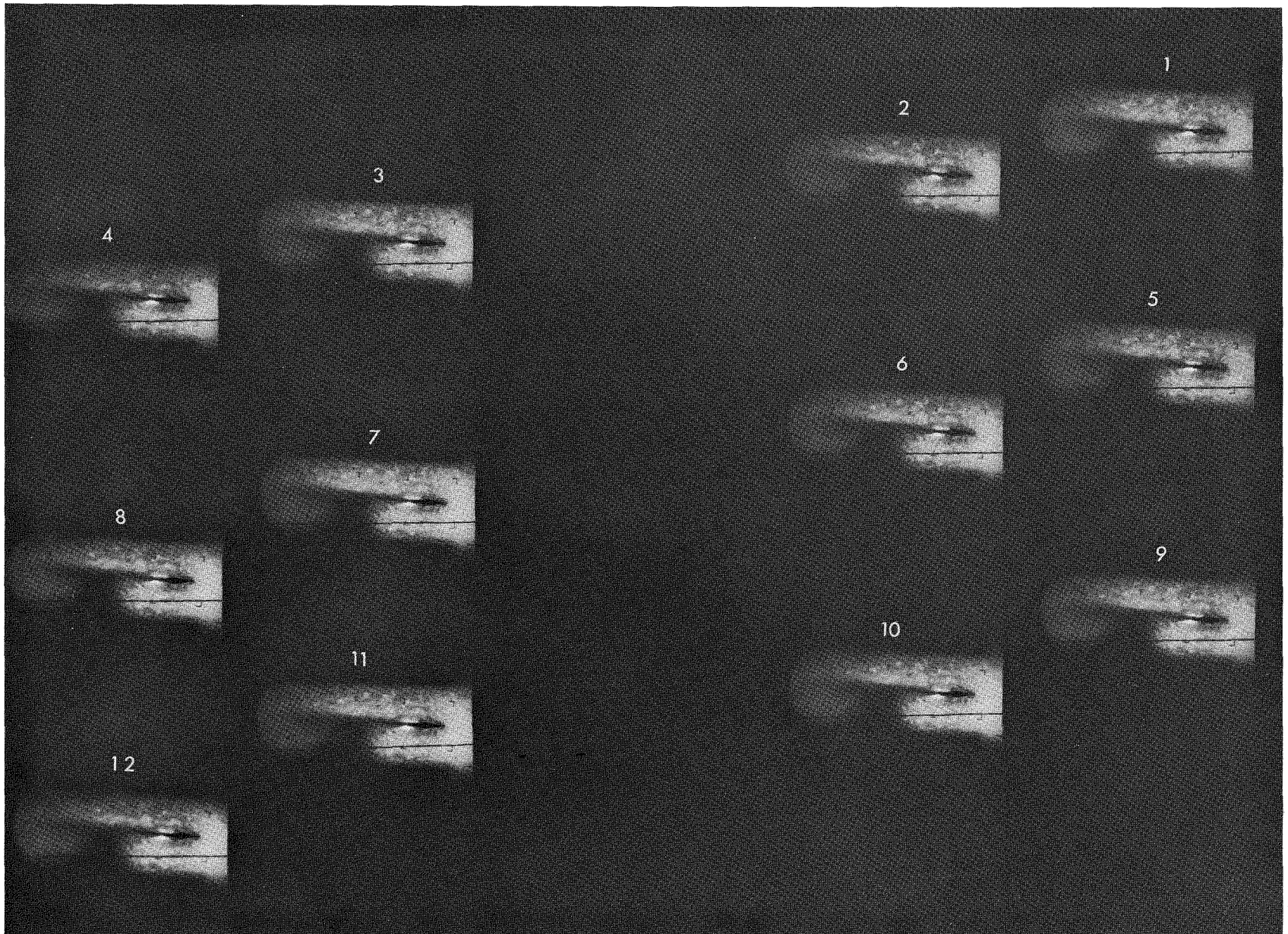

Fig. II-34. Twelve-frame sequence of two-phase supersonic flow over a 10° deflection wedge (800,000 frames/sec)

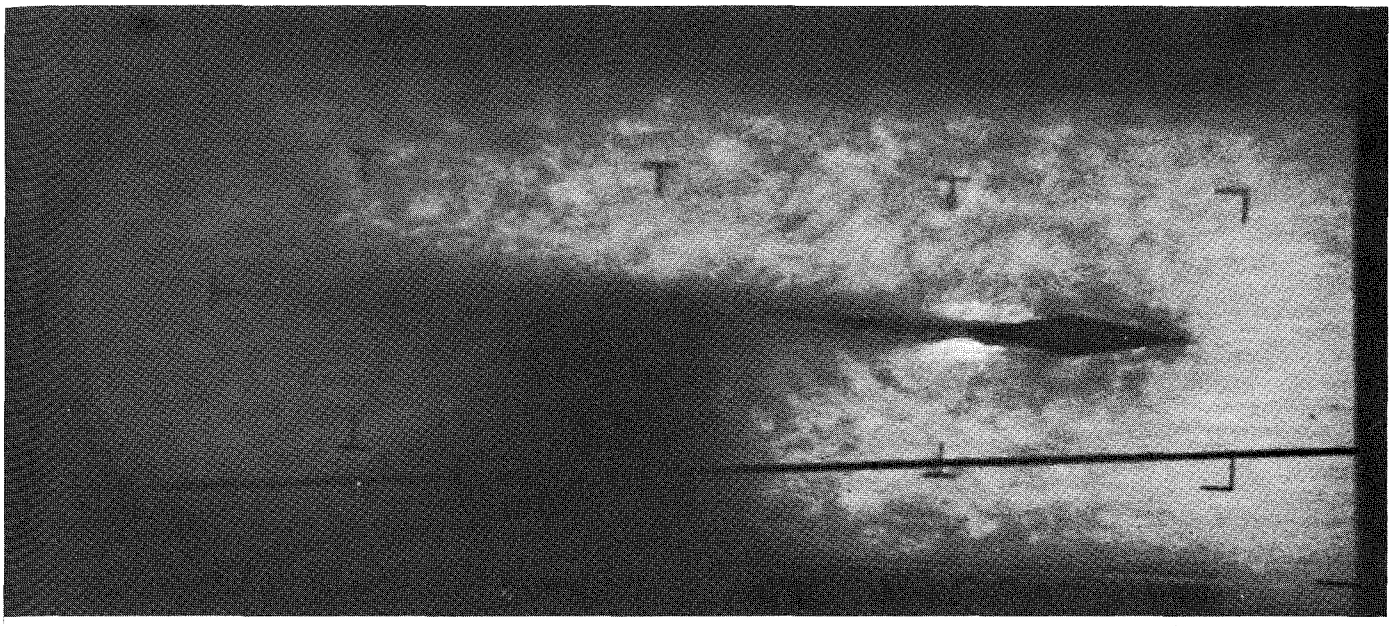

Fig. II-35. Single-frame enlargement of twelve-frame sequence

reached with good results using a 50-million-cp electronic strobe light. Figure II-34 shows a twelve-frame sequence of supersonic flow over a 10° deflection double wedge. Figure II-35 shows a single frame of the sequence, which suffers from graininess due to the relatively fast Tri-X film.

E. Tunnel Flow Characteristics

Exact knowledge of such characteristics of the input flow to the test section as liquid velocity, gas velocity, volume ratio and Mach number is required as a basis for evaluation of all phenomena observed in the test section.

Section III provides this fundamental information as a function of liquid mass flow rate, gas mass flow rate, and boundary-layer knife position, which are more easily measurable parameters.

Considering only the core flow, it is shown in Fig. III-5 that the volume ratio varies with liquid velocity. From Eq. (I-13) of Section I, it is shown that the Mach number of a two-phase continuum is dependent upon the volume ratio (r_v), mass ratio (r_m), mixture velocity (V), and static pressure (P). For a single injector of fixed r_v, the only variation in r_v that occurs in the core is that from duct flow friction. With the r_v known as a function of mixture velocity (V), a graph can be constructed giving the Mach number of the test section as a function of the core velocity for parameters of pressure (P) as shown in Figs. II-36 and II-37. The latter figure shows only Mach numbers between 20 and 90 in the pressure range from 0.01 to 1.0 psia. Because the Mach number is inversely proportional to the square root of the pressure, the limiting tunnel Mach number corresponds to the vapor pressure of the water and dissolved gas at the maximum liquid velocity of 335 ft/second. At a water temperature of 70°F, this corresponds to a limiting Mach number of approximately 100.

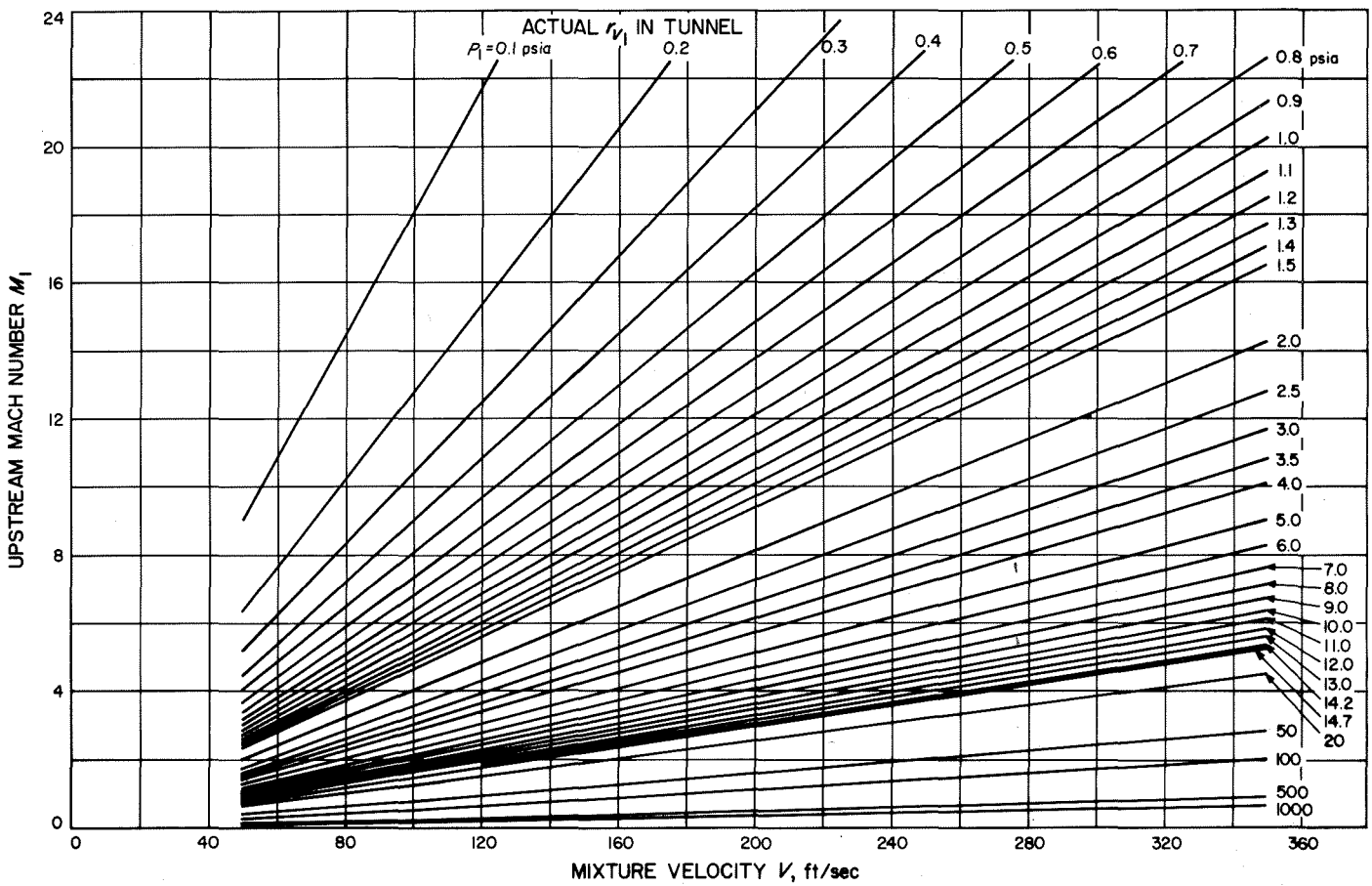

Fig. II-36. Test section Mach number as a function of mixture velocity for various values of static pressure ($0 \leq M \leq 20$)

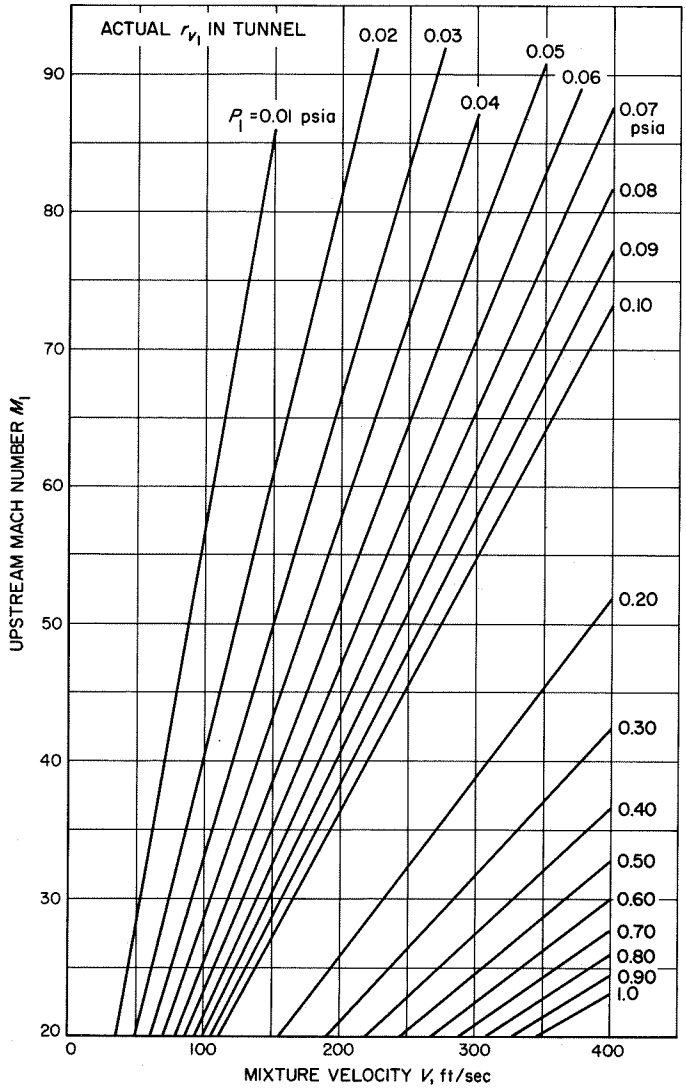

Fig. II-37. Test section Mach number as a function of mixture velocity for various values of static pressure ($20 \leq M \leq 90$)

Nomenclature

P mixture pressure (lb/ft^2)

r_m gas-to-liquid mass ratio

r_v gas-to-liquid volume ratio

V velocity of mixture (ft/sec)

Reference

II-1. Elliott, D. G., Cerini, D. J., Otte, H., and Weinberg, E., "Liquid MHD Power Conversion," in *Supporting Research and Advanced Development*, Space Programs Summary 37-23, Volume IV, pp. 132–136. Jet Propulsion Laboratory, Pasadena, Calif., October 31, 1963.

III. Two-Phase Flow Model

A. Basic Considerations and Fundamentals

The information obtained in acquiring measurements of the core flow prior to its entry into the test section produced a drag model, and an attempt was made to correlate these results with simple geometrical models of the phase distribution.

Relatively straightforward techniques have evolved for the measurement of density, velocity, and temperature in a single-phase duct flow. Not all of these techniques, however, can be used to determine similar characteristics in a two-phase flow because the distributions of the two different media may or may not be known as functions of spacial coordinates and time.

Techniques that measure average gas fractions across flow channels generally employ the attenuation of gamma or beta rays (Refs. III-1 through III-3) or radioactive tracers (Ref. III-4). A high-resolution resistivity probe for determination of local void properties in liquid-gas flows was reported in a paper by Neal and Bankoff (Ref. III-5). This latter method is of primary concern in a gas-liquid, vapor-liquid, or liquid-liquid system in which the continuous phase is an electrical conductor. However, the analysis depends upon known geometrical properties for either phase.

Information gained on supersonic two-phase flows indicates that near the volume ratios of 1:1, simple geometric distributions of one or the other phase are not applicable. Therefore, extensive calibration of such a device would be required again before accurate information could be obtained on high-speed, two-phase flows in the 1:1 volume ratio range.

The injector constructed for the supersonic two-phase tunnel described in Section II could, by its symmetry, give a reasonable expectation of homogeneous transverse gas-liquid distributions for short distances in duct flow, which was confirmed by total head-probe measurements of the injector. It was not known, however, what changes would occur in boundary-layer buildup along the walls of the test section, and how this buildup would affect the void ratio of the remaining core flow. If thrust measurements of the core discharge and input mass flow rates of the liquid and gas in the boundary layer could be taken, such quantities as core void ratio, gas, and liquid velocities could be computed. The ability to remove the boundary layers, then, was required to eliminate peripheral portions

of the flow that moved below the average velocity of the core. Assuming a device for such removal is as that shown in Fig. III-1, then, based on this figure, the force balance on the duct is

$$\mathring{m}_{l_2} V_{l_2} + \mathring{m}_{g_2} V_{g_2} = F - P_2 A_2 \qquad \text{(III-1)}$$

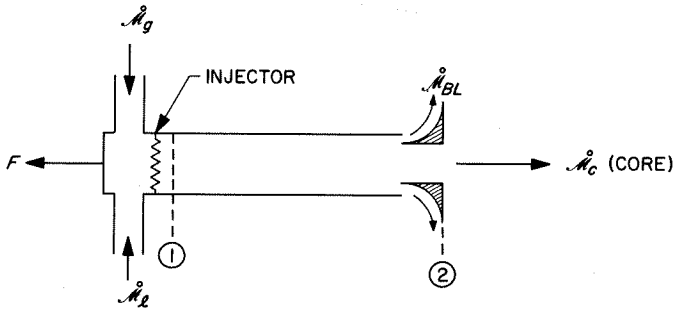

Fig. III-1. Schematic of duct boundary layer removal assembly

Solving for liquid velocity at discharge (position 2, Fig. III-1),

$$V_{l_2} = \frac{F - P_2 A_2 - \mathring{m}_{g_2} V_{g_2}}{\mathring{m}_{l_2}} \qquad \text{(III-2)}$$

where

$$\mathring{m}_{l_2} = \mathring{m}_{l_1} - \mathring{m}_{l_{BL}} \qquad \text{(III-3)}$$

With volume ratios of 1.0 or less at velocities up to 350 ft/sec, $\mathring{m}_{g_2} V_{g_2}$ is approximately 0.1% of F and can be reasonably neglected in the determination of V_{l_2}. The liquid core area can be determined from continuity by

$$A_{l_2} = \frac{\mathring{m}_{l_2}}{(\rho_l V_{l_2})} \qquad \text{(III-4)}$$

Then, with the core discharge area known, the gas area is

$$A_{g_2} = A_2 - A_{l_2} \qquad \text{(III-5)}$$

The local volume fraction of the core is the ratio of gas area to liquid area:

$$r_{v_2} = (A_{g_2}/A_{l_2}) \qquad \text{(III-6)}$$

From continuity, the core gas velocity can be found from the relation,

$$V_{g\,core} = \frac{\mathring{m}_{g\,core}}{A_{g\,core}} \qquad \text{(III-7)}$$

The relative or slip velocity in the core is the difference between the liquid and gas velocities:

$$V_{r_{core}} = V_{l_{core}} - V_{g_{core}} \qquad \text{(III-8)}$$

By repeating all measurements at increments of boundary-layer thickness from the wall to the core, the velocity profiles, local volume ratios, and gas-liquid distributions in the boundary layer can be determined.

If Δ represents an incremental step in measurement of boundary-layer variables, the local boundary-layer velocity U_Δ is given by the relation

$$U_{l_\Delta} \cong \frac{\Delta F}{\Delta \mathring{m}_{BL}} \qquad \text{(III-9)}$$

From the area-mass flow relationship, the incremental liquid area becomes

$$A_{l_\Delta} = \frac{\Delta \mathring{m}_{BL}}{\rho_l U_{l_\Delta}} \qquad \text{(III-10)}$$

the local gas area is given by

$$A_{g_\Delta} = \Delta A - A_{l_\Delta} \qquad \text{(III-11)}$$

from which the local volume ratio is

$$r_{v_\Delta} = \frac{A_{g_\Delta}}{A_{l_\Delta}} \qquad \text{(III-12)}$$

The local slip cannot be determined easily because of the difficulty in measuring the local gas mass flow rate ($\mathring{m}_{g_\Delta}$).

B. Equipment for Thrust and Boundary-Layer Measurement

An equipment designed to provide a flow that was an exact duplicate of the flow in that portion of the tunnel prior to the test section was used to measure thrust and boundary-layer mass-flow rates. This equipment and these

measurements were necessary to determine the composition of the core that flowed through the test section.

The 1:1 gas-to-liquid volume-ratio injector was mounted at the front end of a rectangular duct that measured 1.90 in. high by 0.750 in. wide. The length of the duct to the side boundary-layer removal blades was 8.5 in., which corresponded to that duct in the tunnel. Fixed upper and lower boundary layer removal blades were positioned behind the side blades. Figure III-2 shows the blade assembly with ducts leading perpendicularly to the thrust center line. Figure III-3 is a closeup of the variable

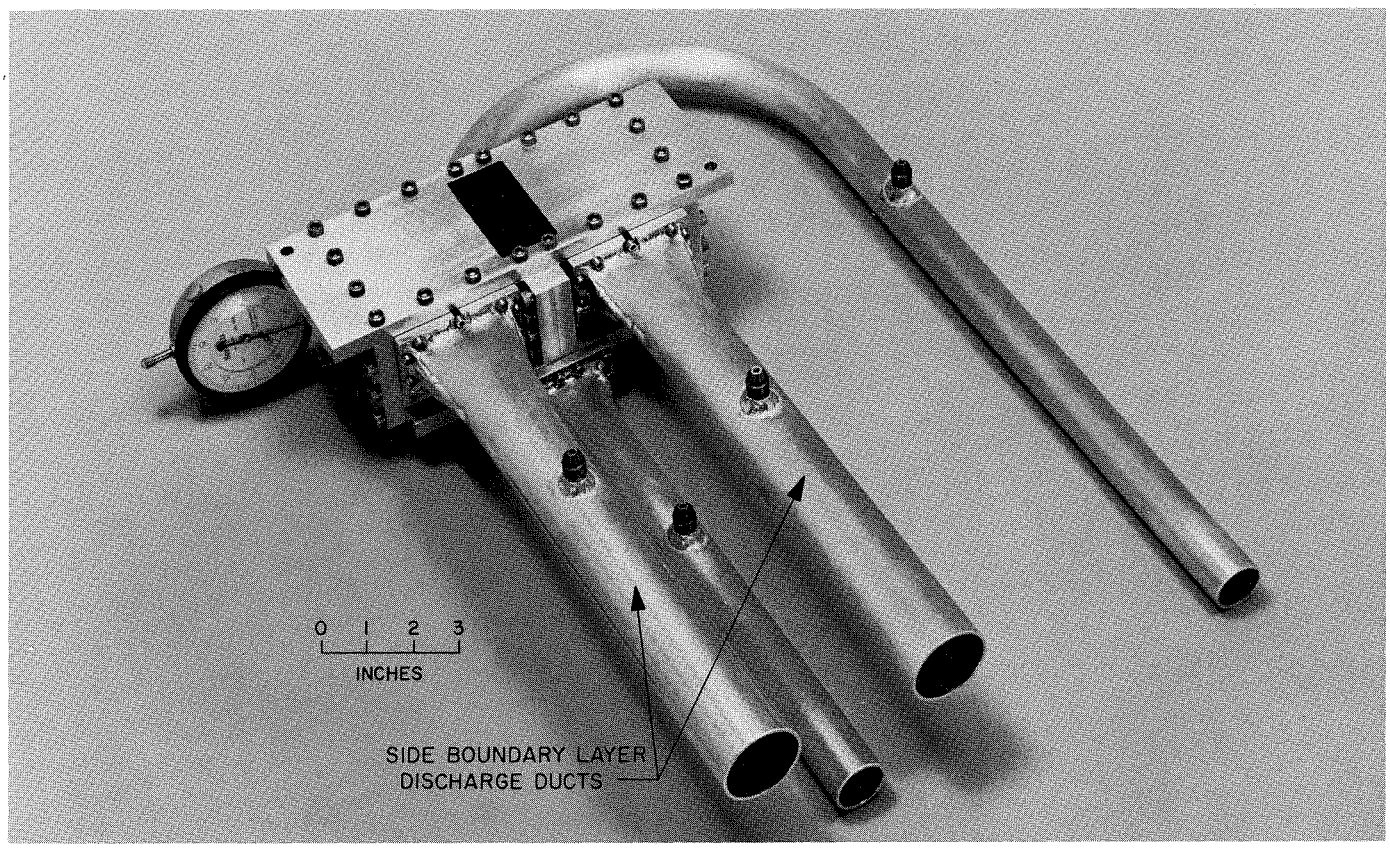

Fig. III-2. Front view of boundary layer removal assembly and ducts

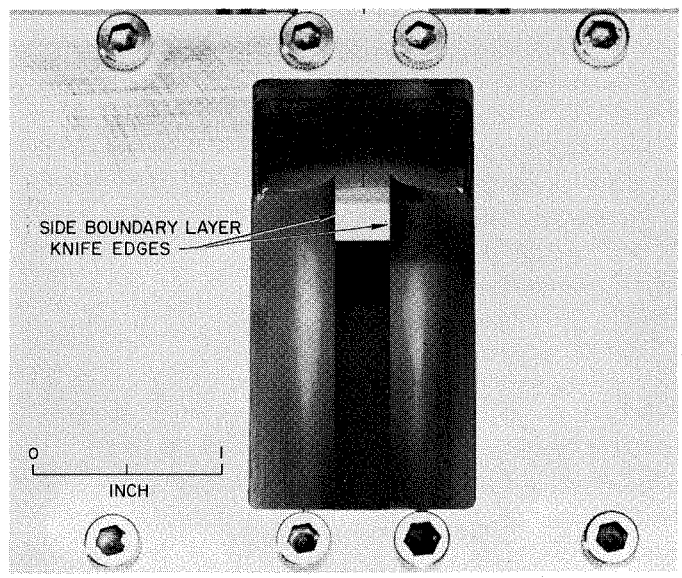

Fig. III-3. Closeup showing side wall knives inside center duct opening

side blades, and Figs. III-4 and III-5 show the fixed blade assemblies and core discharge slot. Figures III-6 and III-7 show the entire assembly mounted on a thrust stand; individual hoses lead from the boundary layer ducts to the weighing tank. A swing gate in the hose discharge assembly allows discharge of the boundary-layer ducts into the weighing tank for a timed period of flow.

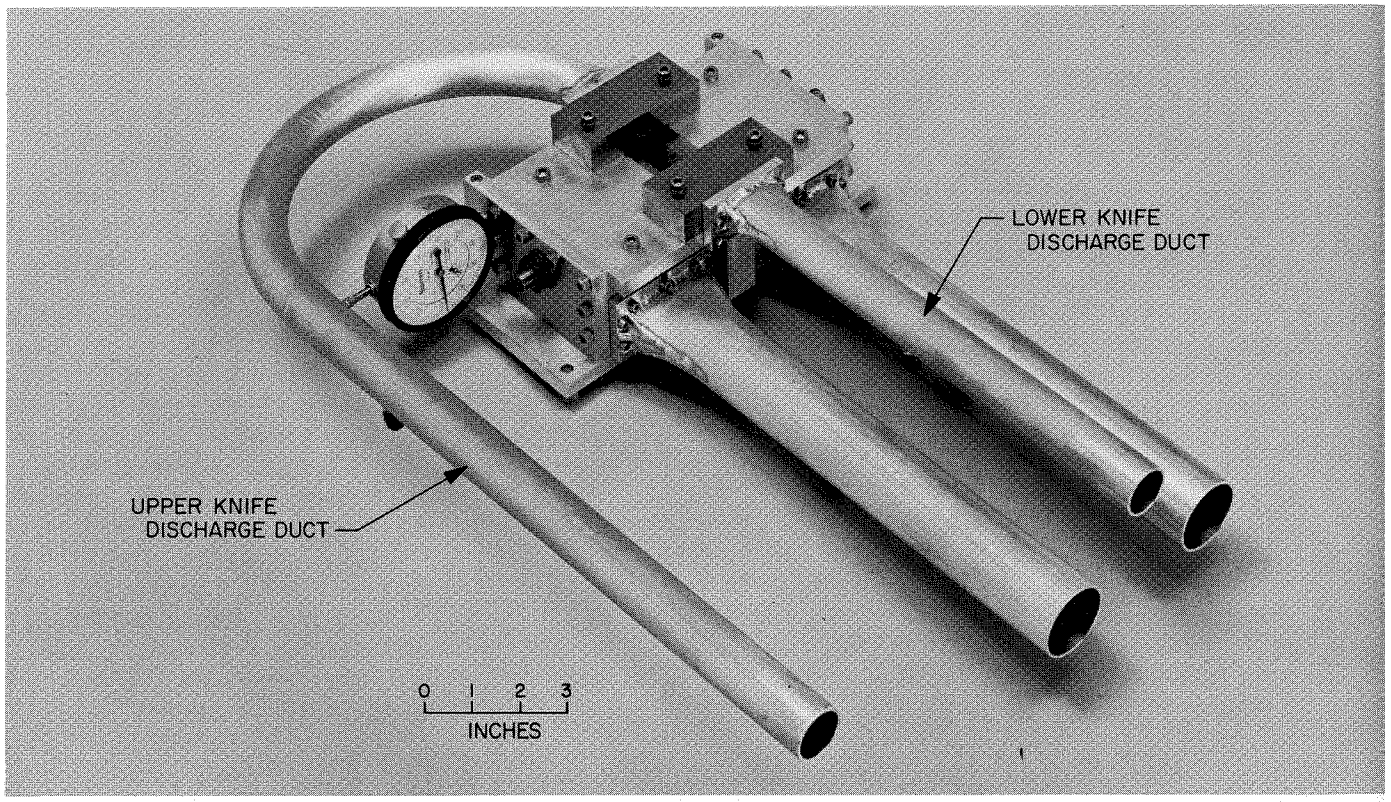

Fig. III-4. Discharge side of boundary layer assembly

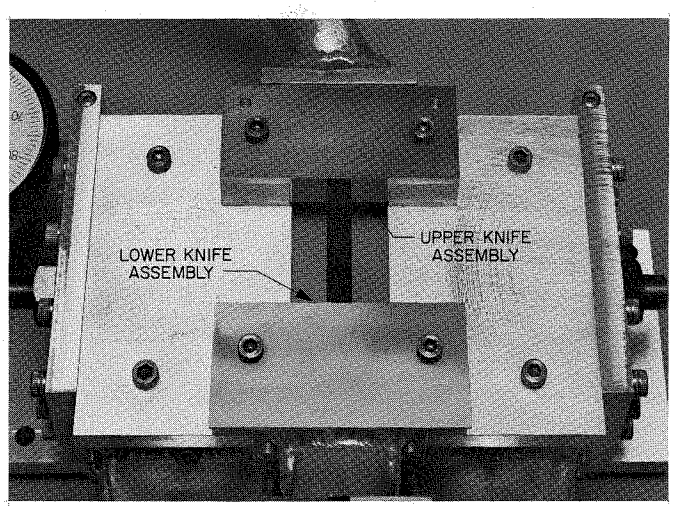

Fig. III-5. Closeup showing upper and lower boundary layer knife assemblies

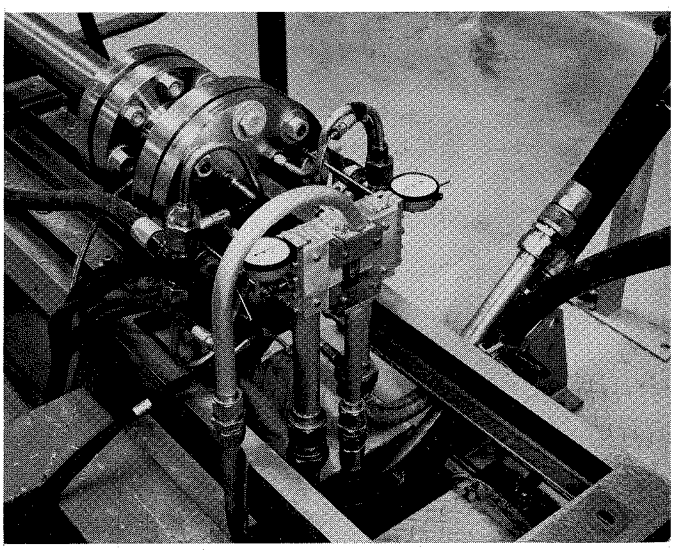

Fig. III-6. Simulated tunnel assembly mounted on test stand

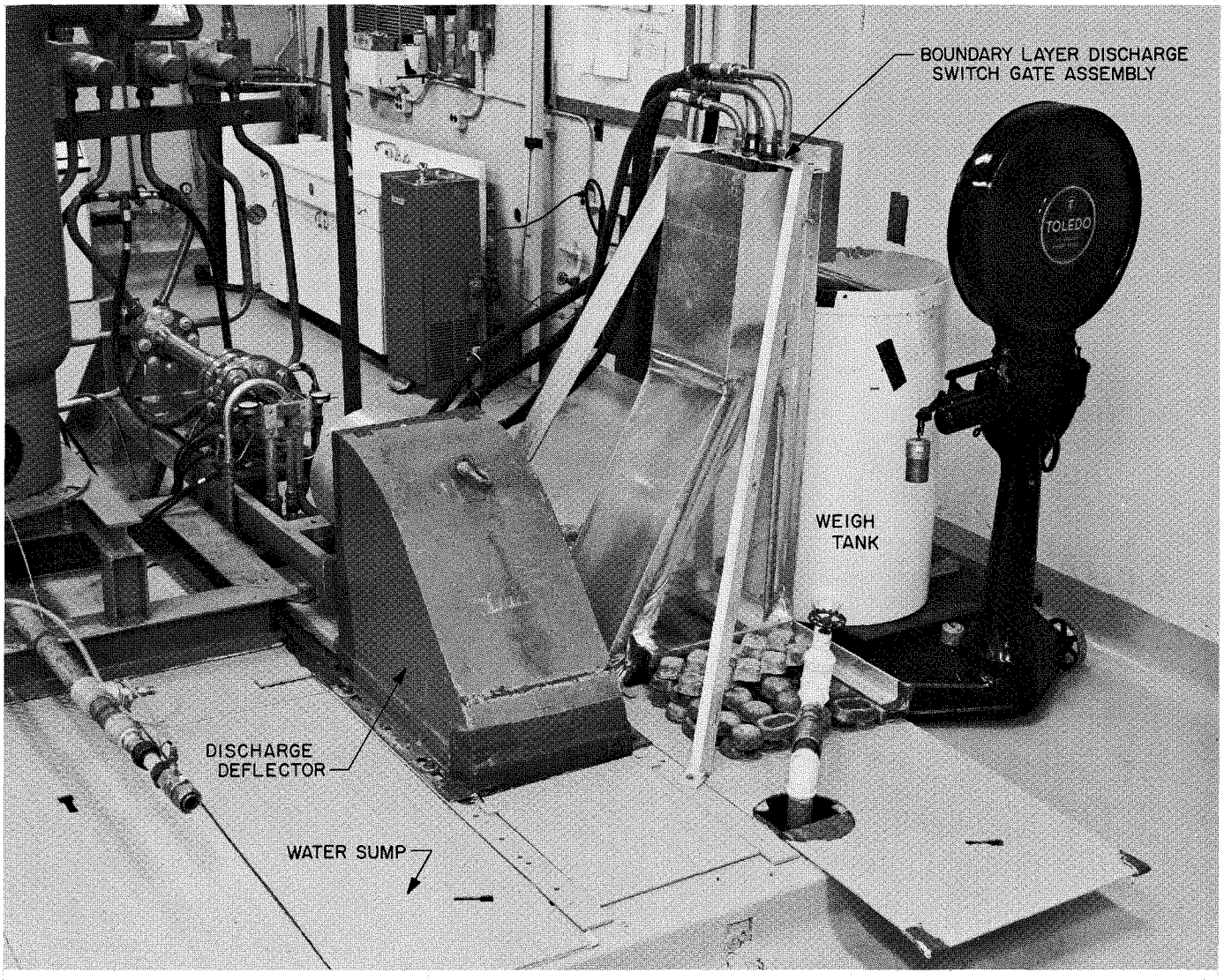

Fig. III-7. Boundary layer discharge rate measuring equipment

Water enters the main water duct through six filters from flexible hoses lying in a plane perpendicular to the thrust center line. Figure III-8 shows the nitrogen control panel, pressure monitoring gauges and digital thrust readout equipment.

Because the side boundary-layer knives were capable of removing up to 50% of the total flow, which amounted to 50 lb/sec (liquid), extensive testing was performed on the effect of back pressure in the flexible lines leading to the weighing tanks. Figure III-9 shows a less than 1%

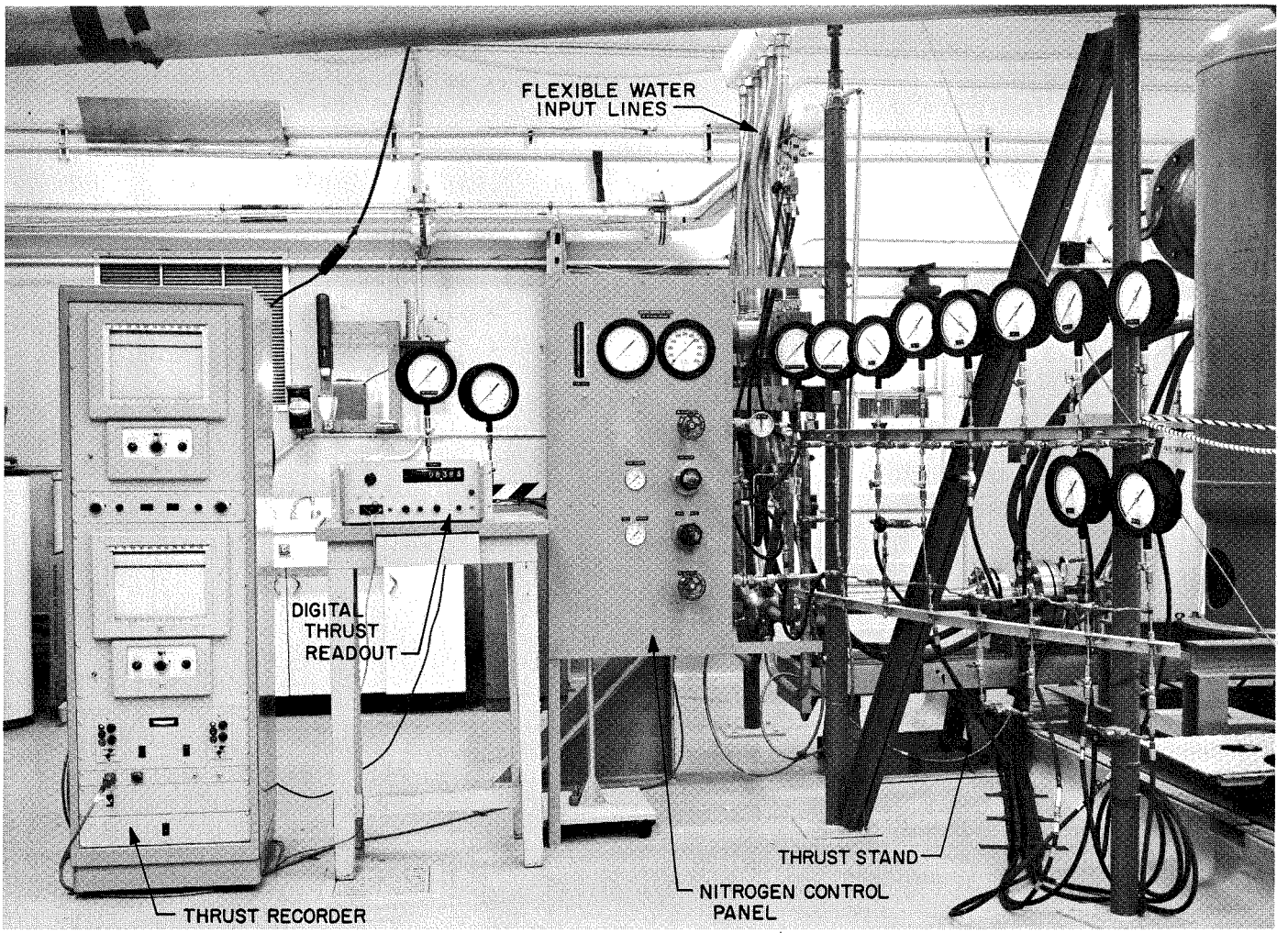

Fig. III-8. Test stand instrumentation

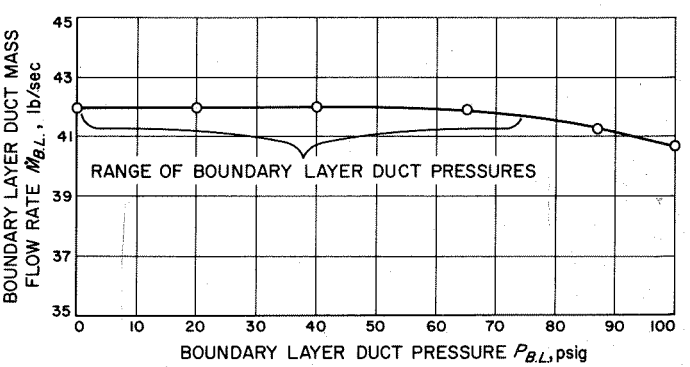

Fig. III-9. Boundary layer mass flow rate as a function of boundary layer duct pressure

change in mass flow rate over the lower 80% of the duct pressures; this corresponds to over 90% of the velocity-boundary-layer depth region.

C. Results from the Flow Model

1. Velocity Profiles

The step-by-step measurement in Eqs. (III-2) and (III-3) of the variables as a function of boundary-layer thickness for five bands of velocity determined the average core velocity as a function of the amount of boundary layer removed (Fig. III-10). The curves approach zero slope at a depth of approximately 0.150 in. from the wall indicating that the core velocity is relatively unaffected by wall friction at a depth from the wall of 0.135 in. or more. This corresponds to a distance of 8.5 in. from the injector, and the boundary layer would naturally grow in depth with a longer duct.

The average core velocity profiles, when divided by the total net liquid mass-flow rate ($\mathring{m}_{l_2}$) and adjusted to a common value at the wall point, formed a reasonably uniform profile (Fig. III-11). This curve helped to determine the curve slope to a boundary layer depth of nearly 0.150 in. The curve tended to dip a few percent in the lower two velocity bands; this suggested an interaction between the boundary layer and the knives.

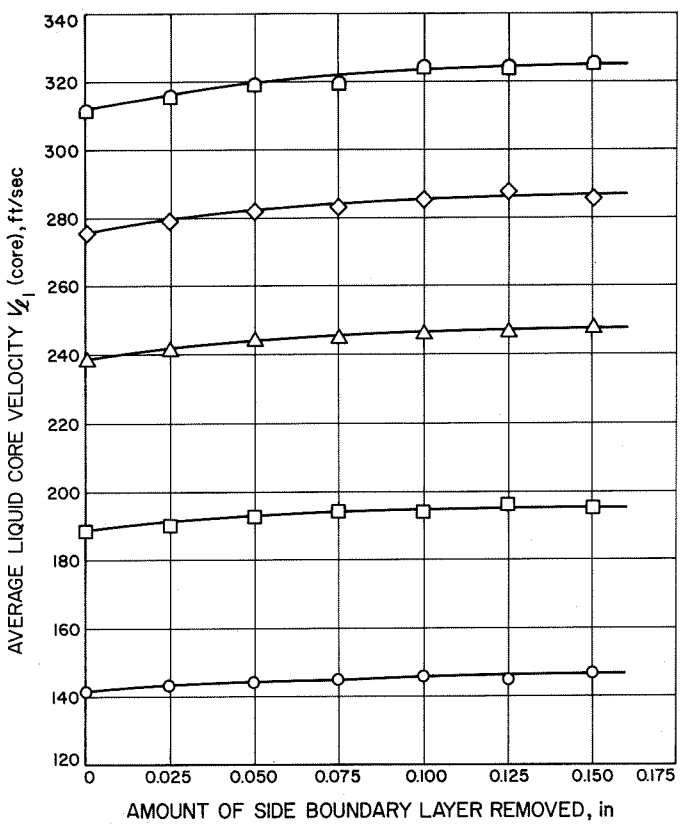

Fig. III-10. Average core velocity as a function of the amount of side boundary layer removed

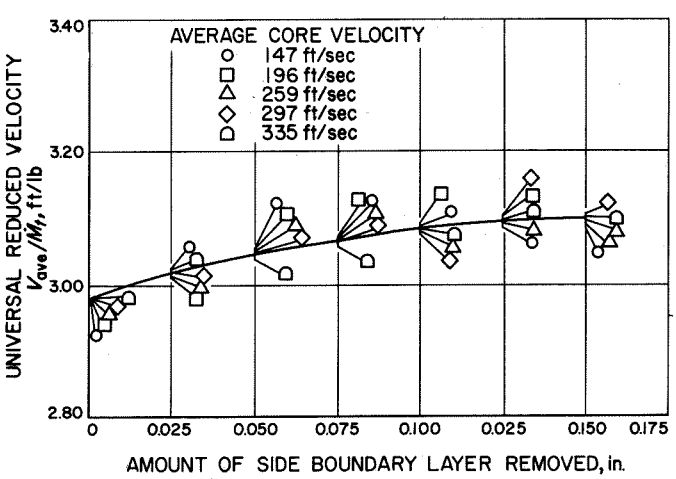

Fig. III-11. Universal reduced velocity as a function of the amount of boundary layer removed

The local liquid velocities ($U_{l_{BL}}$) in the boundary layer were determined in accordance with Eq. (III-9). These values along with the average core value and a zero wall velocity provide a complete velocity profile of the flow. Figures III-12 and III-13 show enlarged and complete velocity profiles across the narrow dimension of the duct.

What appeared to be a gas-free sheet of water to a distance of 0.003 in. from the wall was removed by the boundary-layer knife. This sheet was caused, in part, by the injector construction, in which the outer columns of water overlapped the inner duct walls, and tended to spread out the water over them. A small fraction of gas

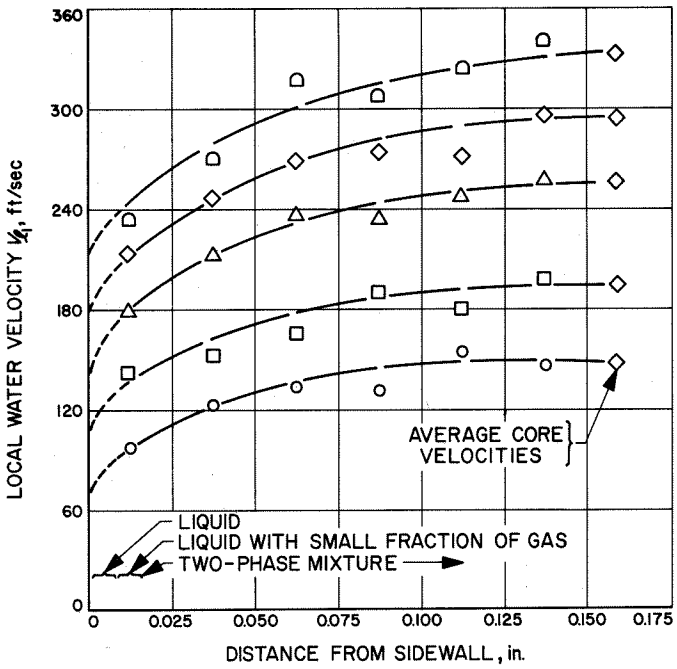

Fig. III-12. Liquid velocity profiles, 10.5 in. downstream from the injector face

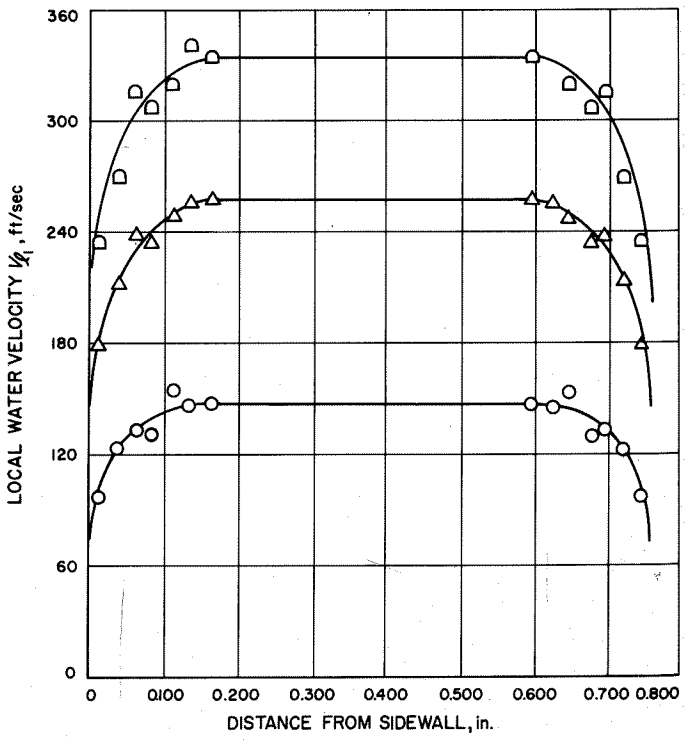

Fig. III-13. Complete liquid velocity profiles, 10.5 in. downstream from the injector face

appeared between 0.003 in. and 0.010 in. from the wall; at distances greater than 0.010 in., a homogeneous two-phase flow existed.

2. Volume Ratio

From Eq. (III-6), the average volume ratio r_v of the core flow can be calculated. Figure III-14 shows the volume ratio remaining in the core as a function of liquid core velocity for various parameters of boundary layer removed.

Because the injector was designed for a volume ratio of 1.0, and, according to Fig. III-14, the volume ratio of the remaining core is less than 1.0 for all velocities, the average volume ratios of gas and liquid in the boundary-layer and core regions are not equal. This is verified in Fig. III-15. For velocities less than 200 ft/sec, the r_v of

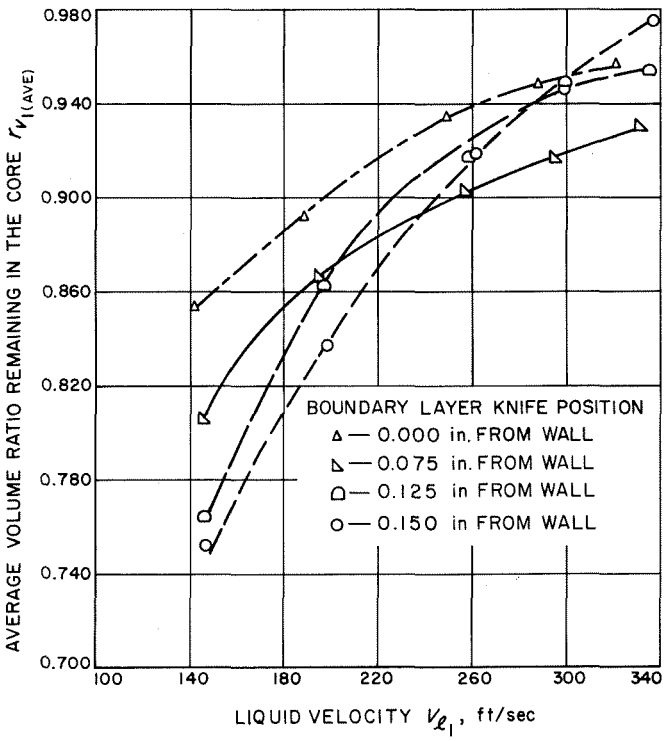

Fig. III-14. Average core volume ratio in the test section as a function of liquid flow velocity for values of the amount of boundary layer

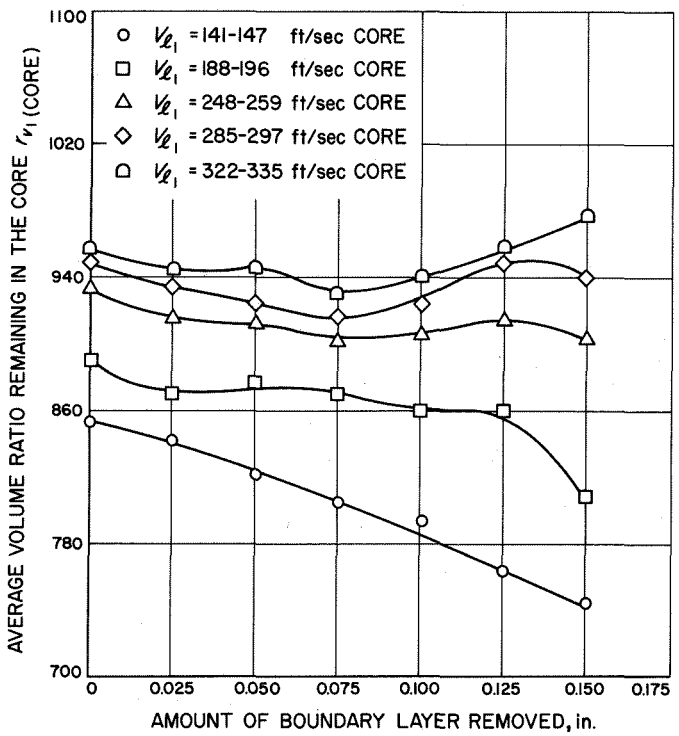

Fig. III-15. Average core volume ratio in the test section as a function of the amount of boundary layer removed

the boundary layer is higher than that of the core; at velocities above 200 ft/sec, however, the values of r_v for the boundary layer and core flows are somewhat closer in value.

At all boundary-layer knife settings, the r_v of the remaining core increases toward 1.0 as velocity is increased. This further confirms a more uniform distribution of gas and liquid at higher velocities.

Weak shock phenomena may exist across the knife blades at the lower velocities. These weak shocks could, by their pressure gradient, diffuse some gas out of the core region and into the boundary layer ducts, in effect decreasing the core r_v and increasing the r_v of the boundary layer. Because these r_v's are greater than 0.7, the gas apparently is in a connected pattern and can move a hundred fold more freely than a nonconnected or random-dispersed pattern. According to Eq. (VII-11), derived in Section VII, in which $\tau_w = \tau_{w_l} \times$ (liquid volume fraction), the variation in the local r_v should have an effect on the local shear stress. Furthermore, a change in τ_w should affect the velocity profile curve. The liquid volume fraction is

$$\frac{\text{liquid volume}}{\text{gas volume} + \text{liquid volume}} = \frac{1}{1 + r_{v_1}}$$

thus

$$\tau_w = \tau_{w_l}\left(\frac{1}{1 + r_{v_1}}\right)$$

Consequently, an increase in r_{v_1} decreases τ_w, and a decrease in r_{v_1} increases τ_w. If, as outlined previously, r_{v_1} increases near the wall, τ_w should decrease and the profile become flatter; if r_{v_1} decreases near the wall, the local τ_w will increase and the profile will be more rounded. From a V_{l_1} of 141 to 330 ft/sec, the profile near the wall becomes more rounded, and r_{v_1} decreases simultaneously in the boundary-layer region.

3. Relative Phase Velocity

The relative phase velocity between the gas and liquid phases as computed from Eq. (III-8) is plotted in Fig. III-16 as a function of gas-to-liquid mass ratio for

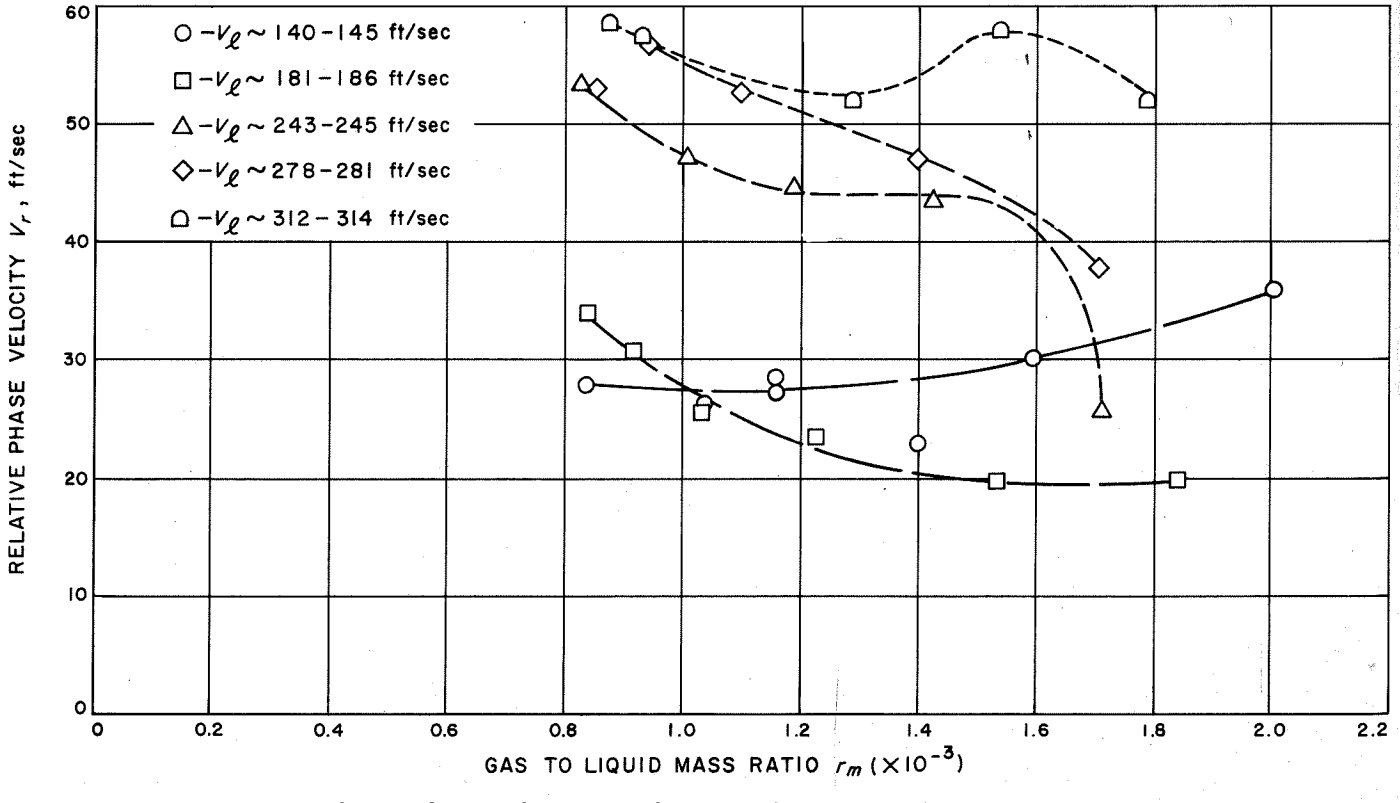

Fig. III-16. Relative phase velocity as a function of mass ratio for values of liquid velocity

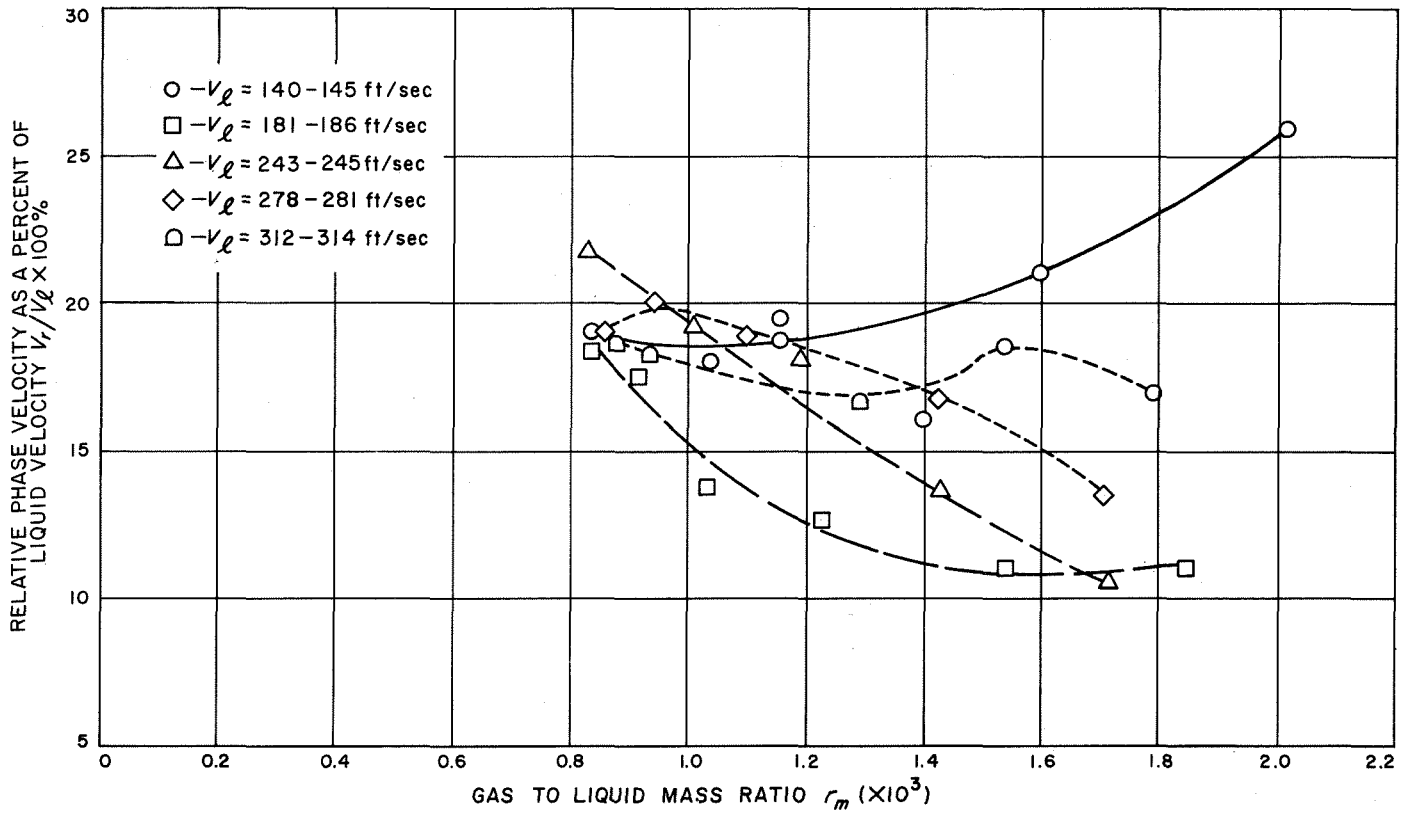

Fig. III-17. Relative phase velocity as a percent of liquid velocity vs mass ratio for values of liquid velocity $V_r = V_l - V_g$

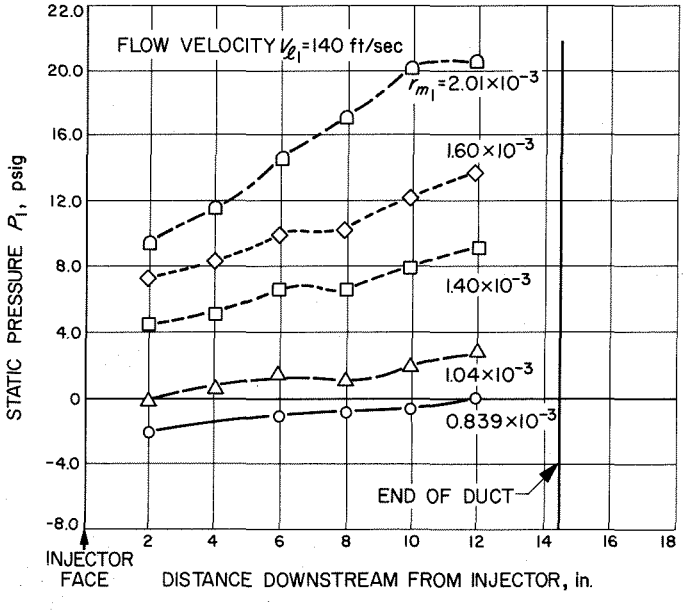

Fig. III-18. Static pressure as a function of distance from the injector for values of mass ratio, V_l = 140 ft/sec

parameters of liquid velocity V_l. In all cases, water velocity exceeds the velocity of the gas regardless of the gas-mass-to-liquid-mass ratio (r_m). In general, relative phase velocity increases with an increase in liquid velocity. Computing the relative phase velocity as a percentage of liquid velocity, the result is plotted in Fig. III-17 as a function of r_m. With one exception ($V_l \sim 180$ ft/sec), the curves are grouped fairly close to the 17 to 20% range and between the r_m values of 0.85×10^{-3} and 1.25×10^{-3}.

The existence of relative phase velocities of this magnitude suggests a positive gradient of pressure in the duct. Figures III-18, III-19, and III-20 are plots of static pressure vs duct position for flows of three different velocities and parameters of r_m. In all cases, a positive pressure gradient is evident. Imposed on the positive pressure gradient are wave-like pressure variations along the distance of the duct, evidence of the existence of weak shock waves. The possible influence of differences in the static pressure taps and gauges is minimized by the fact that the wave pattern changes with variations in such flow qualities as r_m and V_l; a wave minimum, for instance, becomes a wave maximum at the second tap position as shown in Fig. III-20.

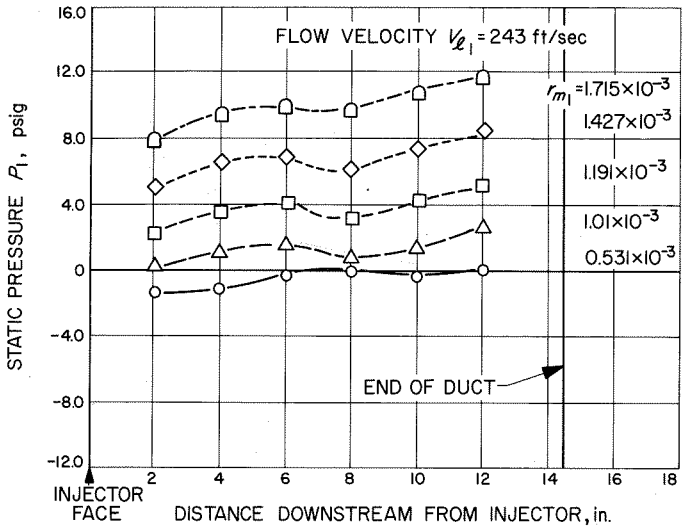

Fig. III-19. Static pressure as a function of distance from the injector for values of mass ratio, V_l = 243 ft/sec

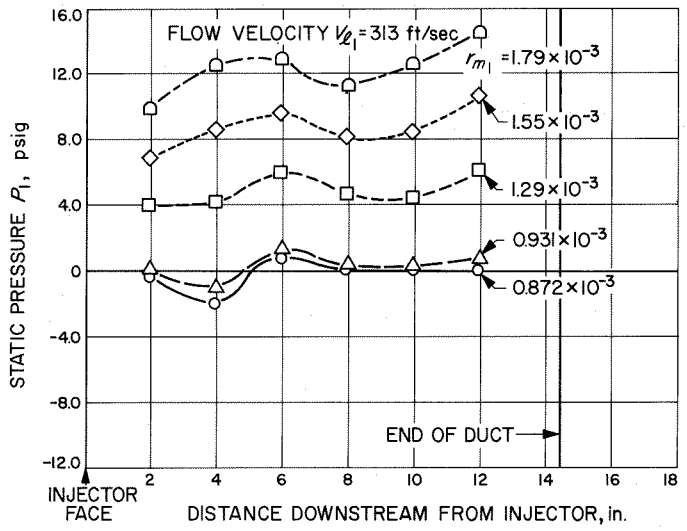

Fig. III-20. Static pressure as a function of distance from the injector for values of mass ratio, V_l = 313 ft/sec

Figure III-21 shows static pressure as a function of distance for an r_m of 1.1×10^{-3} and for three values of velocity. This value of r_m corresponds to the volume ratio of 1.0 for which the injector was designed. Thus it is evident that the r_v of 1.0 occurs with a gauge pressure $P_s = 0.0$ in the downstream vicinity of the injector as expected, but the continuously increasing pressure gradient prevents a simultaneous r_v of 1.0 and P_s of 0.0

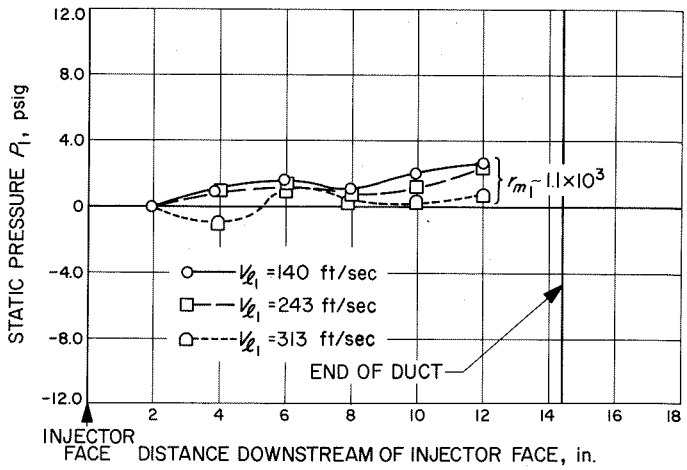

Fig. III-21. Static pressure as a function of distance from the injector for values of liquid velocity

(gauge) at any point further down the duct, except for the superimposed pressure wave variation, of course, which may produce the condition at an isolated point.

The effect of the pressure gradient on the two-phase flow is considered in Fig. III-22, which is a plot of the static pressure gradients as a function of r_m for parameters of liquid velocity. The majority of values lie between 0.05 and 0.5 psi/in. with the largest value reaching 1.1 psi/in.

From a momentum balance of the two-phase flow with pressure and with the maximum gradient of 1.1 psi/in., a velocity change on the order of a few ft/sec/ft may occur. Because the liquid constitutes over 99% of the mass of the mixture, a negligible change in liquid velocity also occurs. However, the gas has been measured at relative velocities up to 60 ft/sec, so the slight pressure gradient apparently causes a velocity separation of the phases.

Assuming such a velocity phase separation, then a balance should exist between the pressure gradient on the mixture and the drag between the phases, or

$$-A_g \Delta P - \tau_{w_p} \Delta A_w = \dot{m}_g \Delta V_g \qquad \text{(III-13)}$$

Assuming however, a steady state in which the phase velocity is constant, then $\Delta V_g = 0$, and

$$-A_g \Delta P = \tau_{w_p} \Delta A_w \qquad \text{(III-14)}$$

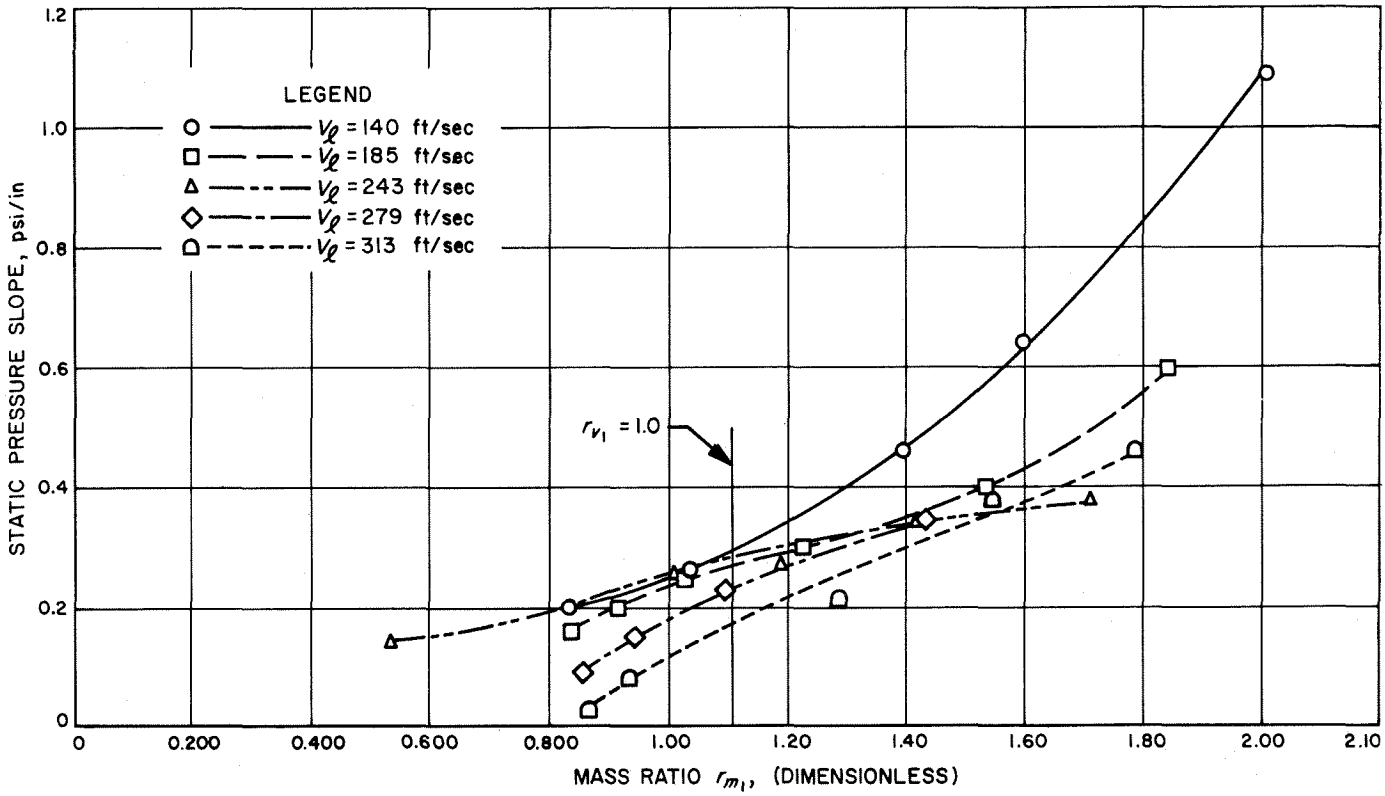

Fig. III-22. Static pressure slope as a function of mass ratio for values of liquid velocity

The form of $\tau_{w_p} \Delta A_w$ that represents the drag force between phases must now be determined.

There are three possibilities for a simple form of this term that depend upon the volume ratio and the proximity to the injector. For $r_v >> 1$, the homogeneous flow model is obviously a water-droplet distribution in a gas. For $r_v << 1.0$, the flow model becomes a gas-bubble distribution in water. The drag coefficient for either model can be determined if the respective droplet and bubble sizes are known. In addition, there are individual water streams in downstream proximity to this type of injector. The orders of magnitude for the three models were calculated as follows to determine any match with the measured pressure gradient term.

For straight jets of water in a gaseous media, the force balance between the gas and liquid is

$$1/2\, \rho_g\, (V_r)^2\, C_f\, N_j A_j\, L_j = A_g\, (P_2 - P_1) \qquad \text{(III-15)}$$

where $N_j\, A_j\, L_j$ = total area of all jets in the pressure rise increment. For a V_r of 50 ft/sec, a jet diameter of 0.070 in., and an applicable value of ρ_g (Fig. III-23), the calculated pressure rise becomes

$$\Delta P = 0.0033 \text{ psi/in.} \qquad \text{(III-16)}$$

which is smaller than the median-measured 0.2 psi/in. by a magnitude of nearly 100.

For water droplets in the shape of spheres dispersed in the gas, the force balance is

$$1/2\, \rho_g\, (V)^2\, C_d\, N_{sph}\, A_{sph} = A_g\, (P_2 - P_1) \qquad \text{(III-17)}$$

Assuming again a $V_r = 50$ ft/sec, the coefficient of drag for either a bubble or a droplet (C_d) can be determined from experimental data, such as that reported by Hoerner (Ref. III-6) by computing the Reynolds number (R_e) for a sphere. An average sphere diameter must be assumed and, from photographic data, a diameter of 0.030 to 0.070 in. is a reasonable approximation. Thus the relative R_e now becomes

$$R_e = \left(\frac{\rho_g\, V_r\, D_{sph}}{\mu_g} \right) \cong 19 \text{ to } 45 \qquad \text{(III-18)}$$

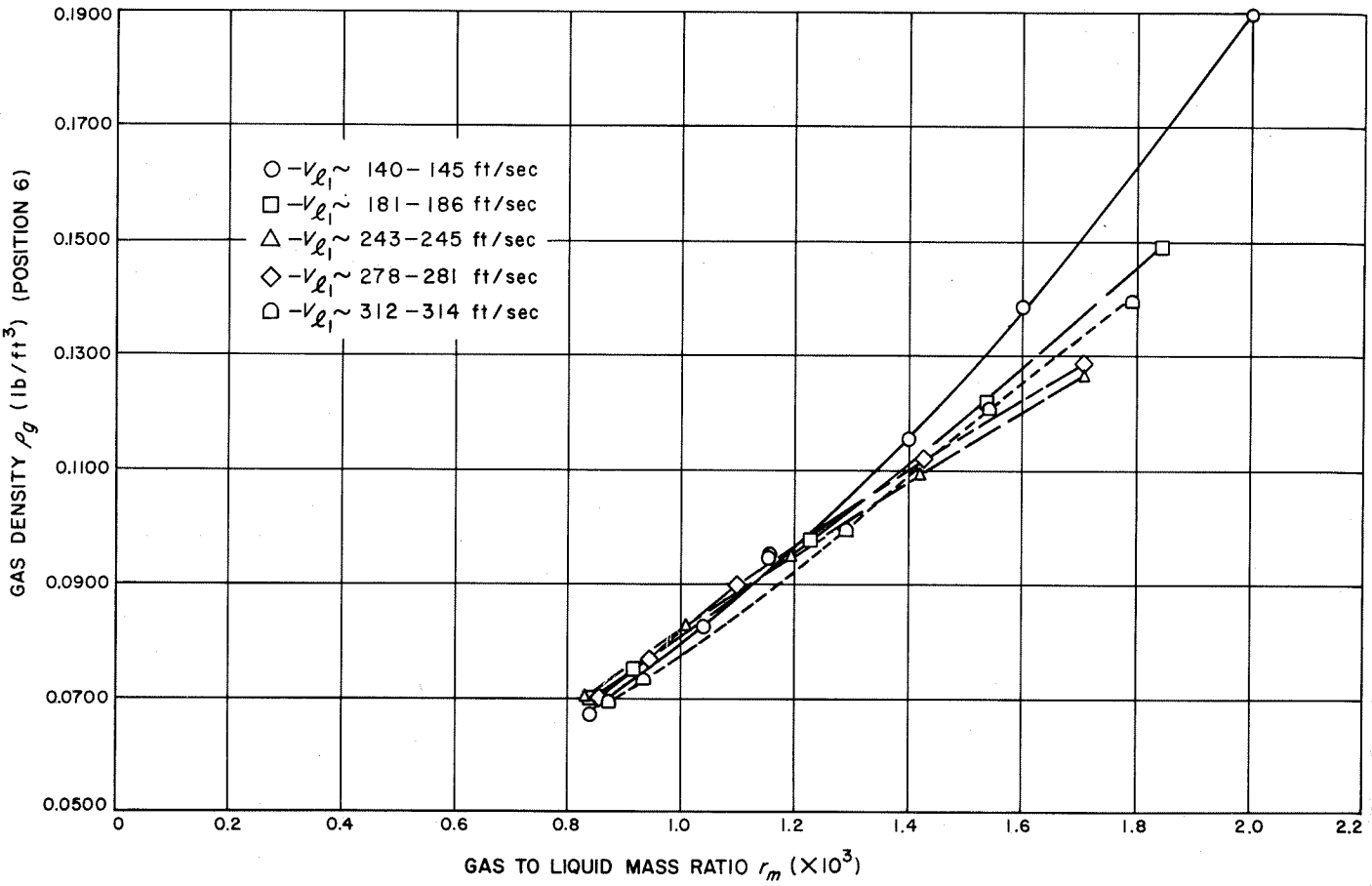

Fig. III-23. Gas density as a function of mass ratio for values of liquid velocity

giving a

$$C_d = 1.3 \text{ to } 2.6 \qquad \text{(III-19)}$$

Solving then for ΔP,

$$\Delta P = 0.731 \text{ to } 2.6 \text{ psi/in.} \qquad \text{(III-20)}$$

a value that, within reasonable adjustment of the sphere size, falls within a factor of 10 of the range of the measured pressure gradients.

Lastly, considering the bubble-in-water model for which the force balance equation is

$$1/2\,\rho_l\,(V_r^2)\,C_d\,N_B\,A_B = A_l\,(\Delta P) \qquad \text{(III-21)}$$

Assuming as before a $V_r = 50$ ft/sec and a bubble size of approximately 0.030 to 0.070 in., the Reynolds number becomes

$$R_e = 1.26 \text{ to } 2.95 \qquad \text{(III-22)}$$

and, from Ref. III-6, the $C_d \cong 2.2$ to 8. The ΔP is calculated to be:

$$\Delta P = 2300 \text{ to } 359 \text{ psi/in.} \qquad \text{(III-23)}$$

These values of ΔP are 1000 to 10,000 times greater than those measured in the upstream flow.

Thus, for the measured pressure gradients of 0.1 to ~0.6 psi/in., it is clearly seen that this range corresponds more closely to the water droplet model than the straight jet or gas bubble models, which are off in calculated pressure gradients by a factor of at least one hundred to ten thousand in opposite directions. Assuming that the flow corresponds to the water droplet model, sufficient information exists to determine the C_d and D of the droplets.

4. Determination of Droplet C_d/D

For the model of water droplets in gas, knowledge of the pressure gradients and relative phase velocities are

sufficient to compute the C_d and D of the droplets, assuming they are spherical and of a nearly uniform size.

From Eq. (III-17), which represents the drag between phases,

$$\Delta P = 1/2\,\rho_g\,(V_r^2)\,C_d\,N_{sph}\,\frac{A_{sph}}{A_g}$$

or, writing known quantities on left side,

$$\frac{2\Delta P\,A_g\,\rho_g}{V_r^2} = A_{sph}\,N_{sph}\,C_d \qquad \text{(III-24)}$$

The number of spheres per unit length ($L = 1$ in.) is

$$\frac{N_{sph}}{L} = \frac{\dfrac{V_l}{L}}{V_{sph}} = \frac{A_l}{\dfrac{4\pi}{3}(R_{sph})^3} = \frac{6A_l}{\pi D_{sph}^3} \qquad \text{(III-25)}$$

and the projected area of a sphere is

$$A_{sph} = \frac{\pi D_{sph}^2}{4} \qquad \text{(III-26)}$$

The right side of Eq. (III-24) becomes

$$A_{sph}\,N_{sph}\,C_d = \frac{\pi D_{sph}^2}{4}\,\frac{6A_l}{\pi D_{sph}^3}\,C_d = \frac{6A_l\,C_d}{4D_{sph}} \qquad \text{(III-27)}$$

giving for Eq. (III-24)

$$\frac{2\Delta P\,A_g\,\rho_g}{V_r^2} = \frac{6A_l\,C_d}{4D_{sph}} \qquad \text{(III-28)}$$

Rearranging,

$$\frac{4\Delta P\,\rho_g}{3V_r^2}\left(\frac{A_g}{A_l}\right) = \frac{C_d}{D_{sph}} \qquad \text{(III-29)}$$

and, noting that

$$\frac{A_g}{A_l} = r_v$$

the ratio of C_d/D then becomes

$$\frac{C_d}{D_{sph}} = \frac{4\Delta P\,\rho_g\,r_v}{3V_r^2} \qquad \text{(III-30)}$$

Values of C_d/D as a function of r_m are plotted as parameters of velocity on Fig. III-24.

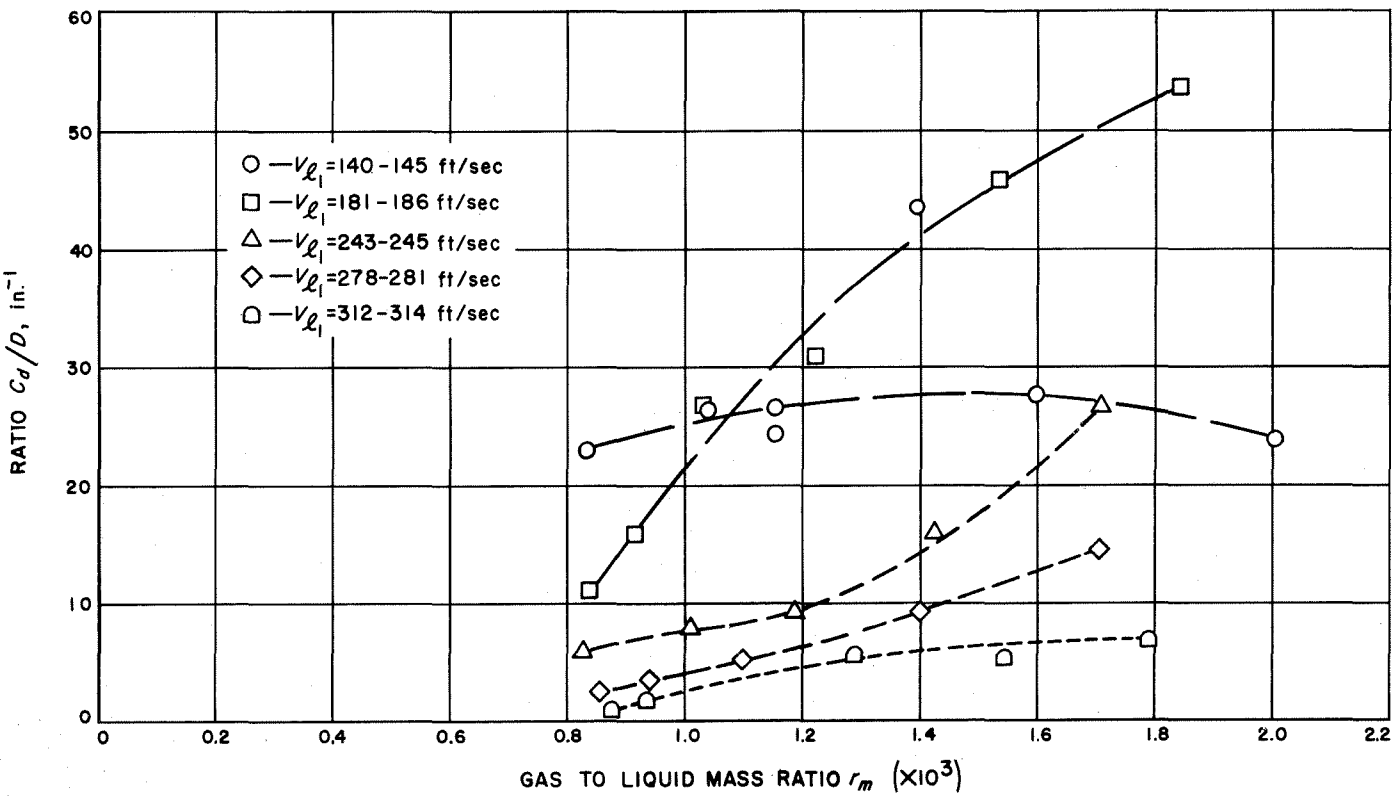

Fig. III-24. Ratio C_d/D as a function of mass ratio for values of liquid velocity

Using three values of r_m, the ratio C_d/D is plotted in Fig. III-25 as a function of liquid velocity, V_{l_1}. The plotted values form a reasonably continuous curve that should yield an analytical relationship between C_d/D and liquid velocity. Choosing a relationship of the form $y = a\exp(-bx)$ where a and b are arbitrary constants, the relationship between C_d/D and velocity becomes

$$C_d/D = a\exp(-b\,V_{l_1}) \qquad \text{(III-31)}$$

By fitting this relationship at two values of velocity, the constants are solved to give

$$C_d/D = 202\exp(-0.01332\,V_l) \qquad \text{(III-32)}$$

Still an additional equation is required to determine individual values for C_d and D. Such an equation exists in the relationship of C_d vs Reynolds number for spheres. From T. E. Stonecypher (Ref. III-7), a close fit to the experimental C_d vs R_e data for spheres can be made in the range of $0.1 \leq R_e \leq 10^4$ with the relationship

$$\log_e C_d = 3.271 - 0.8893(\log_e R_e) + 0.03417(\log_e R_e)^2 + 0.001443(\log_e R_e)^3 \qquad \text{(III-33)}$$

in which

$$R_e = \frac{\rho_g D V_r}{g\mu_g}$$

thus the unknowns C_d and D can be found as functions of V_r which correspond to specific values of V_l. From a combination of Eq. (III-32) and (III-33), the droplet diameter is

$$D = \frac{\text{anti}\log_e[3.271 - 0.8893(\log_e R_e) + 0.03417(\log_e R_e)^2 + 0.001443(\log_e R_e)^3]}{202\exp(-0.0133\,V_l)} \qquad \text{(III-34)}$$

The coefficient of drag of the sphere, derived from Eq. (III-32), is

$$C_d = 202\,D_{sph}\exp(-0.0133\,V_l) \qquad \text{(III-35)}$$

A plot of the experimental C_d vs R_e for spheres, and the fit of Eq. (III-33) and the respective equations of C_d/D vs R_e from the two-phase flow data is shown in Fig. III-26.

Equations (III-34) and (III-35) were solved on an IBM 1620 computer; the results of C_d and D vs R_e are shown in Fig. III-27.

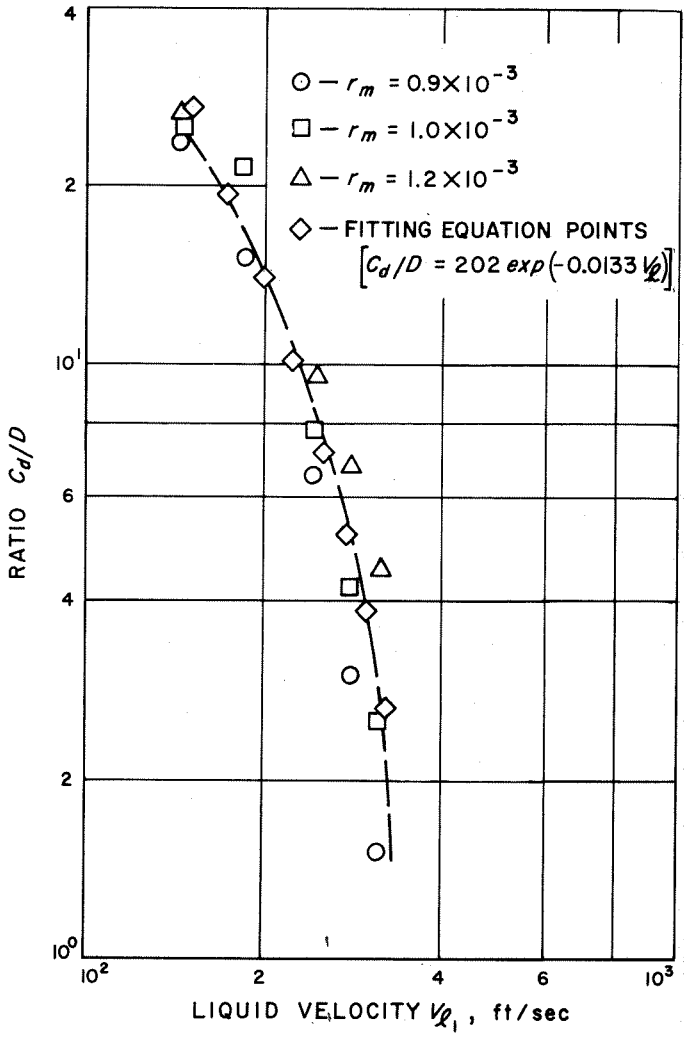

Fig. III-25. Ratio C_d/D plotted as a function of liquid velocity for values of mass ratio

Obviously, the curve of droplet diameter vs Reynolds number is not realistic. The droplets are on a scale of magnitude larger than would be expected from discharge orifices of 0.070 in. ID. According to Rupe (Ref. III-8), jets of water at Reynolds numbers exceeding 100,000 have a strong tendency to break into many small fragments a short distance from the discharge orifice. The Reynolds numbers for the injector tubes, based on the discharge ID, range in values from 86,000 to 290,000. The curve of C_d vs R_e values is correspondingly low.

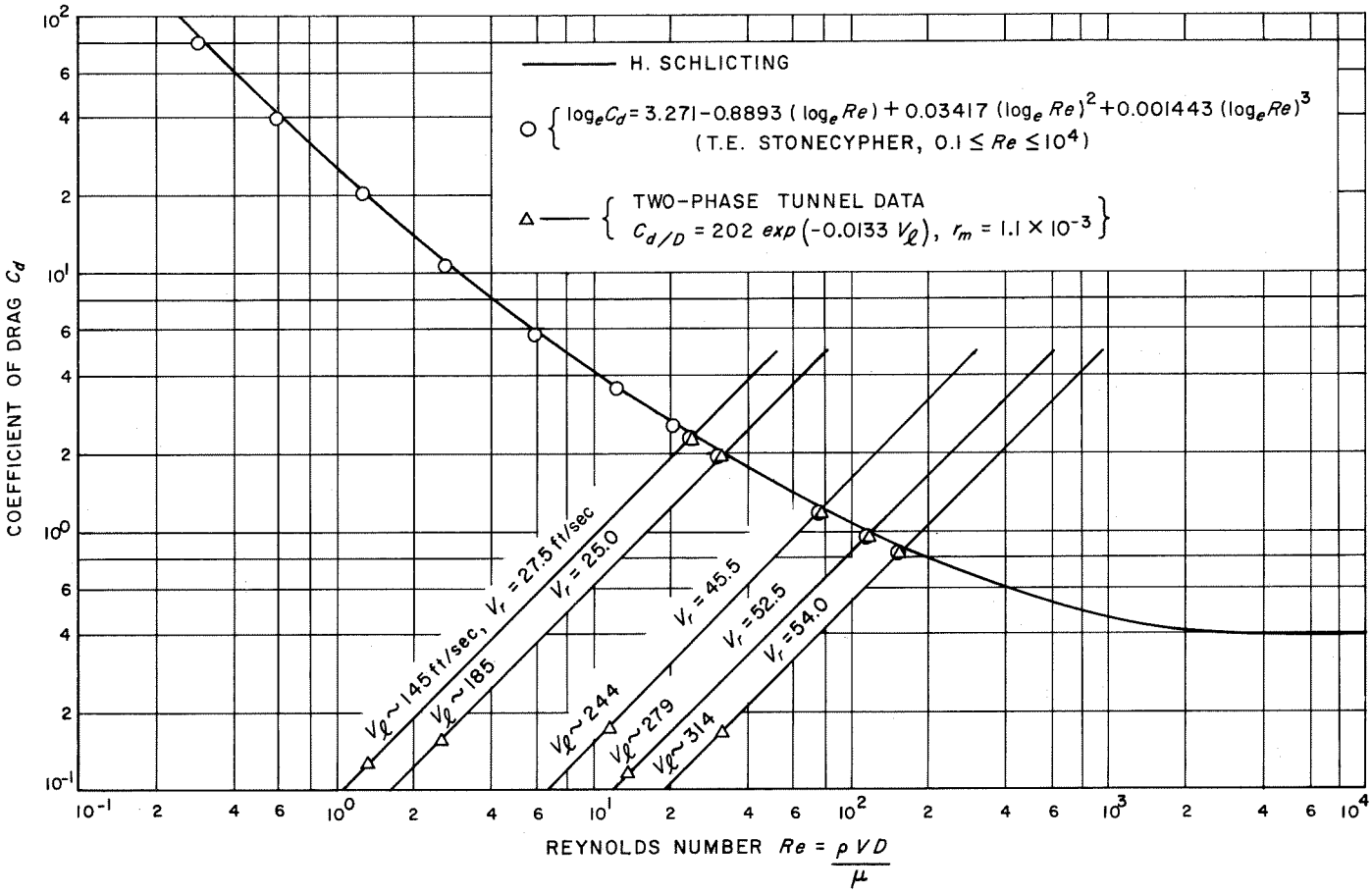

Fig. III-26. Drag coefficient for spheres as a function of the Reynolds number

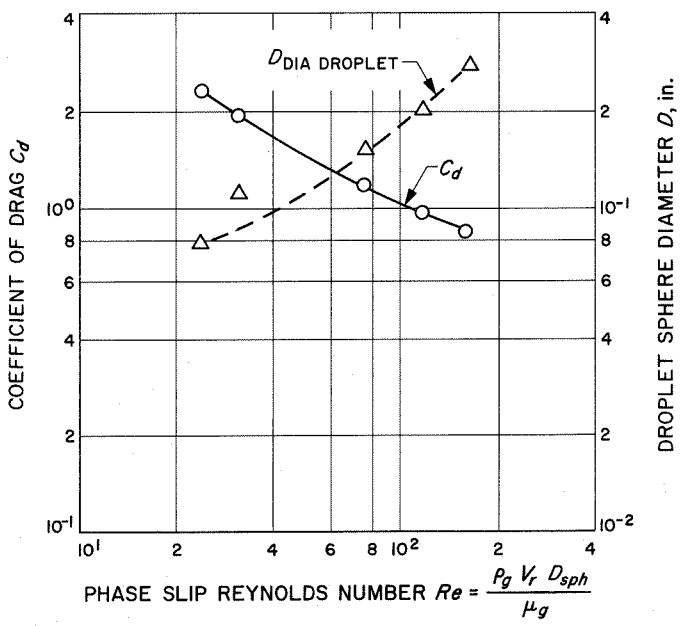

Fig. III-27. Drag coefficient and liquid drop diameter as a function of the relative phase velocity Reynolds number

The droplet-in-gas model is a questionable representation of the measured flow conditions. This is indeed confirmed by the various high-speed (½ μsec shutter speed) still pictures of flow conditions upstream of normal and oblique shocks in Sections V and VI, respectively. Enlargements of these photographs clearly show a bubble structure of two basic size groups in a water matrix. Fine bubbles ranging in size from 0.005 in. to 0.020 in., and medium size bubbles from 0.020 in. to 0.060 in. Generally, the bubbles were formed into chain-like groups orientated predominantly parallel to the direction of flow. With increasing flow velocities, the size of the groups tended to decrease. The interpretation of the fine and medium structure representing bubbles instead of droplets is further confirmed by the high-speed (25,000 frames/sec) motion pictures of flows over wedges. Some of this chain-like structure tends to turn and move parallel to the oblique shock wave, and, in general, in the direction of negative pressure gradients. Water droplets, having significantly higher inertia than the gas, would not be influenced in this way; the droplets tend to enter the shock front parallel to the flow. These observations are discussed further in Section V.

Apparently, in the vicinity of a volume ratio of 1:1, water fragments from the jet streams coalesce more rapidly than gas bubbles, and form a partially continuous media. The structure at the extreme volume ratio of 0.1 is reasonably expected to be bubble-in-liquid, and the structure at the extreme volume ratio of 10 is expected to be a liquid-droplet-in-gas. At the position downstream from the injector where the measurements were made, it is obvious that the flow model did not correspond exactly to the bubble-in-liquid structure because of the relatively high relative phase velocities and correspondingly low pressure gradients. The chain-like arrangement apparently reduces drag on the gas bubbles by three orders of magnitude. At a distance much further from the injector, it is quite possible that the bubbles would tend to separate and, as long as the pressure gradients remained small, thereby reduce their relative phase velocity to negligibly small values.

Additional evidence of the nature of the upstream gas-liquid structure is provided in Section IV from an analysis of the normal shock measurements and photographs. From Figs. IV-4 through IV-8 which show the static pressure gradients for normal shocks of various strengths, it is clear that pressure gradients of 360–400 psi/in. occur at liquid flow velocities of 320–340 ft/sec. According to Fig. III-16, such flow velocities have corresponding relative phase velocities of 50–55 ft/sec. The value of the pressure gradient for the bubble-in-water model with a bubble radius $R = 0.070$ in. and a relative phase velocity $V_r = 50$ ft/sec is about 359 psi/in. This fits well into the measured values of pressure gradient for the normal shock.

The shape of the pressure profile through the shock structure represents, in part, the variation of the inter-phase drag model through the shock. The foot of the curve rises asymptotically from the upstream static pressure at a relatively low gradient to that point where the drag model changes a thousand fold to the correspondingly high-drag distributed, bubble-in-liquid model. From this point, the pressure gradient increases to a very large value until the deceleration of the liquid is sufficient to nearly match the downstream velocity. The pressure gradient then decreases monotonically to zero as the profile is rounded asymptotically to reach the downstream static pressure value.

As stated in Section IV, correlation of the first observable change in the flow structure for a normal shock with the pressure profile curves results simultaneously in a volume ratio of 0.77 and a rapid increase in the pressure gradient to its largest value. This is true for a variety of supersonic upstream velocities, and strongly suggests that the model change occurs at a volume ratio of very nearly $r_{r_1} = 0.77$. The finite length of the initial profile as it asymptotically reaches the upstream pressure for a variety of volume ratio values between 0.75 and 0.96 indicates the existence of a finite wave structure in a gas-connected media.

Further confirmation of a complete change in the flow model under the influence of diffused conical shocks and high acceleration gradients is given in Fig. 8 of Ref. III-9. In separator experiments with two-phase flows (Ref. III-9), the percent liquid bypassing the primary slot remained relatively constant until the volume ratio was reduced to 1.0. The rate of bypass then increased significantly as the ratio was reduced from 1.0 to 0.7, and increased in proportion to the slot width reduction from that point on. Thus, with thousands of g's acceleration on the two-phase film, the liquid would not effectively separate from the entrained bubbles, in the distance allowed, for volume ratios less than 0.7. The fact that the impinging two-phase flow was liquid droplets in a gas-type structure at a volume ratio greater than 1 confirms a change in the model to a distributed bubble-in-water matrix at volume ratios slightly less than 1.0 or $\sim$0.77, and confirms the drag characteristics of that model to be applicable between phases at volume ratios less than 0.77.

Apparently, then, pressure pulses are transmitted through the two-phase continuum according to the velocity of sound relationship derived in Section I. Sustained pressure gradients as created by developing boundary layers, however, tend to separate the phases. The gas is influenced most strongly by its density relative to that of the pure liquid; the applicable gas-liquid model is a further influence.

Further, it is obvious that while the mixture behaves very well as a continuum for shock propagation (as demonstrated in Sections IV and V), it is not necessarily isotropic with respect to the propagation of pressure gradients. Because this type of injector produces the chain-like bubble structure in the upstream flow, the propagation of pressure pulses or sound waves will occur more easily in the direction of flow than in the direction perpendicular to the flow.

Nomenclature

A cross sectional area, duct (ft^2)

A_b cross sectional area, bubble (ft^2)

A_g cross sectional area, gas, local (ft^2)

A_j surface area of liquid jet (ft^2)

A_l cross sectional area, liquid, local (ft^2)

A_{sph} cross sectional area, sphere (ft^2)

C_d coefficient of drag, bubble or droplet

C_f coefficient of friction

D sphere diameter (ft)

F thrust (lb_f)

$\mathring{m}_g$ mass flow rate, gas (slugs/sec)

$\mathring{m}_l$ mass flow rate, liquid (slugs/sec)

N_B number of bubbles

N_γ number of liquid jets

N_{sph} number of liquid spheres

r_v gas-to-liquid, volume, ratio, static

R_e Reynolds number

U boundary layer velocity (ft/sec)

V_g velocity, gas phase (ft/sec)

V_l velocity, liquid phase (ft/sec)

V_r relative velocity between gas and liquid phases (ft/sec)

ρ_g density, gas phase ($slugs/ft^3$)

ρ_l density, liquid phase ($slugs/ft^3$)

τ_w wall shear stress, mixture (lb/ft^2)

τ_{w_l} wall shear stress, liquid (lb/ft^2)

τ_{w_ρ} shear stress between phases (lb/ft^2)

Subscripts

BL boundary layer

Δ local value based on incremental steps in the independent variables

P phase

References

III-1. Petrick, M., Report 5787, Argonne National Laboratory, 1958.

III-2. Hooker, H. H., and Popper, G. F., Report 5766, Argon National Laboratory, 1958.

III-3. Perkins, H. C., Jr., Yusuf, M., and Leppert, G., *Nucl. Sec. Eng.*, vol. 11, p. 304, 1961.

III-4. Dengler, C. E., PhD. Thesis, Massachusetts Institute of Technology, Cambridge, Massachusetts, 1952.

III-5. Neal, L. G., and Bankoff, S. G., "A High Resolution Resistivity Probe for Determination of Local Void Properties in Gas-Liquid Flow," *A. I. Ch. E. Journal*, vol. 490, pp. 490–494, July 1963.

References (contd)

III-6. Hoerner, S. F., *Fluid Dynamic Drag*, published by the author, pp. 3–8, 1958.

III-7. Stonecypher, T. E., *Quarterly Progress Report on Engineering Research*, Report No. P-60-17, Rohm and Haas Company, Huntsville, Ala., December 1960.

III-8. Rupe, J. H., *On the Dynamic Characteristics of Free-Liquid Jets and a Partial Correlation with Orifice Geometry*, Technical Report 32-207, Jet Propulsion Laboratory, Pasadena, Calif., January 1962.

III-9. Elliott, D., Cerini, D. J., Weinberg, E., "Investigation of Liquid MHD Power Conversion," in *3rd Bi-Annual Aerospace Power Systems Conference, Philadelphia, Penn.*, AIAA paper No. 64–760, September 1964.

IV. Normal Shocks

A. Fundamentals

For the isothermal two-phase continuum developed in Section I, the normal shock-wave relationships can be developed by the usual analysis in which the shock wave is fixed with respect to the frame of reference and the two-phase mixture flows into the shock. Let subscript 1 denote the region ahead of the shock and subscript 2 the region behind as shown in Fig. IV-1. The continuity equation across the normal shock is

$$\rho_1 V_1 = \rho_2 V_2 \tag{IV-1}$$

and the momentum equation is

$$\rho_1 V_1^2 - \rho_2 V_2^2 = P_2 - P_1 \tag{IV-2}$$

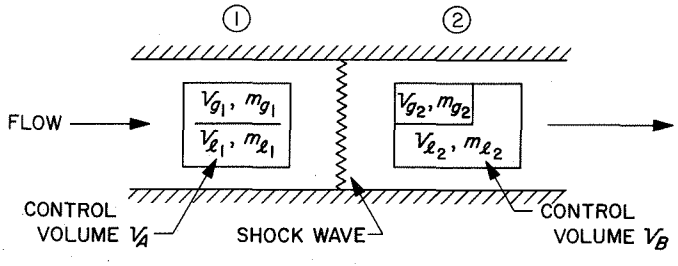

Fig. IV-1. Schematic of normal shock and control surface volume

From Eq. (I-1), which is the density of the mixture,

$$\rho = \rho_l \left(\frac{1 + r_m}{1 + r_v} \right)$$

or

$$\rho_1 = \rho_{l_1} \left(\frac{1 + r_{m1}}{1 + r_{v_1}} \right)$$

and

$$\rho_2 = \rho_{l_2} \left(\frac{1 + r_{m_2}}{1 + r_{v_2}} \right) \tag{IV-3}$$

and, from Eq. (I-4), the isothermal equation of state is

$$r_v P = \text{constant}, \text{or} \qquad r_{v_1} P_1 = r_{v_2} P_2 \tag{IV-4}$$

In addition, a relationship must be established between r_{m_1} and r_{m_2} that will provide sufficient equations to define the downstream unknown quantities in terms of the upstream conditions. With reference to Fig. IV-1, let

$$V_A = V_B \tag{IV-5}$$

By continuity, the mass flow rates upstream and downstream are equal:

$$\mathring{m}_{g_1} = \mathring{m}_{g_2} \tag{IV-6}$$

$$\mathring{m}_{l_1} = \mathring{m}_{l_2} \tag{IV-7}$$

By definition, the mass ratios are

$$r_{m_1} = \frac{m_{g_1}}{m_{l_1}} \tag{IV-8}$$

$$r_{m_2} = \frac{m_{g_2}}{m_{l_2}} \tag{IV-9}$$

For homogeneous mixtures (without pressure gradients),

$$\begin{aligned} U_{l_1} &= U_{g_1} \\ U_{l_2} &= U_{g_2} \end{aligned} \tag{IV-10}$$

Defining a cross-sectional area for each phase component, and assuming a unit length for the control volumes, Eqs. (IV-8) and (IV-9) can be written,

$$r_{m_1} = \frac{m_{g_1}}{m_{l_1}} = \frac{\rho_{g_1} A_{g_1}}{\rho_{l_1} A_{l_1}} \tag{IV-11}$$

$$r_{m_2} = \frac{m_{g_2}}{m_{l_2}} = \frac{\rho_{g_2} A_{g_2}}{\rho_{l_2} A_{l_2}} \tag{IV-12}$$

Equations (IV-11) and (IV-12) can be multiplied by the velocity ratios of Eq. (IV-10) to obtain mass flow ratios:

$$r_{m_1} = \frac{\rho_{g_1} A_{g_1} U_{g_1}}{\rho_{l_1} A_{l_1} U_{l_1}} = \frac{\mathring{m}_{g_1}}{\mathring{m}_{l_1}} \tag{IV-13}$$

$$r_{m_2} = \frac{\rho_{g_2} A_{g_2} U_{l_2}}{\rho_{l_2} A_{l_2} U_{l_2}} = \frac{\mathring{m}_{g_2}}{\mathring{m}_{l_2}} \tag{IV-14}$$

By Eqs. (IV-6) and (IV-7), however, the mass flow ratios are equal:

$$\frac{\mathring{m}_{g_1}}{\mathring{m}_{l_1}} = \frac{\mathring{m}_{g_2}}{\mathring{m}_{l_2}}$$

Therefore,

$$r_{m_1} = r_{m_2} \tag{IV-15}$$

Combining Eqs. (IV-1) and (IV-2),

$$\rho_1 V_1^2 - \frac{\rho_1^2 V_1^2}{\rho_2} = P_2 - P_1 \tag{IV-16}$$

Combining Eqs. (IV-4) and (IV-16) to eliminate P_1,

$$P_2 = \rho_1 V_1^2 \left(1 - \frac{\rho_1}{\rho_2}\right) \frac{1}{1 - r_{v_2}/r_{v_1}} \tag{IV-17}$$

From Eq. (IV-3),

$$\frac{\rho_1}{\rho_2} = \frac{\rho_{l_1}}{\rho_{l_2}} \left(\frac{1 + r_{m_1}}{1 + r_{m_2}}\right) \left(\frac{1 + r_{v_2}}{1 + r_{v_1}}\right) \tag{IV-18}$$

Assuming that $\rho_{l_1} = \rho_{l_2}$ (for $P_2 < 1000$ psi), and combining Eq. (IV-15) with Eq. (IV-18) and substituting the result into Eq. (IV-17),

$$P_2 = \rho_l V_1^2 \frac{r_{v_1}(1 + r_{m_1})}{(1 + r_{v_1})^2} \tag{IV-19}$$

Comparing Eqs. (IV-19) and (I-5), the pressure ratio becomes

$$\frac{P_2}{P_1} = M_1^2 \tag{IV-20}$$

Combining Eqs. (IV-4) and (IV-20), the downstream volume ratio is

$$r_{v_2} = \frac{r_{v_1}}{M_1^2} \tag{IV-21}$$

Combining Eqs. (IV-1), (IV-18), and (IV-21), the downstream mixture velocity is

$$V_2 = \frac{V_1}{M_1^2} \left(\frac{M_1^2 + r_{v_1}}{1 + r_{v_1}}\right) \tag{IV-22}$$

By definition, the downstream Mach number is

$$M_2 = \frac{V_2}{c_2}$$

which, with Eq. (I-5) for c_2, leaves

$$M_2 = \frac{V_2}{(1 + r_{v_2})} \left[\frac{\rho_l r_{v_2}(1 + r_{m_2})}{P_2}\right]^{1/2} \tag{IV-23}$$

Substituting Eq. (IV-22) for V_2 and combining Eq (I-5), the downstream Mach number is

$$M_2 = \frac{1}{M_1}, \text{or} \qquad \text{(IV-24)}$$

$$M_2 M_1 = 1 \qquad \text{(IV-25)}$$

B. Results

During operation of the supersonic tunnel described in Section II, it was found that restriction of the flow by the back-pressure valve created a normal shock downstream of the test section. Further restriction drove the shock upstream through the test section to the position of the upper and lower boundary layer knives. The static pressure taps, separated by 0.2 in. along the center line of the test section, provided static pressure sampling through the depth of the shock structure, and the three-axis probe provided both total head and static pressure surveys through the depth, width, and height of the structure. The total head surveys, however, will be discussed in detail in Section VI.

The thickness of the test section as adjusted by the position of the side boundary layer knives had a definite effect on the observable shock phenomena. With maximum boundary layer removal, the tunnel thickness was reduced to 0.308 in., and the normal shock phenomena appeared as two black lines approximately 0.10 in. apart (Fig. IV-2). The two lines tend to merge into one because the camera lens center line was not on the center line of the shock. As the width of the test section increased, the depth of the observable shock phenomena increased to a maximum approaching 1.0 in. (Fig. IV-3).

Referring to Fig. I-4, the characteristic time for the collapse of a 0.010 in. diameter bubble at ~200 ft/sec is about 10^{-5} sec, which is approximately the time required for the mixture to travel 0.05 in. Further, the time required to reach 90% of thermodynamic equilibrium is approximately 1 μsec, which is the time required to travel 1 in. at the downstream velocity.

The effect of the dynamic and thermal relaxation times is spread of the shock structure in depth. Considering the observable effects, however, the reduction in bubble size caused by the initial compression upon encountering the shock front would be evidenced by greater light transmission of the liquid region near the shock; this transmission is evident between the dark lines of Fig. IV-2. The rebound of the bubbles and other turbulent motion would

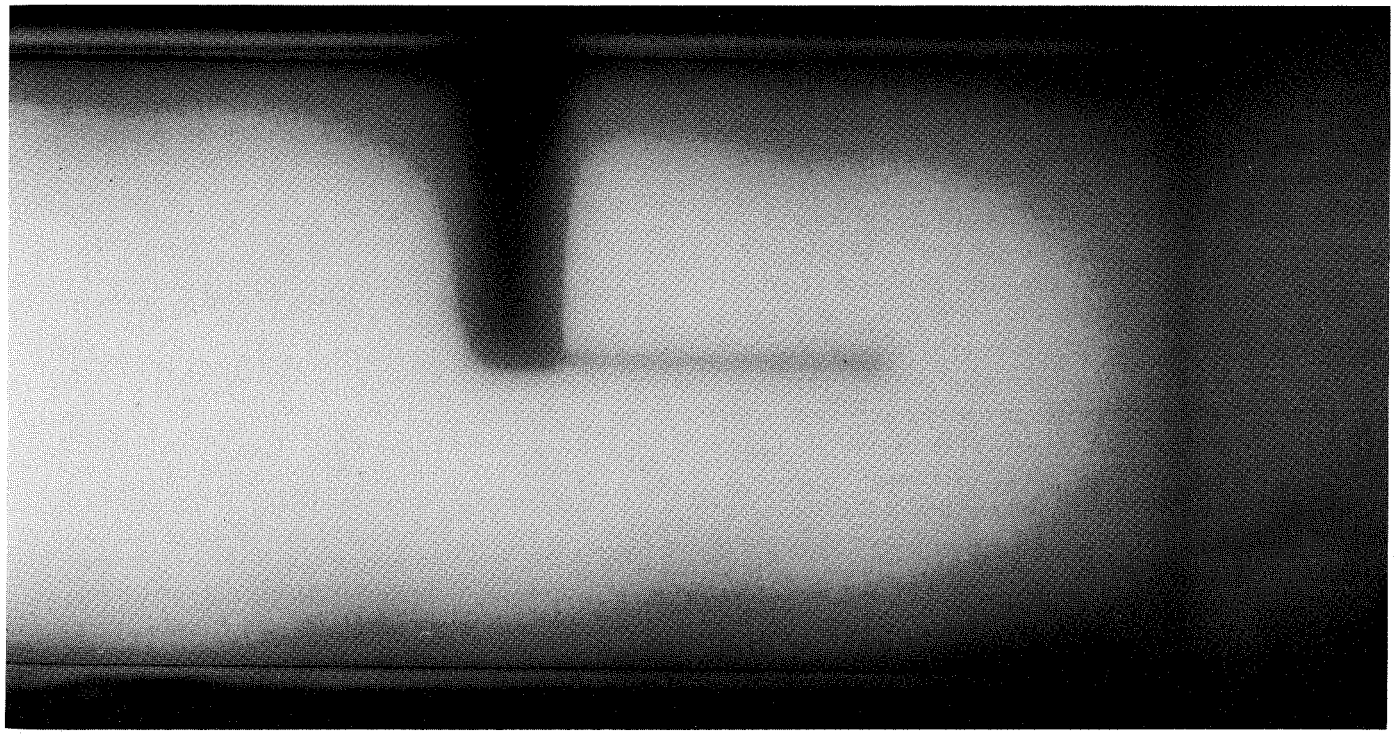

Fig. IV-2. Normal shock ($M_1 \sim 4.0$)

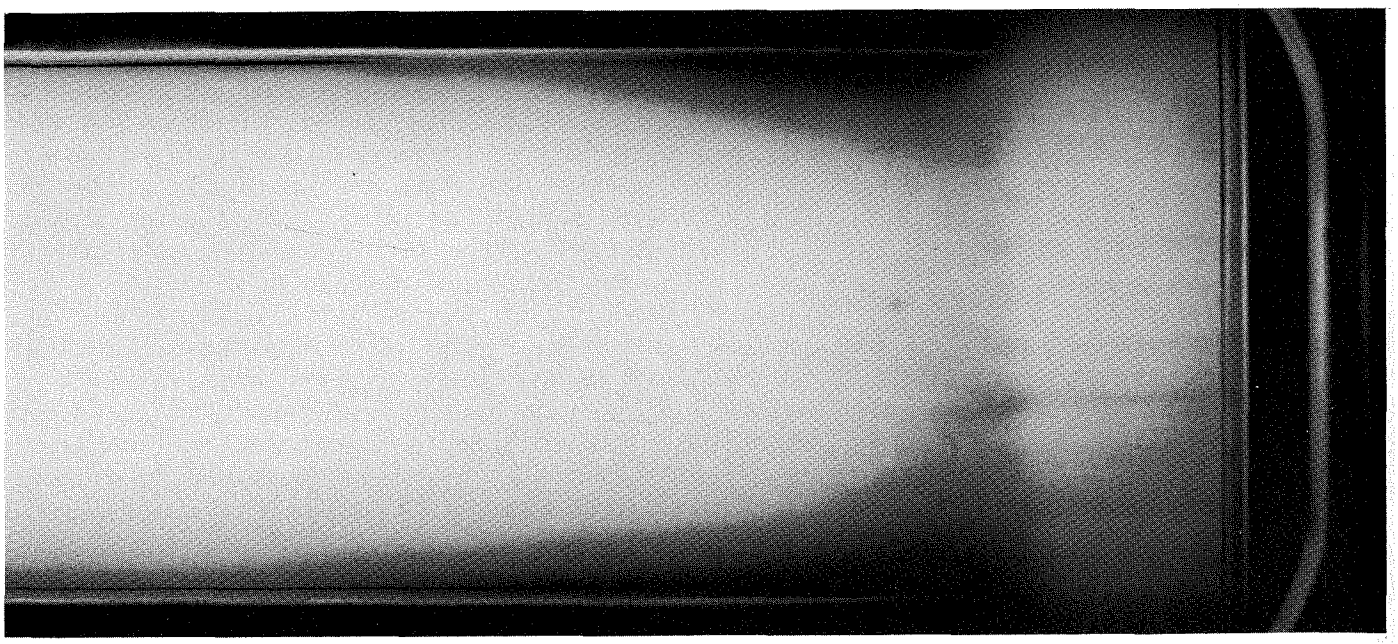

Fig. IV-3. Normal shock ($M_1 = 5.0$)

result in subsequent darkening of the near-liquid region; this is evident in the second black line and the shaded region shown in Fig. IV-3. The region in which thermodynamic equilibrium was being established would be characterized by a gradual increase in the transmission of light as the bubble sizes decreased.

1. Static Pressure Profiles

The static pressure rise across the shock structure was not discontinuous, but spread out as expected from the discussion of the flow model in Section III. In such a gas-liquid continuum, static pressure gradients can be sustained only by the drag between the phases. As established in Section III, the bubbles upstream are arranged in chains with a relatively low C_d. The entrance of these chains into the shock front compresses the bubbles and destroys their connecting chain structure, which effectively increases the relative C_d between the phases. Thus the pressure gradient immediately after the initial bubble compression is indicative of the C_d change within the shock structure. After reaching maximum C_d, the pressure gradient should decrease with the pressure, and approach its downstream value asymptotically as the bubble size is established by thermal equilibrium.

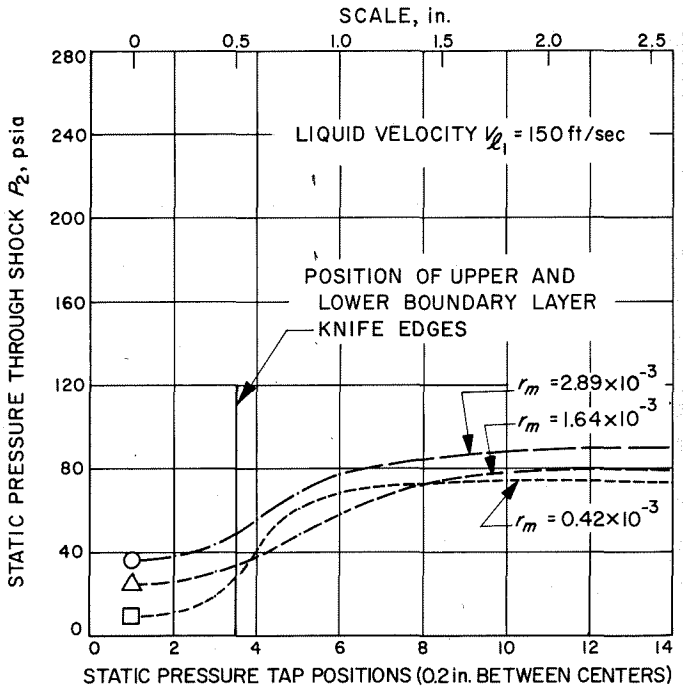

Fig. IV-4. Static pressure as a function of horizontal position through a normal shock for values of mass ratio (V = 150 ft/sec)

Figures IV-4 through IV-8 represent the static pressure through the shock structure for parameters of mass ratio (r_m) and mixture velocities ranging from 150 ft/sec to 340 ft/sec. The profiles are reasonably close in general shape to those expected from the flow model. At lower velocities, the profiles reach further upstream with more gentle gradients; at the higher velocities, the leading foot

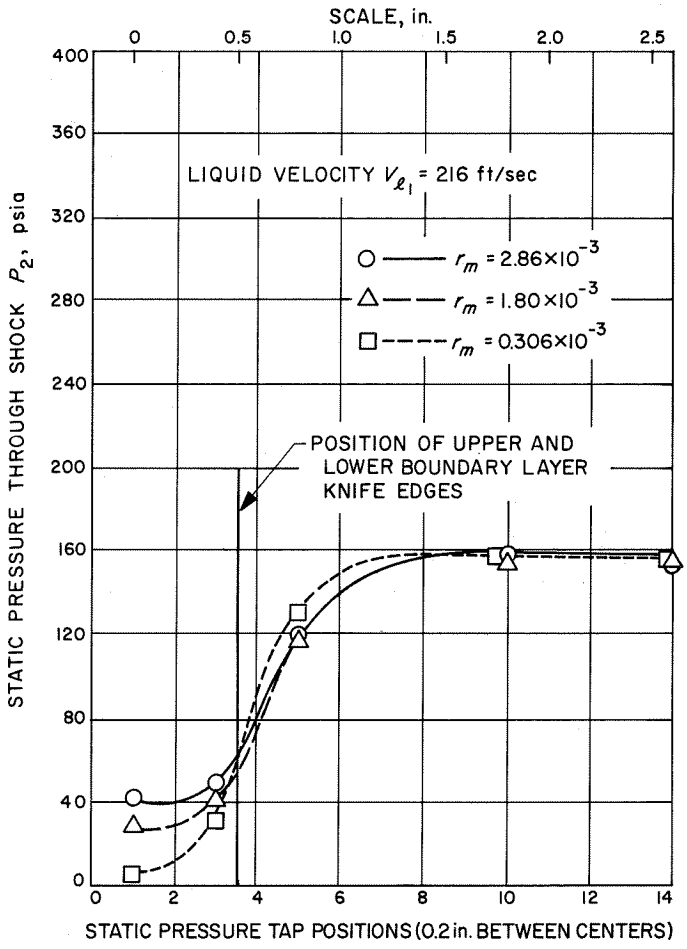

Fig. IV-5. Static pressure as a function of horizontal position through a normal shock for values of mass ratio (V = 216 ft/sec)

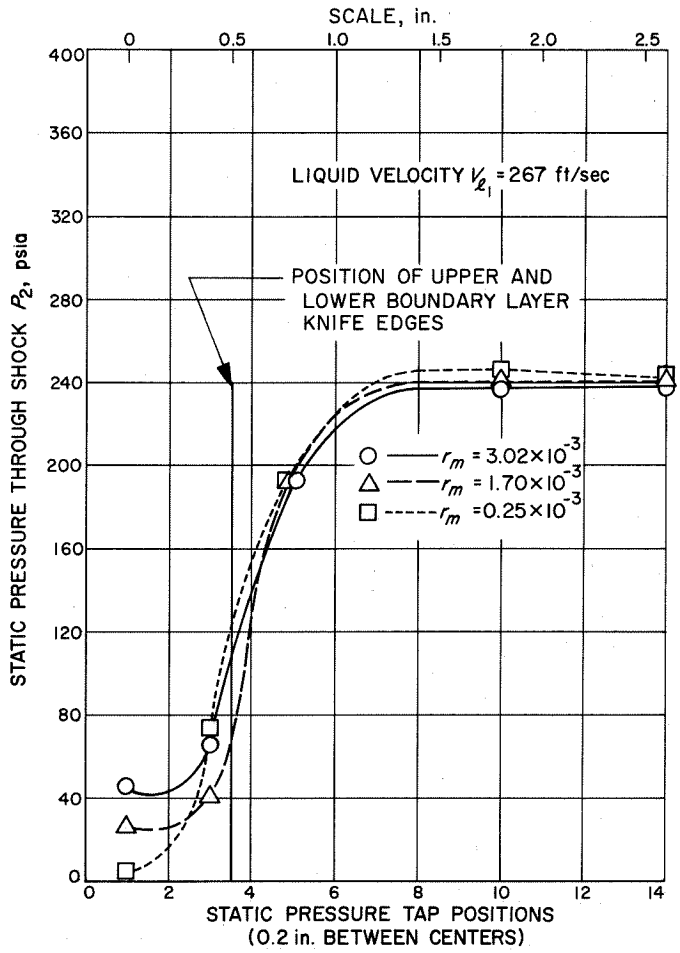

Fig. IV-6. Static pressure as a function of horizontal position through a normal shock for values of mass ratio (V = 267 ft/sec)

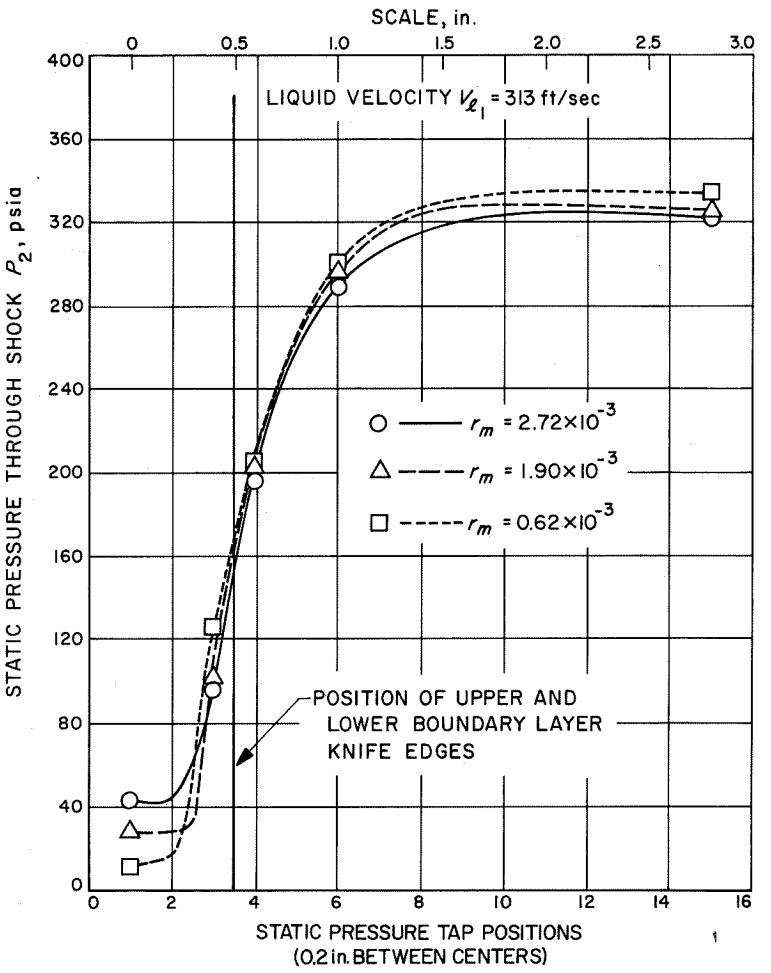

Fig. IV-7. Static pressure as a function of horizontal position through a normal shock for values of mass ratio (V = 313 ft/sec)

of the profile is shortened, and the gradients reach very large values.

Correlation of the pressure profile curves with the first visual evidence of a change in the upstream flow pattern as it approaches the shock position indicates that changes in visual density, bubble size, and bubble orientation occur simultaneously with the relatively rapid increase in pressure gradient for a nearly constant volume ratio equal to 0.77. Downstream of the shock position, water deceleration occurs rapidly as evidenced by the high pressure gradient. The asymptotic approach of the pressure profile to the downstream pressure occurred at nearly equal distances from the shock holding point for all cases; this suggests a strong similarity between the downstream model and the temperature relaxation times.

Reduction of the gas-to-liquid mass ratio at all velocities tends to steepen the maximum pressure gradient, as expected from the better distribution of bubbles upon compression. Further, a reduction in r_m slightly increases the Mach number. This increase, in turn, increases the pressure ratio (P_2/P_1); this latter increase is evident in Figs. IV-4 through VI-8.

Profiles for shock strengths of less than Mach 2 were not obtained in the tunnel because the foot of the profile curves extended beyond the initial pressure taps of the test section. The shape of the shock pressure profile depends upon the upstream mixture velocity, volume ratio, and any isotropy of gas-phase distribution. For initial volume ratios less than 0.77, the shock pressure profile will be reasonably narrow for all supersonic velocities; for volume ratios greater than 0.77, the leading portion of the profile can be expected to extend with both a reduction in velocity and an increase in volume ratio, although this extension will remain finite.

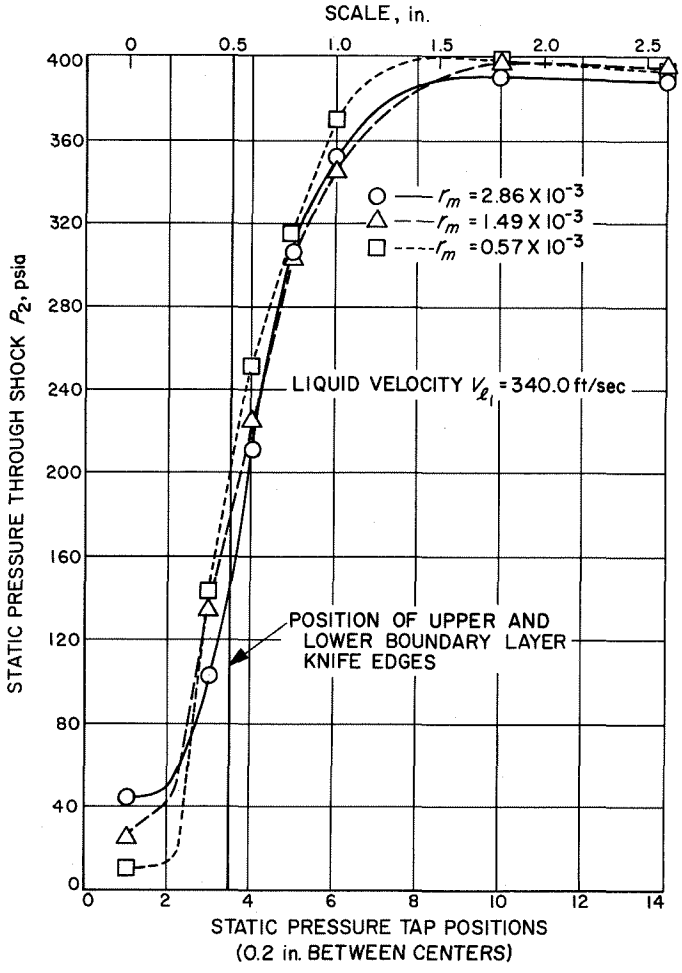

Fig. IV-8. Static pressure as a function of horizontal position through a normal shock for values of mass ratio (V = 340 ft/sec)

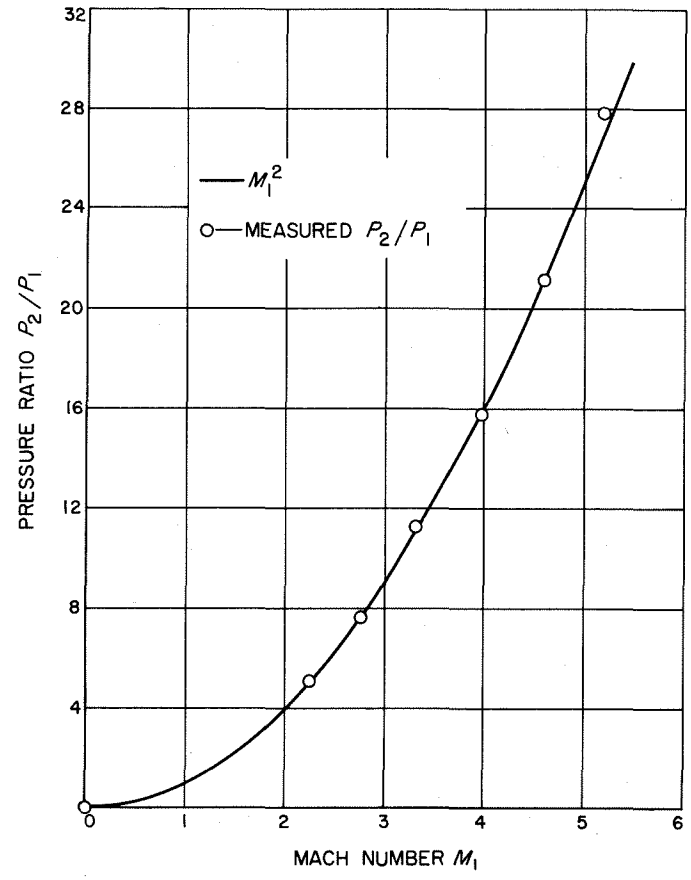

Fig. IV-9. Pressure ratio as a function of Mach number for a normal shock

2. Static Pressure Ratio

According to Eq. (IV-20), the static pressure ratio across a normal shock is proportional to the square of the Mach number. Because Mach number includes mixture velocity, r_v and r_m, the validity of this simple proportionality supplies strong confirmation of the basic isothermal relations developed through Eq. (IV-25) and the parameters of actual tunnel operation. A plot of the asymptotic static pressure ratio vs the isothermal theory is given in Fig. IV-9. The results of the plot fall within 2% of the theory through the full range of tunnel velocities, and, at lower pressures, exceed a Mach number of 6.

The variation of static pressure with velocity is plotted in Fig. IV-10 for a range of r_{v_1} from 0.1 to 1.0, and in Fig. IV-11 for a range of 1.0 to 10.0. From the two graphs it is evident that the maximum (P_2/P_1) ratio occurs

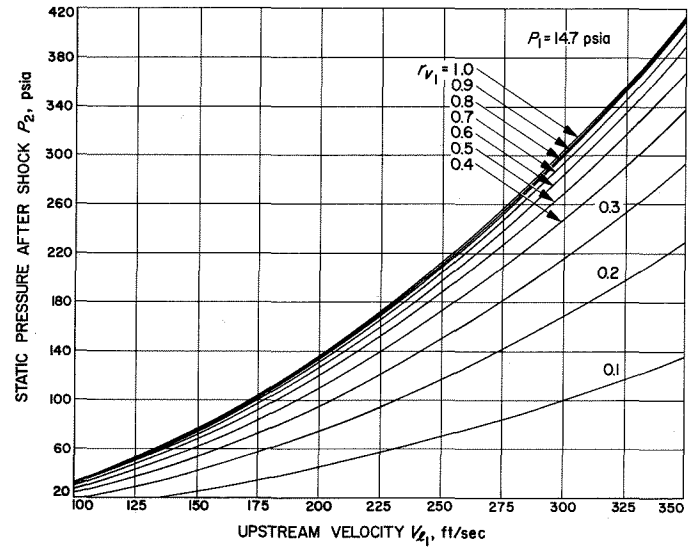

Fig. IV-10. Downstream static pressure as a function of upstream velocity for volume ratios of $0.1 \leq r_{v_1} \leq 1.0$, for a normal shock

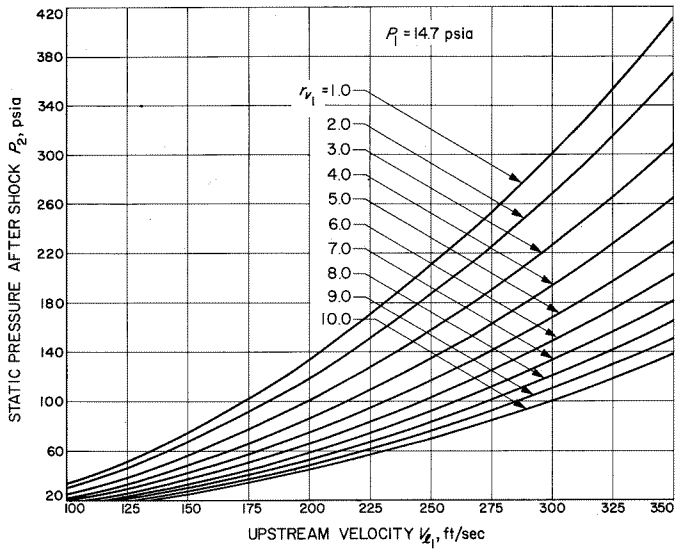

Fig. IV-11. Downstream static pressure as a function of upstream velocity for volume ratios of $1 \leq r_{v_1} \leq 10$

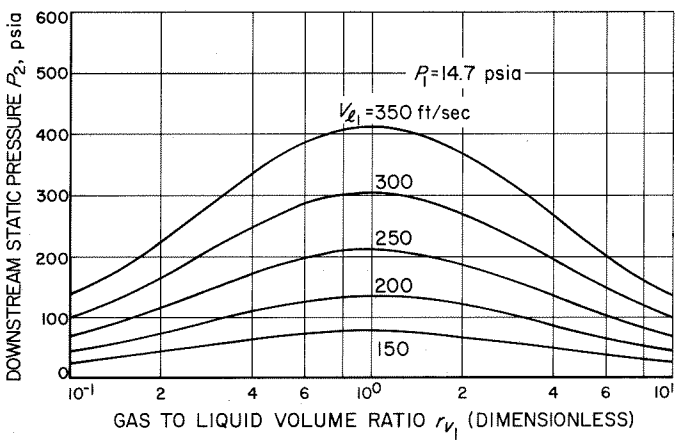

Fig. IV-12. Downstream static pressure as a function of volume ratio for values of upstream velocity

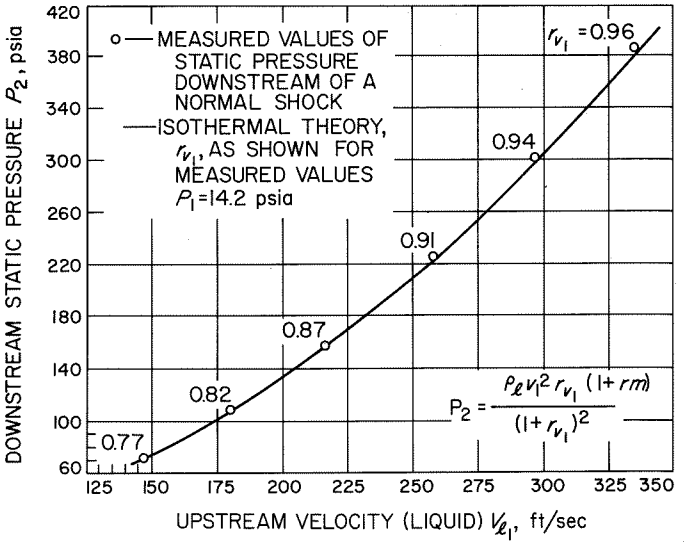

Fig. IV-13. Downstream static pressure as a function of upstream velocity for specific tunnel r_v flow values

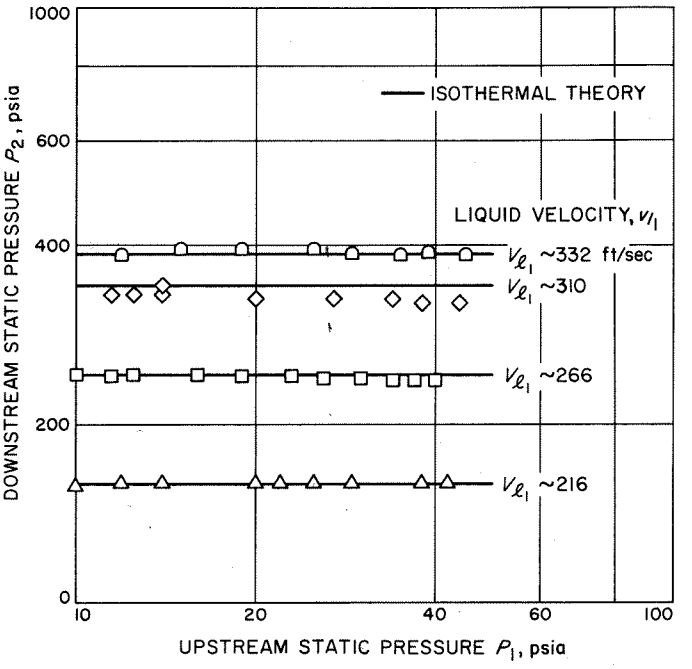

Fig. IV-14. Downstream static pressure as a function of upstream static pressure for values of upstream velocity

for an $r_{v_1} = 1.0$, and drops off on either side of that value as shown in Fig. IV-12. Further, a graph of the static pressure (P_2) vs velocity (V_1) for the actual tunnel volume ratios is shown in Fig. IV-13. The agreement is equally as close as in Fig. IV-9. Of further significance, V_{l_1} was used for mixture velocity and appears to be a valid representation of the latter at these void ratios even with the 20% relative phase velocities that exist upstream.

The near independence of the downstream static pressure on the upstream static pressure, except as a weak function of r_m, is shown in Fig. IV-14. Over a pressure range $10 \leq P_1 \leq 45$ psia there is little variation in P_2 for the four liquid velocities shown. Over a wider range of pressure, however, the effect of an r_m increase with pressure becomes noticeable above a pressure of $P_1 = 100$ psia, barely noticeable for low values of (r_{v_1}), and more strongly noticeable as r_{v_1} increases (Figs. IV-15, IV-16, and IV-17).

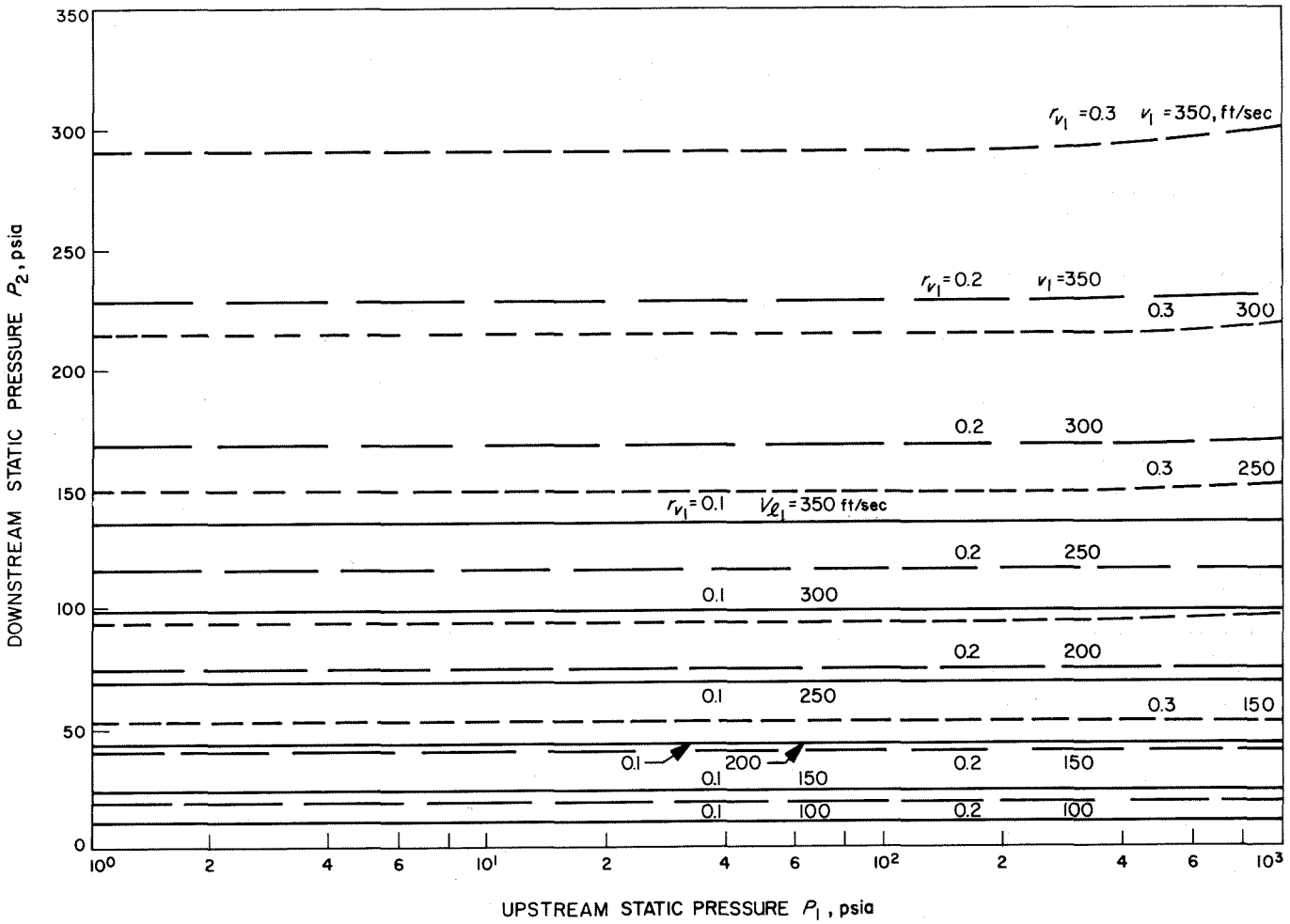

Fig. IV-15. Downstream static pressure as a function of upstream static pressure for values of upstream velocity and volume ratios of $0.1 \leq r_{v_1} \leq 0.3$

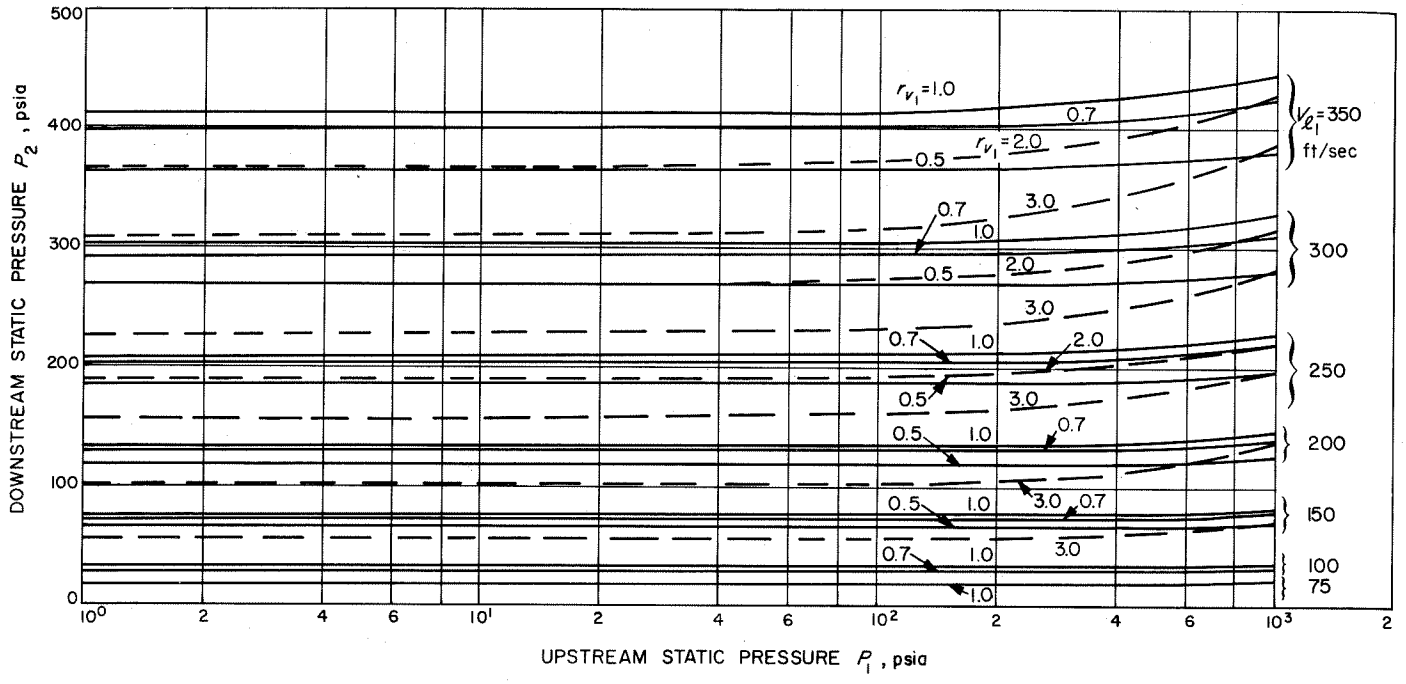

Fig. IV-16. Downstream static pressure as a function of upstream static pressure for values of upstream velocity and volume ratios of $0.5 \leq r_{v_1} \leq 2.0$

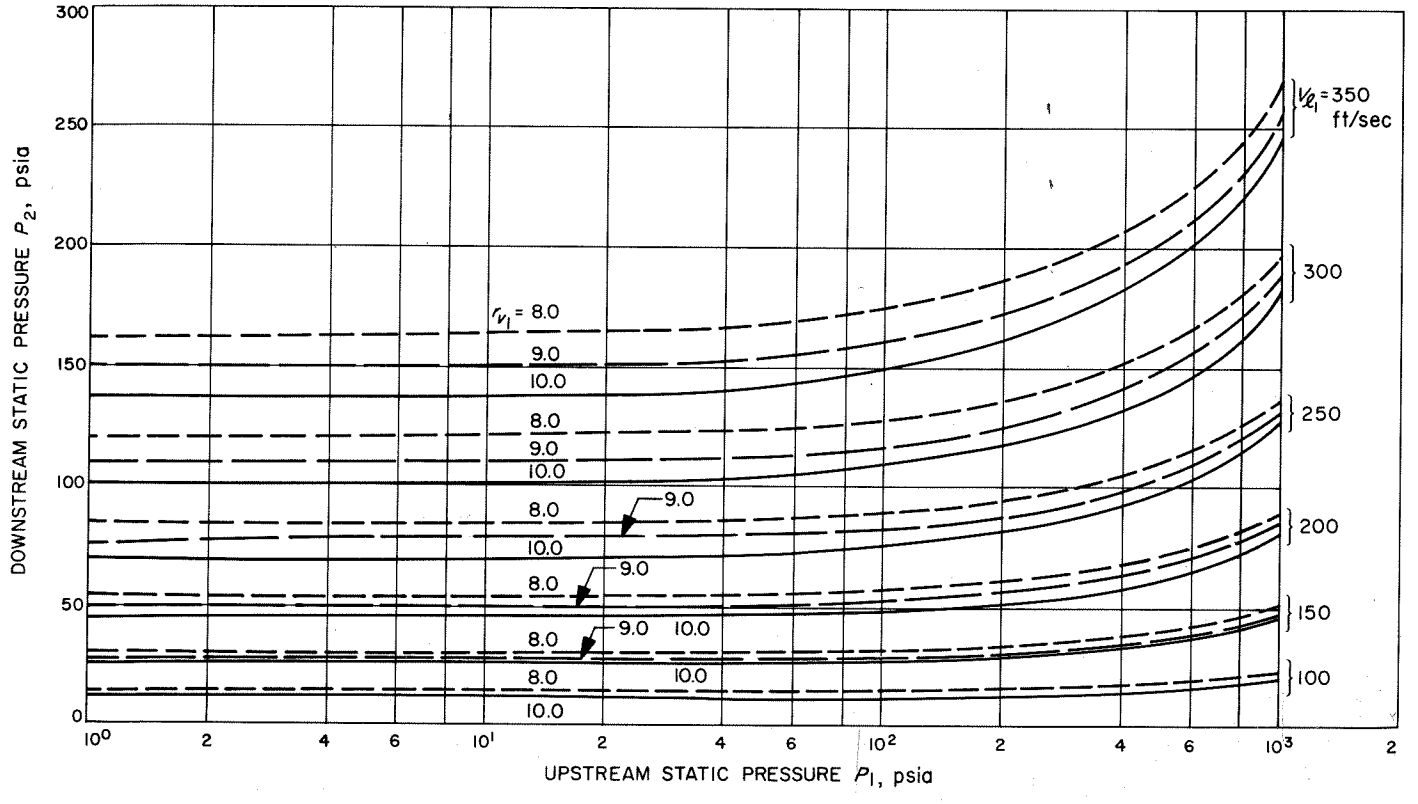

Fig. IV-17. Downstream static pressure as a function of upstream static pressure for values of upstream velocity and volume ratios of $8 \leq r_{v_1} \leq 10$

3. Downstream Volume Ratio

The downstream volume ratio could not be measured directly for lack of suitable instrumentation. The validity of Eq. (IV-21) can be inferred only from the close correlation of the data with Eq. (IV-20), from which Eq. (IV-21) was developed. For reference, a plot of downstream volume ratio (r_{v_2}) vs upstream Mach number for values of r_{v_1} from 0.1 to 10.0 is shown in Fig. IV-18.

4. Downstream Mixture Velocity

The downstream mixture velocity cannot be measured conveniently in a thrust arrangement as was the upstream velocity. However, sufficient movement of bubble strata occurred downstream of the normal shock to permit mixture velocity determination from analysis of the Dynafax sequences. A plot of the downstream-to-upstream velocity ratio (V_2/V_1) as a function of Mach number is shown in Fig. IV-19. The data agrees within 10% of the isothermal theory based on Eq. (IV-22) up to a Mach number approaching 12. Because the strata observed in the flow is necessarily close to the wall, it will be somewhat slowed in its travel through the test section by the development of a wall boundary layer, which is also evident in the results plotted. The theoretical velocity ratio (V_2/V_1) vs Mach number (M_1) over the range of volume ratios $0.1 \leqq r_{v_1} \leqq 10.0$ is shown in Fig. IV-20.

5. Downstream Mach Number

The downstream Mach number cannot be determined by measurement until the downstream volume ratio (r_{v_2}) can be accurately measured. The theoretical isothermal relationship according to Eq. (IV-24) is shown in Fig. IV-21.

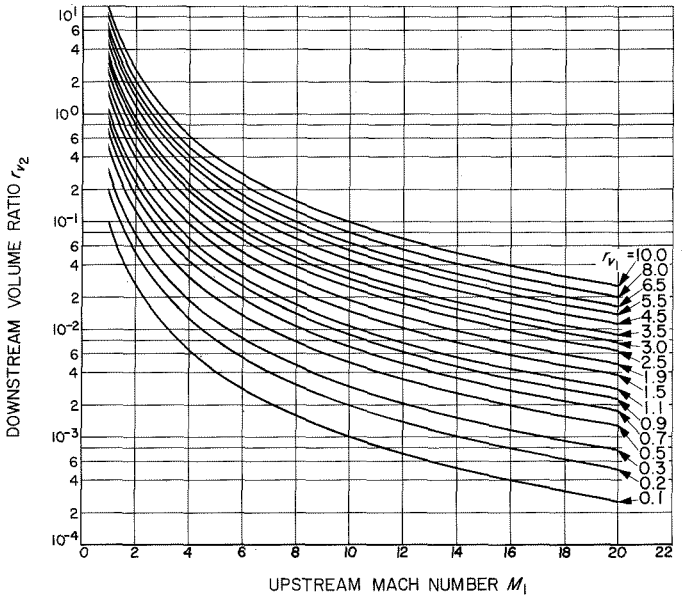

Fig. IV-18. Downstream volume ratio as a function of upstream Mach number for values of r_{v_1}

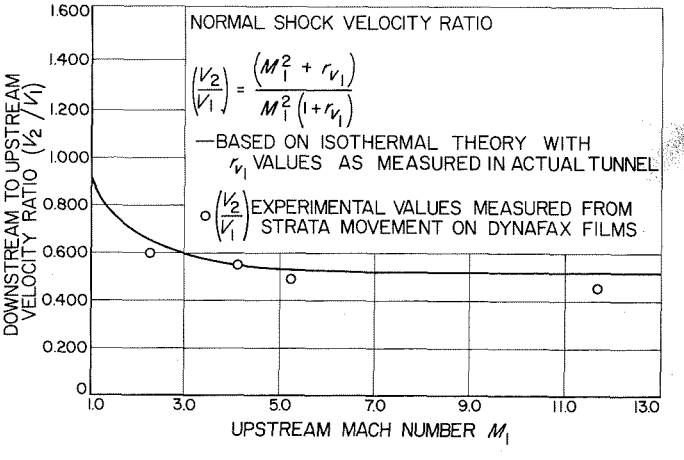

Fig. IV-19. Velocity ratio as a function of upstream Mach number at actual tunnel r_{v_1} values

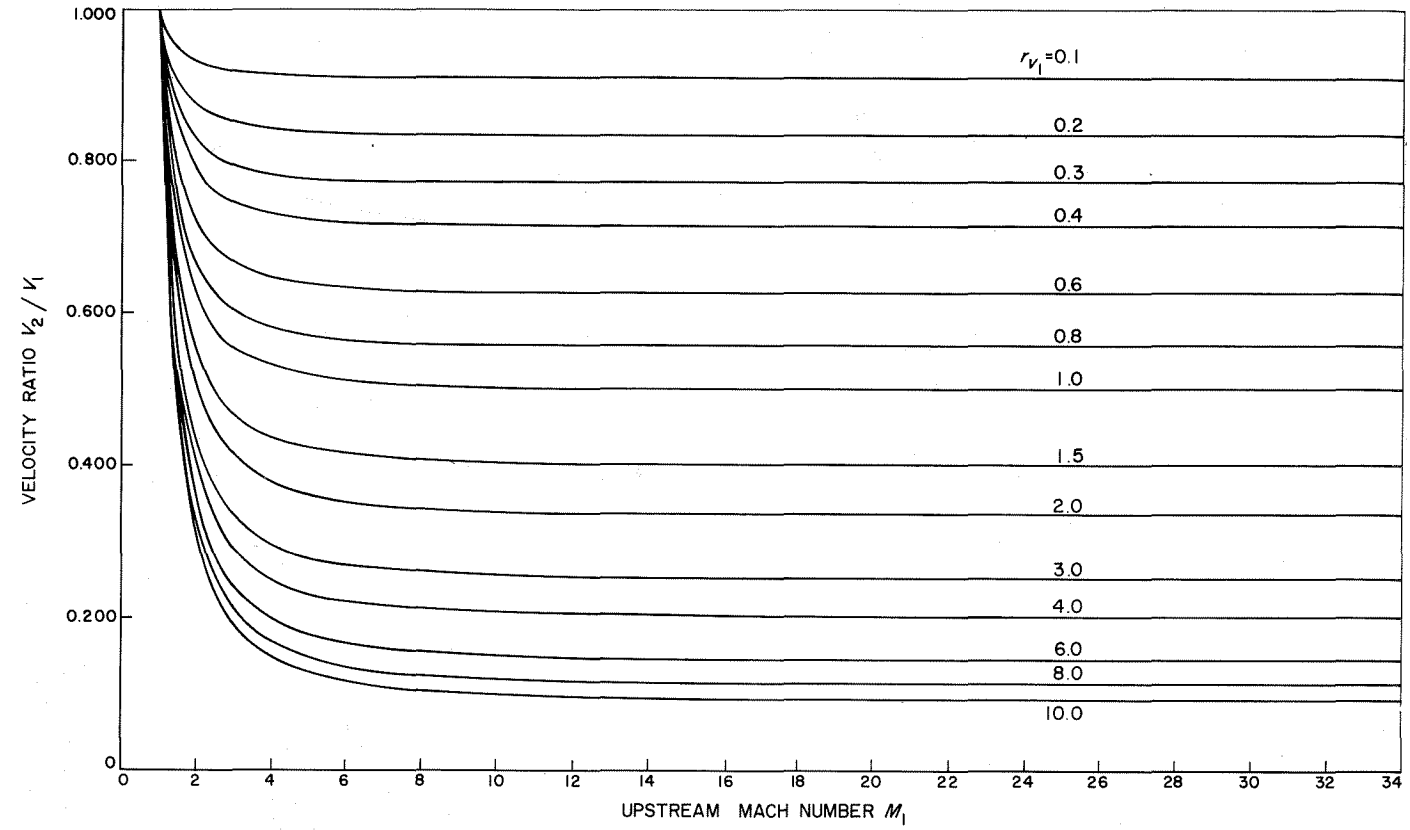

Fig. IV-20. Velocity ratio as a function of upstream Mach number for values of upstream volume ratio

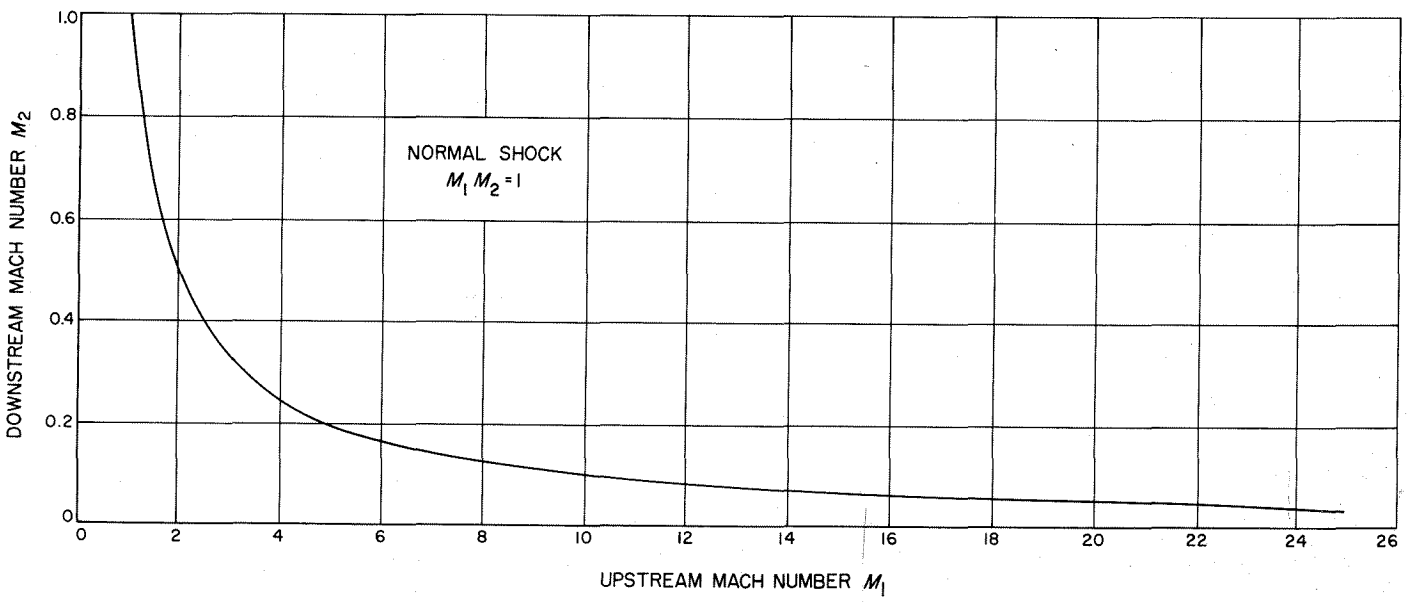

Fig. IV-21. Downstream Mach number as a function of upstream Mach number

6. Photographic Analysis

Single photos taken at exposures of 1/50 to 1/75 sec reveal the quasi-stationary features of the two-phase normal shock phenomena. Figure IV-2 shows an essentially narrow dark line for the shock structure, with the side walls set at minimum width. Visually, a dark-light-dark set of lines appeared, the second of which proved difficult to retain on black and white film. As the tunnel width increased, the shock structure depth (the region of darkening) increased as shown in Figs. IV-22 and IV-23. The upstream pressures for these two flow conditions of $M_1 = 3.4$ (Fig. IV-22) and $M_1 = 4.2$ (Fig. IV-23) were above atmospheric, and forced the shock structure to seek greater accommodation upstream, which accounts for its slight convex curvature.

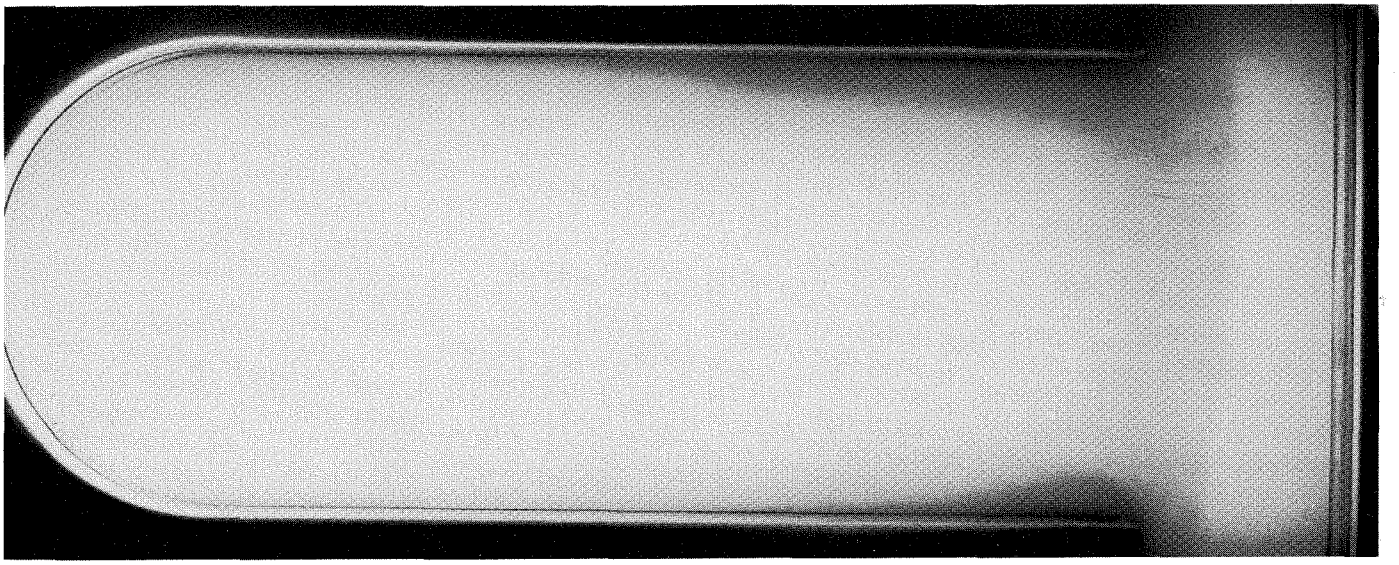

Fig. IV-22. Normal shock, $V_{l_1} = 304$ ft/sec, $M_1 = 3.4$

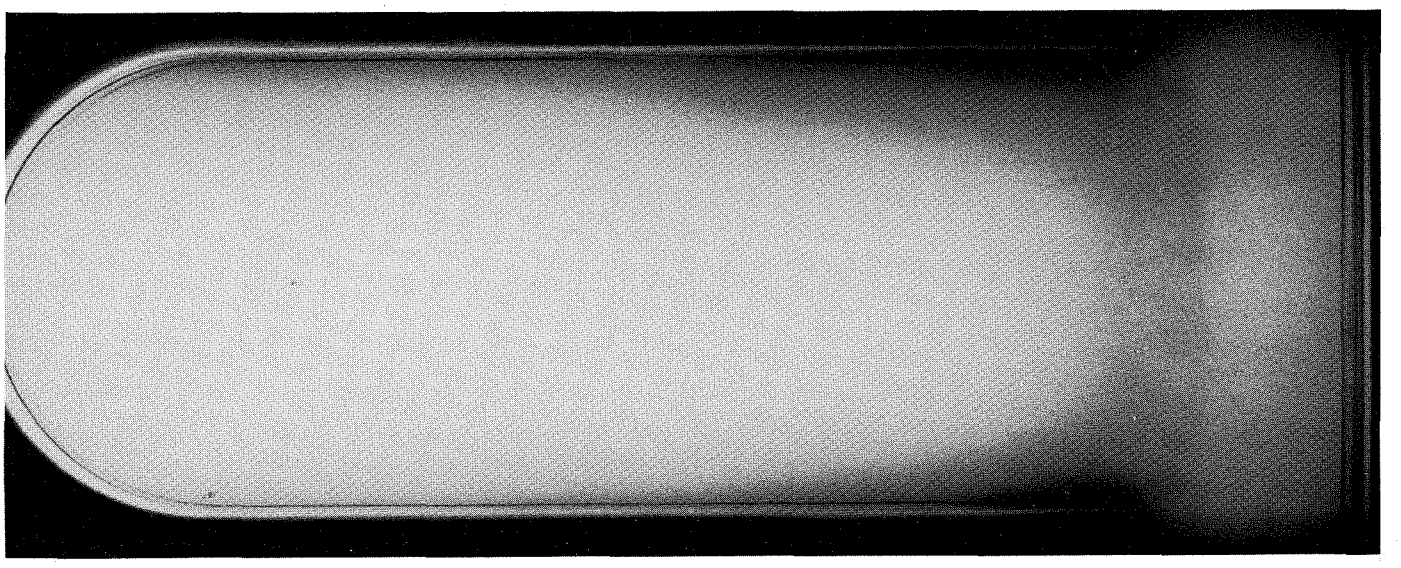

Fig. IV-23. Normal shock, $V_{l_1} = 304$ ft/sec, $M_1 = 4.2$

Figures IV-24 and IV-25 show normal shocks at Mach numbers 5.8 and 8.2, respectively. At pressures below atmospheric, thickening has occurred at the base of the shock because of interaction with water drawn into the free stream from the free surface between the tunnel discharge and the knife edges. The visible depth of shock structure has decreased because of the lower r_{v_2} value that resulted from the increased Mach number (M_1) in accordance with Eq. (IV-21).

Figures IV-26 and IV-27, taken at an exposure of ½ μsec, show the fine structure of the flow and shock phenomena at Mach numbers 3.9 and 4.1, respectively. The slight decrease in upstream pressure needed to increase the Mach number has made a significant difference in the amount of fine structure (bubbles) that can be seen in the downstream area behind the shock front. The bubble-connected chains in the upstream flow are discernible in the area to the right of the shock front.

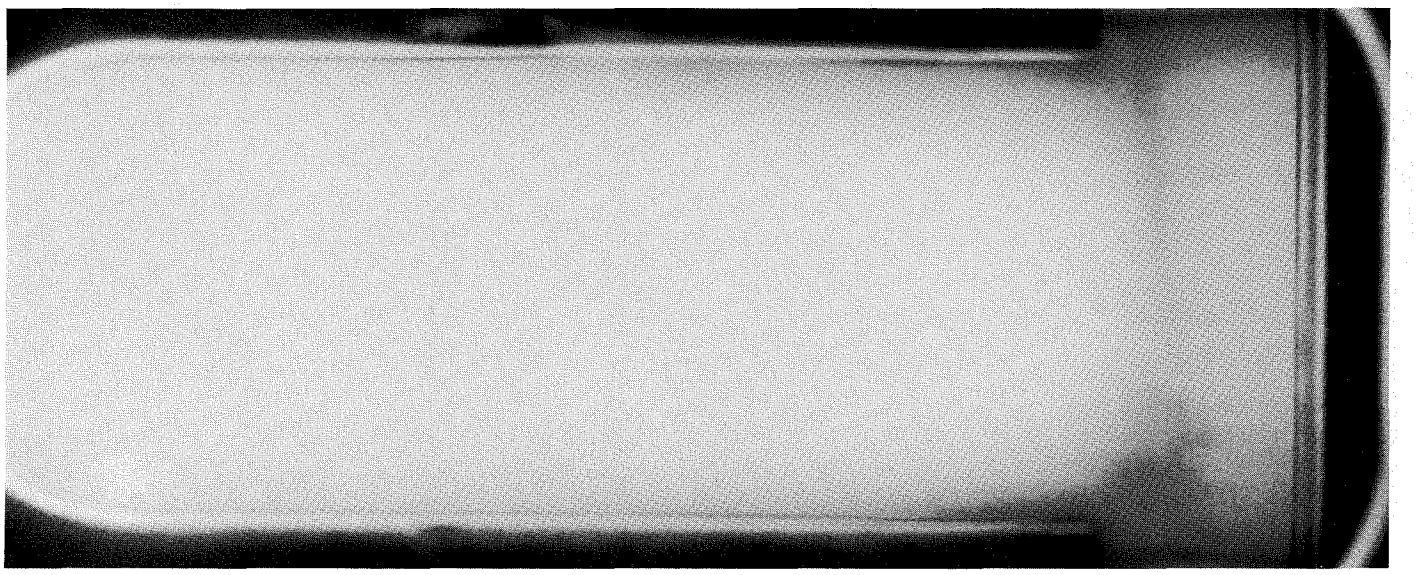

Fig. IV-24. Normal shock, $V_{l_1} = 346$ ft/sec, $M_1 = 5.8$

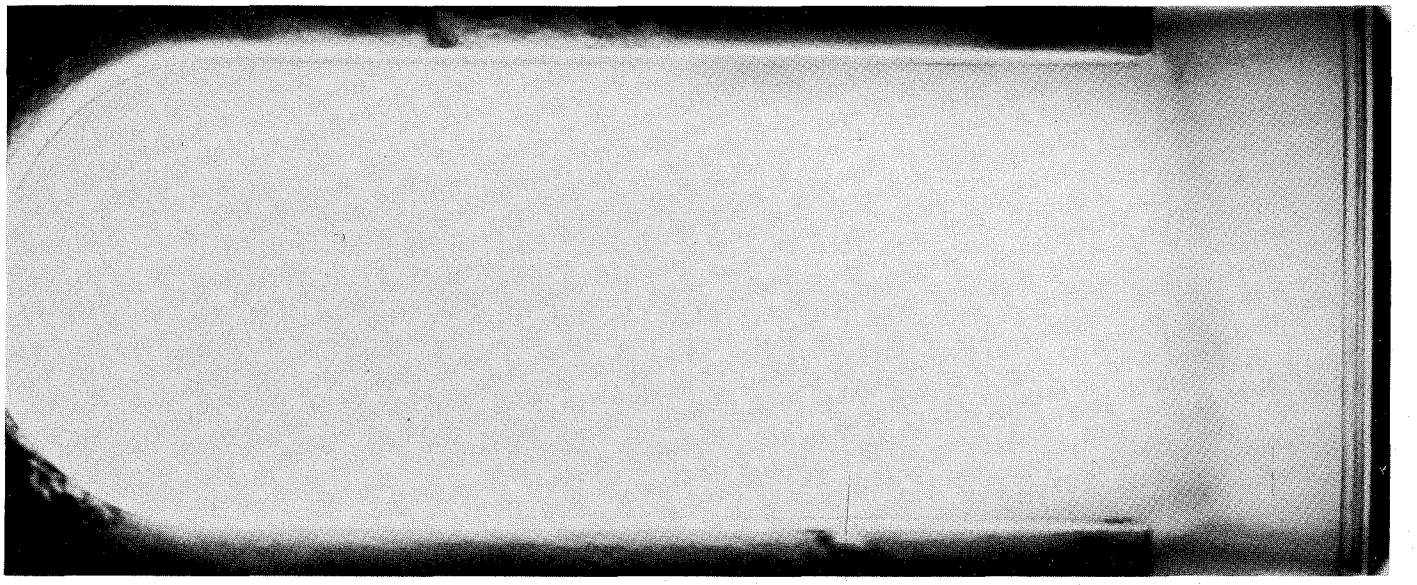

Fig. IV-25. Normal shock, $V_{l_1} = 304$ ft/sec, $M_1 = 8.2$

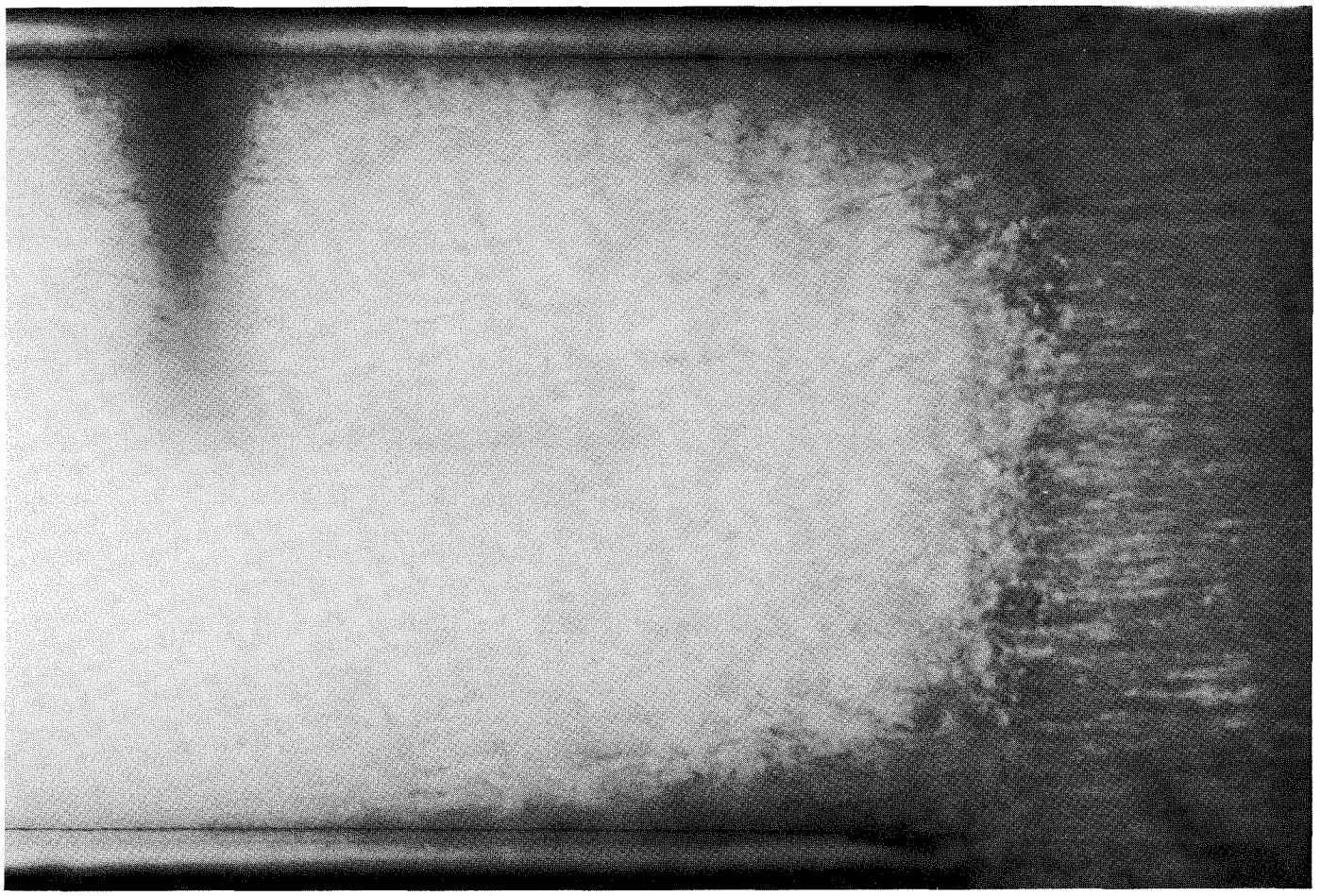

Fig. IV-26. Normal shock at ½-μsec exposure, $V_{l_1} = 310$ ft/sec, $M_1 = 3.95$

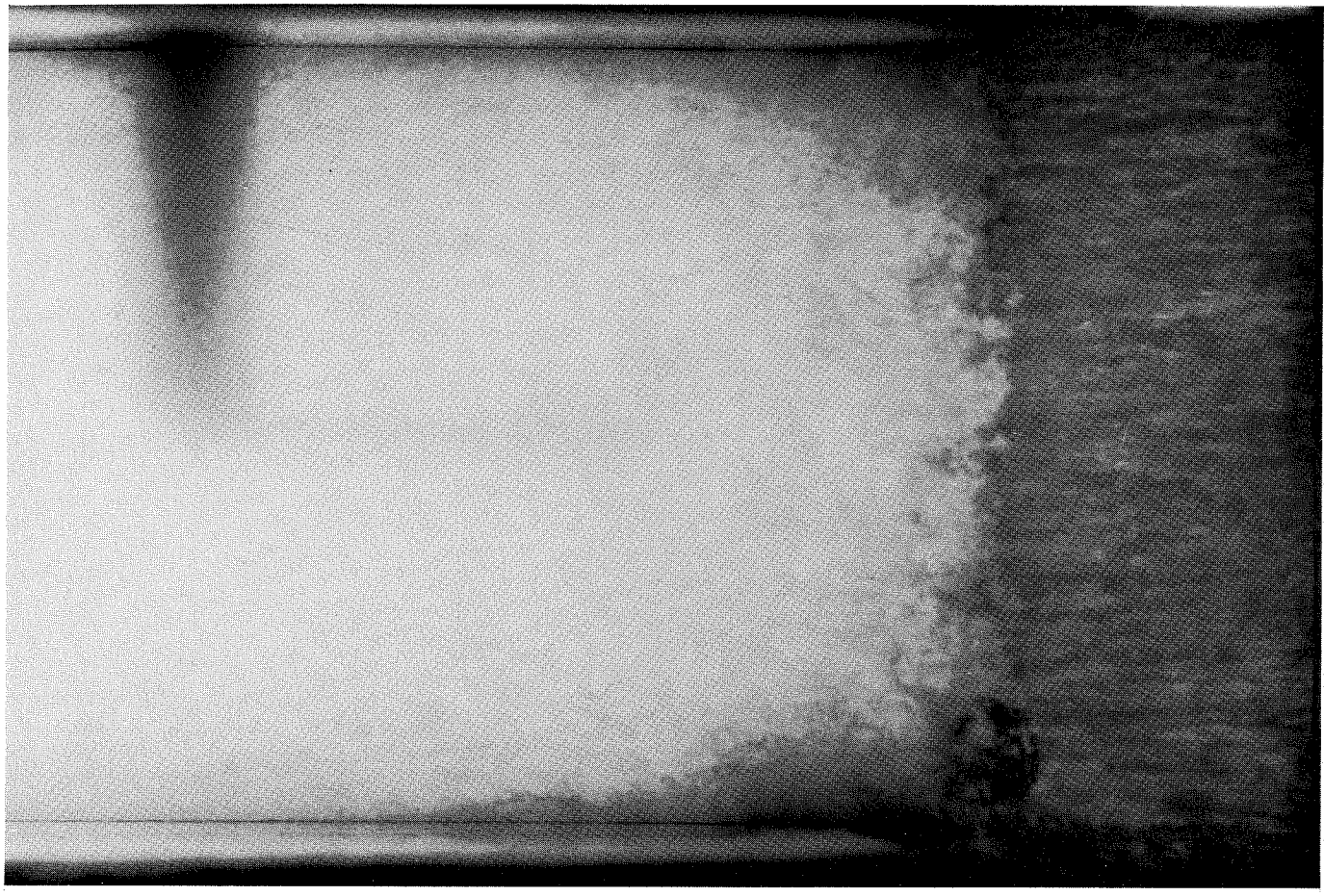

Fig. IV-27. Normal shock at ½-μsec exposure, $V_{l_1} = 310$ ft/sec, $M_1 = 4.1$

Nomenclature

A_g	cross-sectional area, gas, local (ft²)
A_l	cross-sectional area, liquid, local (ft²)
c	velocity of sound in mixture (ft/sec)
C_d	coefficient of drag, bubble or droplet
M	Mach number
m_g	mass of gas (slugs)
$\dot{m}_g$	mass of gas flow rate (slug/sec)
m_l	mass of liquid (slugs)
$\dot{m}_l$	mass of liquid flow rate (slug/sec)
P	pressure, static (lb_f/ft^2)
r_m	gas-to-liquid mass ratio
r_v	gas-to-liquid volume ratio
U_g	gas velocity in control volume (ft/sec)
U_l	liquid velocity in control volume (ft/sec)
$\mathcal{V}_g$	volume, gas phase (ft³)
$\mathcal{V}_l$	volume, liquid phase (ft³)
V	mixture velocity (ft/sec)
V_g	velocity, gas phase (ft/sec)
V_l	velocity, liquid phase (ft/sec)
ρ	mixture density (slugs/ft³)
ρ_g	density, gas phase (slugs/ft³)
ρ_l	density, liquid phase (slugs/ft³)

Subscripts

1	upstream of shock
2	downstream of shock

V. Oblique Shocks

A. Fundamentals

The normal shock analysis of Section IV can be extended to oblique shock waves with relative ease for the isothermal case by using the geometrical relationships common to the derivation of oblique shock relations for gaseous single-phase media. The equations of continuity and momentum, mixture density and velocity, the isothermal equation of state, the mixture density relation, and the geometrical relationships form a complete set of equations for determination of downstream flow characteristics.

With reference to Fig. V-1, the continuity equation can be written as

$$\rho_1 u_1 \sin\beta = \rho_2 (u_2 \sin\beta - v_2 \cos\beta) \qquad \text{(V-1)}$$

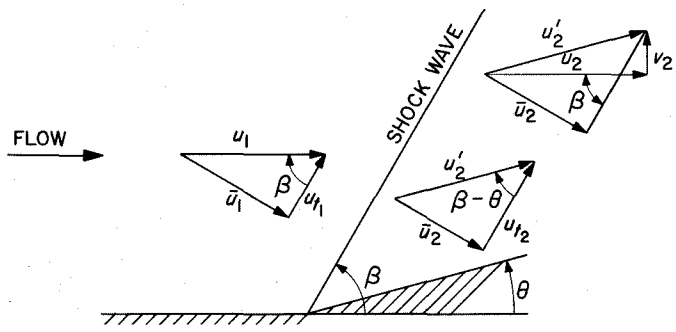

Fig. V-1. Oblique shock relationships

The momentum equations normal and parallel to the shock wave are

$$\text{(normal)}\ P_1 + \rho_1 u_1^2 \sin^2\beta = P_2 + \rho_2 (u_2 \sin\beta - v_2 \cos\beta)^2 \qquad \text{(V-2)}$$

$$\text{(parallel)}\ \rho_1 u_1^2 \sin\beta \cos\beta = \rho_2 (u_2 \sin\beta - v_2 \cos\beta)(u_2 \cos\beta + v_2 \sin\beta) \qquad \text{(V-3)}$$

The isothermal equation of state remains

$$P r_v = \text{constant}$$

or

$$P_1 r_{v_1} = P_2 r_{v_2} \qquad \text{(V-4)}$$

the mixture density is:

$$\rho_i = \frac{(1 + r_{m_i})}{(1 + r_{v_i})} \qquad \text{(V-5)}$$

where i can take values of 1 or 2 and the Mach number:

$$M_i = \frac{V_i}{C_i} = \frac{V_i}{(1 + r_{v_i})} \left[\frac{\rho_l r_{v_i} (1 + r_{m_i})}{P_i} \right]^{1/2} \qquad \text{(V-6)}$$

Dividing Eq. (V-3) by Eq. (V-1),

$$\frac{u_1 - u_2}{v_2} = \tan\beta \tag{V-7}$$

By geometry from Fig. V-1,

$$\frac{v_2}{u_2} = \tan\theta \tag{V-8}$$

Substituting Eq. (V-8) into Eq. (V-7),

$$u_2 = \frac{u_1}{(1 + \tan\beta\tan\theta)} \tag{V-9}$$

or

$$v_2 = u_2\tan\theta = \frac{u_1\tan\theta}{(1 + \tan\beta\tan\theta)} \tag{V-10}$$

Substituting Eq. (V-1) for ρ_2 in Eq. (V-2) and solving for $(P_2 - P_1)$,

$$P_2 - P_1 = \rho_1 u_1 \sin\beta\,[(u_1 - u_2)\sin\beta + v_2\cos\beta] \tag{V-11}$$

Substituting Eqs. (V-9) and (V-10) into Eq. (V-11),

$$P_2 - P_1 = \rho_1 u_1^2\left[\frac{\sin\beta\sin\theta}{\cos(\beta - \theta)}\right] \tag{V-12}$$

Substituting Eq. (V-4) for P_2 in Eq. (V-12),

$$P_1\left(\frac{r_{v_1}}{r_{v_2}} - 1\right) = \rho_1 u_1^2\left[\frac{\sin\beta\sin\theta}{\cos(\beta - \theta)}\right] \tag{V-13}$$

From Eq. (V-5) and the previous (Section IV) relation $r_{m_1} = r_{m_2}$, the ratio ρ_1/ρ_2 for normal and oblique shocks becomes

$$\frac{\rho_1}{\rho_2} = \frac{(1 + r_{v_2})}{(1 + r_{v_1})} \tag{V-14}$$

Then, using Eqs. (V-14), (V-1), (V-9), and (V-10), the expression $(r_{v_1}/r_{v_2} - 1)$ can be computed in terms of β, θ, and r_{v_1}:

$$\left(\frac{r_{v_1}}{r_{v_2}} - 1\right) = \frac{(r_{v_1} + 1)(\sin^2\beta + \cos^2\beta)}{\sin\beta\left[-\sin\beta + \dfrac{r_{v_1}\cos\beta}{\tan\theta} - \dfrac{\cos^2\beta\,(1 + r_{v_1})}{\sin\beta}\right]} \tag{V-15}$$

Substituting Eqs. (V-15) and (V-6) into Eq. (V-13),

$$\frac{1}{M_1^2} = \frac{(-\sin^3\beta\sin\theta) + r_{v_1}(\sin^2\beta\cos\beta\cos\theta) - (\sin\beta\cos^2\beta\sin\theta)(1 + r_{v_1})}{r_{v_1}[\cos(\beta - \theta)]} \tag{V-16}$$

The pressure-ratio-Mach-number relationship from Section IV was:

$$\frac{P_2}{P_1} = M_1^2 \tag{V-17}$$

The component of velocity normal to the oblique shock is

$$\bar{u}_1 = u_1\sin\beta \tag{V-18}$$

Expanding Eq. (V-17) and substituting Eq. (V-18) for $\bar{u}_1$,

$$\frac{P_2}{P_1} = M_{N_1}^2 = \frac{\rho_l\,\bar{u}_1^2(1 + r_{m_1})\,r_{v_1}}{P_1(1 + r_{v_1})^2} = \frac{\rho_l\,u_1^2(1 + r_{m_1})\,r_{v_1}\sin^2\beta}{P_1(1 + r_{v_1})^2}$$

or

$$\frac{P_2}{P_1} = M_1^2\sin^2\beta$$

Solving for P_2,

$$P_2 = P_1 M_1^2\sin^2\beta\ (\text{downstream pressure}) \tag{V-19}$$

From Eq. (V-4),

$$\frac{P_2}{P_1} = \frac{r_{v_1}}{r_{v_2}}$$

or, substituting for P_2/P_1 from Eq. (V-19),

$$\frac{r_{v_2}}{r_{v_1}} = (M_1^2 \sin^2 \beta)^{-1}$$

Solving for r_{v_2}

$$r_{v_2} = r_{v_1} (M_1^2 \sin^2 \beta)^{-1} \text{ (downstream volume ratio)} \tag{V-20}$$

From Eq. (V-6),

$$M_2^2 = \frac{(u_2')^2}{(1 + r_{v_2})^2} \left[\frac{\rho_1 r_{v_2} (1 + r_{m_2})}{P_2} \right] \tag{V-21}$$

By geometry,

$$u_2' = \frac{u_2}{\cos \theta} \tag{V-22}$$

Substituting Eq. (V-9) into Eq. (V-18),

$$u_2' = \frac{u_1}{(\cos \theta + \tan \beta \sin \theta)} \tag{V-23}$$

Substituting Eqs. (V-19), (V-20), and (V-23) for P_2, r_{v_2}, and $(u_2')^2$, respectively, in Eq. (V-21) gives, for M_2,

$$M_2 = \frac{M_1 (1 + r_{v_1})}{(\cos \theta + \tan \beta \sin \theta)(M_1^2 \sin^2 \beta + r_{v_1})} \text{ (downstream Mach number)} \tag{V-24}$$

Equations (V-16), (V-19), (V-20), and (V-22) are sufficient to describe the downstream flow and the shock geometry for any initial values of Mach number (M_1), volume ratio, pressure, and flow deflection angle. It is to be noted, however, that in consideration of the substantial distances required for the completion of the relaxation processes in any shock structure as found in Section IV, the foregoing derivation is somewhat idealized. A portion of any deflection geometry will necessarily involve incomplete relaxation processes, and its extent will be strongly dependent upon the proximity of the shock wave to the deflecting surface.

1. Limiting Deflection Angle for Oblique Shock Attachment

Equation (V-16) cannot be solved for shock angle β and, consequently, solutions of β for initial values of deflection angle θ, M_1 and r_{v_1} must be solved by iteration on a digital computer. Such solutions have been obtained and are shown in subsequent figures. The envelopes of applicability for θ as a function of Mach number M_1 are shown in Fig. V-2. It is readily apparent that a limiting value of θ exists for each value of Mach number M_1 beyond which the shock wave will become unattached, and the oblique shock relations will cease to apply. Corresponding values of β and the pressure ratios P_2/P_1 are also shown in Fig. V-2. For $r_{v_1} < 1.0$, the limiting values of θ are nearly reached by Mach number 10; for $2.0 \leq r_{v_1} \leq 10.0$, however, the limiting values of θ are not reached until nearly Mach number 20.

2. Shock Angle β

Shock angle β as a function of Mach number (M_1) has been plotted for values of deflection angle θ in Figs. V-3 through V-24. The first eleven figures have a Mach number range from $0 \leq M_1 \leq 10$, and the last eleven from $0 \leq M_1 \leq 100$. Each graph in both ranges is constructed for a fixed value of r_{v_1} in the volume ratio range of $0.1 \leq r_{v_1} \leq 1.6$ in 0.2 increments. The upper limiting values of β for each curve of θ correspond to the envelope of limiting values as drawn in Fig. V-2.

It is evident in the succession of graphs that an increase in r_{v_1} increases the maximum θ for which an oblique shock attachment can occur, while simultaneously decreasing the shock angle β for any fixed value of M_1 and θ. Further, β is a strong function of the Mach numbers near the limiting minimum Mach numbers, decreasing to a lower limit near $M_1 = 20$. Beyond $M_1 = 20$, the majority of the β vs M_1 curves are nearly flat.

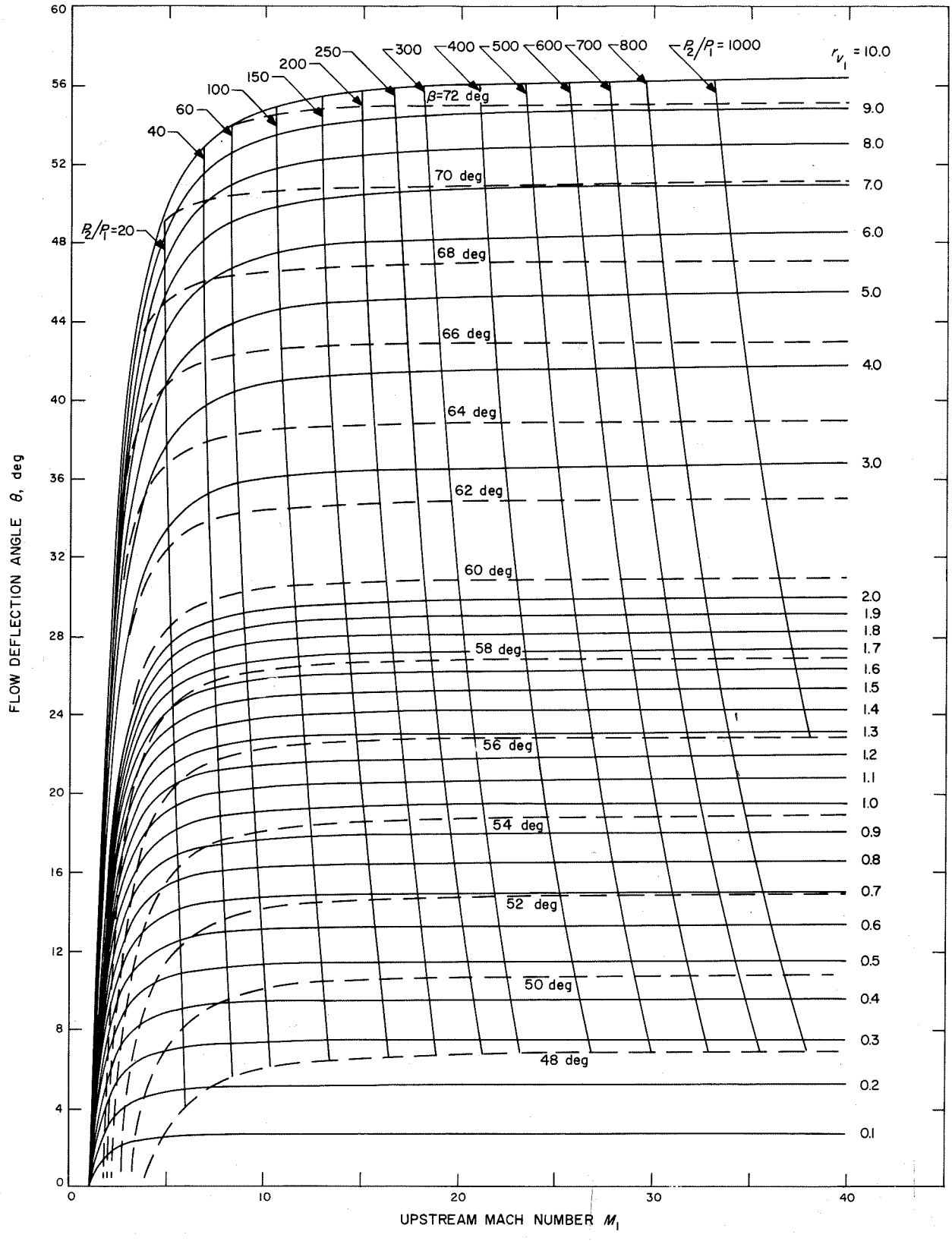

Fig. V-2. Limiting deflection angles and pressure ratios for oblique shocks as a function of Mach number

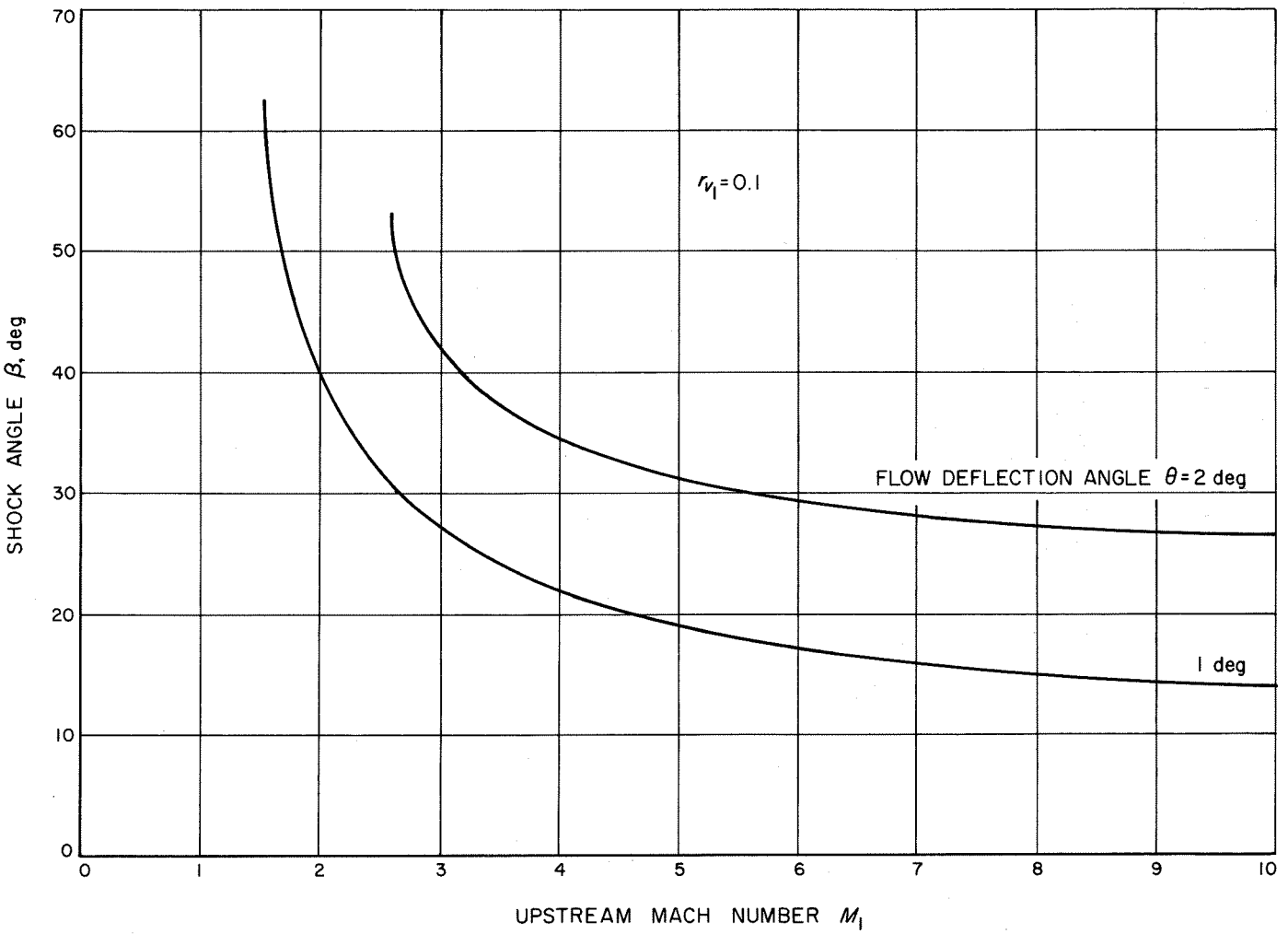

Fig. V-3. Oblique shock angle as a function of Mach number for values of deflection angles ($r_{v_1} = 0.1$, $M_1 = 1$ to 10)

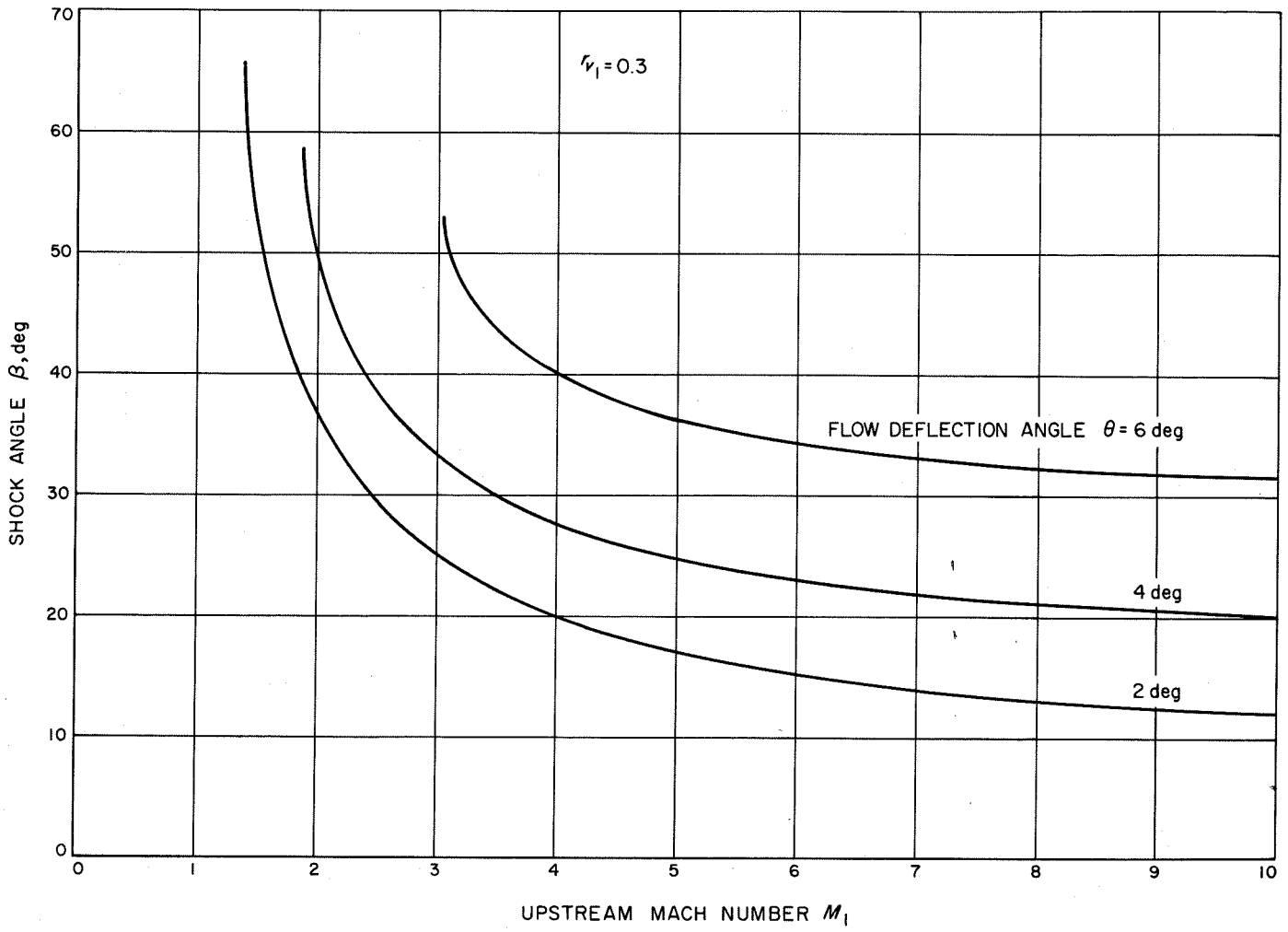

Fig. V-4. Oblique shock angle as a function of Mach number for values of deflection angles ($r_{v_1} = 0.3$, $M_1 = 1$ to 10)

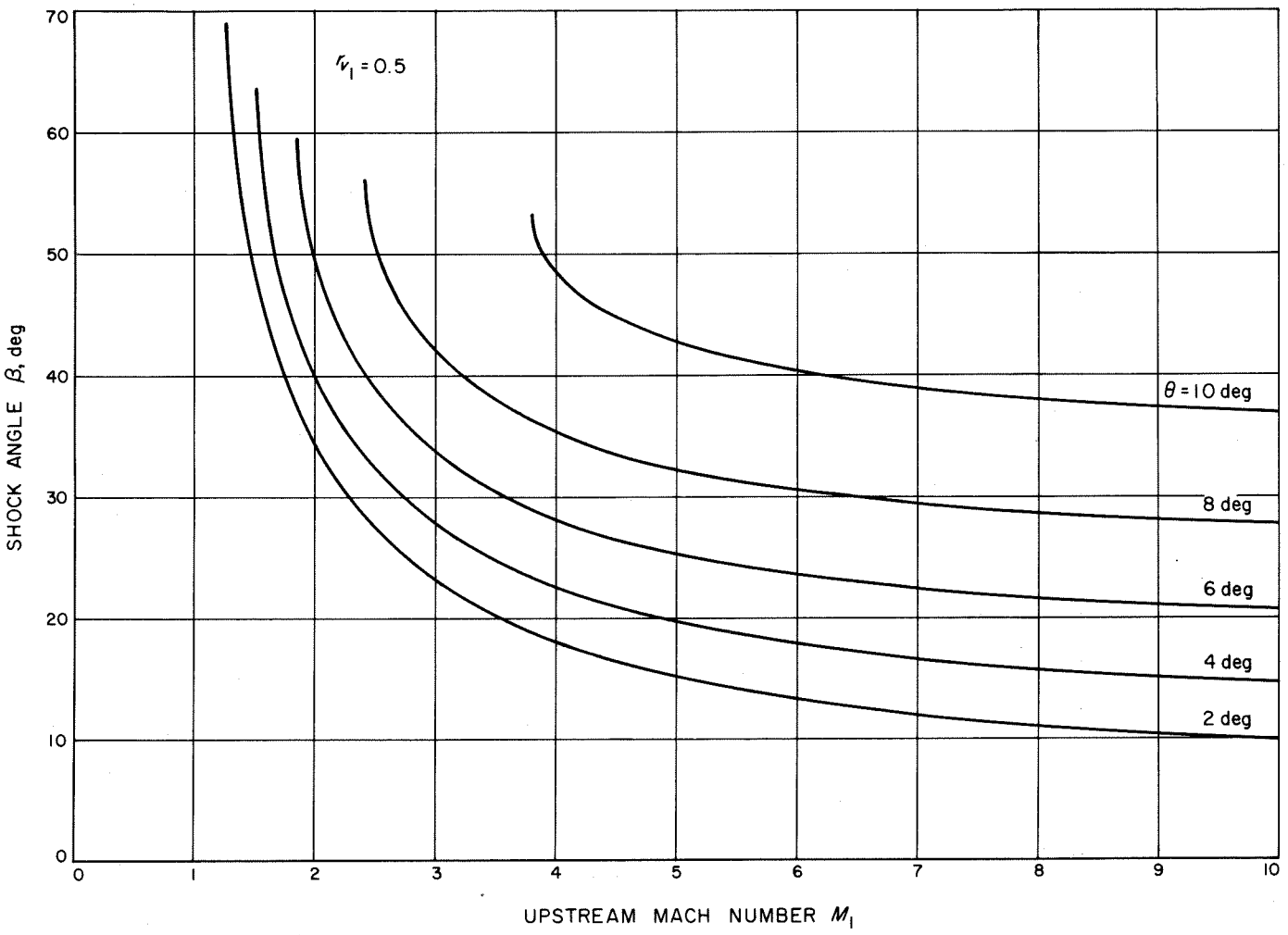

Fig. V-5. Oblique shock angle as a function of Mach number for values of deflection angles ($r_{v_1} = 0.5$, $M_1 = 1$ to 10)

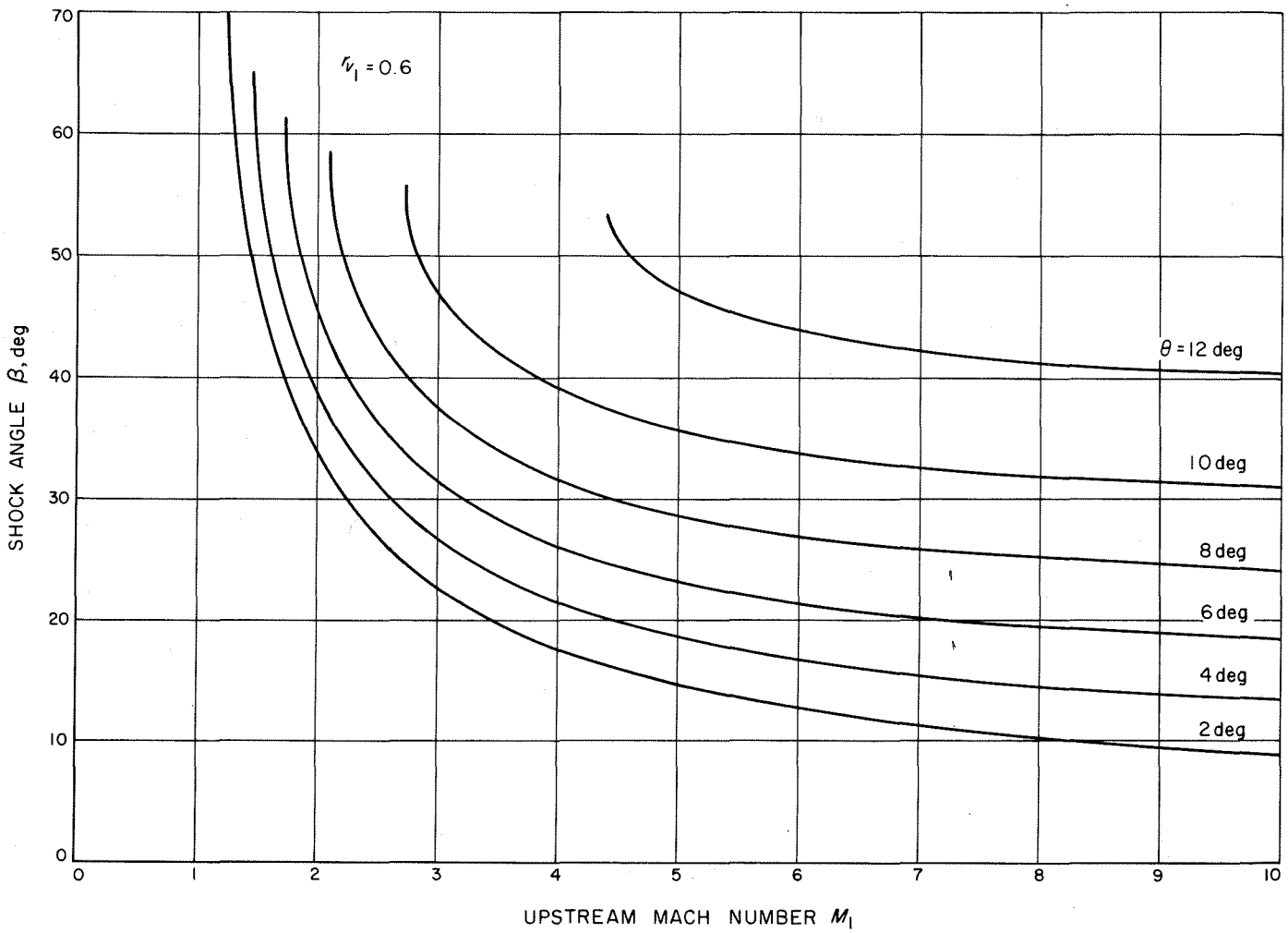

Fig. V-6. Oblique shock angle as a function of Mach number for values of deflection angles ($r_{v_1} = 0.6$, $M_1 = 1$ to 10)

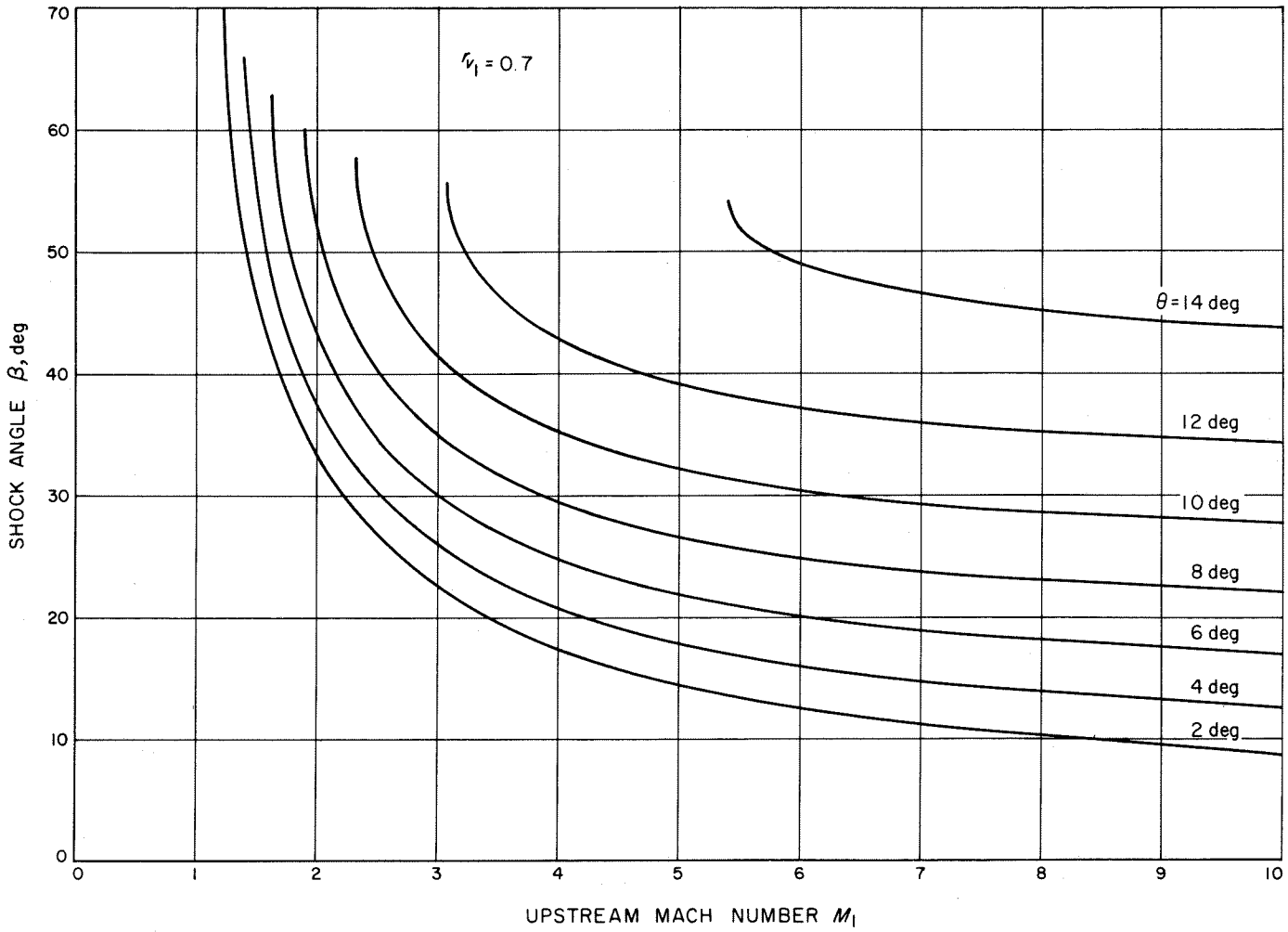

Fig. V-7. Oblique shock angle as a function of Mach number for values of deflection angles ($r_{v_1} = 0.7$, $M_1 = 1$ to 10)

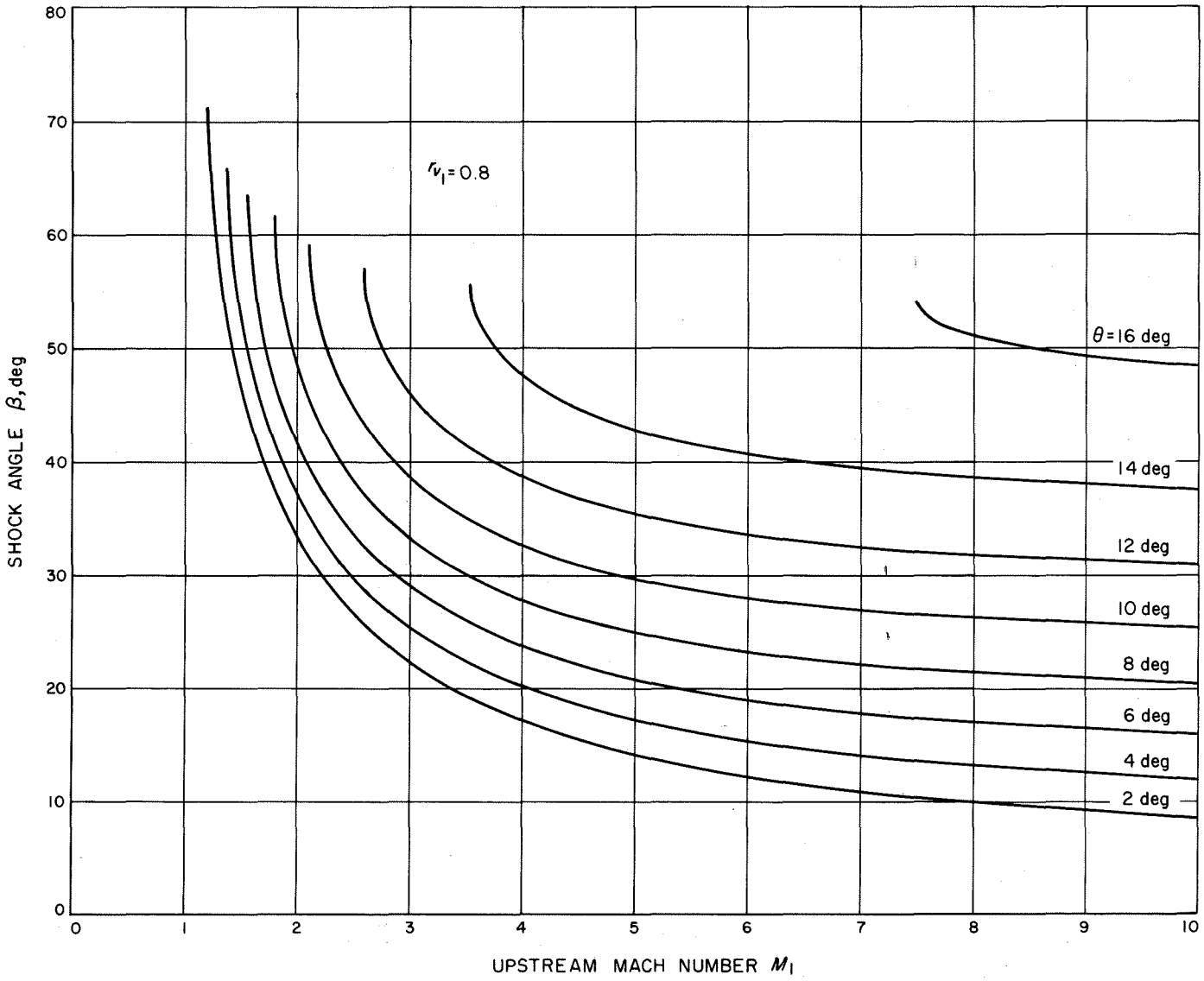

Fig. V-8. Oblique shock angle as a function of Mach number for values of deflection angles ($r_{v_1} = 0.8$, $M_1 = 1$ to 10)

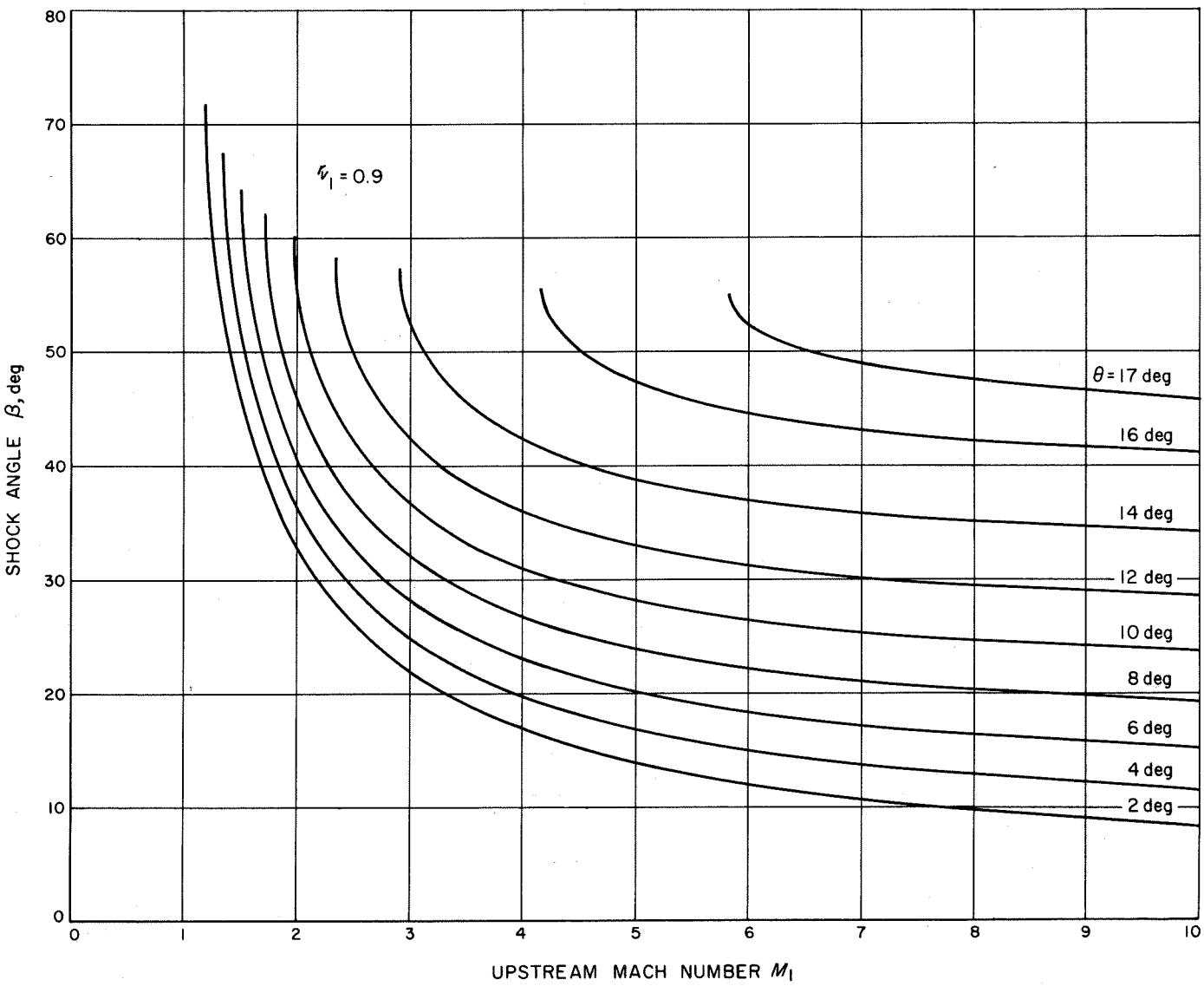

Fig. V-9. Oblique shock angle as a function of Mach number for values of deflection angles ($r_{v_1} = 0.9$, $M_1 = 1$ to 10)

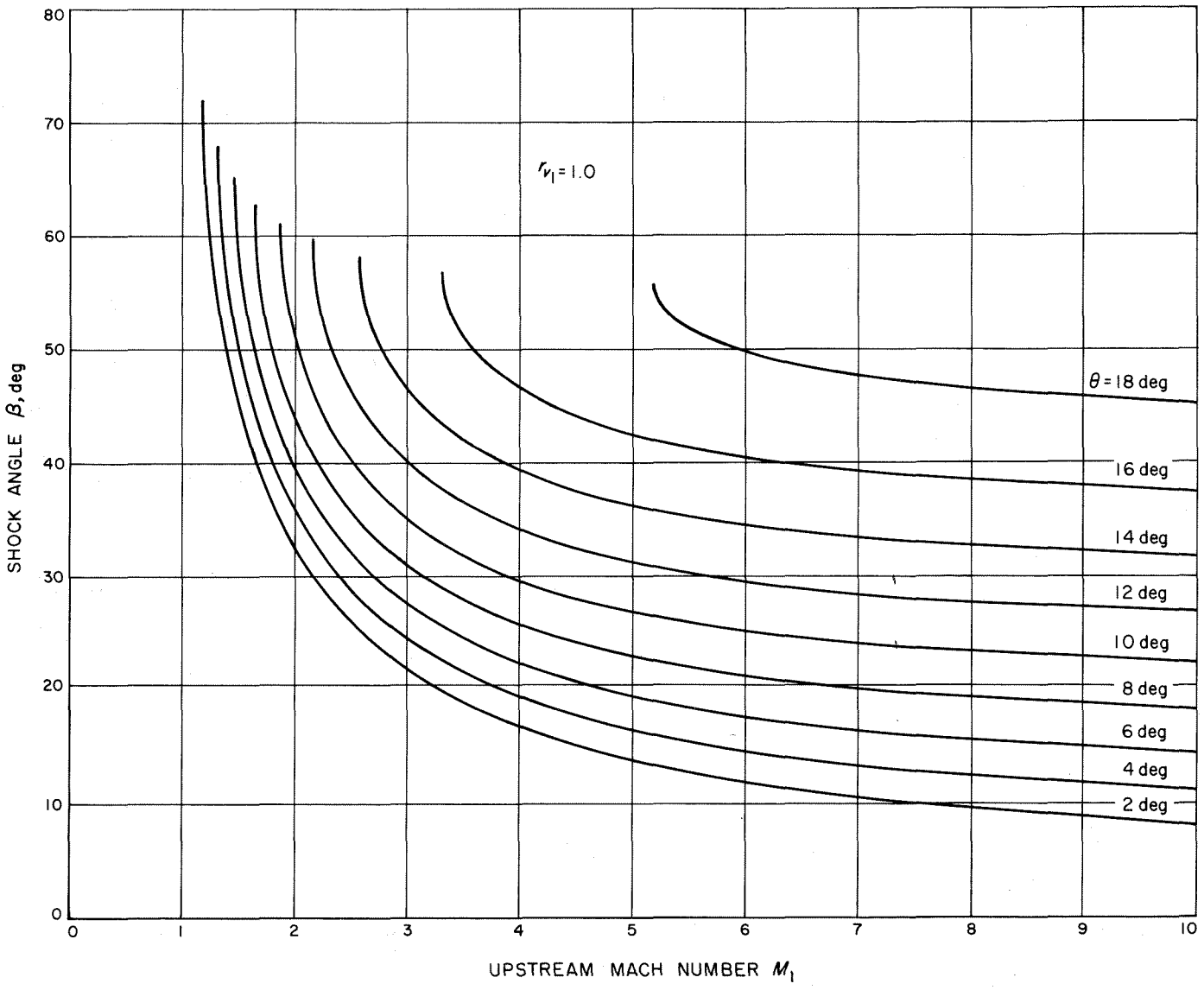

Fig. V-10. Oblique shock angle as a function of Mach number for values of deflection angles ($r_{v_1} = 1.0$, $M_1 = 1$ to 10)

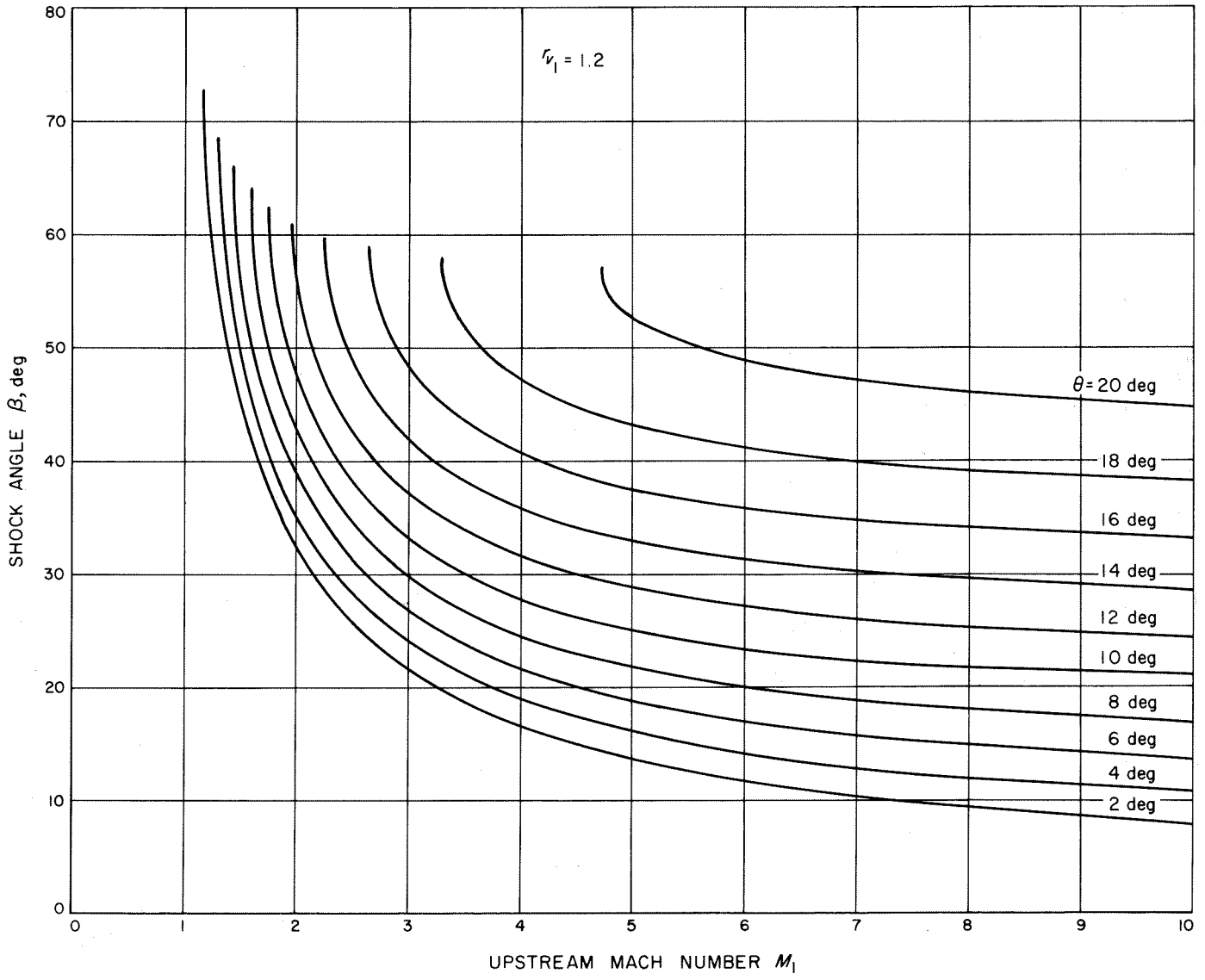

Fig. V-11. Oblique shock angle as a function of Mach number for values of deflection angles ($r_{v_1} = 1.2$, $M_1 = 1$ to 10)

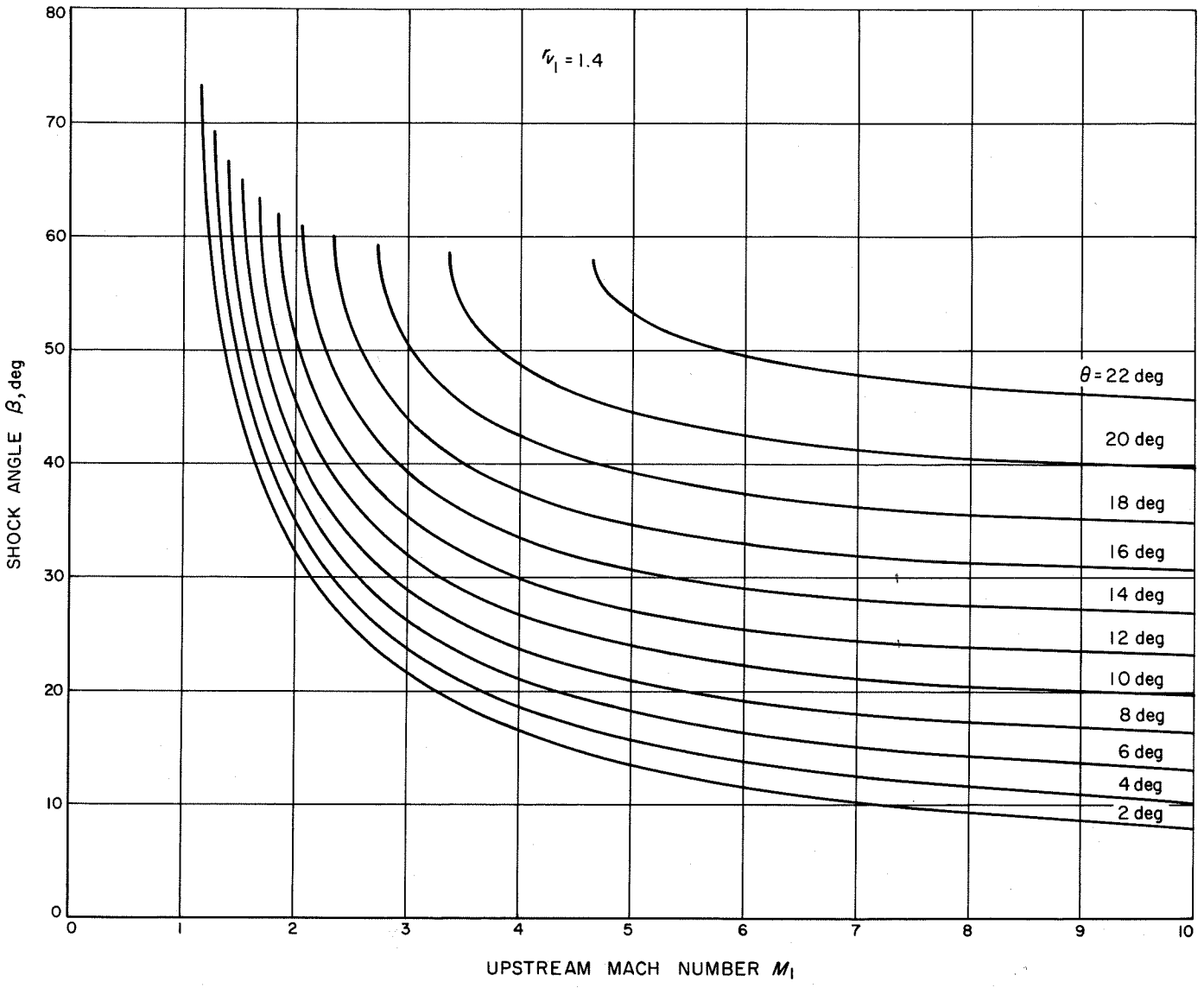

Fig. V-12. Oblique shock angle as a function of Mach number for values of deflection angles ($r_{v_1} = 1.4$, $M_1 = 1$ to 10)

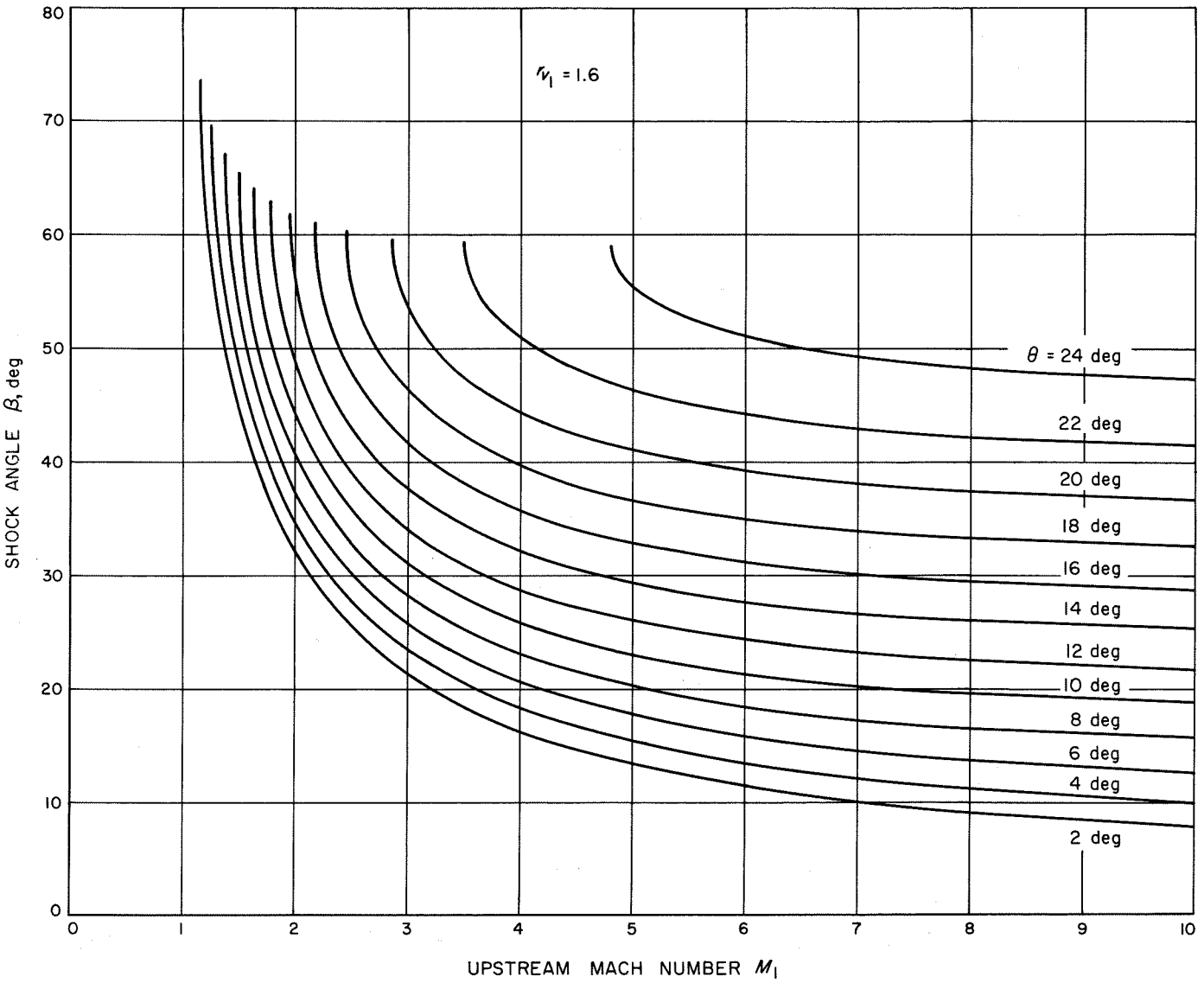

Fig. V-13. Oblique shock angle as a function of Mach number for values of deflection angles ($\nu_{v_1} = 1.6$, $M_1 = 1$ to 10)

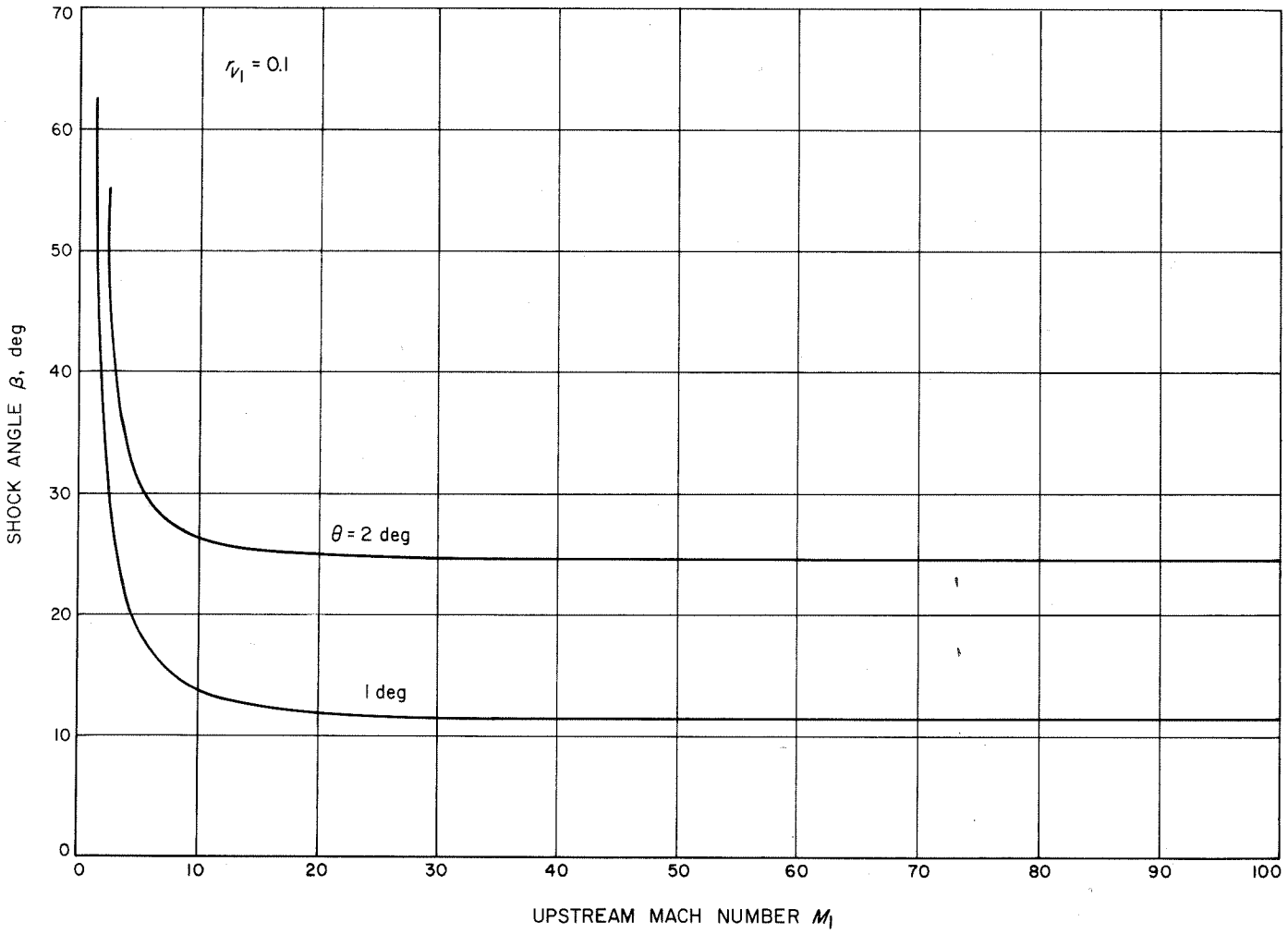

Fig. V-14. Oblique shock angle as a function of Mach number for values of deflection angles ($r_{v_1} = 0.1$, $M_1 = 1$ to 100)

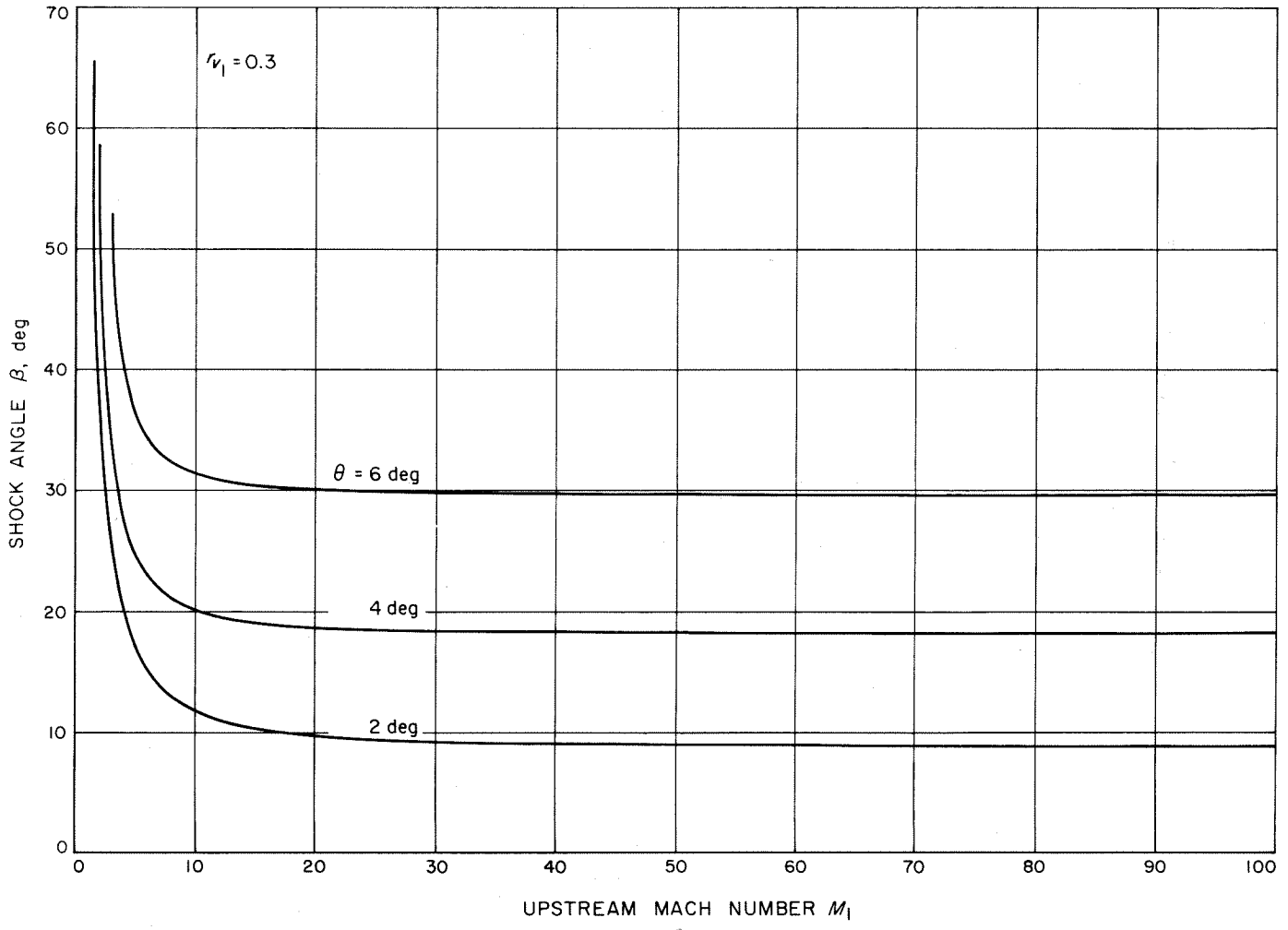

Fig. V-15. Oblique shock angle as a function of Mach number for values of deflection angles ($r_{v_1} = 0.3$, $M_1 = 1$ to 100)

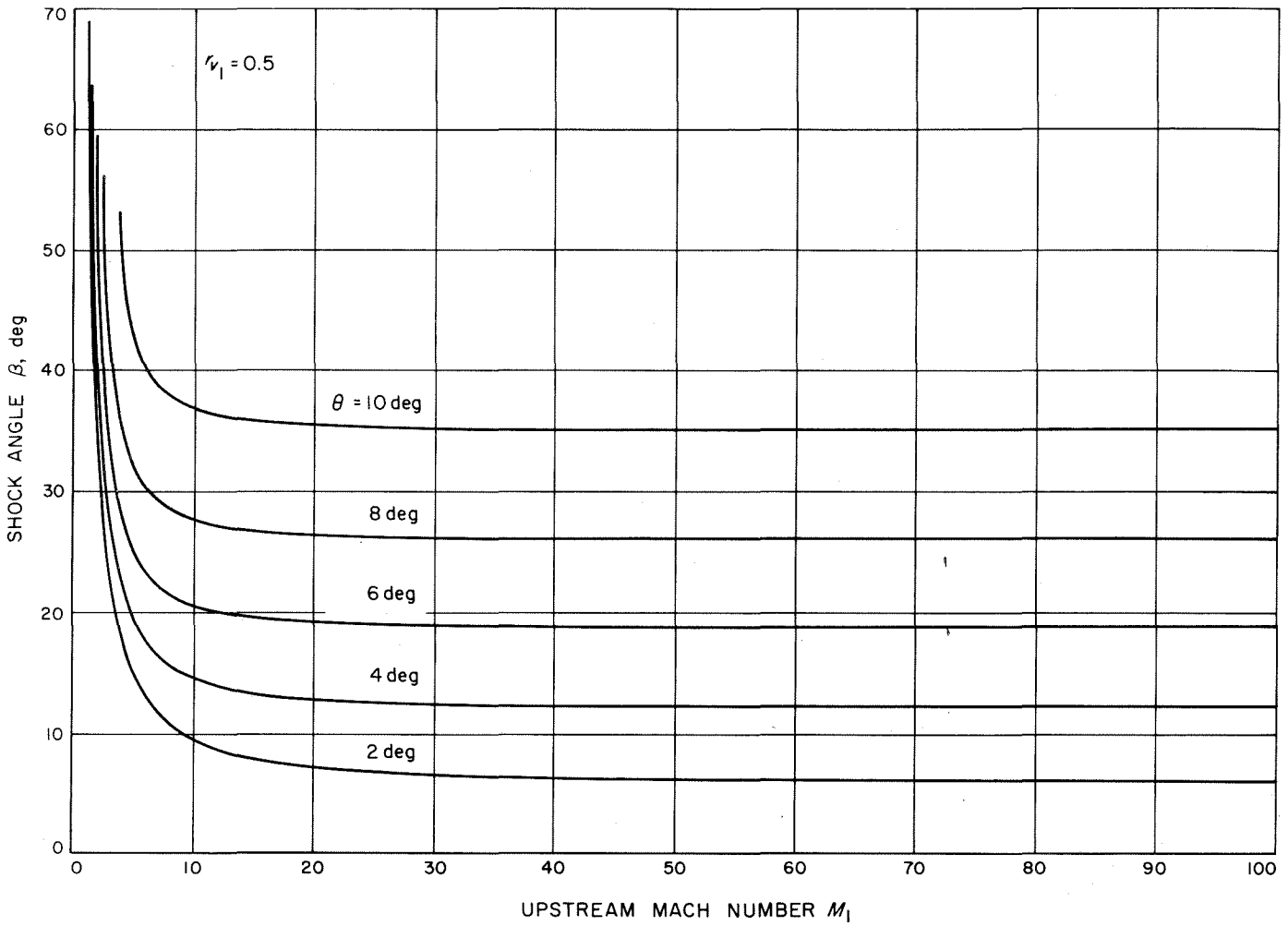

Fig. V-16. Oblique shock angle as a function of Mach number for values of deflection angles ($r_{v_1} = 0.5$, $M_1 = 1$ to 100)

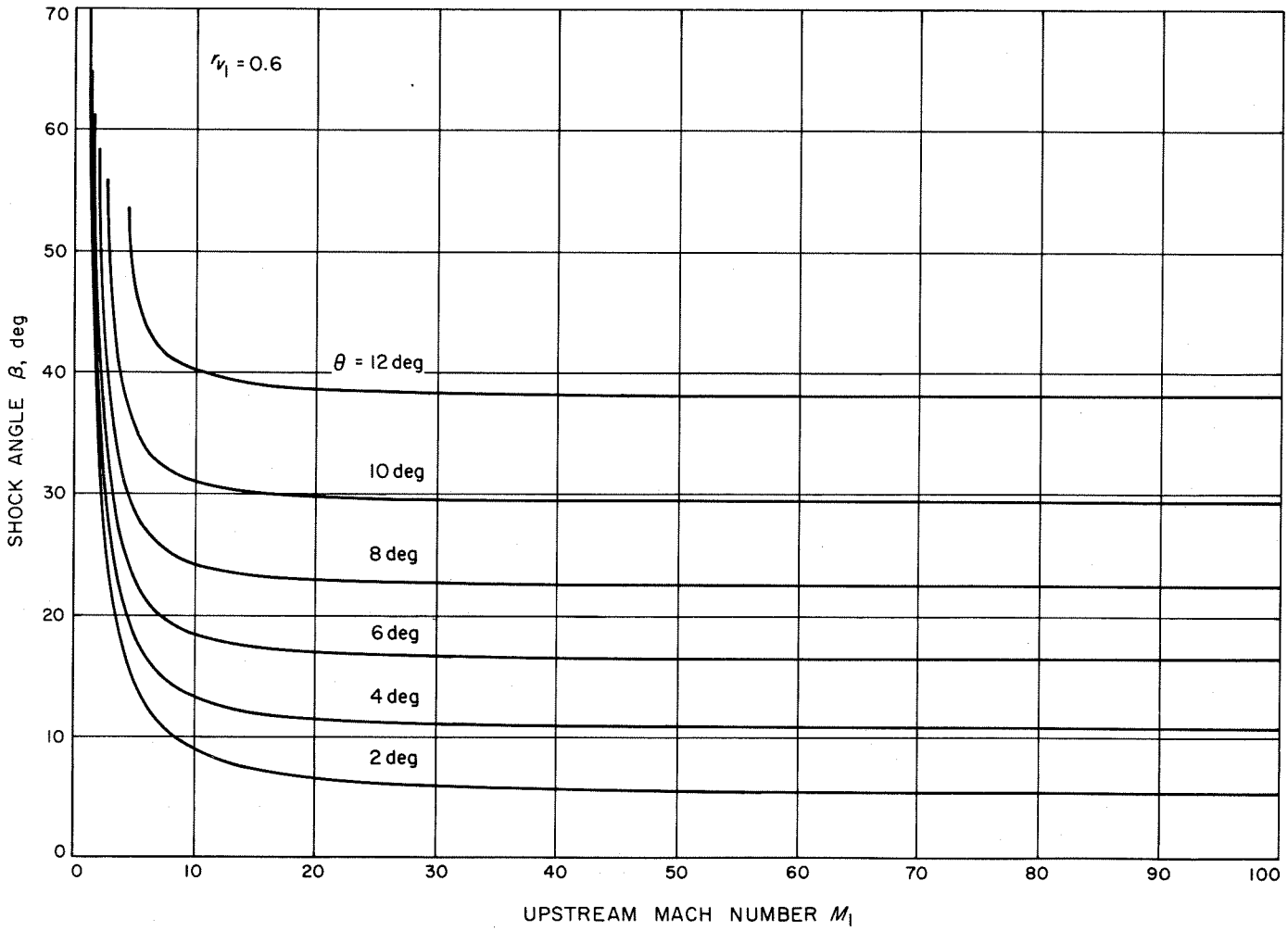

Fig. V-17. Oblique shock angle as a function of Mach number for values of deflection angles ($r_{v_1} = 0.6$, $M_1 = 1$ to 100)

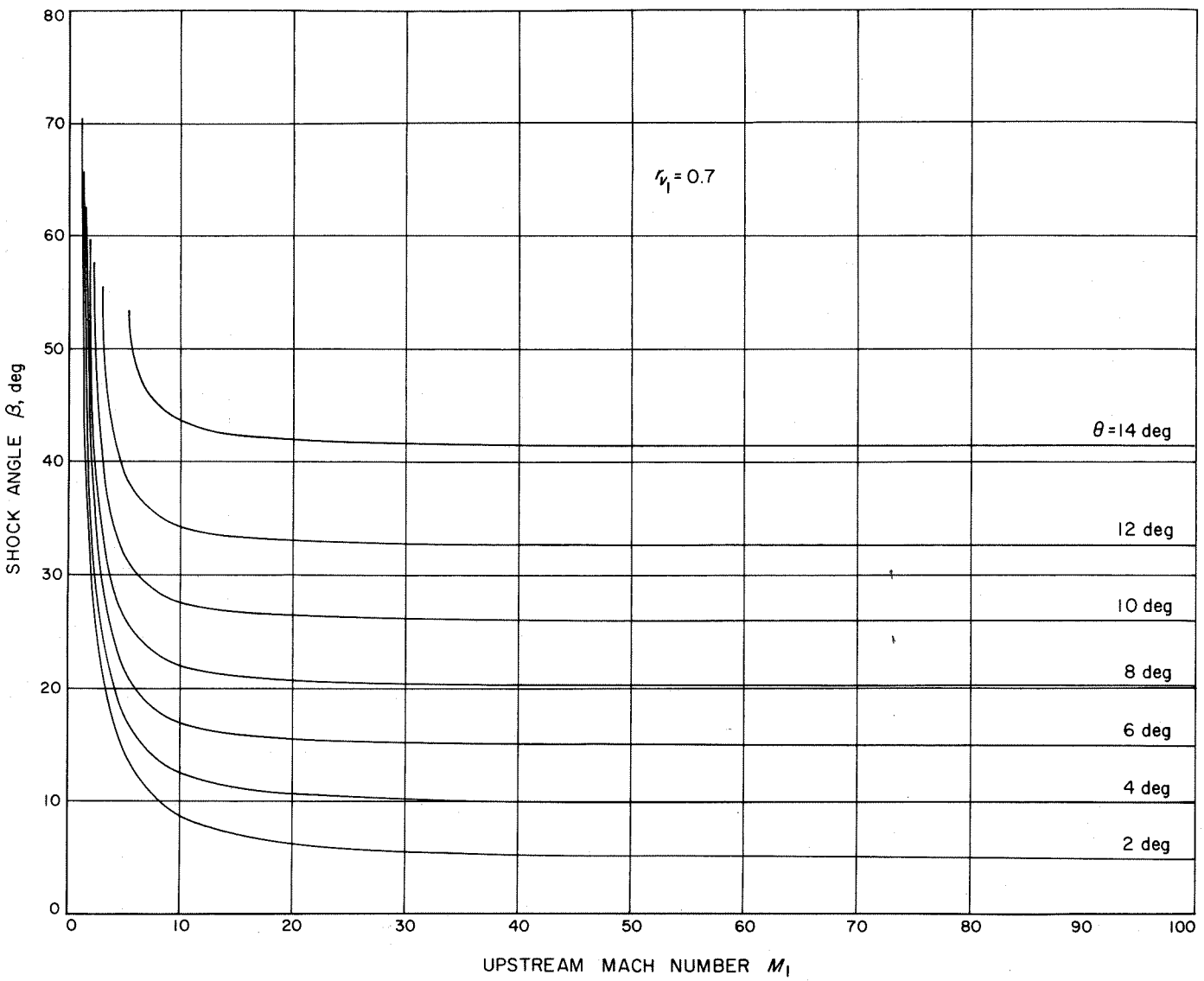

Fig. V-18. Oblique shock angle as a function of Mach number for values of deflection angles ($r_{v_1} = 0.7$, $M_1 = 1$ to 100)

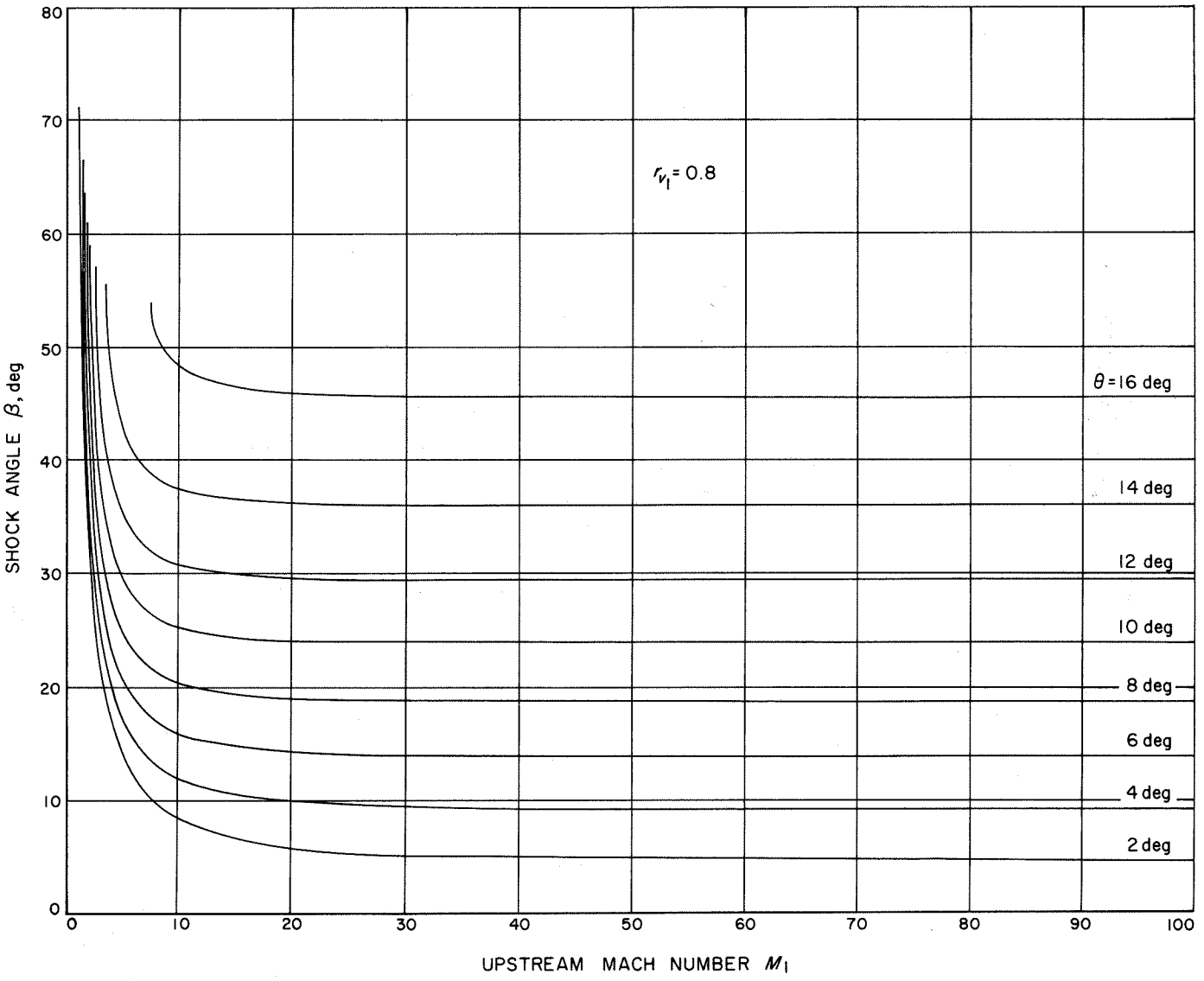

Fig. V-19. Oblique shock angle as a function of Mach number for values of deflection angles ($r_{v_1} = 0.8$, $M_1 = 1$ to 100)

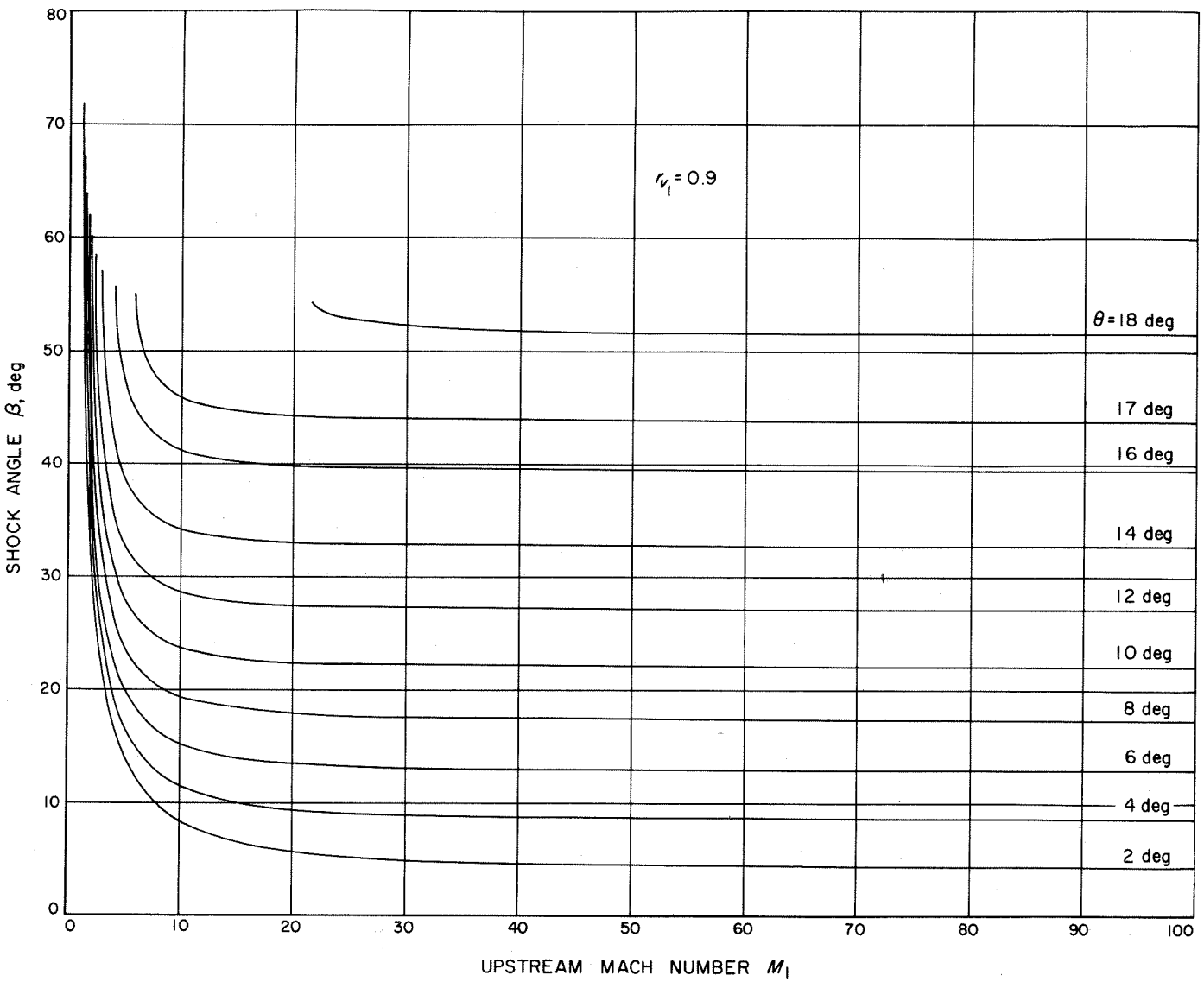

Fig. V-20. Oblique shock angle as a function of Mach number for values of deflection angles ($r_{v_1} = 0.9$, $M_1 = 1$ to 100)

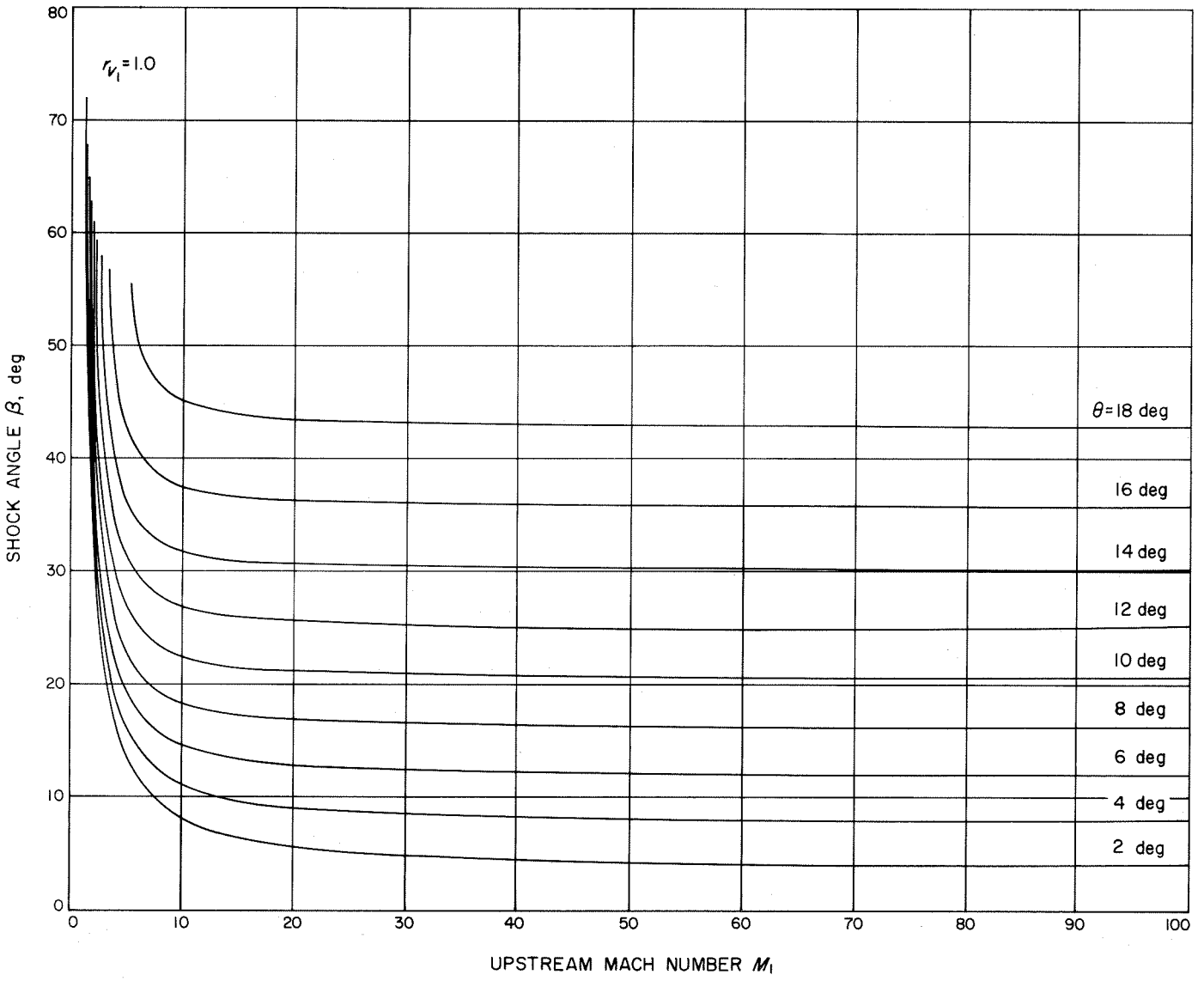

Fig. V-21. Oblique shock angle as a function of Mach number for values of deflection angles ($r_{v_1} = 1.0$, $M_1 = 1$ to 100)

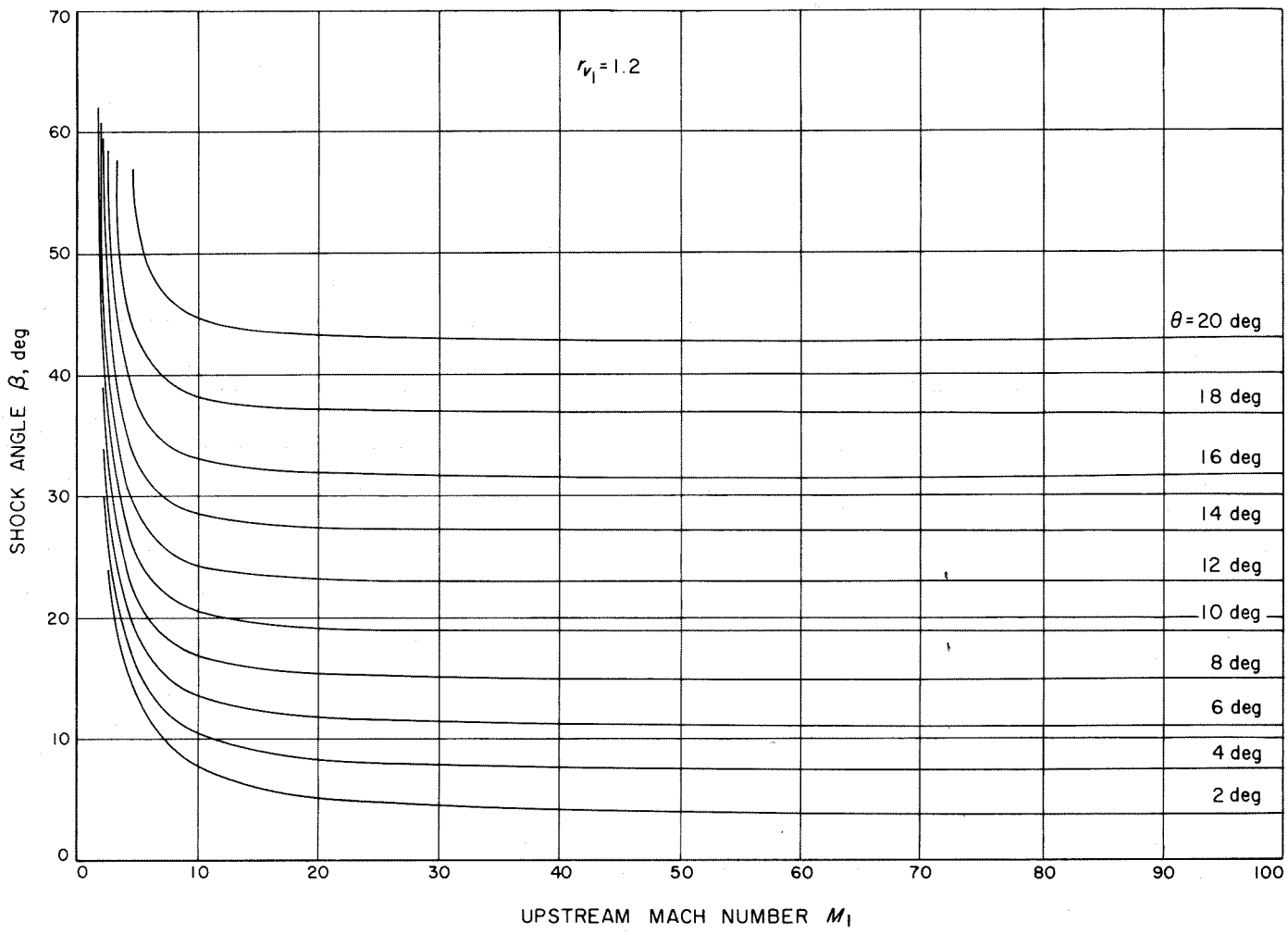

Fig. V-22. Oblique shock angle as a function of Mach number for values of deflection angles ($r_{v_1} = 1.2$, $M_1 = 1$ to 100)

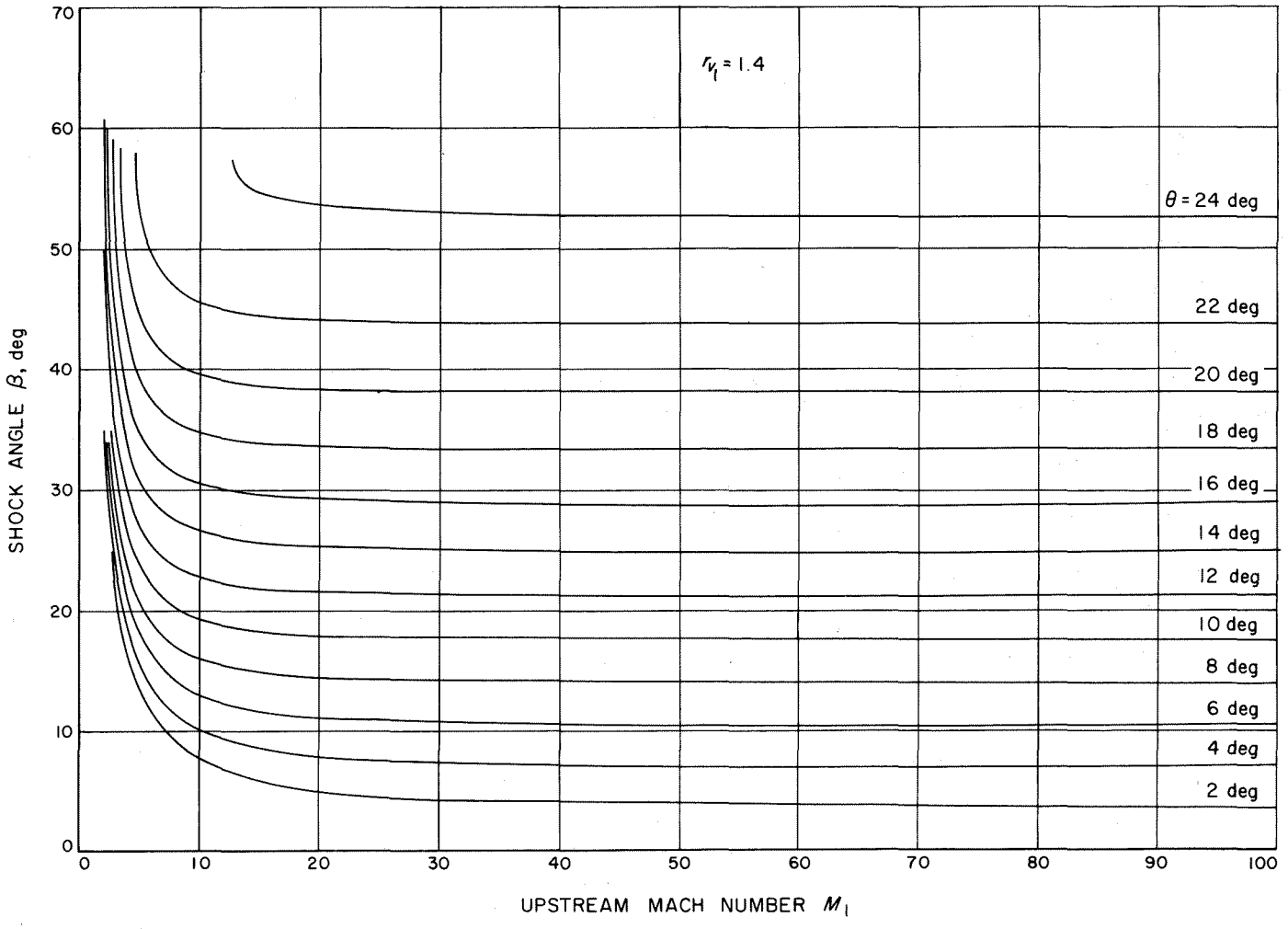

Fig. V-23. Oblique shock angle as a function of Mach number for values of deflection angles ($r_{v_1} = 1.4$, $M_1 = 1$ to 100)

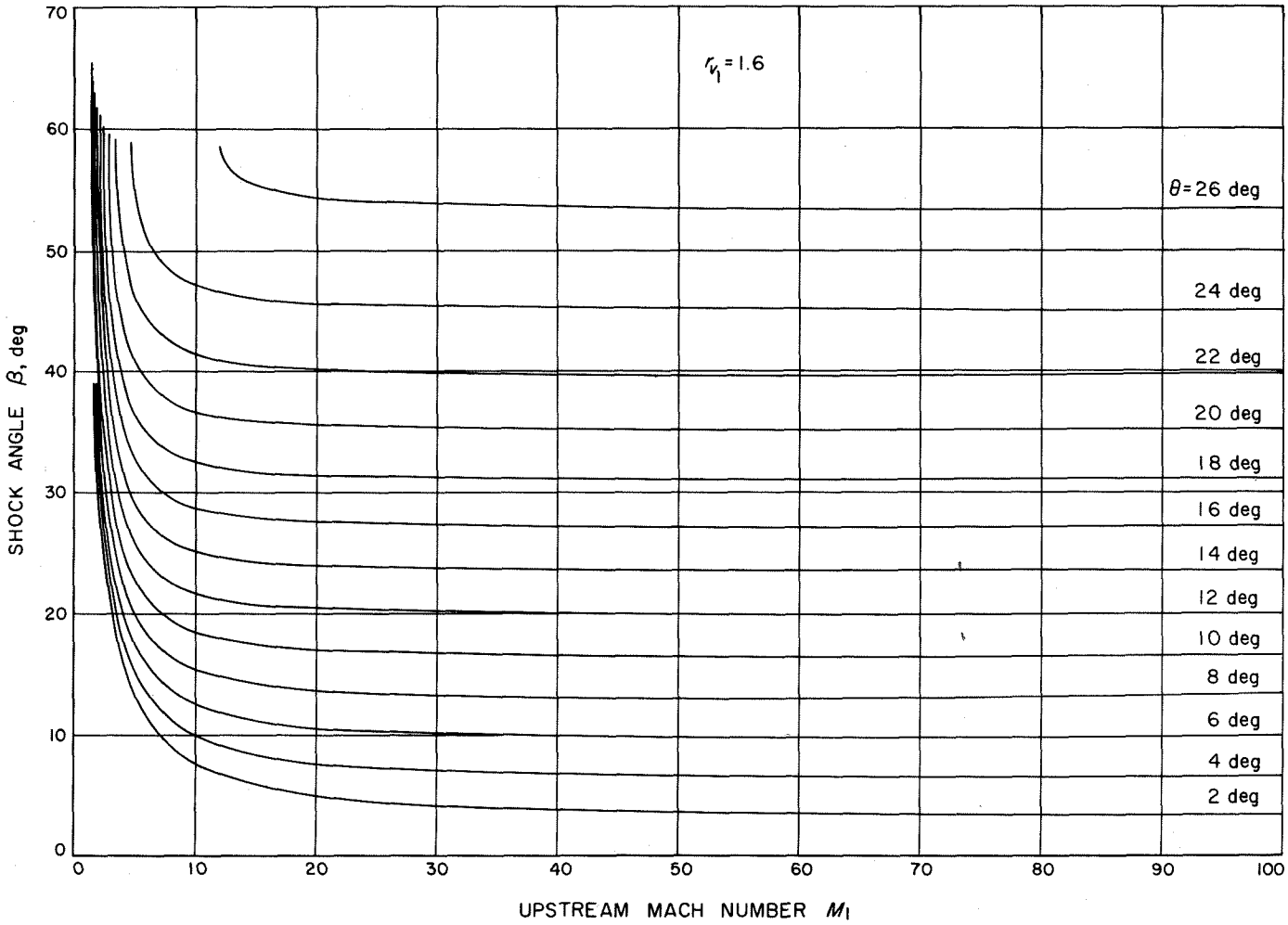

Fig. V-24. Oblique shock angle as a function of Mach number for values of deflection angles ($r_{v_1} = 1.6$, $M_1 = 1$ to 100)

3. Pressure Ratio (P_2/P_1)

Pressure ratio (P_2/P_1) from Eq. (V-19) is a simple function of initial Mach number and shock angle β. However, β is not generally part of the initial known characteristics of a supersonic flow configuration. As a function of M_1 and deflection angle θ, (P_2/P_1) is far more interesting, although no simple dependence on θ exists in Eq. (V-19) to eliminate β. Figures V-25 through V-30 show (P_2/P_1) as a function of M_1 for values of θ with each figure representing a fixed value of r_{v_1} from 0.5 through 1.0. Figures V-31 through V-41 show the same plotted relationship for an extended Mach number range of 0 to 70, and the additional r_{v_1} values from 0.1 through 1.6 in steps of 0.2 r_v.

Note that pressure ratios exceeding 10^3 exist for Mach numbers exceeding 50 at medium deflection angles as the void ratio r_{v_1} increases beyond 1.0.

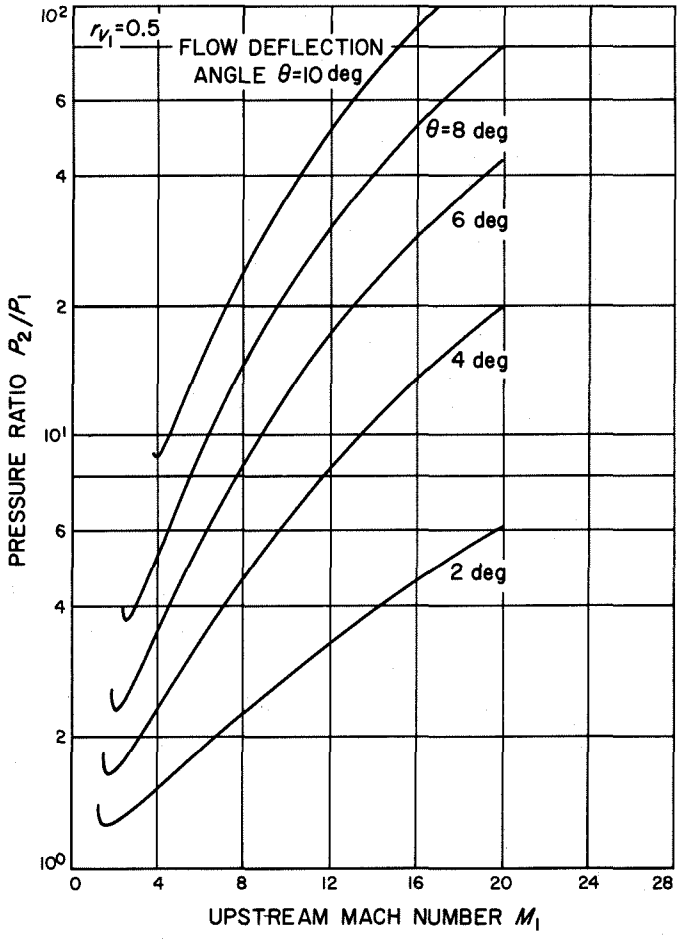

Fig. V-25. Oblique shock pressure ratio as a function of Mach number for values of deflection angle (r_{v_1} = 0.5, M_1 = 0 to 28)

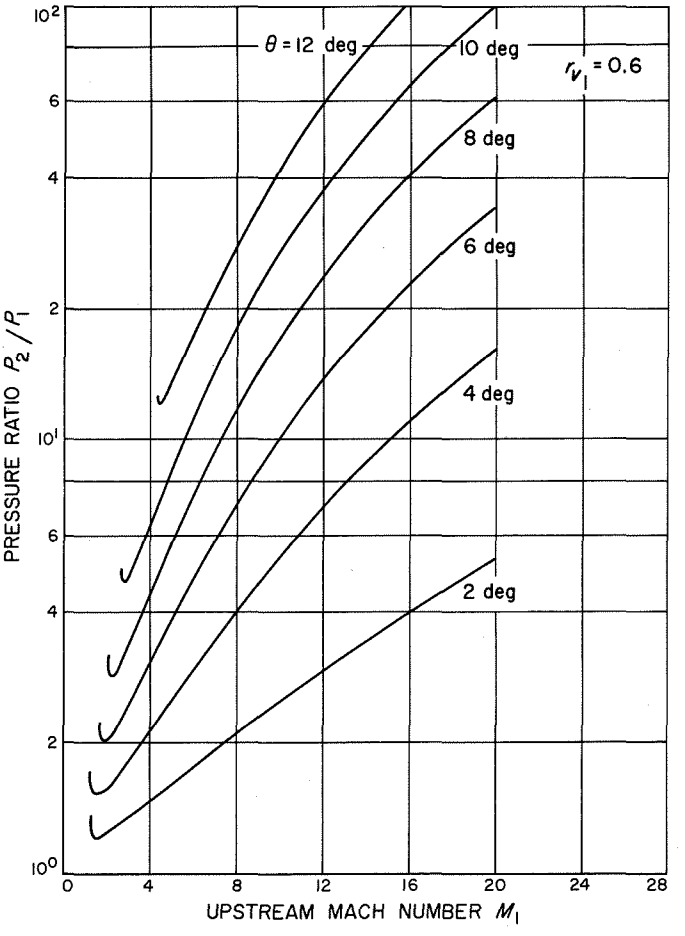

Fig. V-26. Oblique shock pressure ratio as a function of Mach number for values of deflection angle (r_{v_1} = 0.6, M_1 = 0 to 28)

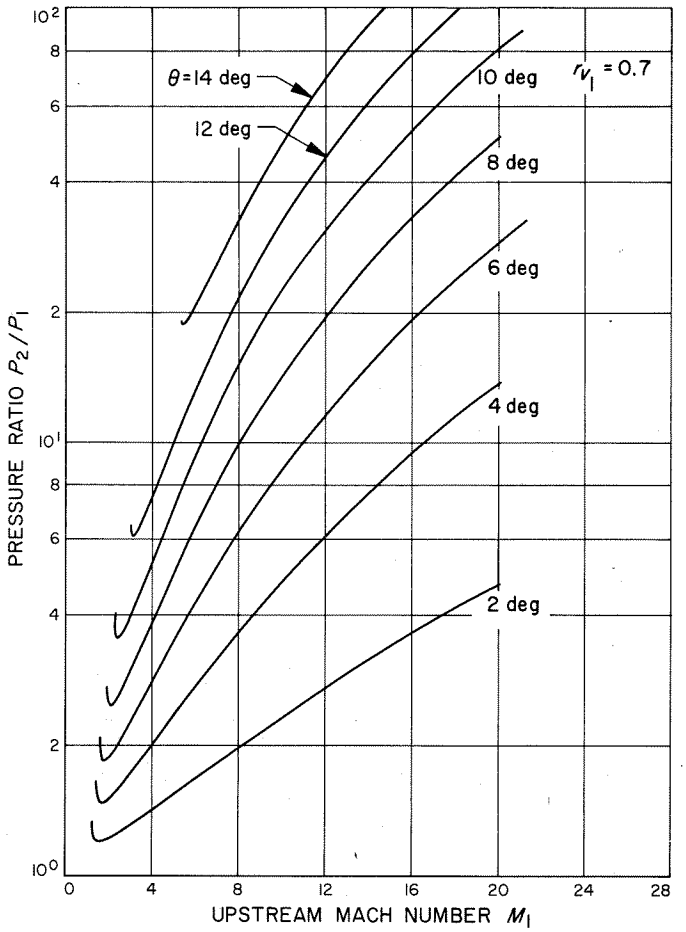

Fig. V-27. Oblique shock pressure ratio as a function of Mach number for values of deflection angle ($r_{v_1} = 0.7$, $M_1 = 0$ to 28)

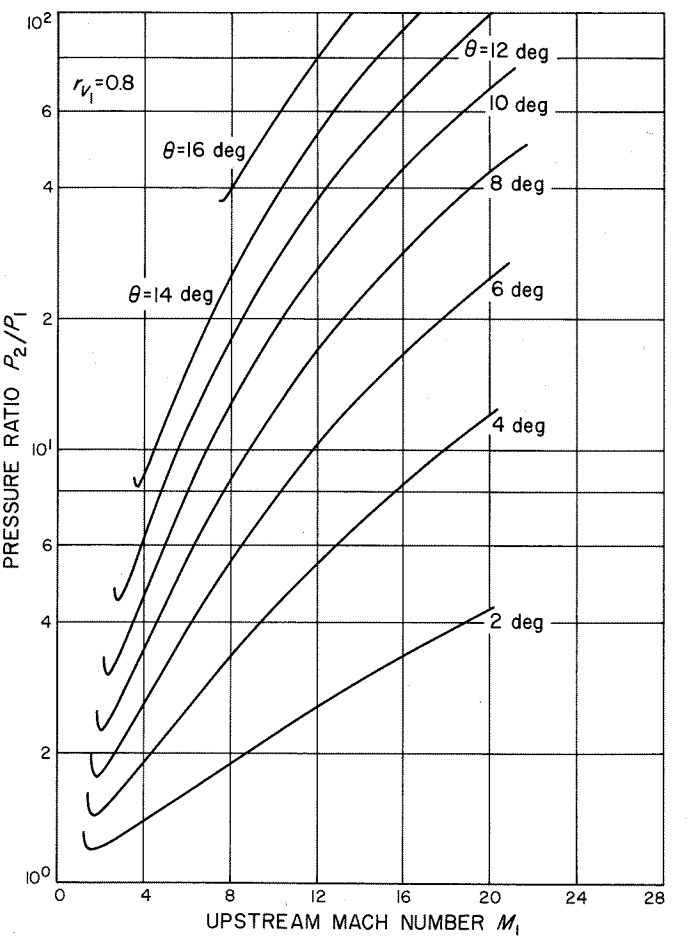

Fig. V-28. Oblique shock pressure ratio as a function of Mach number for values of deflection angle ($r_{v_1} = 0.8$, $M_1 = 0$ to 28)

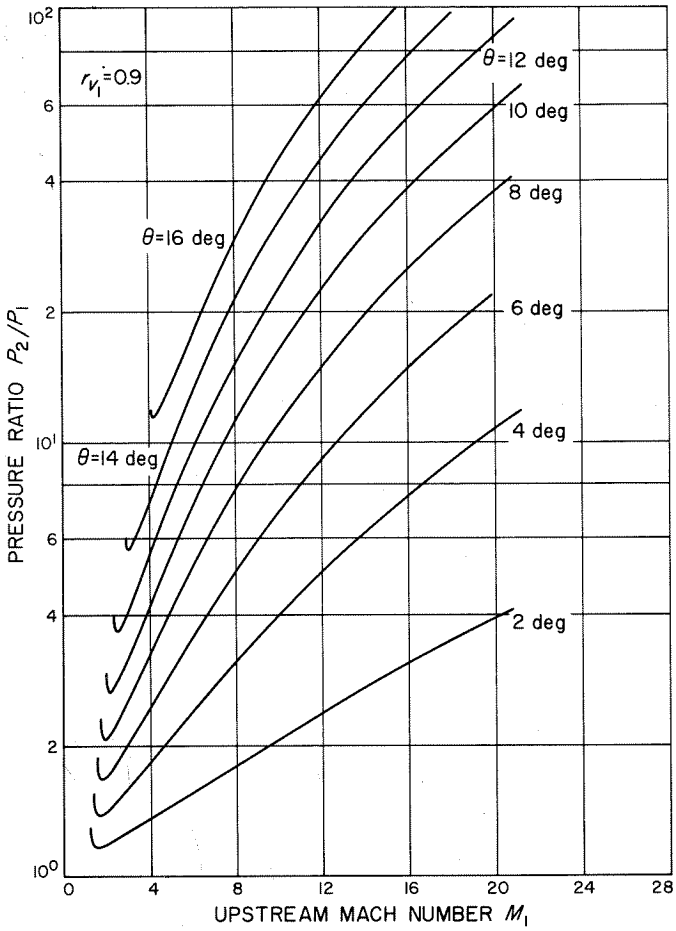

Fig. V-29. Oblique shock pressure ratio as a function of Mach number for values of deflection angle ($r_{v_1} = 0.9$, $M_1 = 0$ to 28)

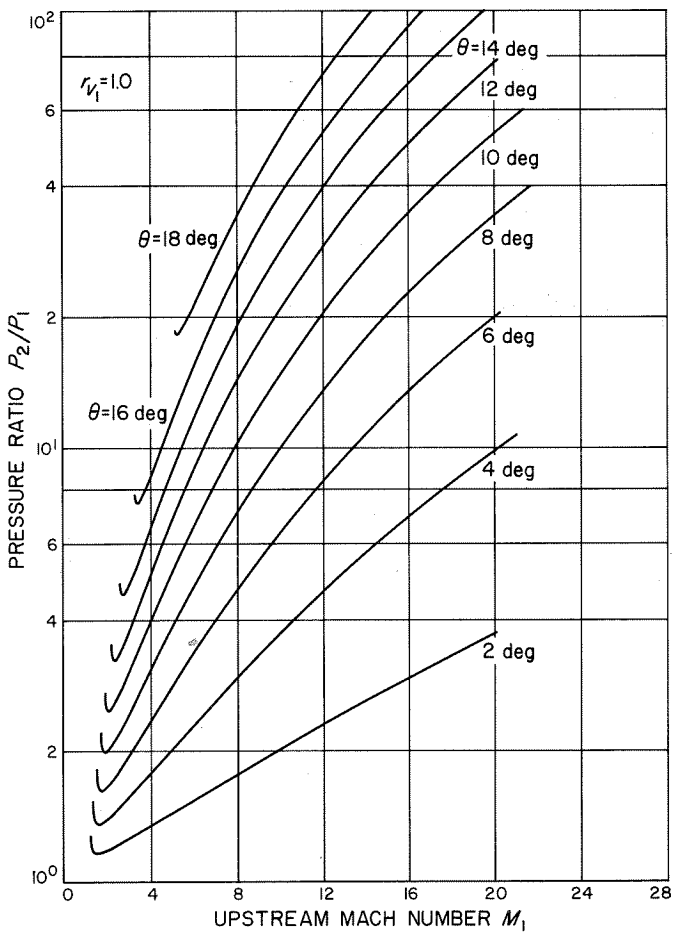

Fig. V-30. Oblique shock pressure ratio as a function of Mach number for values of deflection angle ($r_{v_1} = 1.0$, $M_1 = 0$ to 28)

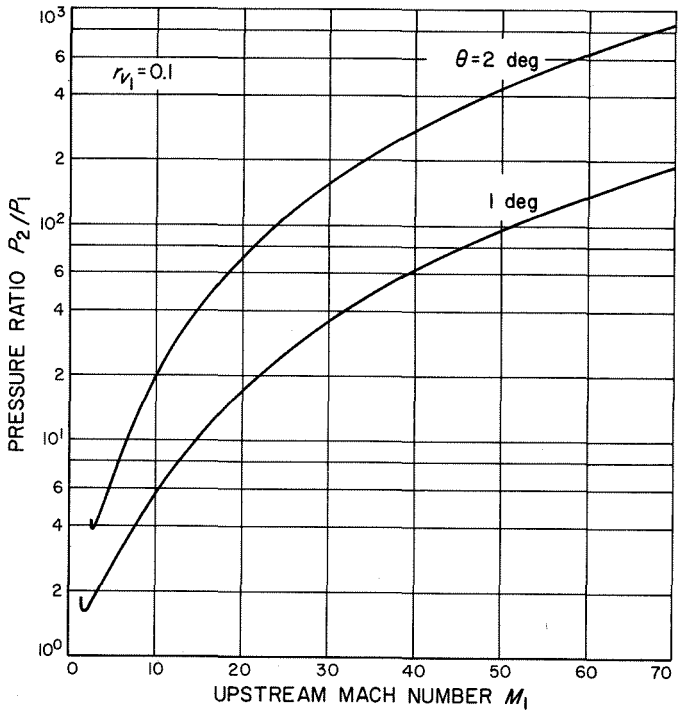

Fig. V-31. Oblique shock pressure ratio as a function of Mach number for values of deflection angle ($r_{V_1} = 0.1$, $M_1 = 0$ to 70)

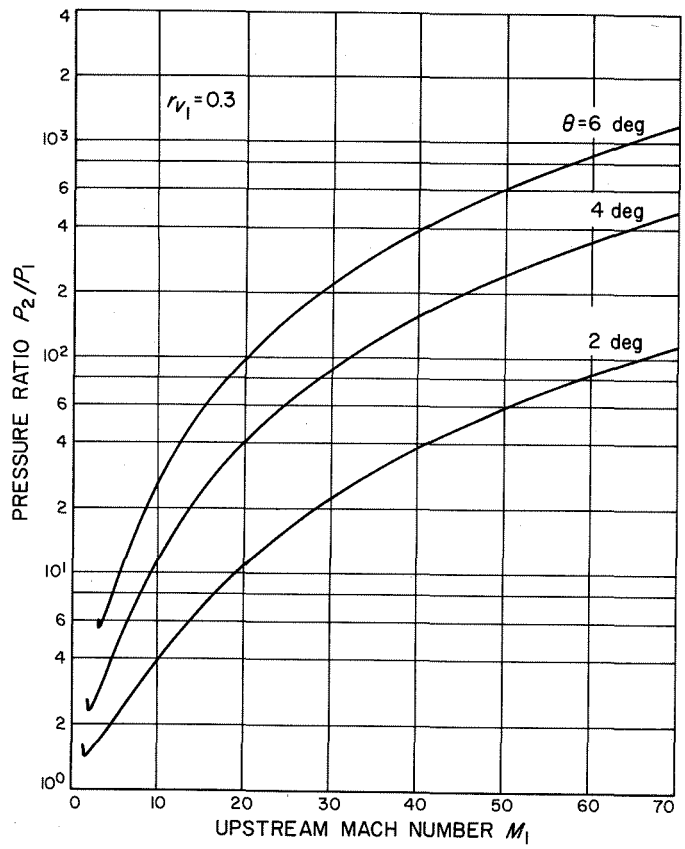

Fig. V-32. Oblique shock pressure ratio as a function of Mach number for values of deflection angle ($r_{V_1} = 0.3$, $M_1 = 0$ to 70)

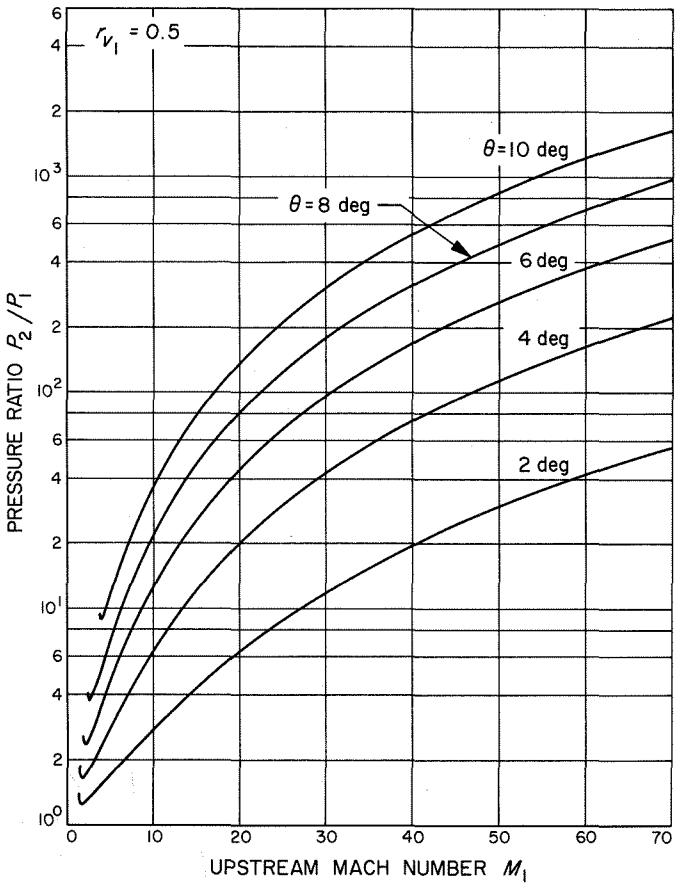

Fig. V-33. Oblique shock pressure ratio as a function of Mach number for values of deflection angle ($r_{v_1} = 0.5$, $M_1 = 0$ to 70)

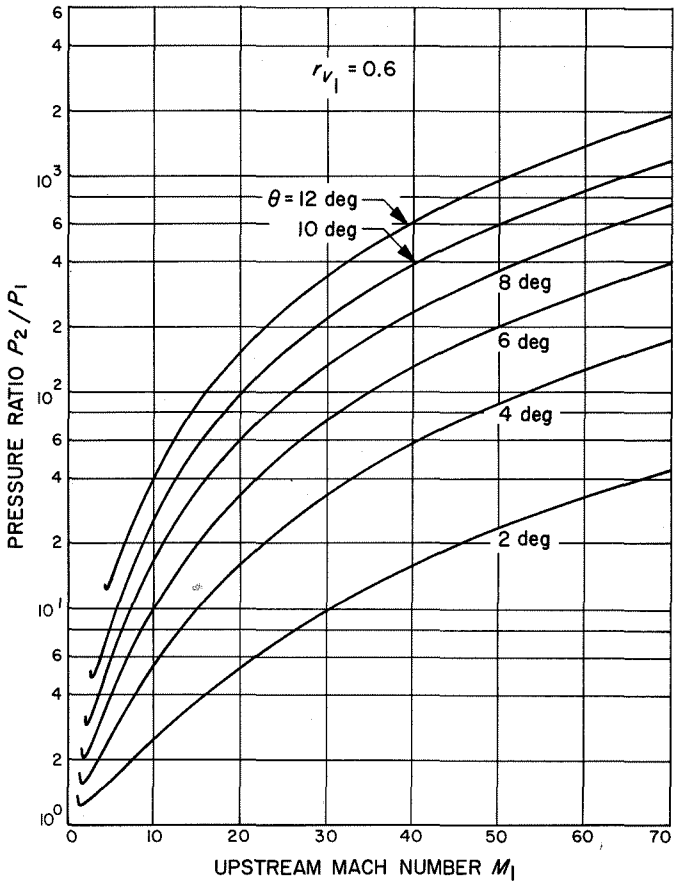

Fig. V-34. Oblique shock pressure ratio as a function of Mach number for values of deflection angle ($r_{v_1} = 0.6$, $M_1 = 0$ to 70)

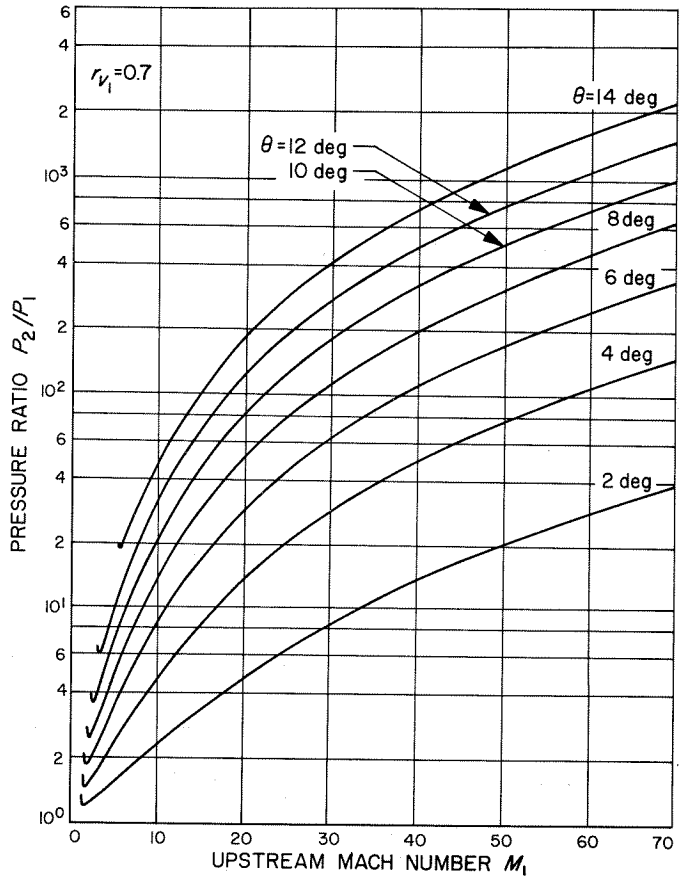

Fig. V-35. Oblique shock pressure ratio as a function of Mach number for values of deflection angle ($r_{v_1} = 0.7$, $M_1 = 0$ to 70)

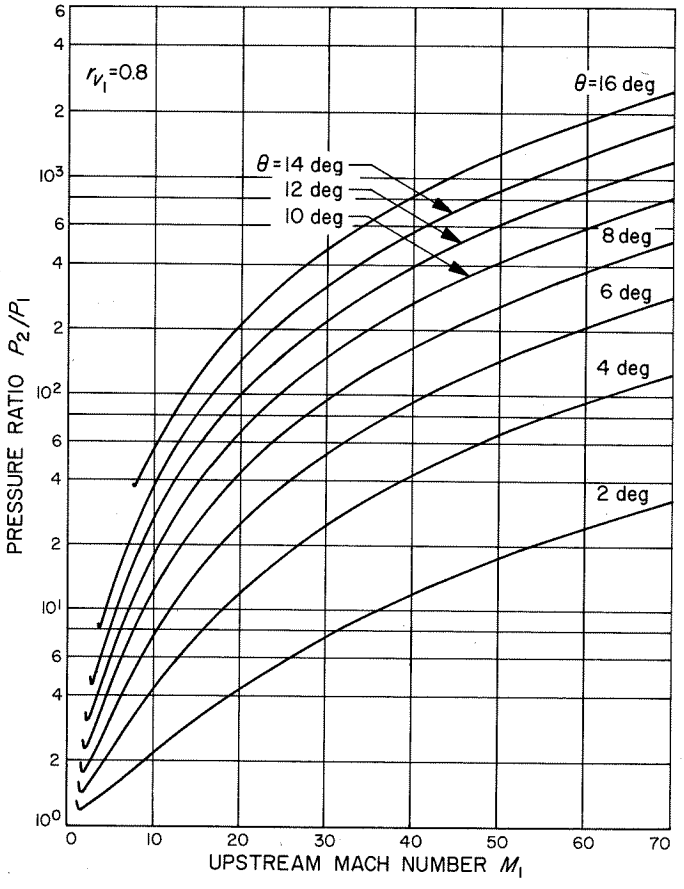

Fig. V-36. Oblique shock pressure ratio as a function of Mach number for values of deflection angle ($r_{v_1} = 0.8$, $M_1 = 0$ to 70)

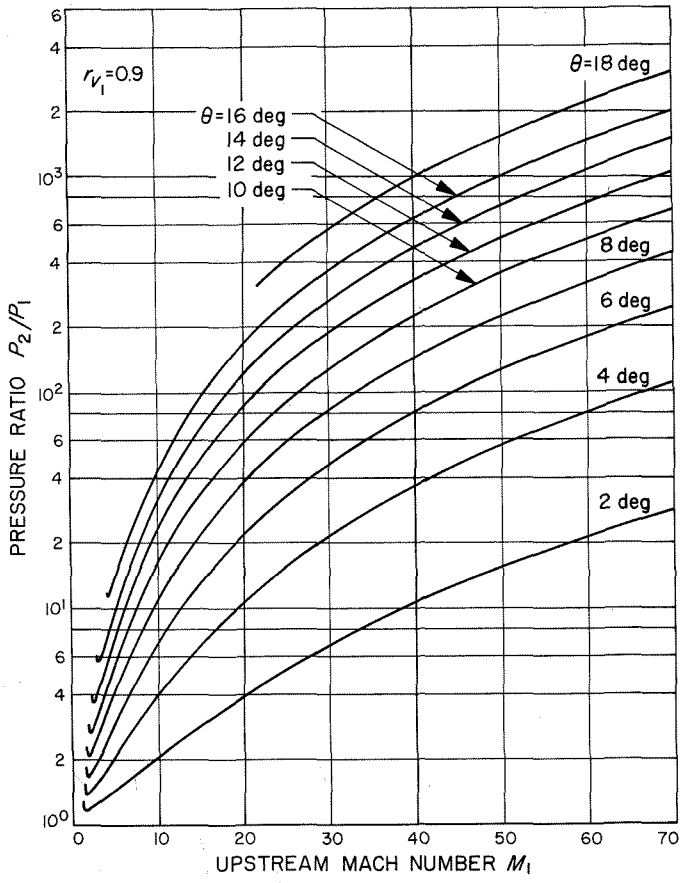

Fig. V-37. Oblique shock pressure ratio as a function of Mach number for values of deflection angle ($r_{v_1} = 0.9$, $M_1 = 0$ to 70)

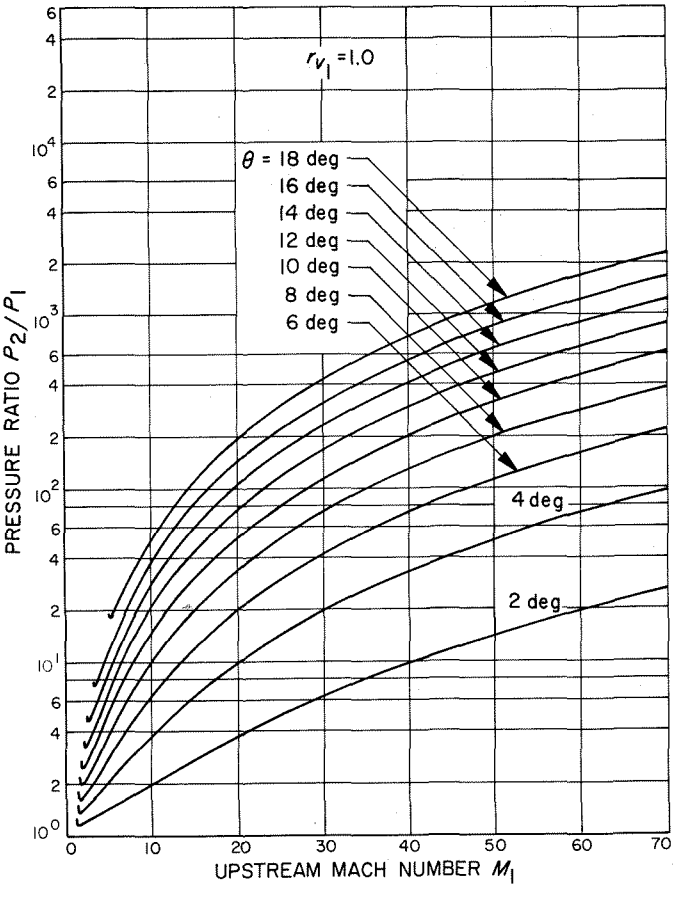

Fig. V-38. Oblique shock pressure ratio as a function of Mach number for values of deflection angle ($r_{v_1} = 1.0$, $M_1 = 0$ to 70)

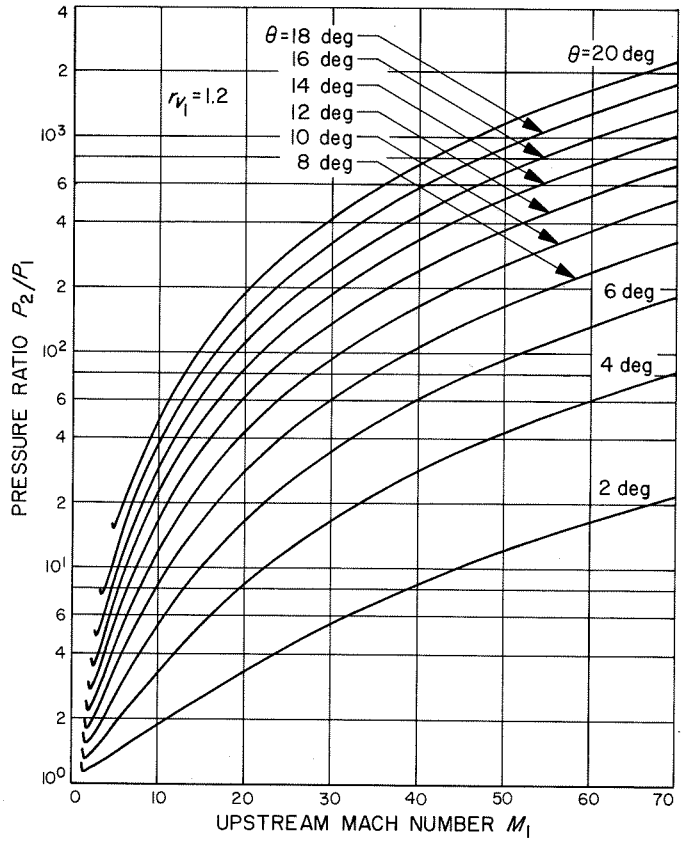

Fig. V-39. Oblique shock pressure ratio as a function of Mach number for values of deflection angle ($r_{v_1} = 1.2$, $M_1 = 0$ to 70)

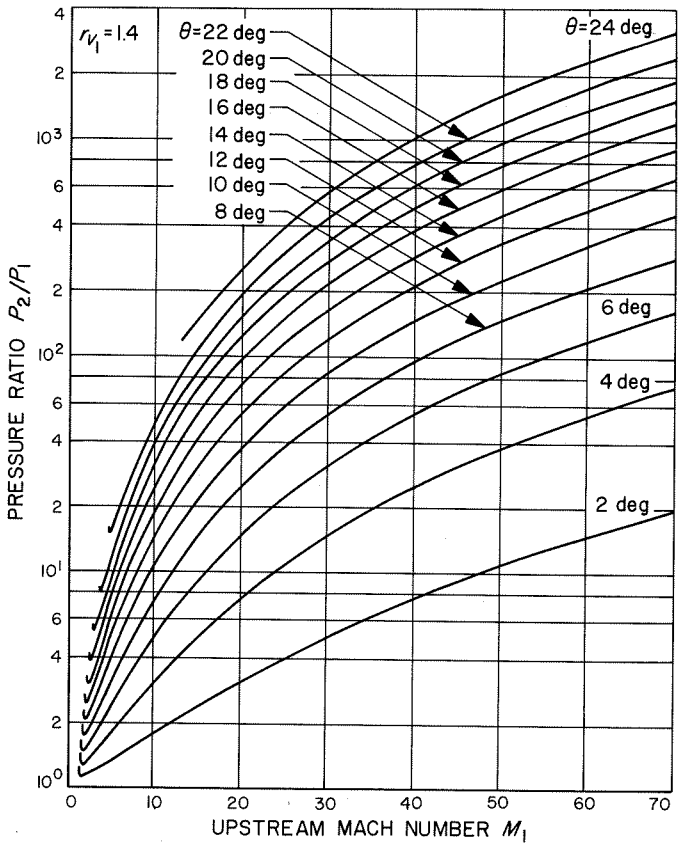

Fig. V-40. Oblique shock pressure ratio as a function of Mach number for values of deflection angle ($r_{v_1} = 1.4$, $M_1 = 0$ to 70)

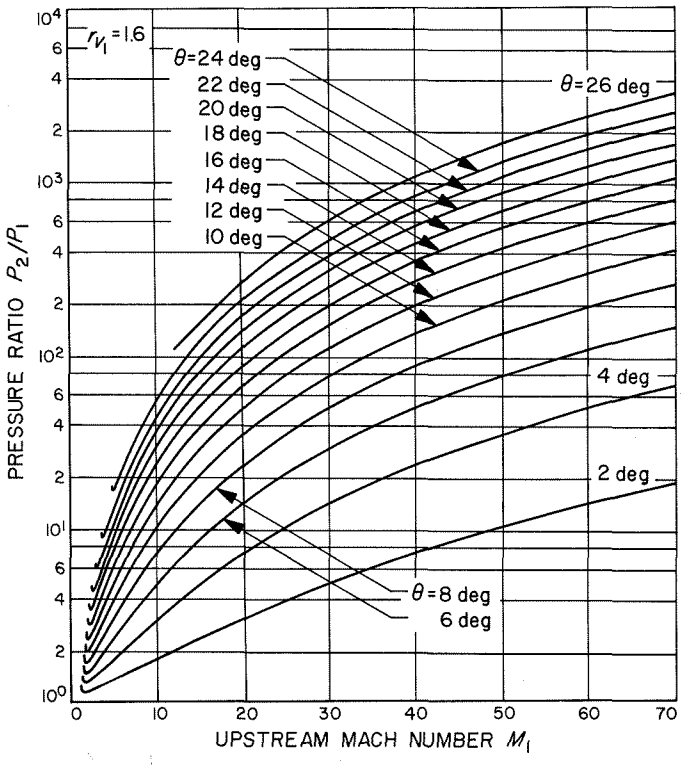

Fig. V-41. Oblique shock pressure ratio as a function of Mach number for values of deflection angle ($r_{v_1} = 1.6$, $M_1 = 0$ to 70)

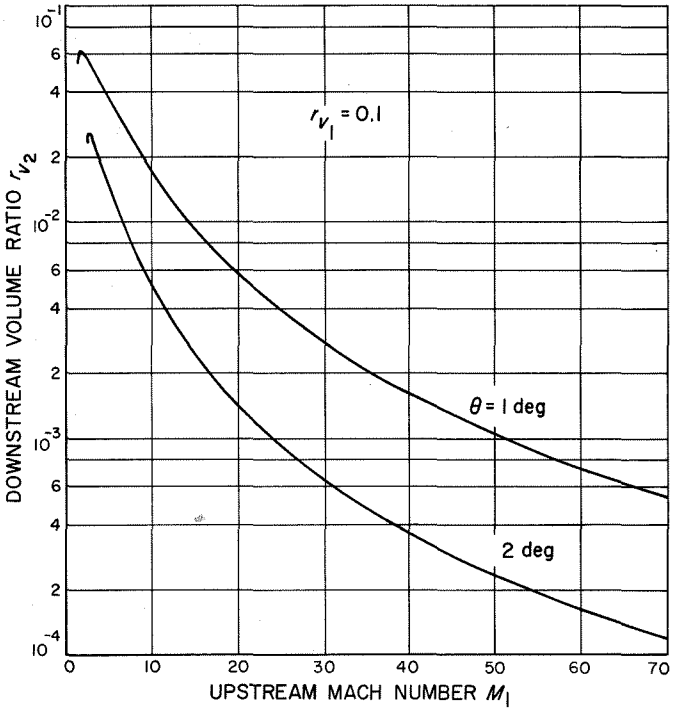

Fig. V-42. Oblique shock downstream volume ratio as a function of Mach number for values of deflection angle ($r_{v_1} = 0.1$)

4. Ratio of Volume Ratio (r_{v_2}/r_{v_1})

The ratio of the volume ratios shown in Eq. (V-20) is the reciprocal of the pressure ratio and the downstream volume ratio (r_{v_2}), and follows directly as a reciprocal function of pressure ratio (P_2/P_1). In the same manner as subsection 3, the volume ratio r_{v_2} is plotted in Figures V-42 through V-52 as a function of Mach number M_1 for values of deflection angle θ on individual graphs of fixed upstream volume ratio (r_{v_1}).

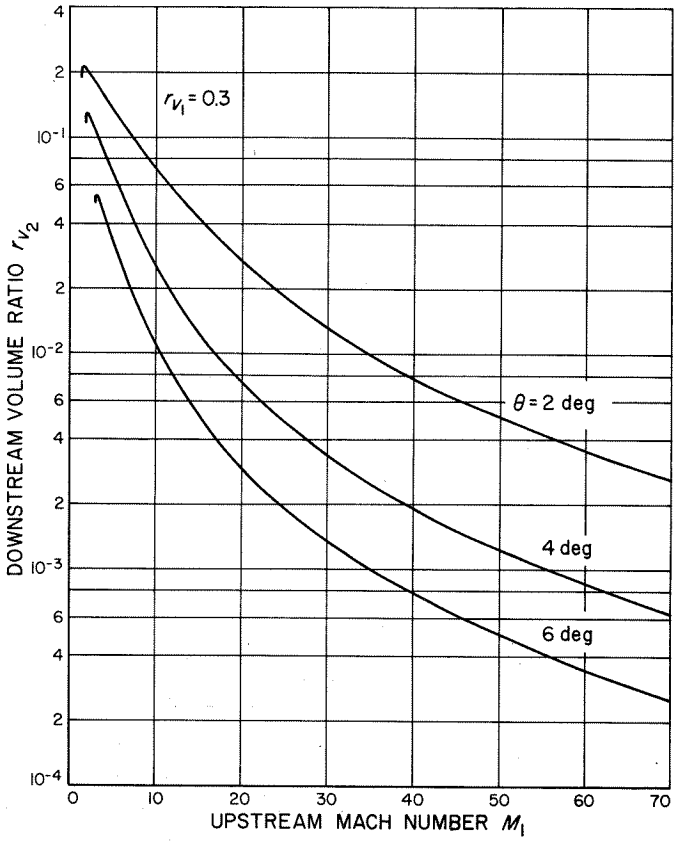

Fig. V-43. Oblique shock downstream volume ratio as a function of Mach number for values of deflection angle ($r_{v_1} = 0.3$)

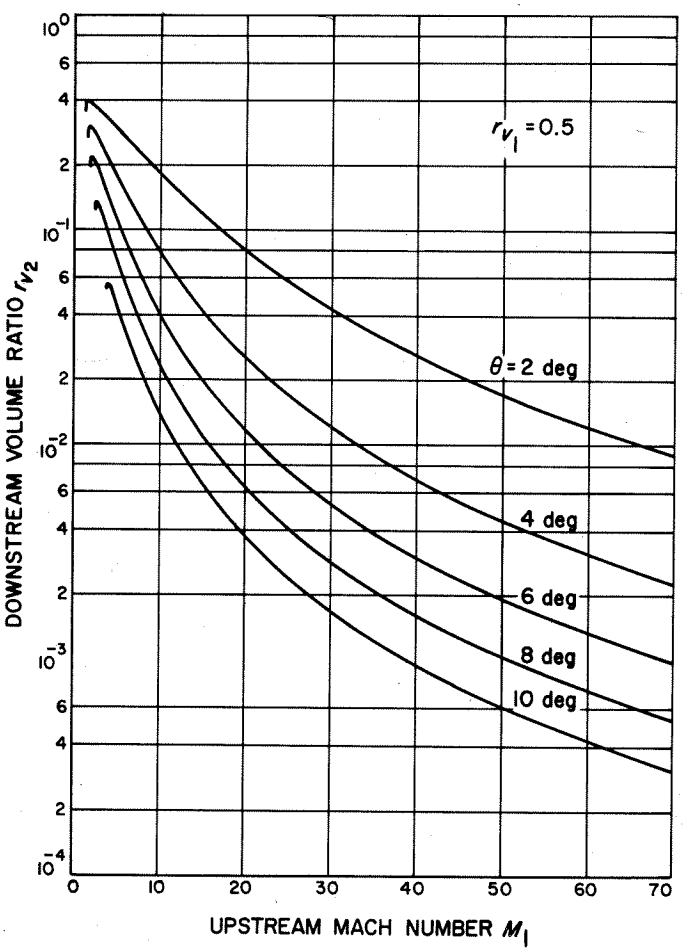

Fig. V-44. Oblique shock downstream volume ratio as a function of Mach number for values of deflection angle ($r_{v_1} = 0.5$)

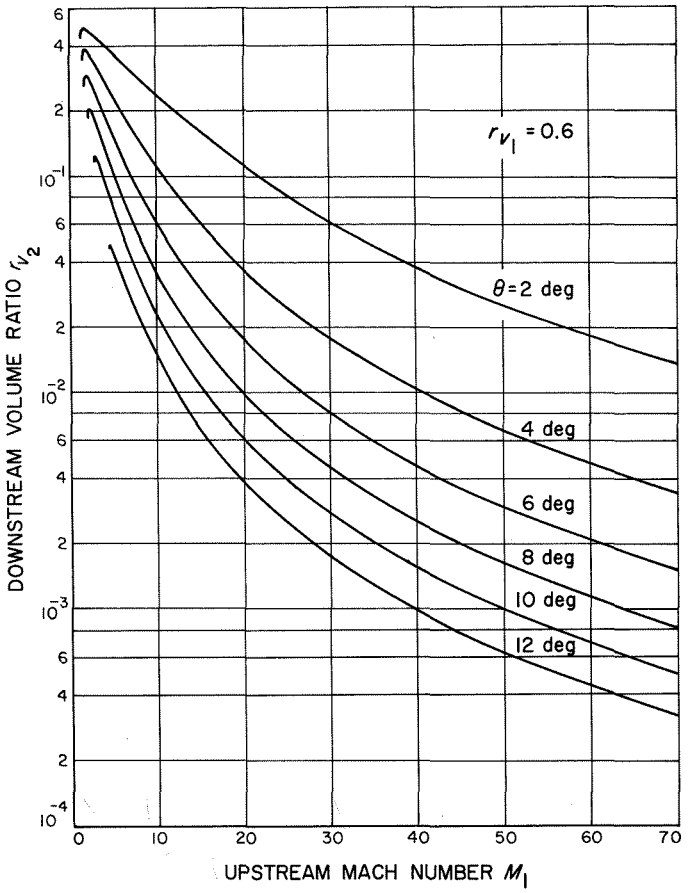

Fig. V-45. Oblique shock downstream volume ratio as a function of Mach number for values of deflection angle ($r_{v_1} = 0.6$)

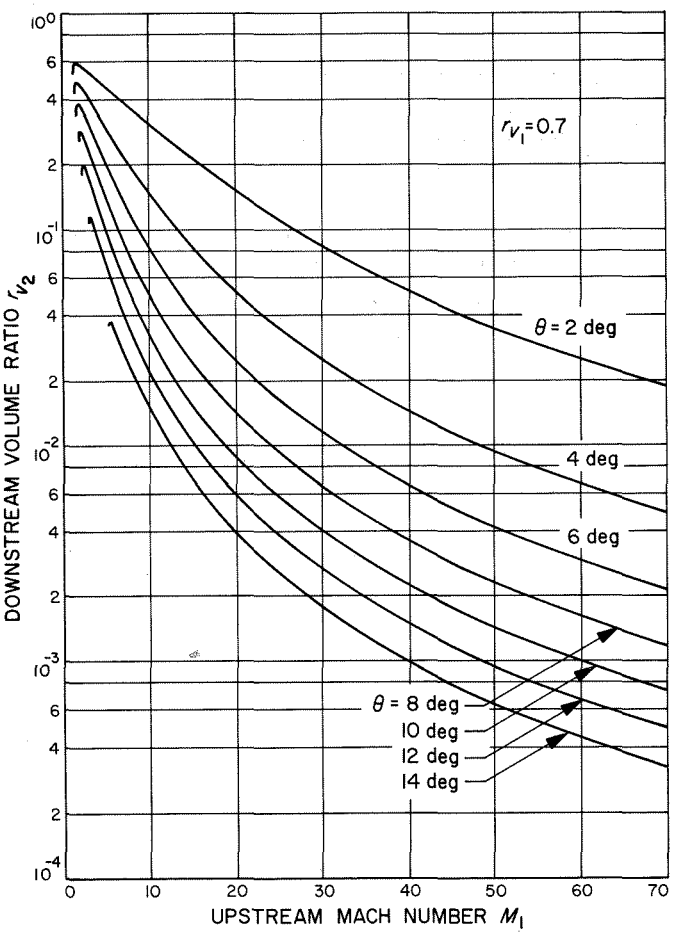

Fig. V-46. Oblique shock downstream volume ratio as a function of Mach number for values of deflection angle ($r_{v_1} = 0.7$)

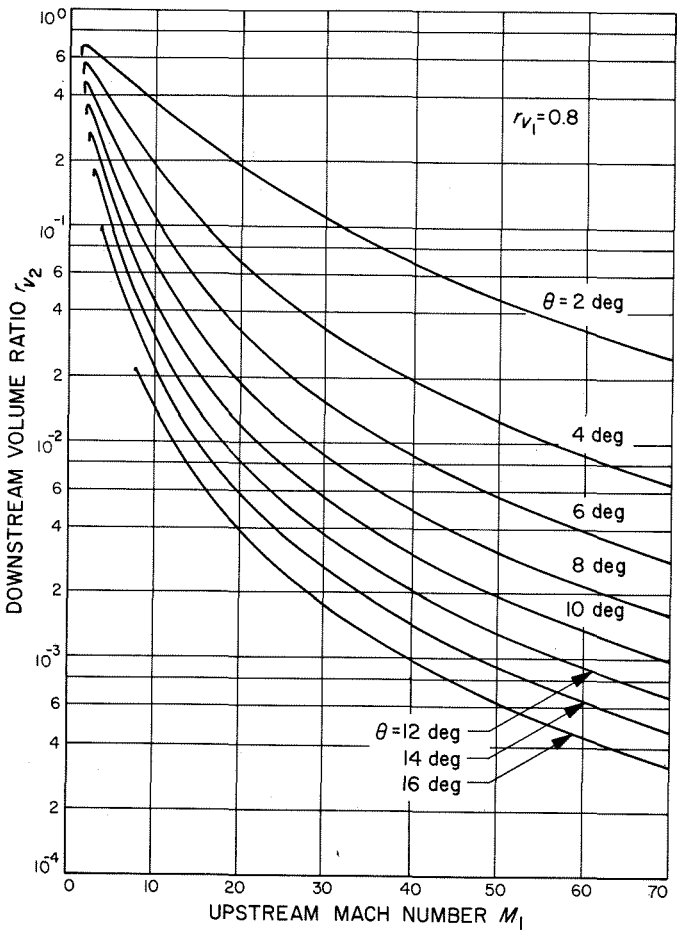

Fig. V-47. Oblique shock downstream volume ratio as a function of Mach number for values of deflection angle ($r_{v_1} = 0.8$)

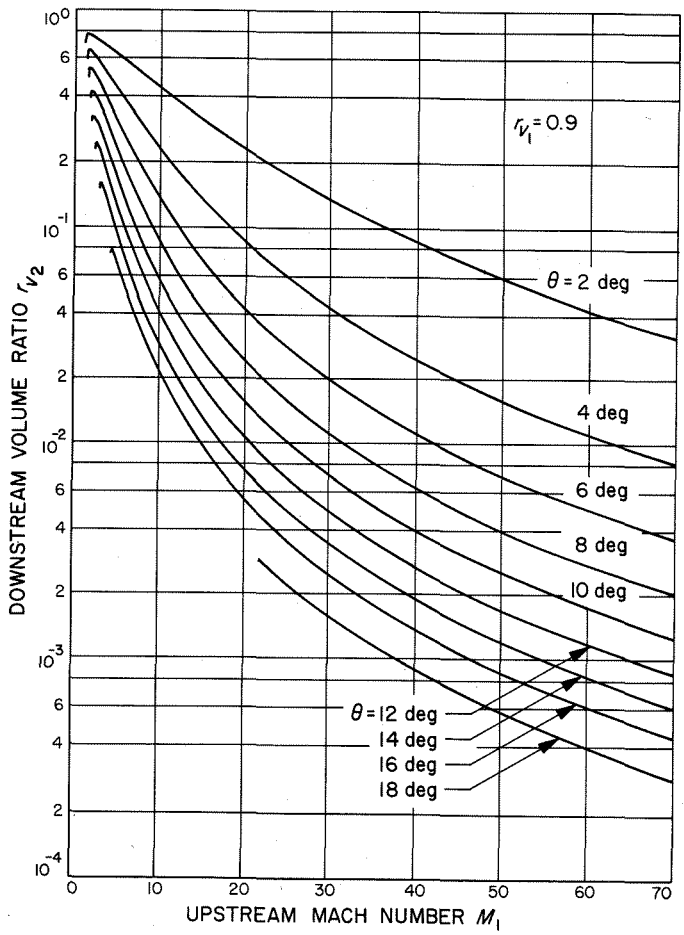

Fig. V-48. Oblique shock downstream volume ratio as a function of Mach number for values of deflection angle ($r_{v_1} = 0.9$)

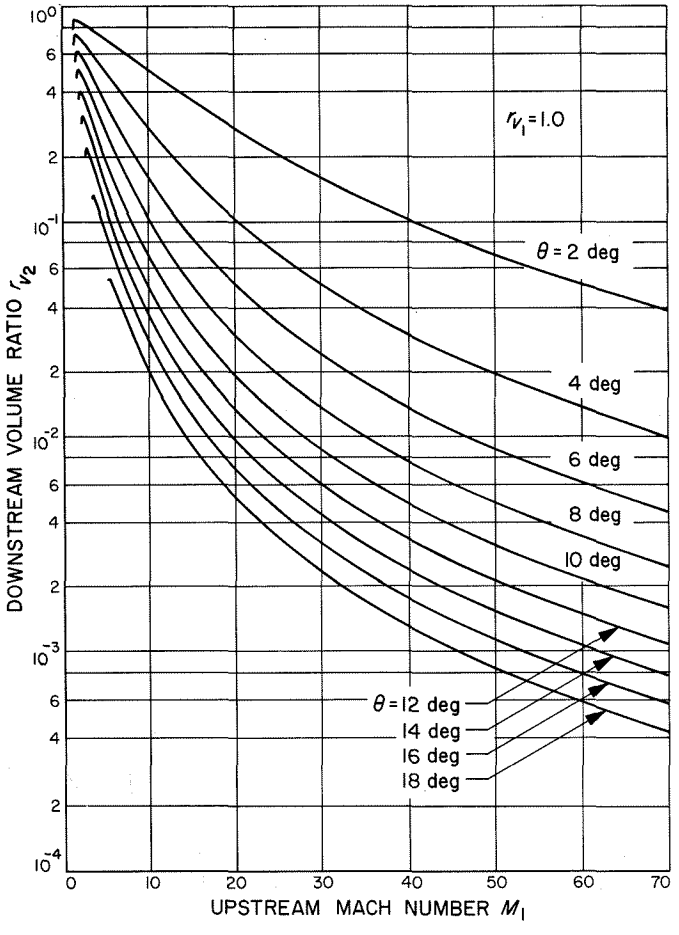

Fig. V-49. Oblique shock downstream volume ratio as a function of Mach number for values of deflection angle ($r_{v_1} = 1.0$)

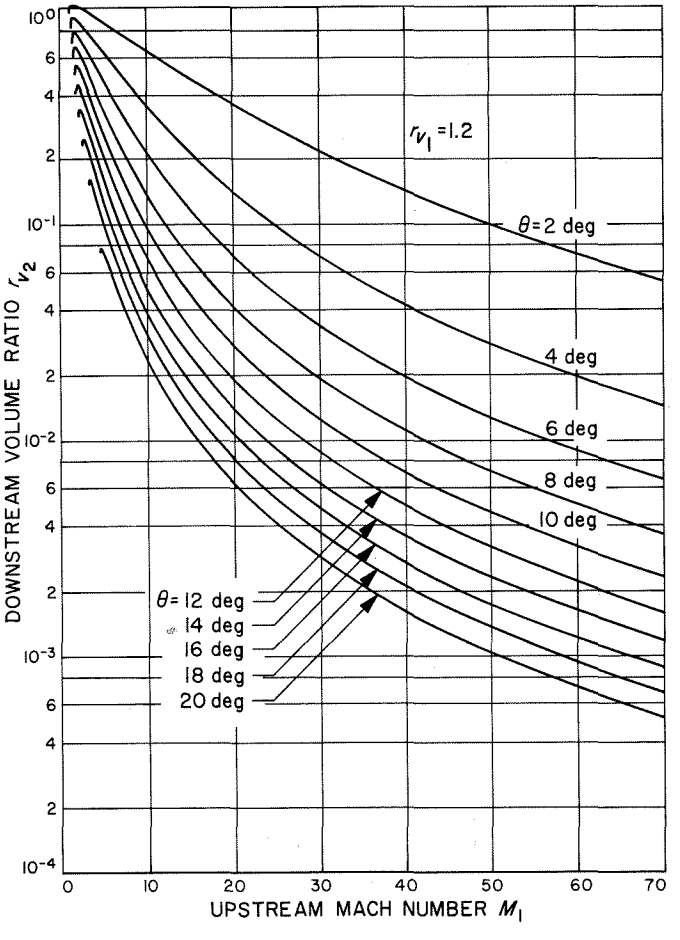

Fig. V-50. Oblique shock downstream volume ratio as a function of Mach number for values of deflection angle ($r_{v_1} = 1.2$)

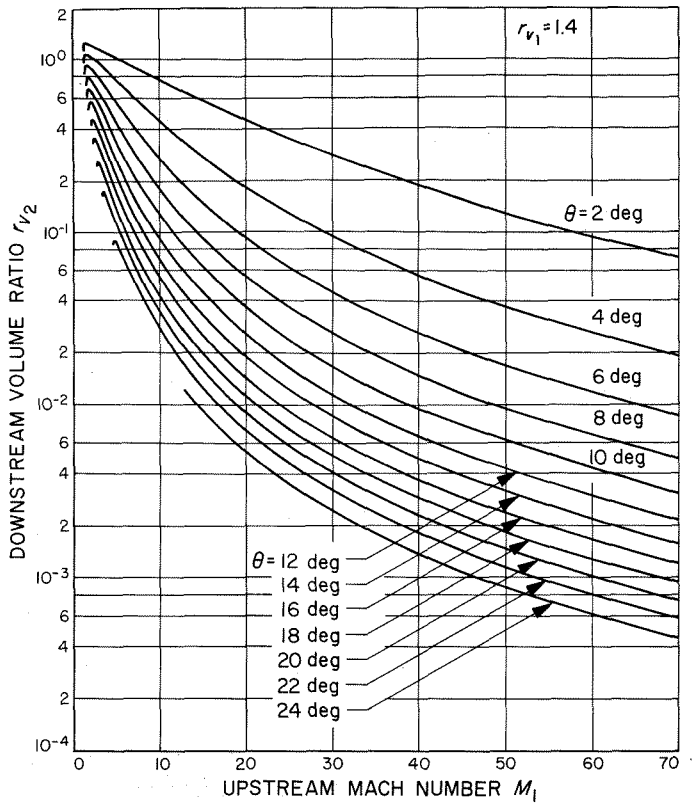

Fig. V-51. Oblique shock downstream volume ratio as a function of Mach number for values of deflection angle ($r_{v_1} = 1.4$)

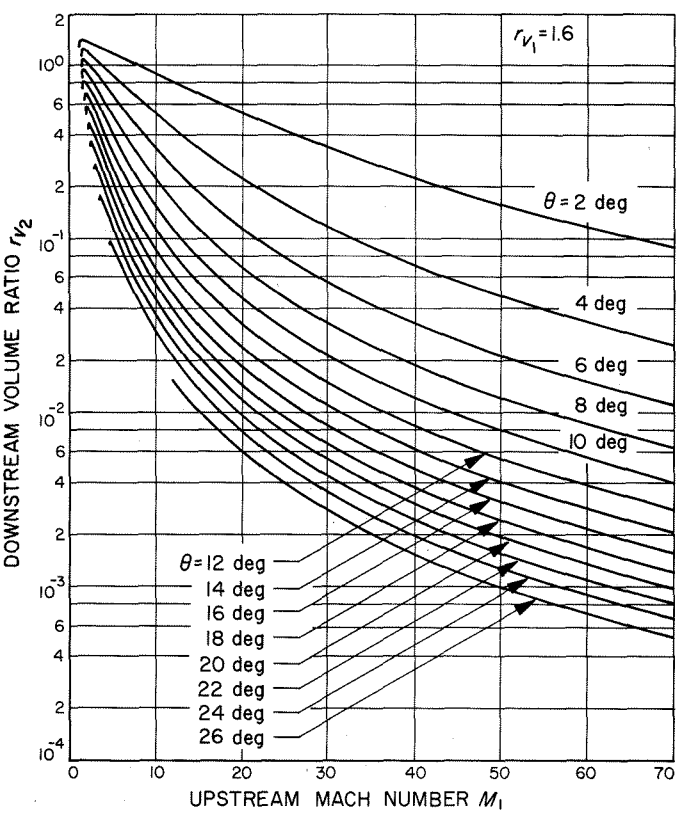

Fig. V-52. Oblique shock downstream volume ratio as a function of Mach number for values of deflection angle ($r_{v_1} = 1.6$)

5. Downstream Mach Number

The downstream Mach number (M_2) in Eq. (V-24) is a function of the four variables M_1, r_{v_1}, β, θ, which have the relationship given in Eq. (V-16). By constraining the four variables through Eq. (V-16), the values of downstream Mach number can be determined from Eq. (V-22). Plots of M_2 as a function of M_1 for values of θ are represented in Figs. V-53 through V-63, each of which represent a fixed value of volume ratio r_{v_1} for the range $0.1 \leq r_{v_1} \leq 1.6$ in increments of 0.2 r_v.

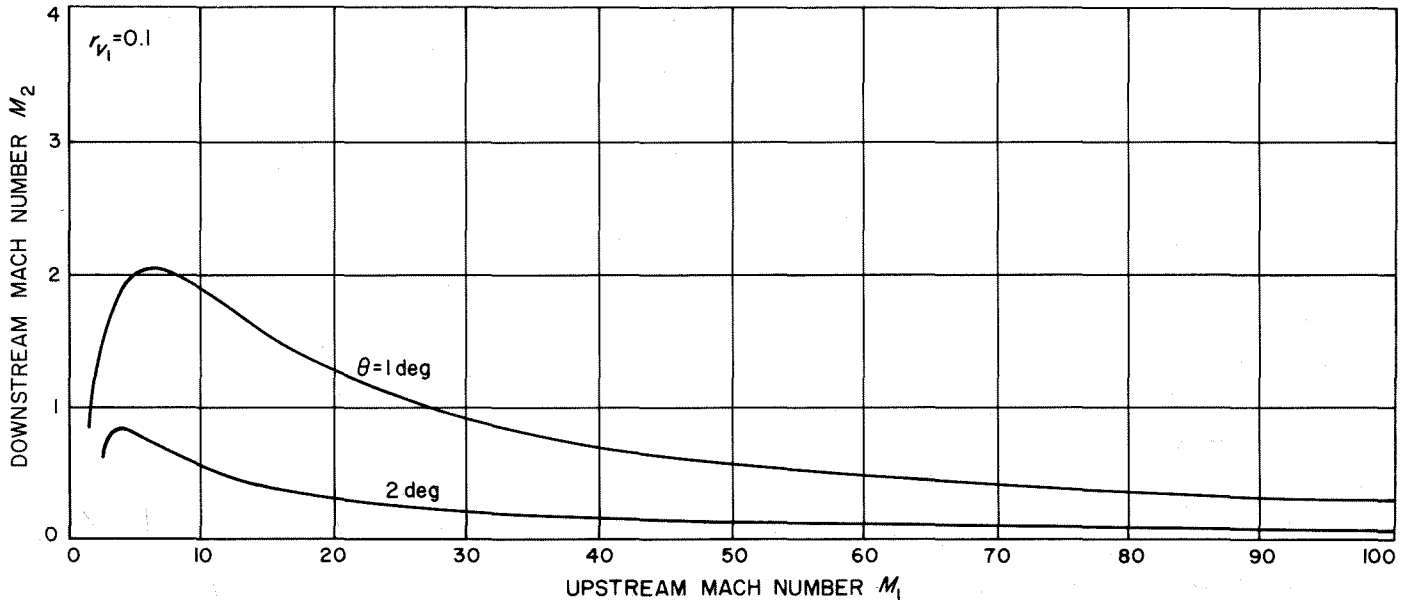

Fig. V-53. Oblique shock downstream Mach number as a function of the upstream Mach number for values of deflection angle ($r_{v_1} = 0.1$)

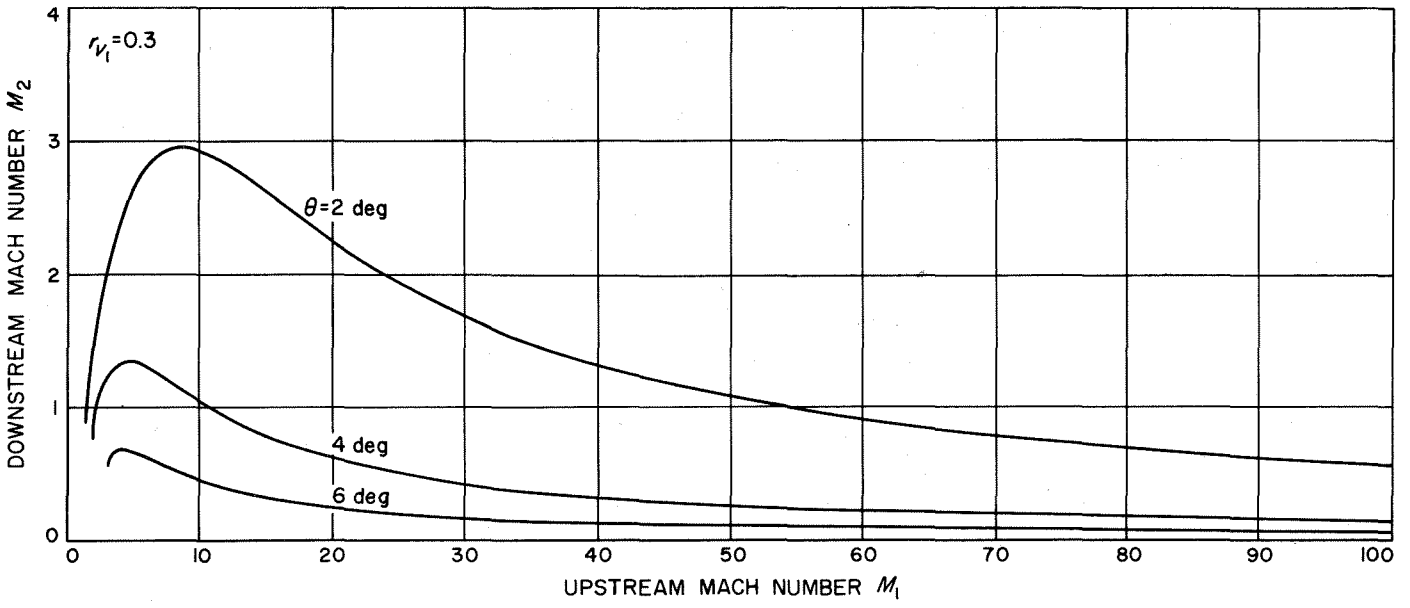

Fig. V-54. Oblique shock downstream Mach number as a function of the upstream Mach number for values of deflection angle ($r_{v_1} = 0.3$)

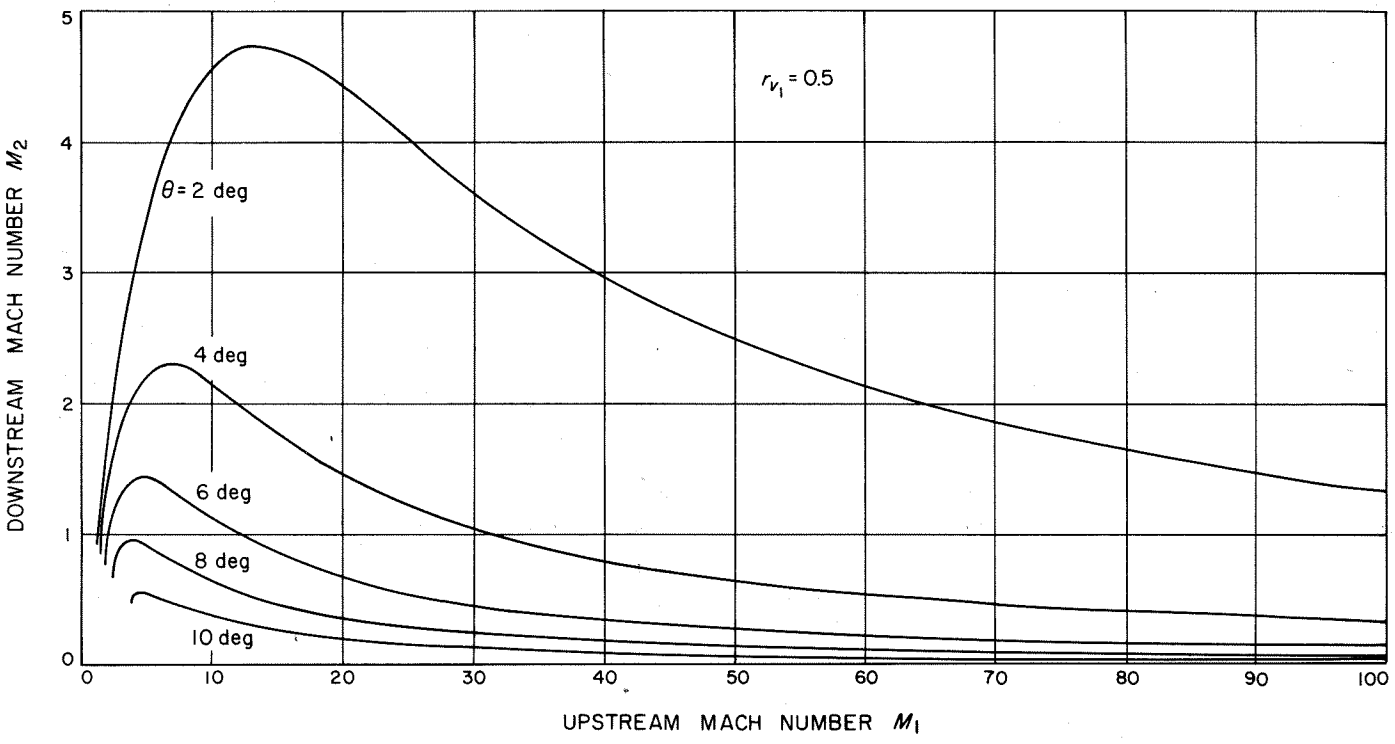

Fig. V-55. Oblique shock downstream Mach number as a function of the upstream Mach number for values of deflection angle ($r_{v_1} = 0.5$)

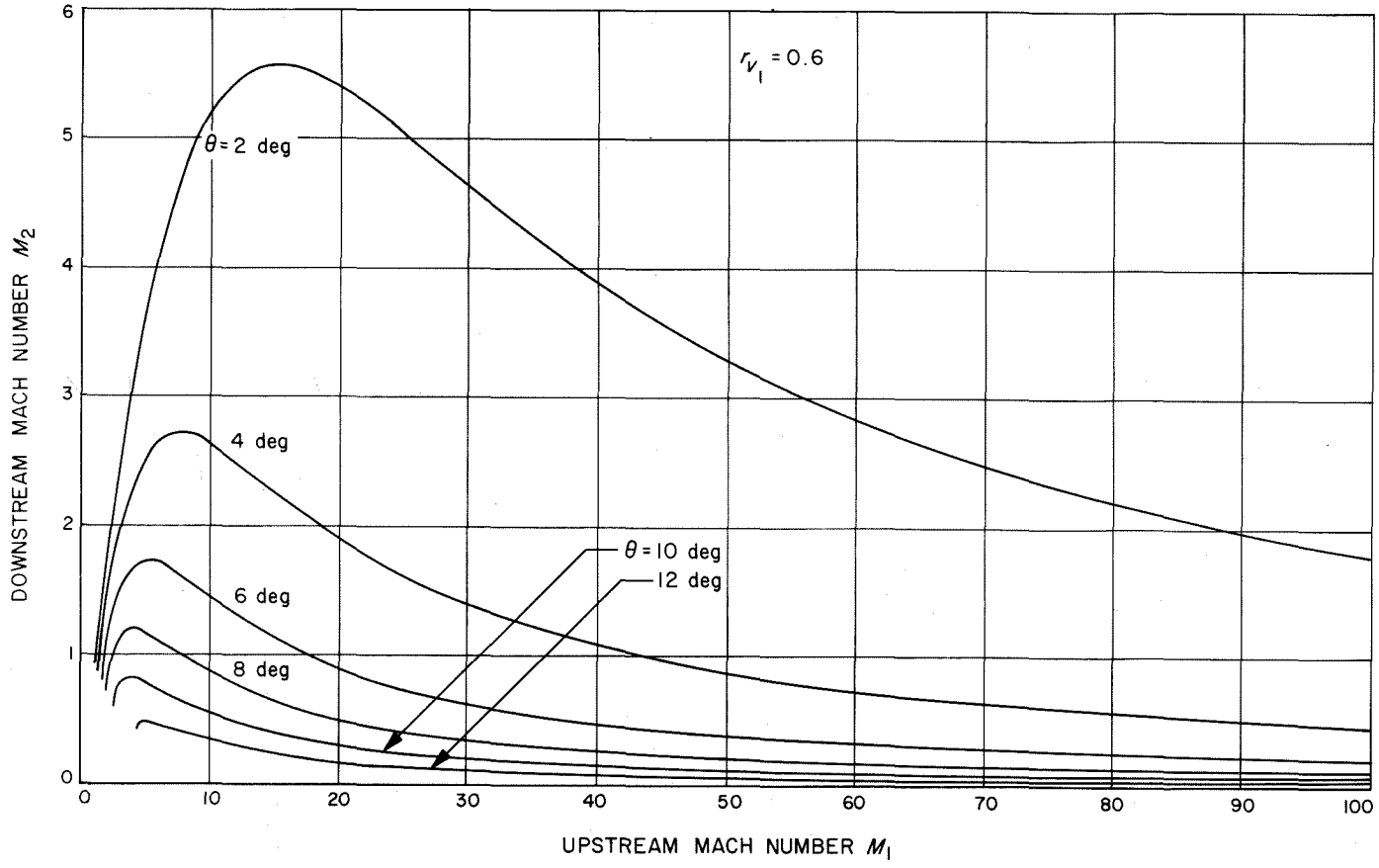

Fig. V-56. Oblique shock downstream Mach number as a function of the upstream Mach number for values of deflection angle ($r_{v_1} = 0.6$)

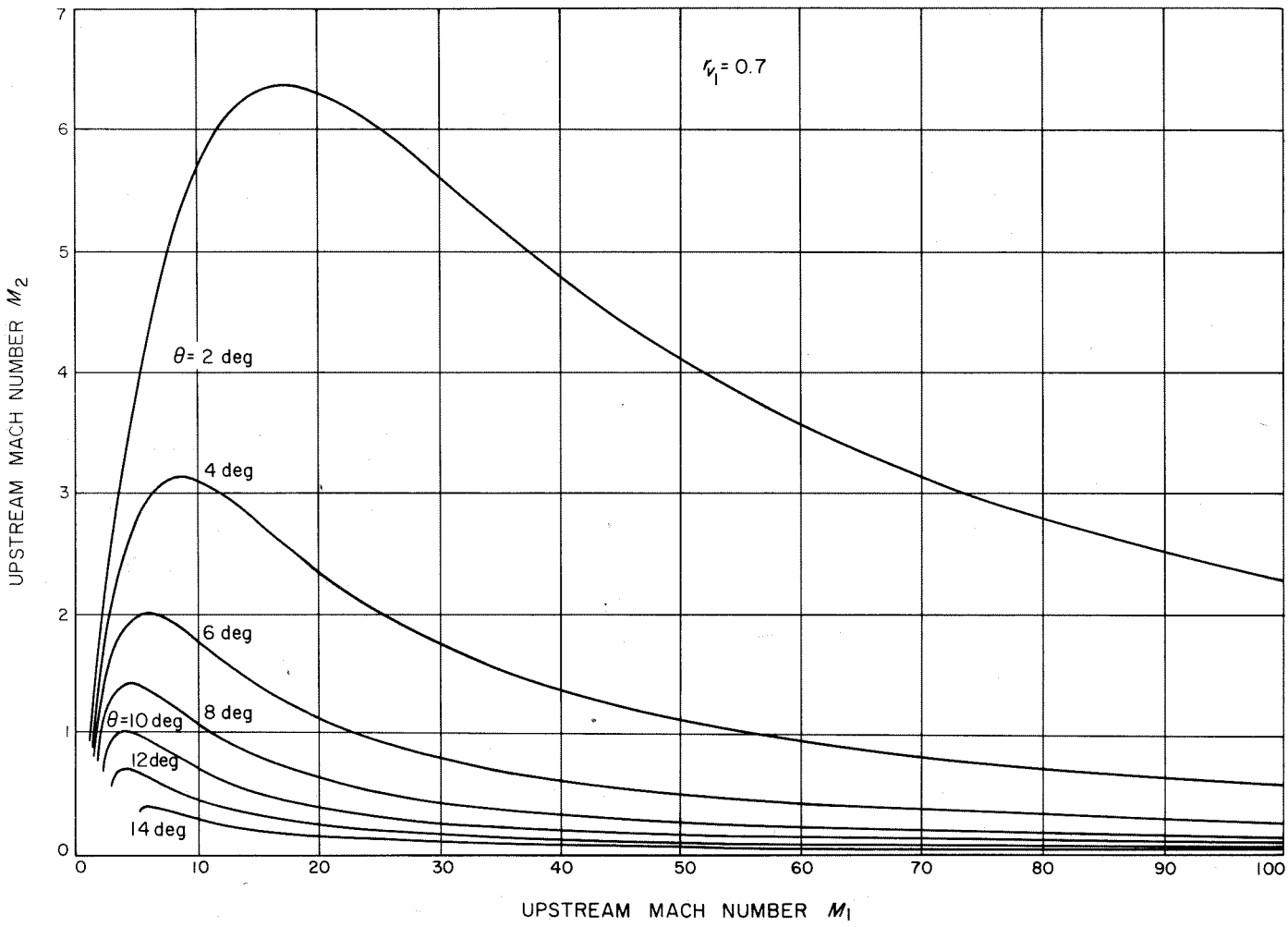

Fig. V-57. Oblique shock downstream Mach number as a function of the upstream Mach number for values of deflection angle ($r_{v_1} = 0.7$)

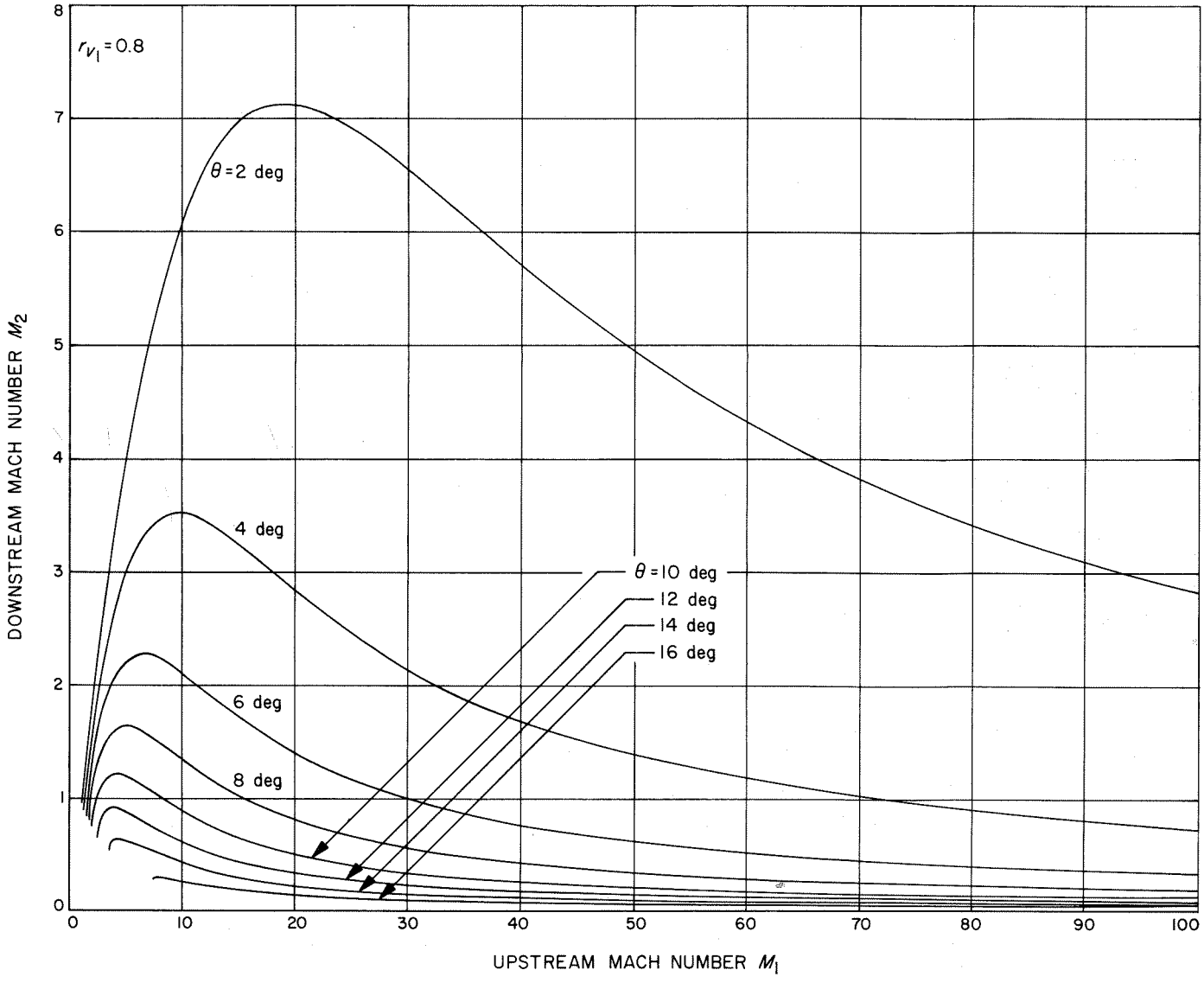

Fig. V-58. Oblique shock downstream Mach number as a function of the upstream Mach number for values of deflection angle ($r_{v_1} = 0.8$)

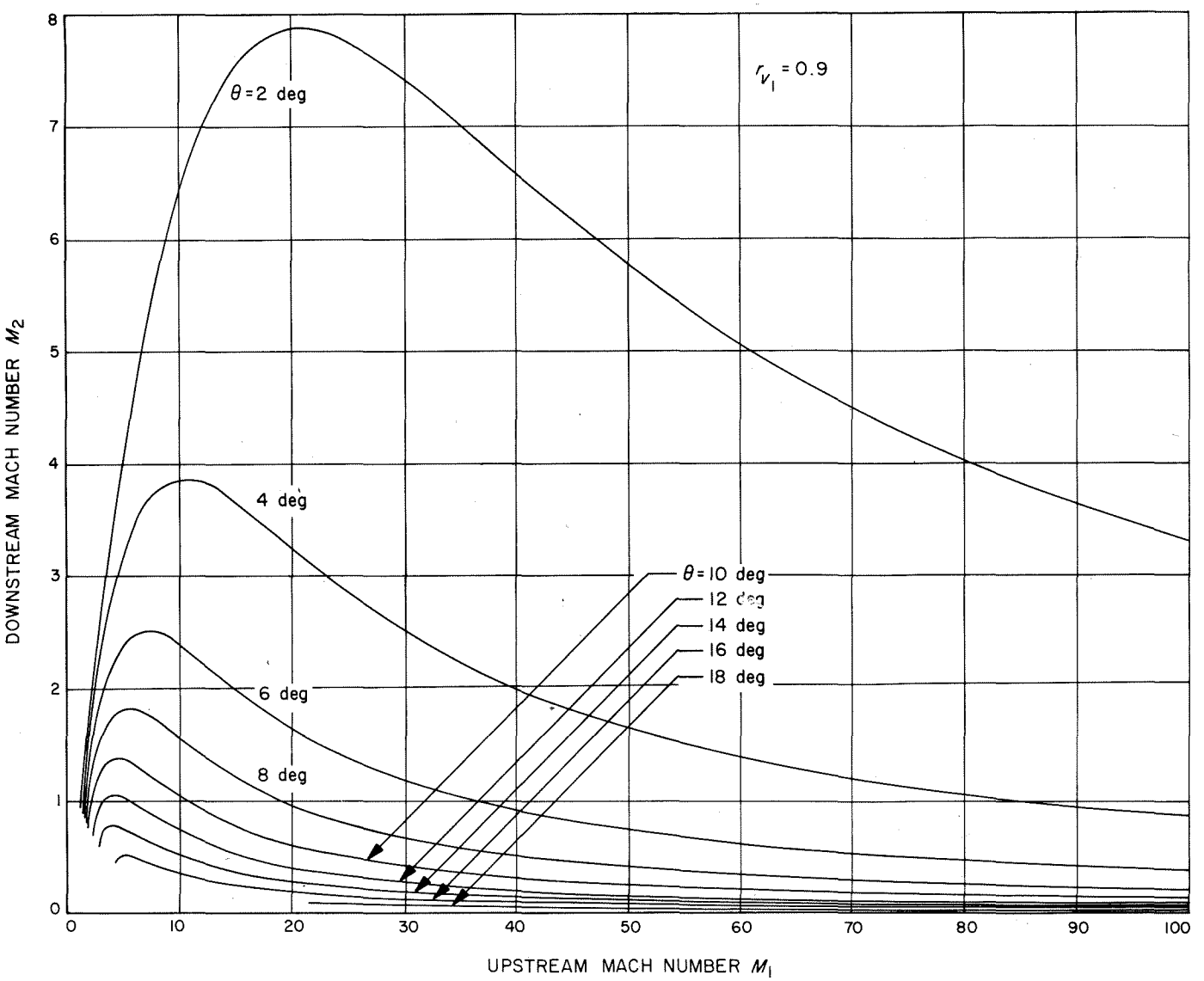

Fig. V-59. Oblique shock downstream Mach number as a function of the upstream Mach number for values of deflection angle ($r_{v_1} = 0.9$)

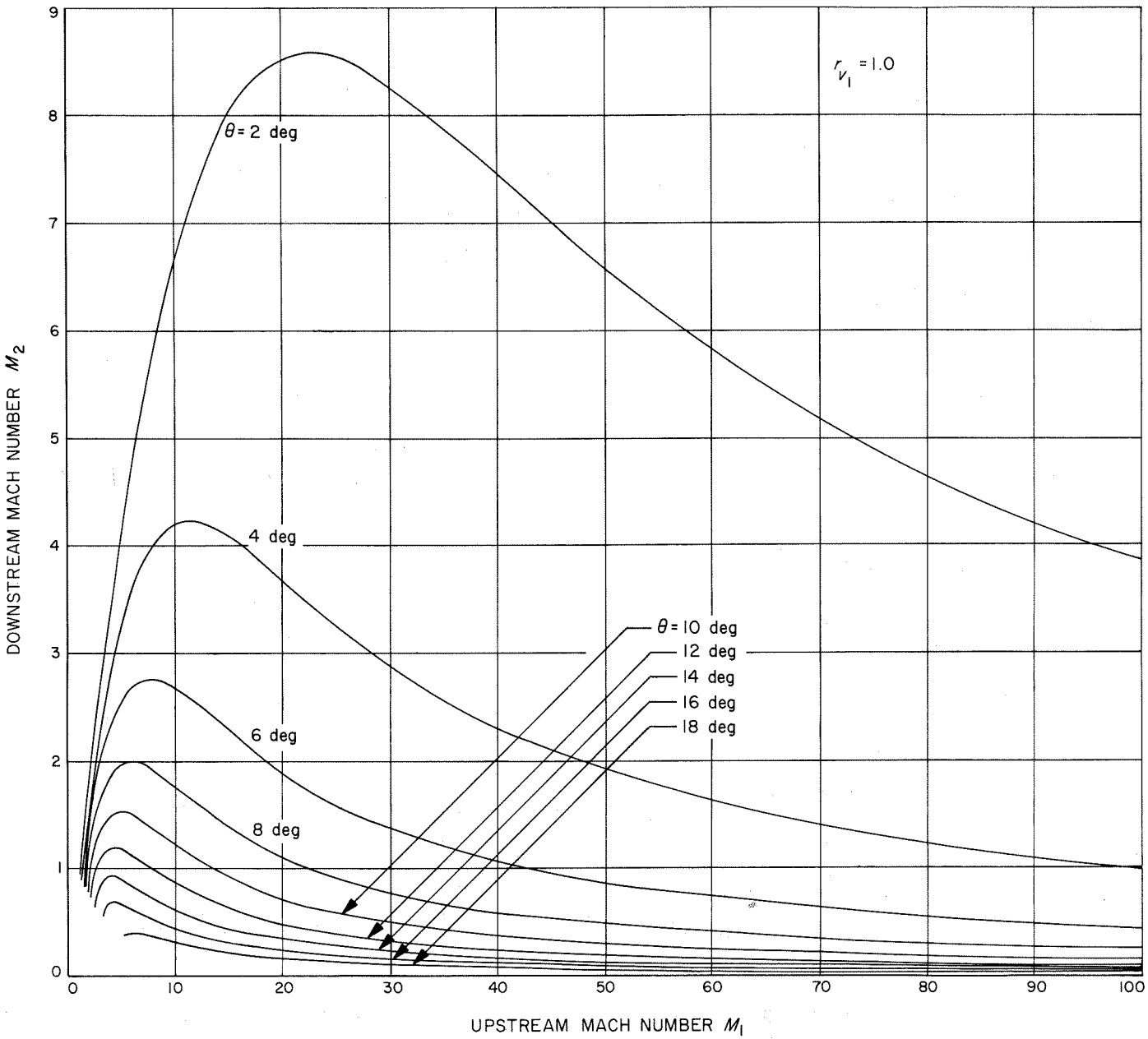

Fig. V-60. Oblique shock downstream Mach number as a function of the upstream Mach number for values of deflection angle ($r_{v_1} = 1.0$)

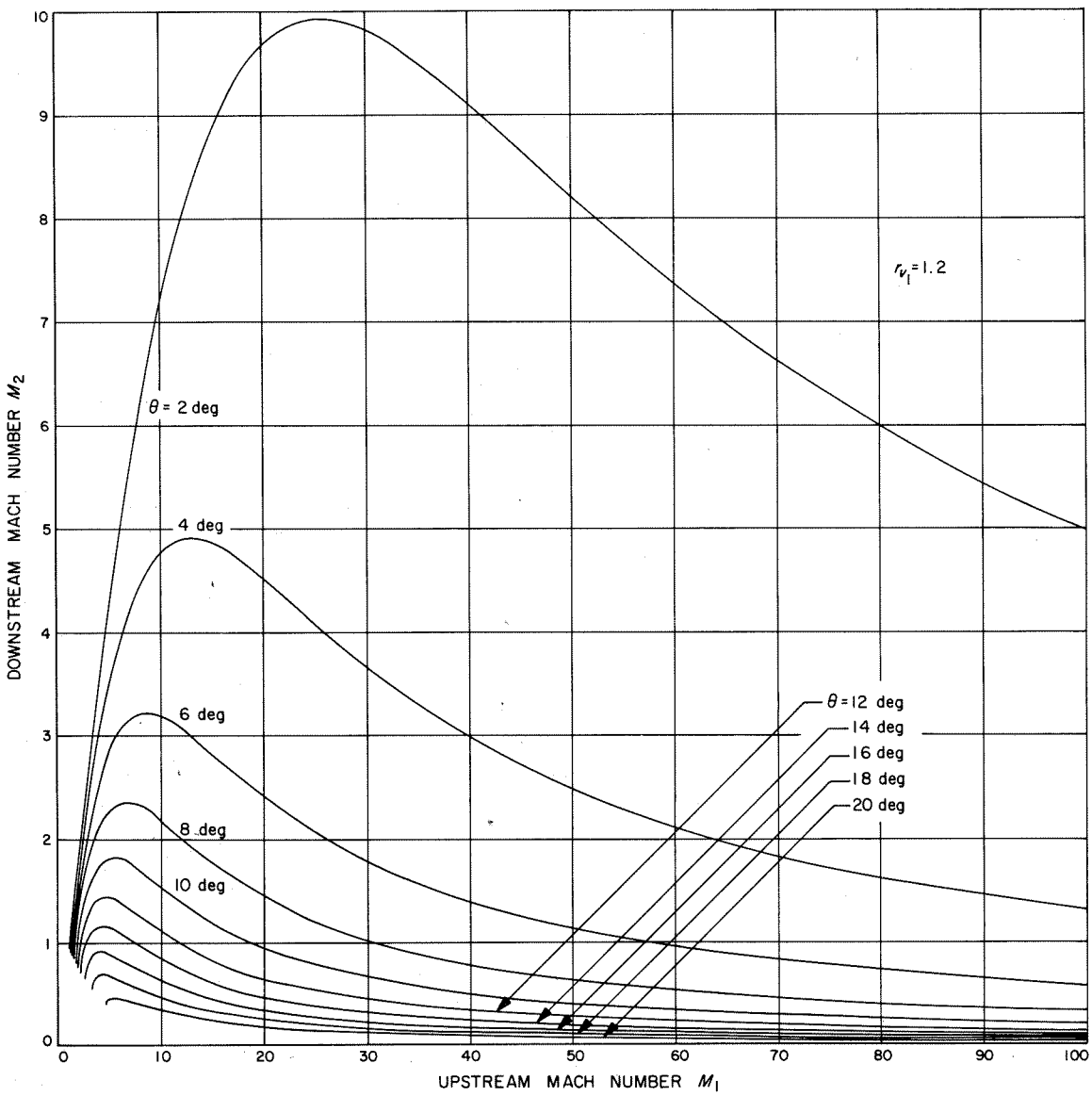

Fig. V-61. Oblique shock downstream Mach number as a function of the upstream Mach number for values of deflection angle ($r_{v_1} = 1.2$)

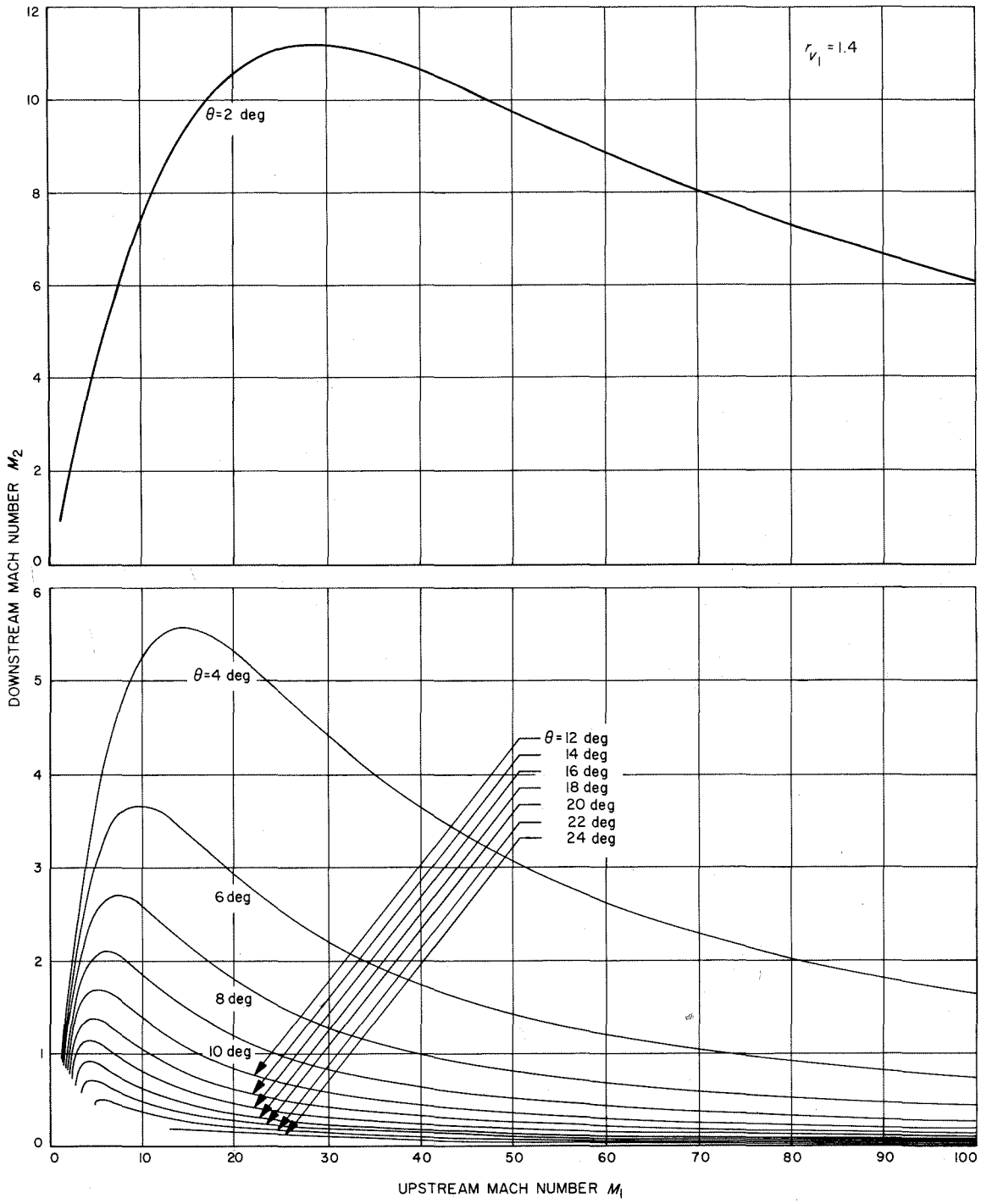

Fig. V-62. Oblique shock downstream Mach number as a function of the upstream Mach number for values of deflection angle ($r_{v_1} = 1.4$)

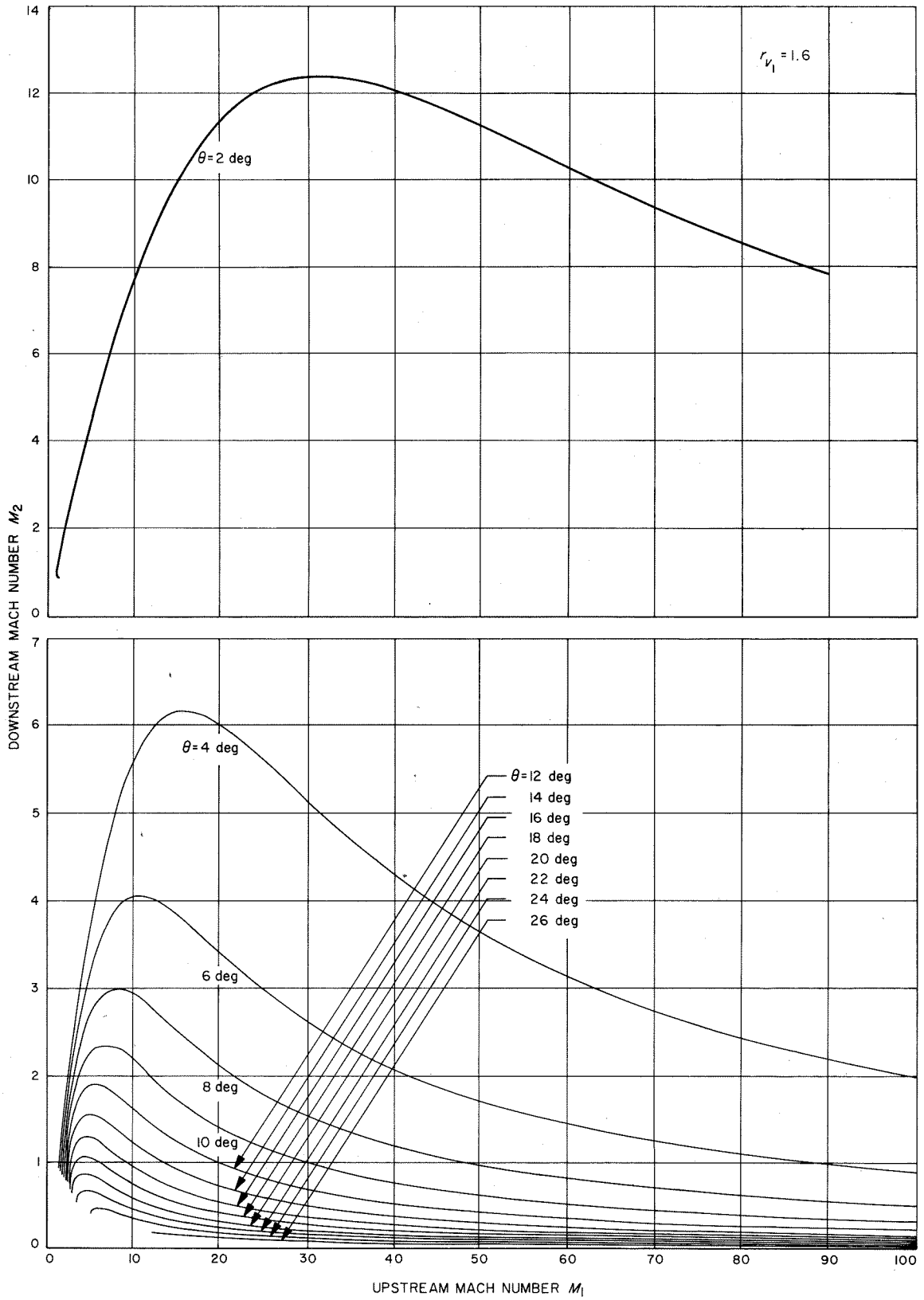

Fig. V-63. Oblique shock downstream Mach number as a function of the upstream Mach number for values of deflection angle ($r_{v_1} = 1.6$)

B. Results of Supersonic Two-Phase Flow at Various Deflection Angles

The model support described in Subsection II-B supported double wedges of varying deflection angles at the center line of the test section for the creation of oblique shock phenomena. The wedges extended to within 0.001 in. of the transparent side walls and were restrained from lateral vibration by a rubber insert that was preloaded by compression against the side wall. Examples of 10° deflection and 20° deflection wedges are shown in Figs. V-64 and V-65, respectively. The relatively high

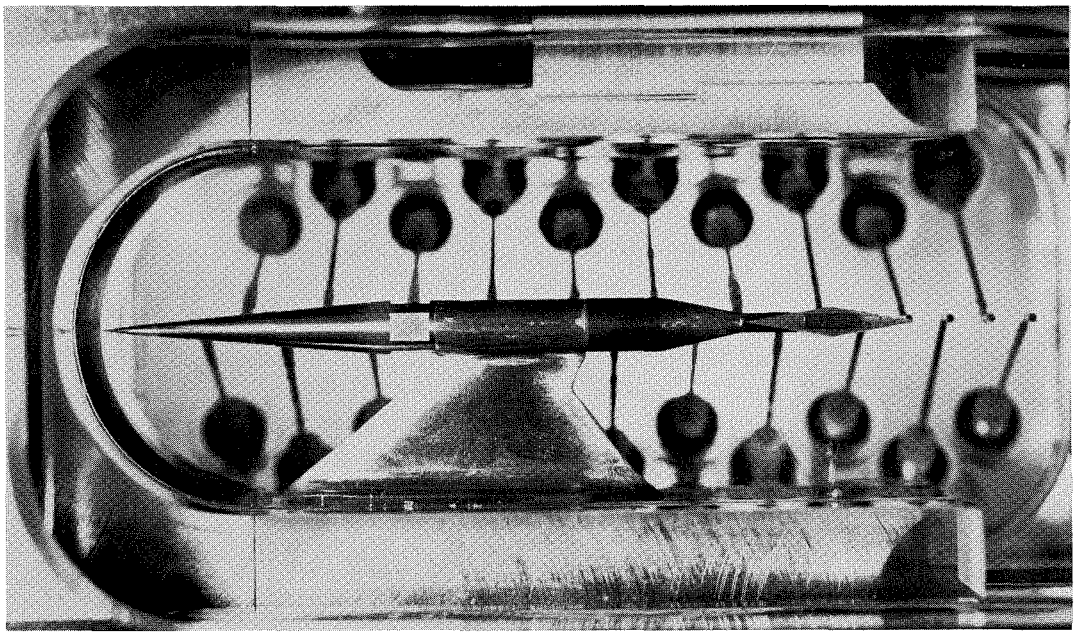

Fig. V-64. The 10° deflection double wedge mounted in tunnel test section

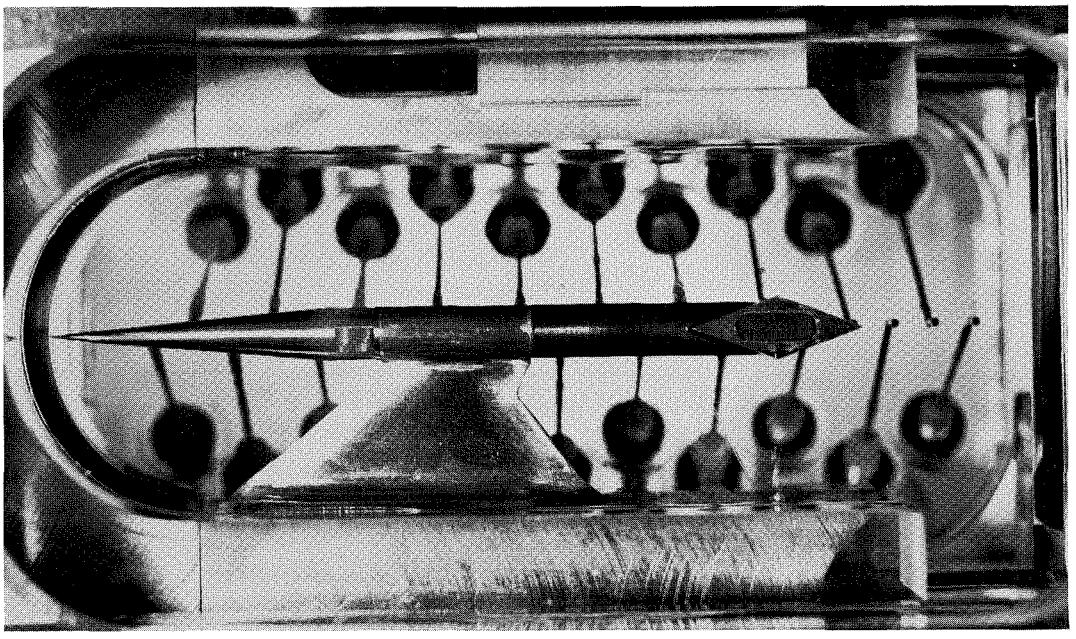

Fig. V-65. The 20° deflection double wedge mounted in tunnel test section

pressure loadings on any internal surface not parallel to the flow made symmetrical test shapes the most desirable.

The model width for the wedges was 0.500 in., which, when placed symmetrically within the tunnel, allowed the removal of a maximum boundary layer depth of 0.127 in. on each side. According to Fig. III-12, the side wall velocity at this boundary layer depth should be within 2% of the core velocity. The 0.001 in. space between the edge of the wedges and the transparent wall proved sufficient for the establishment of a nonattached shock and/or boundary layer flow about the leading edge of the rubber bumper. This flow is apparent in most pictures of the wedge flows, but, fortunately, lies sufficiently behind the leading edge of the wedge to permit measurement of angle and pressure in the initial oblique shock phenomena.

Static pressure measurements behind the oblique shocks were taken from a static tap probe operated by the main probe assembly, and the aggregate of center line taps between the leading edge and the apex of the wedge. In the regions of lower Mach number (<10), the static taps showed pressures reasonably close to the moveable probe values. For wedges of 10° or less deflection and at Mach numbers greater than about 5, the moveable probe, by reason of its geometry, was not capable of an approach to the surface of the wedge sufficient to permit measurements.

Static taps in the leading wedge surfaces would have been more desirable, but such an installation was too complex for this phase of the project. The instrumentation used, however, did provide pressure information at the lower Mach number ranges sufficient to confirm the validity of the isothermal oblique shock-pressure relationships.

As stated in Section II, flow in the tunnel can reach a Mach number of 5 at atmospheric pressure, but, with a reduction in pressure as given in Eq. (V-6), the Mach number can reach exceedingly high values. Reduction in pressure is accomplished by reducing the gas flow through the tunnel and the fixed r_v injector. The limit of reduction is the vapor pressure of the water, which corresponds approximately to Mach 100 at the full liquid velocity of 335 ft/sec. At Mach numbers exceeding 10, cavitation began to damage the plexiglass side walls, preventing use of the tunnel at relatively low water vapor pressures over a long period of time. The highest test Mach numbers, then were limited to about 18+.

Because the leading portions of the test wedges occupy a zone in which the relaxation processes are not complete, some curvature of the oblique shock waves is evident in the various test series that are described below. Therefore, measurements of the shock-wave angles were made, in most cases, parallel to the most representative portion of the wave, and in consideration of the intersection of the wave with the wedge centerline, and its nearness to the leading edge of the wedge. Motion picture sequences were examined in depth to determine the most representative portion of the shock wave under the various flow conditions. In all cases, complete sets of measurements for a series were used for comparison with theoretical predictions.

1. The 4° Deflection Wedge

The 4° deflection wedge was subjected to input Mach numbers (M_1) ranging from 2.2 to 18.5 at corresponding tunnel volume ratios from 0.76 to 0.96. Because the Mach number is a function of both mixture velocity and pressure, a test series was made with runs at constant pressures and various velocities, and runs at constant velocities and various pressures to determine the behavior of the Mach number through such oblique shock variables as the shock angle (β) and the downstream pressure P_2.

Figure V-66 shows the variation of β as a function of M_1. At 4° deflection, the separation of the 0.7 and 1.0 r_{v_1} curves is smaller than the scatter of the data; thus, no significant confirmation of tunnel r_v can be gained from this figure. From $M_1 = 2.75$ to $M_1 = 18.5$, the resultant data lies generally in the region of the theoretical curves, with the water velocities of $V_{l_1} = 180$ ft/sec and $V_{l_1} = 335$ ft/sec closest to the theoretical. The lower velocity of $V_{l_1} = 147$ ft/sec tended to give higher values of β in the region $2.2 \leq M_1 \leq 2.75$. Some interaction between the wedge shock and the top and bottom tunnel walls was visibly evident at the lower Mach numbers, which suggests that the test section choked near a Mach number of 2.2.

Figure V-67 shows pressure ratio as a function of Mach number. The scatter in the data again is wider than the r_{v_1} band for the tunnel test section. The data is reasonably grouped about the r_{v_1} band, however.

A constant-pressure sequence of increasing Mach numbers on Type 413 infrared Polaroid film is shown in Fig. V-68. Atmospheric pressure was maintained as the water velocity was increased from 140 ft/sec to 335 ft/sec in seven steps for a Mach number range of $2.11 \leq M_1 \leq 5.18$.

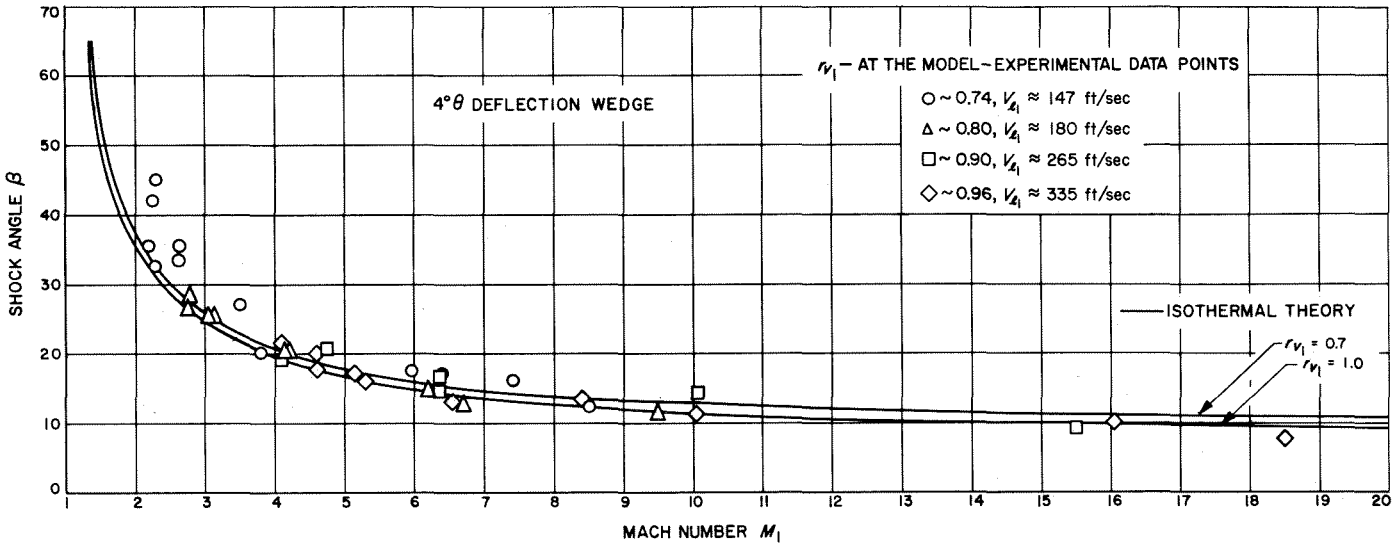

Fig. V-66. Measured values of shock angle as a function of Mach number for a 4° deflection wedge

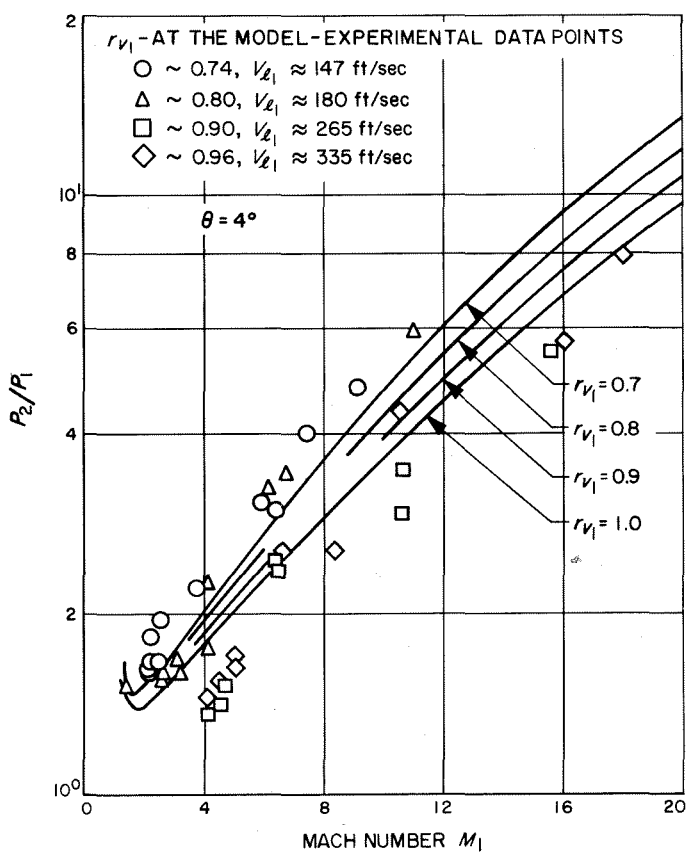

Fig. V-67. Measured values of pressure ratio as a function of Mach number for a 4° deflection wedge

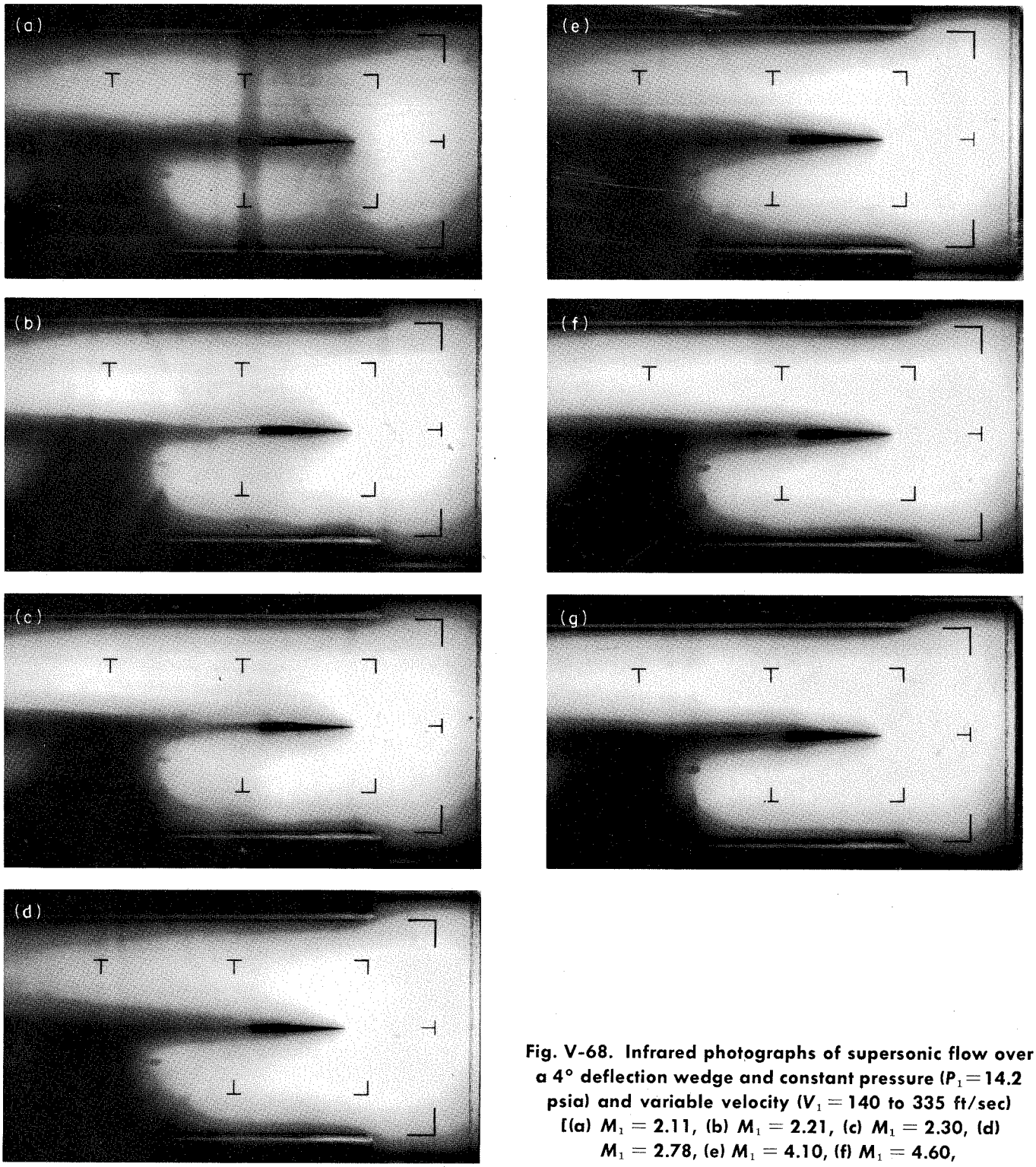

Fig. V-68. Infrared photographs of supersonic flow over a 4° deflection wedge and constant pressure ($P_1 = 14.2$ psia) and variable velocity ($V_1 = 140$ to 335 ft/sec) [(a) $M_1 = 2.11$, (b) $M_1 = 2.21$, (c) $M_1 = 2.30$, (d) $M_1 = 2.78$, (e) $M_1 = 4.10$, (f) $M_1 = 4.60$, (g) $M_1 = 5.18$]

In pictures (a), (b), (d), and (e) of Fig. V-68, back flowing lines that have no relationship to the flow appear behind the wedge tip. They are roller patterns from the Polaroid developing mechanism. The leading edge of the shock phenomena is readily discernible in pictures (b), (c), (d), (e), (f), and (g). The slope of the leading edge oblique shock in pictures (a) and (g), however, must be determined with the help of similar infrared and high-speed (½-μsec) exposures in the same Mach numbers, respectively.

Constant-velocity–variable-pressure sequences were made for four values of liquid velocity ranging from 147 ft/sec to 335 ft/sec. The volume ratio remains a constant value for each sequence, because r_{v_1} in the test section is primarily a function of V_{l_1}. Figure V-69 shows a sequence of increasing Mach numbers for a V_{l_1} of 147 ft/sec, an r_{v_1} of 0.750, a P_1 from 14.2 to 1.30 psia, and an M_1 from 2.25 to 7.40. Roller marks are evident in pictures (a), (b), and (c) of Fig. V-69 and should be ignored. The oblique shock from the leading edge of the wedge is discernible in all pictures of this figure.

Figure V-70 shows an increasing Mach number sequence for a constant V_{l_1} of 181 ft/sec, an r_{v_1} of 0.800, a P_1 from 14.2 to 1.20 psia, and an M_1 from 3.08 to 9.50. Note the oblique shocks leading from the upper and lower boundary layer knives at lower than atmospheric pressures in pictures (c) and (d). This is due in part to the

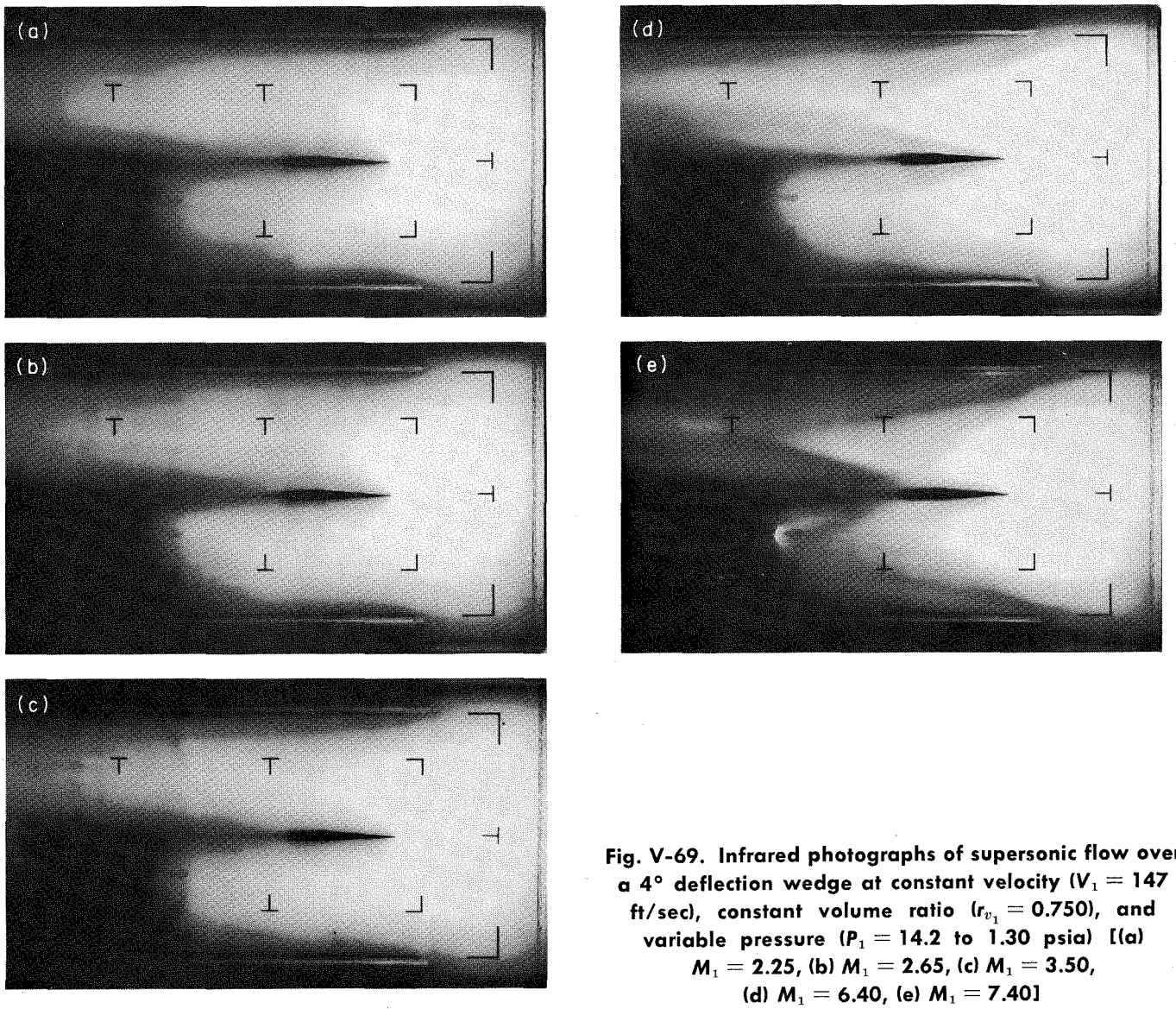

Fig. V-69. Infrared photographs of supersonic flow over a 4° deflection wedge at constant velocity (V_1 = 147 ft/sec), constant volume ratio (r_{v_1} = 0.750), and variable pressure (P_1 = 14.2 to 1.30 psia) [(a) M_1 = 2.25, (b) M_1 = 2.65, (c) M_1 = 3.50, (d) M_1 = 6.40, (e) M_1 = 7.40]

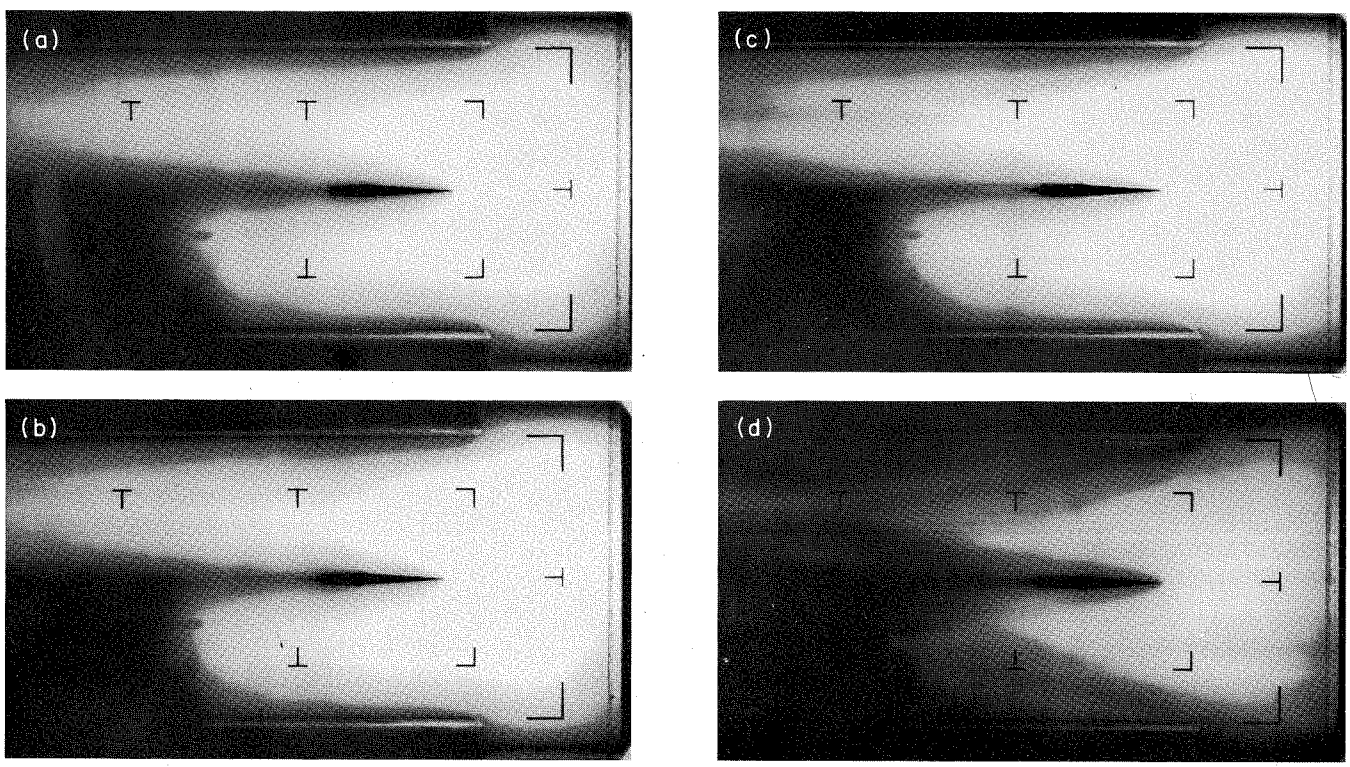

Fig. V-70. Infrared photographs of supersonic flow over a 4° deflection wedge at constant velocity ($V_1 = 181$ ft/sec), constant volume ratio ($r_{v_1} = 0.80$), and variable pressure ($P_1 = 14.2$ to 1.20 psia) [(a) $M_1 = 3.08$, (b) $M_1 = 4.20$, (c) $M_1 = 6.20$, (d) $M_1 = 9.50$]

entry of some gas and liquid between the sidewall and knife into the free stream at pressures below the inner jacket pressure, which is atmospheric.

Figure V-71 shows an increasing Mach number sequence for a constant V_{l_1} of 266 ft/sec, an r_{v_1} of 0.900, and a P_1 of 14.2 to 1.07 psia for a corresponding range of $4.75 \leqq M_1 \leqq 18$. More distinct traces of the shock from the leading edge of the wedge appear with higher velocity, particularly on the lower side of the wedge in pictures (b) and (c).

Figure V-72 shows an increasing Mach number sequence at the highest constant of $V_{l_1} = 335$ ft/sec, an r_{v_1} of 0.963, and a P_1 of 14.2 to 5.39 psia for a corresponding range of M_1 from 5.30 to 10. The shock from the lower leading edge of the wedge continues to appear more strongly along with a barely discernible shock from the leading edge of the rubber bumper that is located in a slot in the wedge between the wall and wedge endface.

Pictures (a) through (c) of Fig. V-73, at ½-μsec exposures, show an increasing Mach number sequence at a constant P_1 of 14.2 psia, and a range of $2.32 \leqq M_1 \leqq 5.17$. Shock phenomena can be readily seen in pictures (a) and (b) of Fig. V-73, but they lie sufficiently close to the wedge in pictures (c), (d), (e) to make necessary an enlargement for analysis.

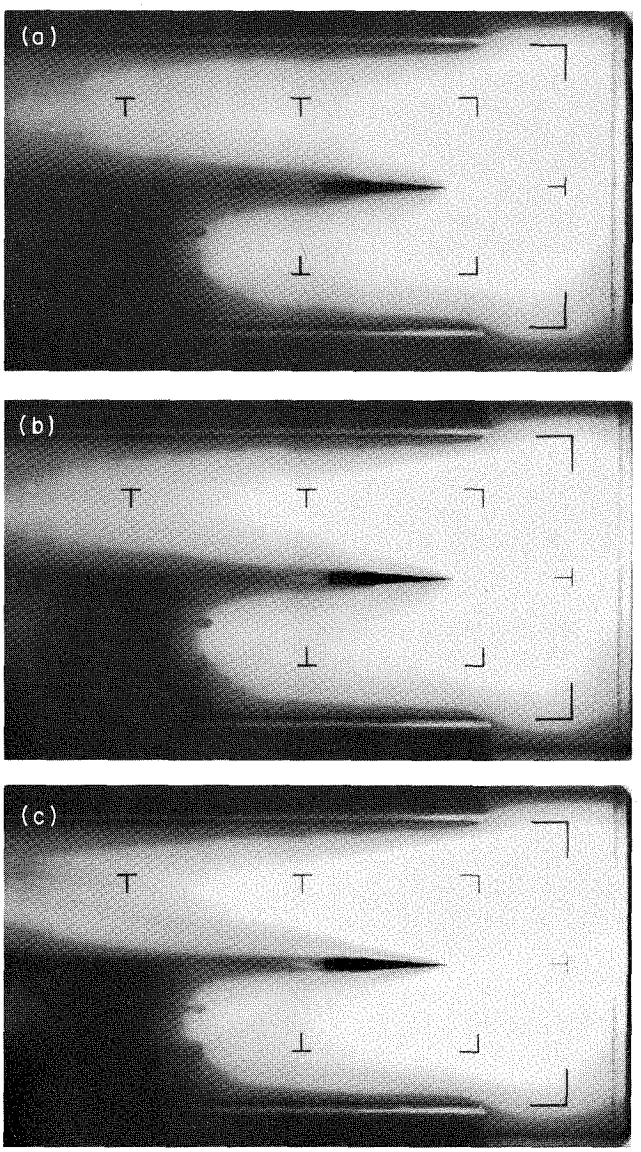

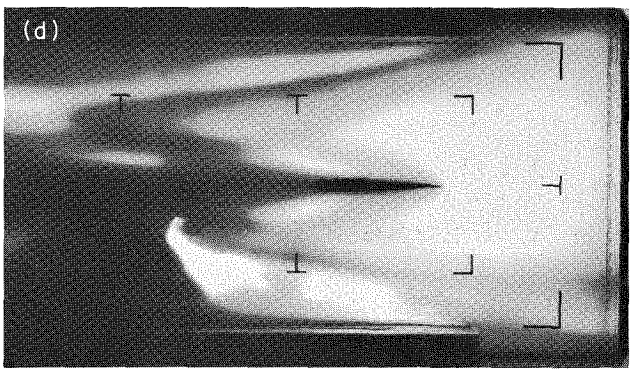

Fig. V-71. Infrared photographs of supersonic flow over a 4° deflection wedge at constant velocity ($V_1 = 266$ ft/sec), constant volume ratio ($r_{v_1} = 0.90$), and variable pressure ($P_1 = 14.2$ to 1.07 psia) [(a) $M_1 = 4.75$, (b) $M_1 = 6.35$, (c) $M_1 = 10.55$, (d) $M_1 = 18+1$

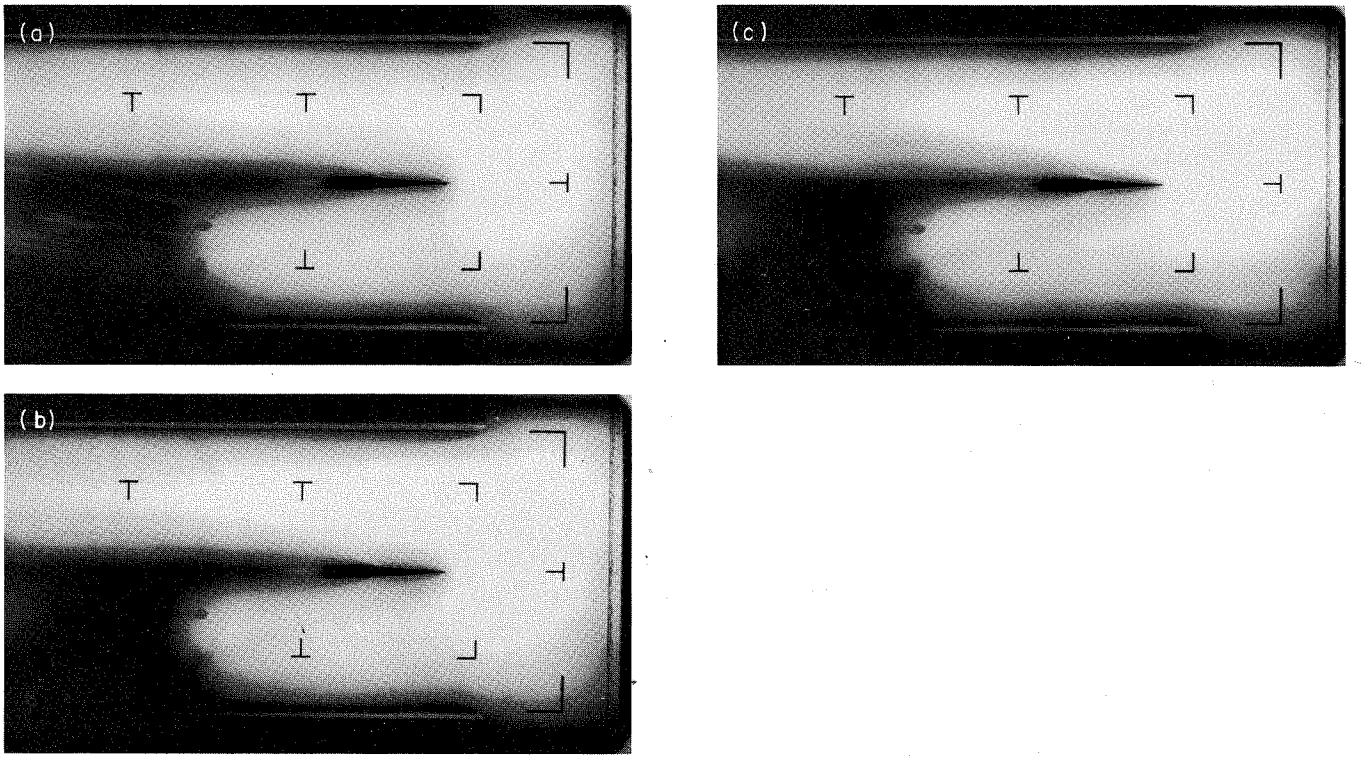

Fig. V-72. Infrared photographs of supersonic flow over a 4° deflection wedge at constant velocity ($V = 335$ ft/sec), constant volume ratio ($r_{v_1} = 0.963$), and variable pressure ($P_1 = 14.2$ to 5.39 psia) [(a) $M_1 = 5.30$, (b) $M_1 = 8.40$, (c) $M_1 = 10+$]

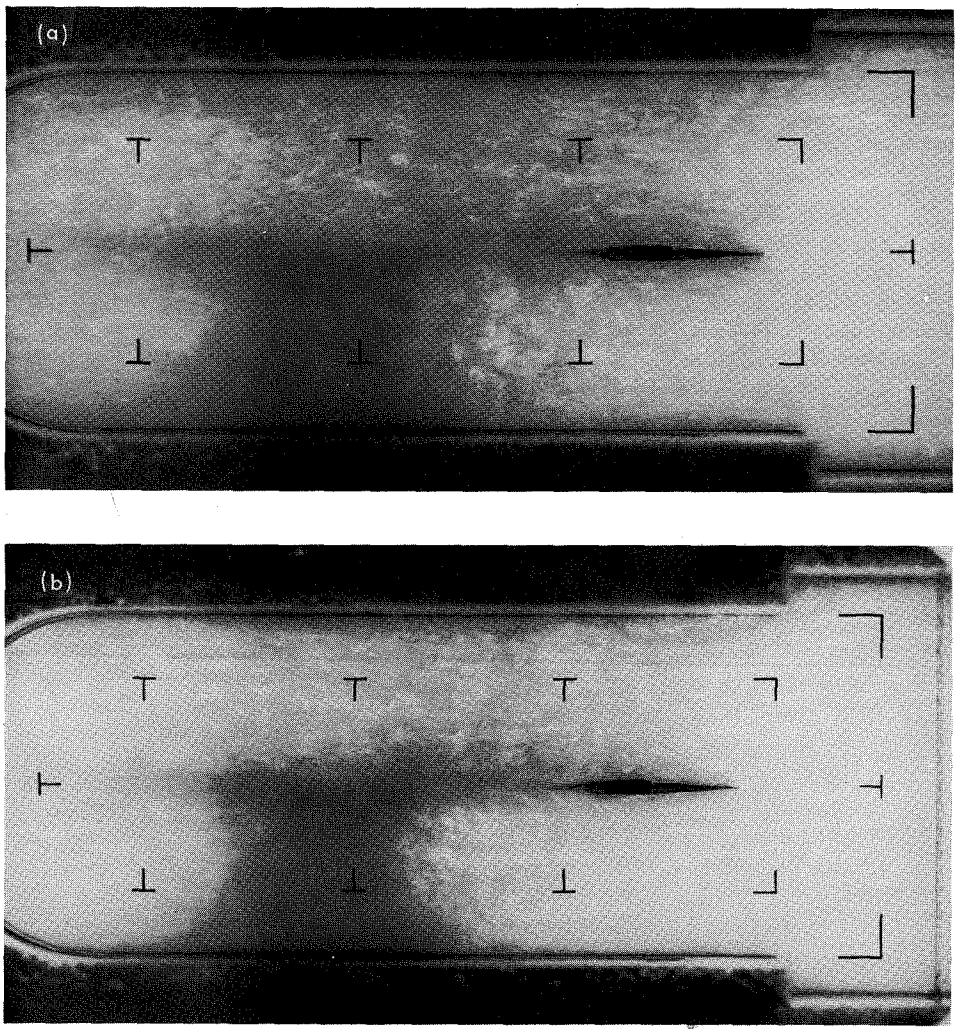

Fig. V-73. One-half-μsec exposures of supersonic flow over a 4° deflection wedge at constant pressure ($P_1 = 14.2$ psia), and variable volume ratio ($r_{v_1} = 0.76$ to 0.96) [(a) $V_1 = 152$ ft/sec, $M_1 = 2.32$, (b) $V_1 = 179$ ft/sec, $M_1 = 2.75$, (c) $V_1 = 265$ ft/sec, $M_1 = 4.10$, (d) $V_1 = 297$ ft/sec, $M_1 = 4.60$, (e) $V_1 = 335$ ft/sec, $M_1 = 5.17$]

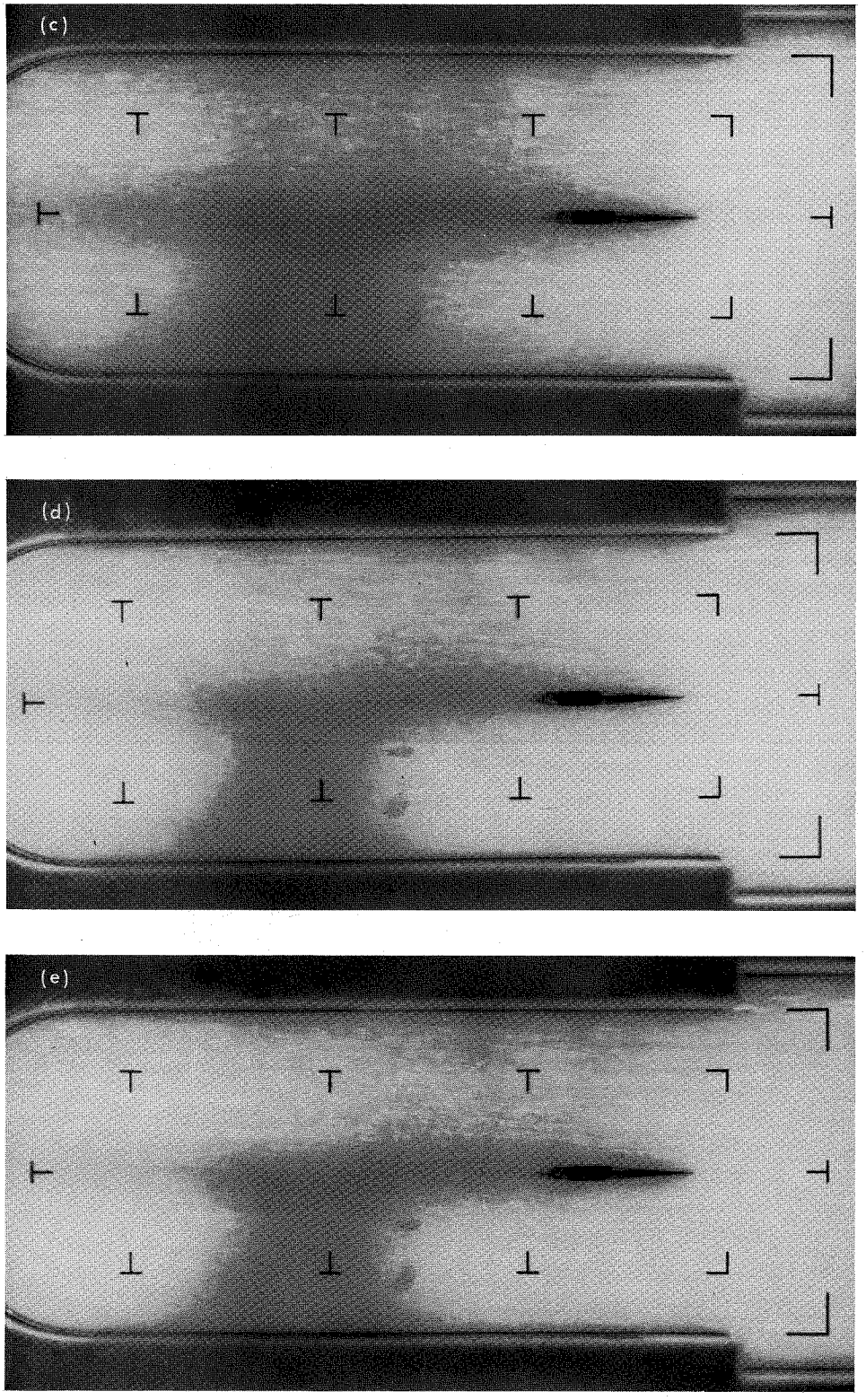

Fig. V-73 (contd)

Figure V-74 shows an increasing Mach number sequence at a constant V_{l_1} of 180 ft/sec over a range of $2.78 \leqq M_1 \leqq 11$. Pictures (a) through (d) of Fig. V-74 are similar to those of corresponding Mach numbers in Fig. V-73; picture (e) of Fig. V-74, however, shows the strong oblique shocks from the upper and lower knife edges caused by the entry of water and gas into the test section. Further, interaction because of water on the side walls seems to have occurred at the side knife edges. These interactions appear to be weak because they produced no significant change in the static pressure.

Figure V-75 shows an increasing Mach number sequence at a constant velocity of 335 ft/sec. The comments on pictures (a) through (c) of Fig. V-74 apply to pictures (a) through (c) of this figure as well. Picture (d) of Fig. V-75, however, was made with all gas shut off; only dissolved gas and liquid vapor combined to form the gas voids. The Mach number is considerably in excess of 18, but, due to the damaging effect of cavitation on the side walls at the junction of the lower knife shock and the lower oblique shock from the wedge, time sufficient for the pressure instrumentation to reach a steady value could not be allowed. There is an interesting change in the phenomena near the tip of the wedge under these conditions; a rounding seems to occur as if the shock had become unattached near the point, yet the trailing shock angles appear to remain near the values of those near the tip just prior to this change.

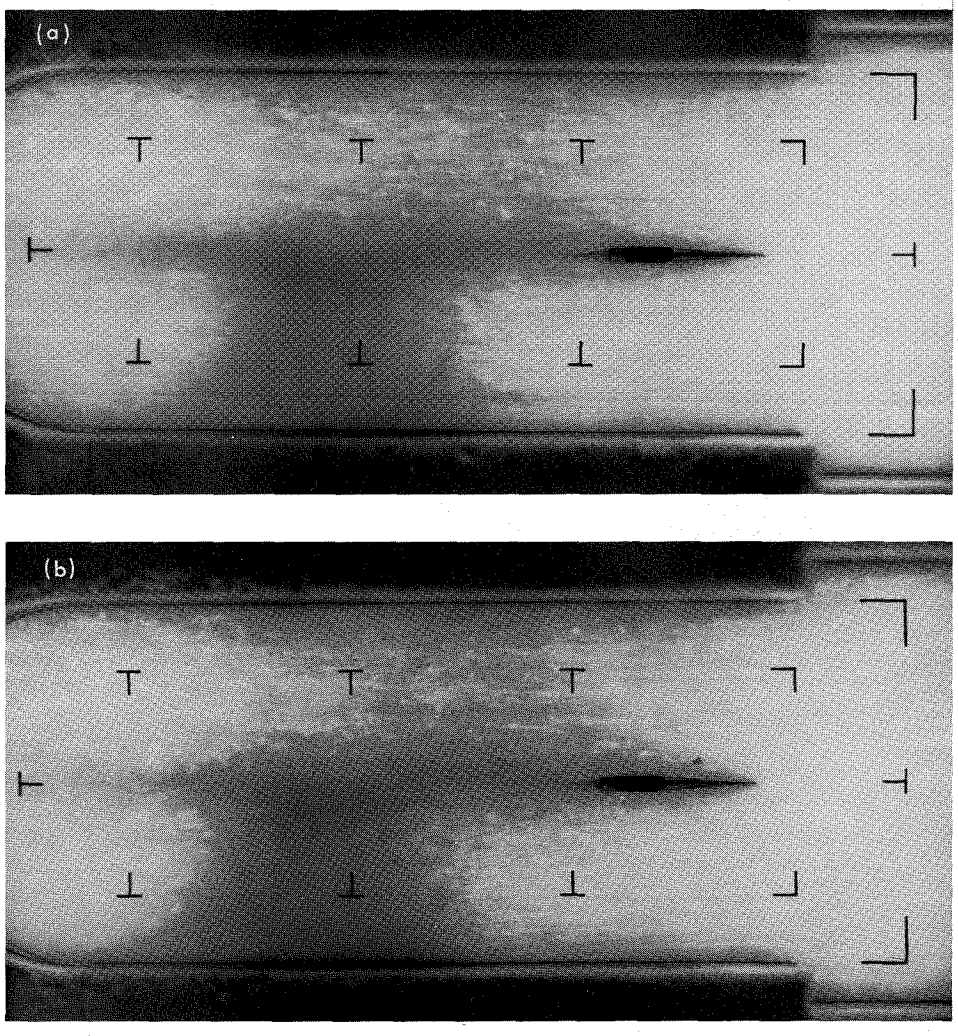

Fig. V-74. One-half-μsec exposures of supersonic flow over a 4° deflection wedge at constant velocity (V_1 = 180 ft/sec), constant volume ratio, and variable pressure [(a) M_1 = 2.78, (b) M_1 = 3.16, (c) M_1 = 4.15, (d) M_1 = 6.70, (e) M_1 = 11+]

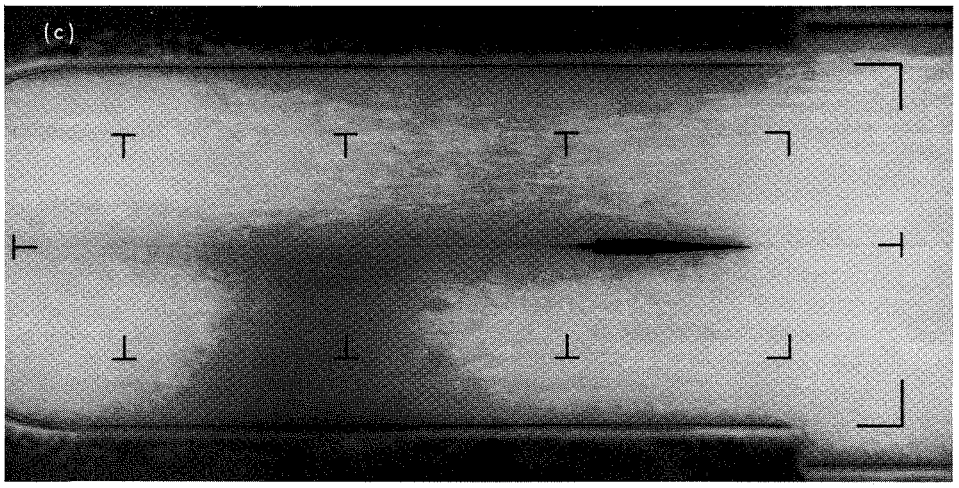

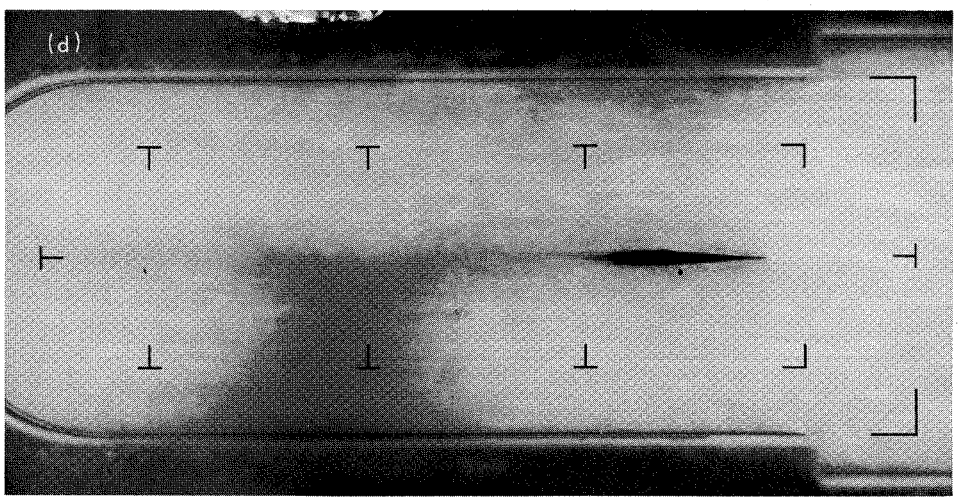

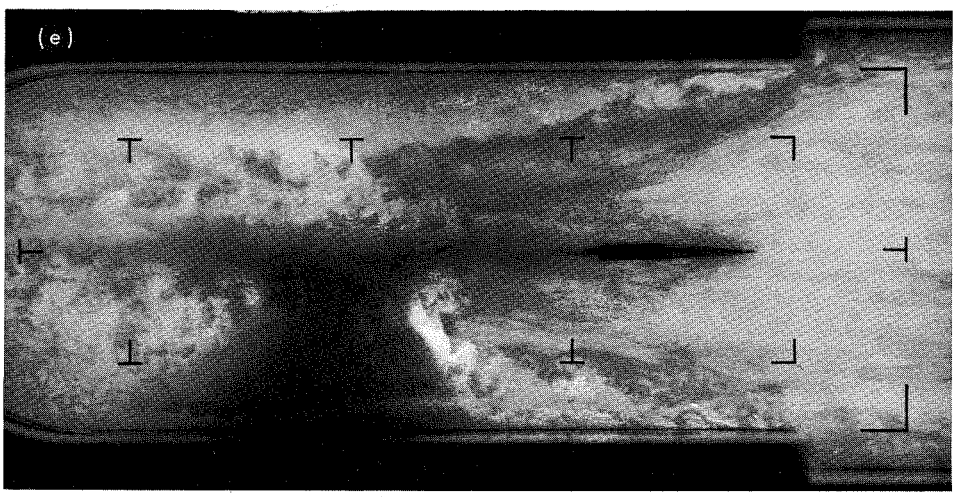

Fig. V-74 (contd)

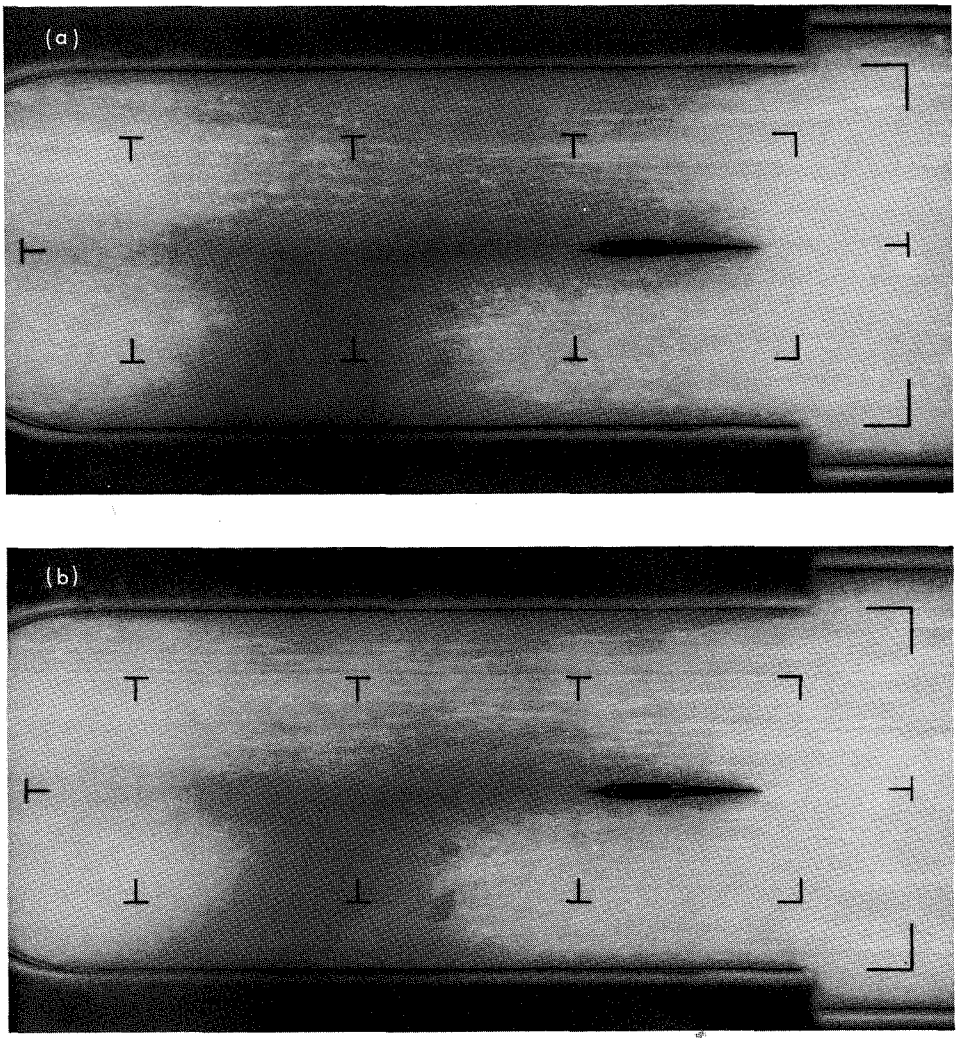

Fig. V-75. One-half-μsec exposures of supersonic flow over a 4° deflection wedge at constant velocity ($V_1 = 335$ ft/sec), constant volume ratio ($r_{v_1} = 0.96$), and variable pressure [(a) $M_1 = 6.55$, (b) $M_1 = 10.56$, (c) $M_1 = 16.10$, (d) $M_1 = 18+$]

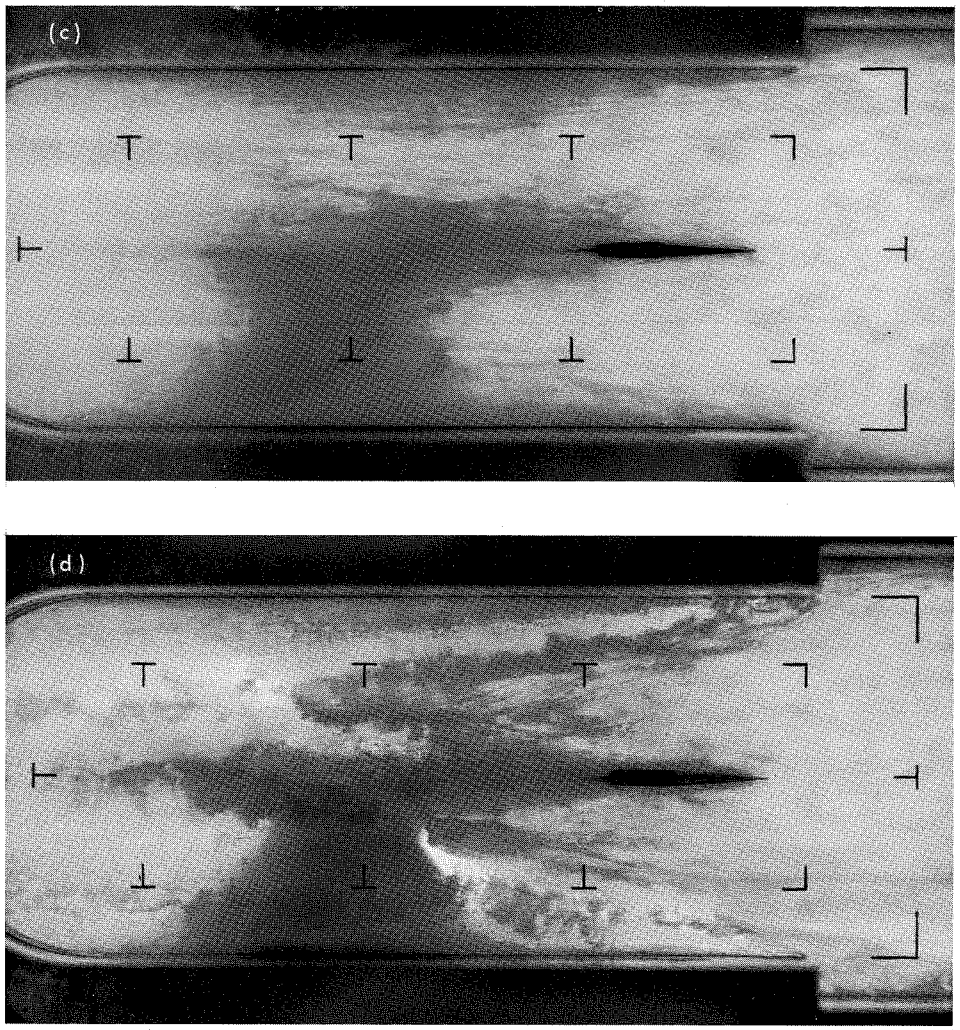

Fig. V-75 (contd)

2. The 10° Deflection Wedge

The 10° deflection wedge model was subjected to flow conditions ranging in Mach number (M_1) from 2.7 to 19 at tunnel volume ratios (r_{v_1}) between 0.75 and 0.96. This deflection angle produced shock phenomena far more clearly discernible than those of the 4° model.

The effect of a change in r_{v_1} is more pronounced at a deflection of 10° than at lesser deflection values. Therefore four separate figures (Figs. V-76 through V-79) are used for r_{v_1} of 0.75, 0.8, 0.9 and 0.96, which correspond to the liquid flow velocities of 149 ft/sec, 180 ft/sec, 265 ft/sec and 335 ft/sec, respectively.

The experimental data points between $M_1 = 2.2$ and 2.7 on Fig. V-76 confirm the sharp upturn of the theoretical curve in this region and the ultimate disattachment of the oblique shock at Mach numbers less than 2.2. The data at Mach numbers between 10 and 20 in Fig. V-79 closely substantiate the validity of the asymptotic nature of the theoretical curve to a constant value in the upper Mach number ranges.

Between these extremes, the close correlation of the data points with the β curves at the different values of r_{v_1} strongly confirms the variation in r_{v_1} that occurs in the tunnel test section for different liquid velocities. This is more clearly evident in Fig. V-80, which includes the four β curves of fixed r_{v_1} and a dotted β vs M_1 curve that corresponds to the actual r_{v_1} variation in the tunnel at constant pressure with variable liquid velocity. The experimental data closely follows the dotted curve.

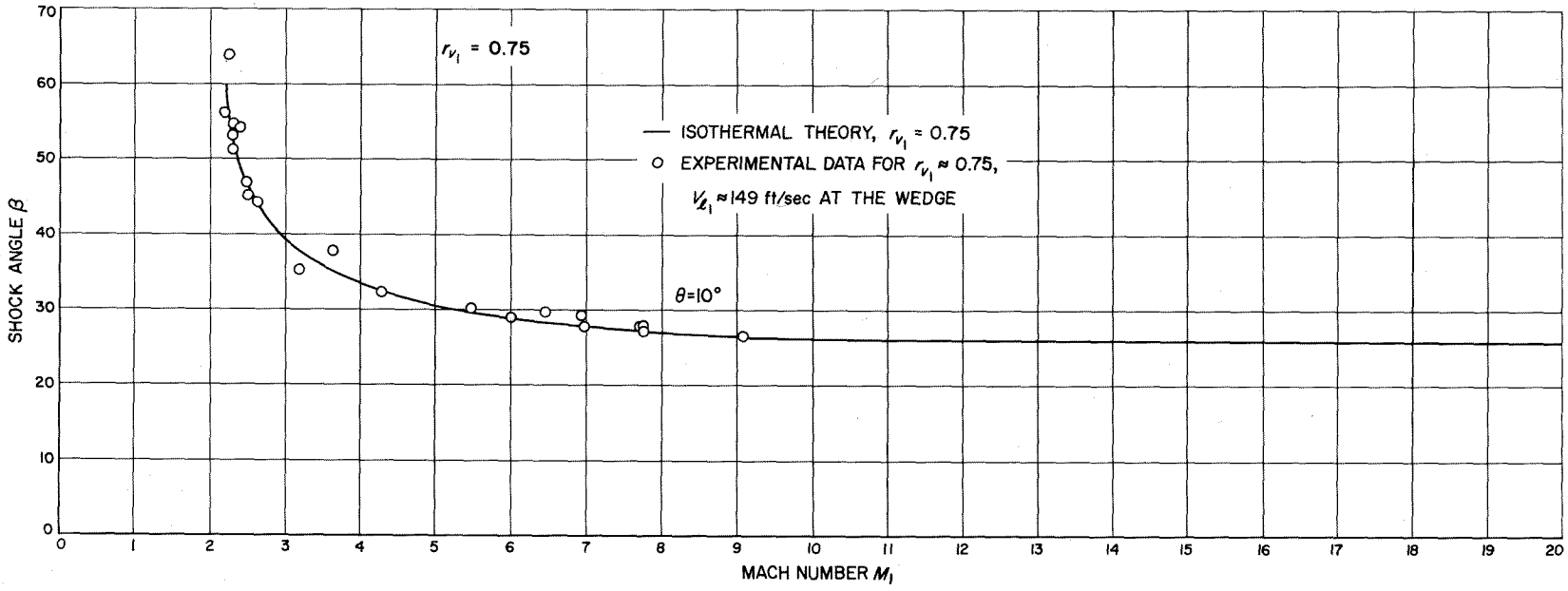

Fig. V-76. Oblique shock angle as a function of Mach number for a 10° deflection wedge at a constant velocity (V_1 = 149 ft/sec)

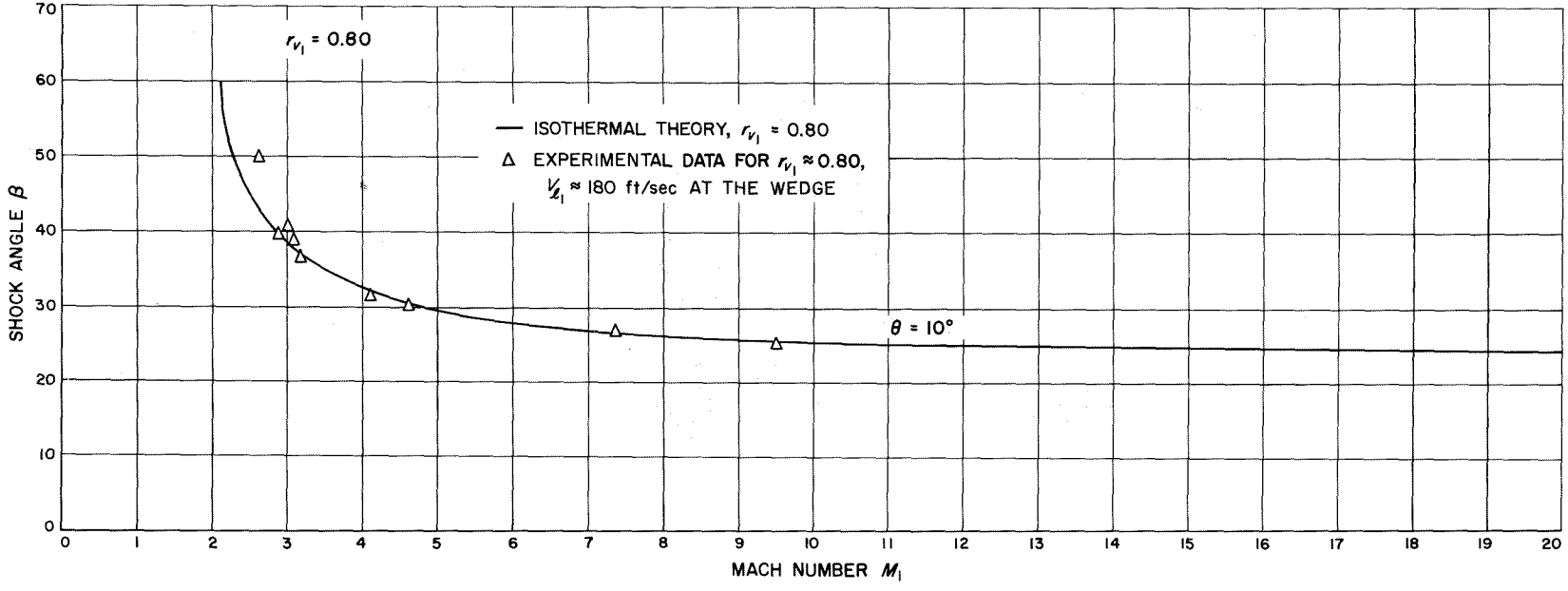

Fig. V-77. Oblique shock angle as a function of Mach number for a 10° deflection wedge at a constant velocity (V_1 = 180 ft/sec)

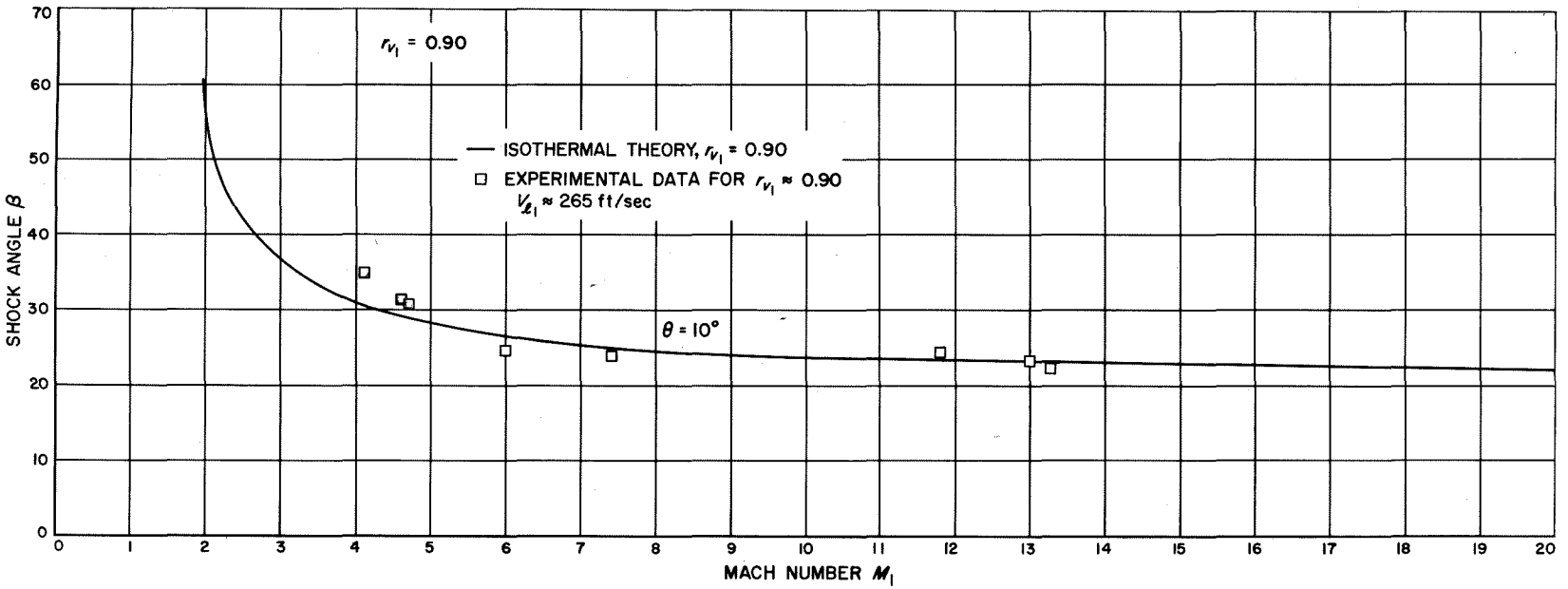

Fig. V-78. Oblique shock angle as a function of Mach number for a 10° deflection wedge at a constant velocity (V_1 = 265 ft/sec)

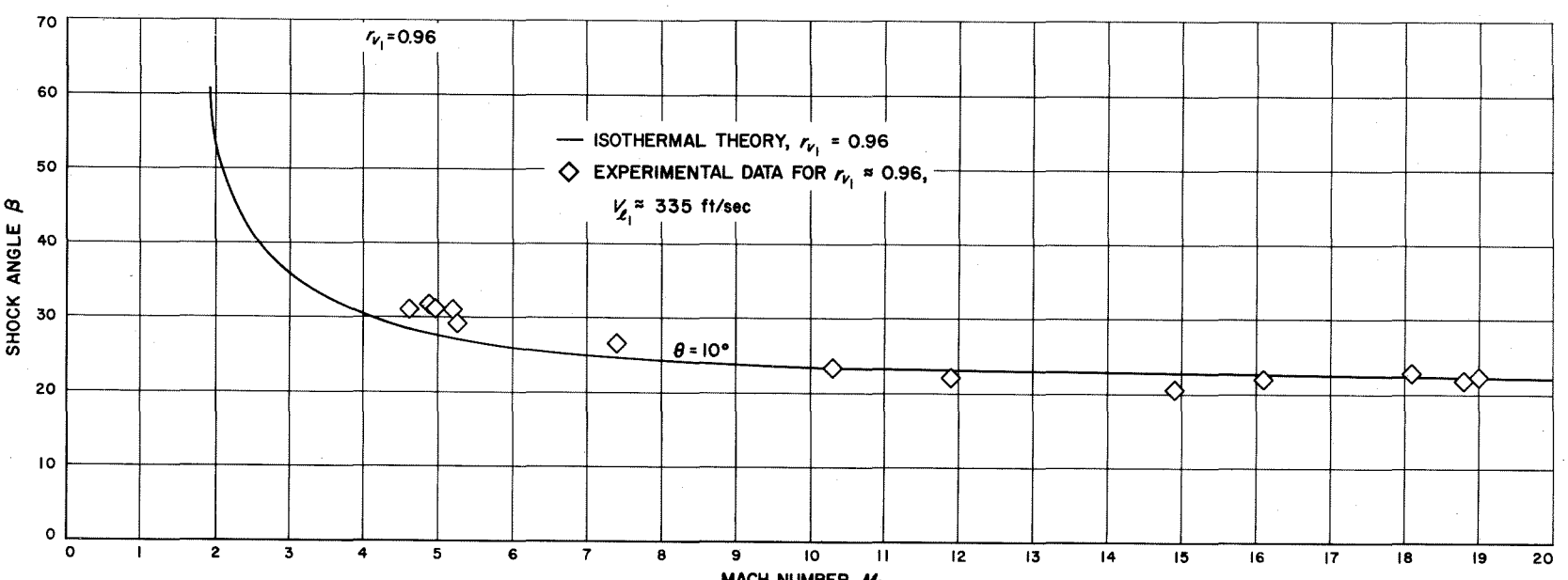

Fig. V-79. Oblique shock angle as a function of Mach number for a 10° deflection wedge at a constant velocity (V_1 = 335 ft/sec)

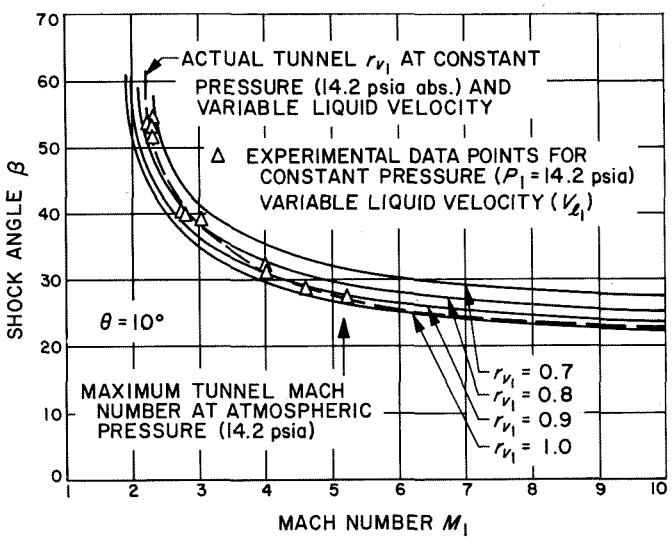

Fig. V-80. Oblique shock angle as a function of Mach number for a 10° deflection wedge at variable velocity and variable Mach number

The pressure ratios (P_2/P_1) as a function of Mach number are displayed similarly on four graphs of constant r_{v_1}; pressure ratios of 0.75, 0.8, 0.9, and 0.96 are shown in Figs. V-81, V-82, V-83, V-84, respectively. At the two lower liquid velocities of 149 ft/sec (Fig. V-81) and 180 ft/sec (Fig. V-82), the experimental data closely approximates the isothermal theory. For the lowest velocity in particular, the pressure ratio is lower at the limiting Mach numbers than predicted by theory. Quite possibly this is due to a diffusion of gas at the relatively low shock strengths.

At the two highest liquid velocities of 266 ft/sec (Fig. V-83) and 335 ft/sec (Fig. V-84), the experimental pressure ratios for Mach numbers greater than 4.2 clearly exceed that predicted by isothermal theory. In the latter case, however, the scatter is sufficiently great to make the suggestion of a firm trend questionable. Below $M_1 = 4.2$, the data approximates the isothermal theory reasonably well.

Figure V-85 shows a sequence of increasing Mach numbers at a constant pressure of $P_1 = 14.2$ psia, in which liquid velocity increases from 151 to 335 ft/sec, and the volume ratio increases from 0.75 to 0.96, respectively. At the lowest Mach number, the oblique shock from the leading edge of the wedge is barely discernible, and, for accurate measurement, the shock must be located by an isodensity analysis of the negative and a comparison with ½-μsec exposures at the same Mach number. A change in flow direction parallel to the wedge surface is evident in

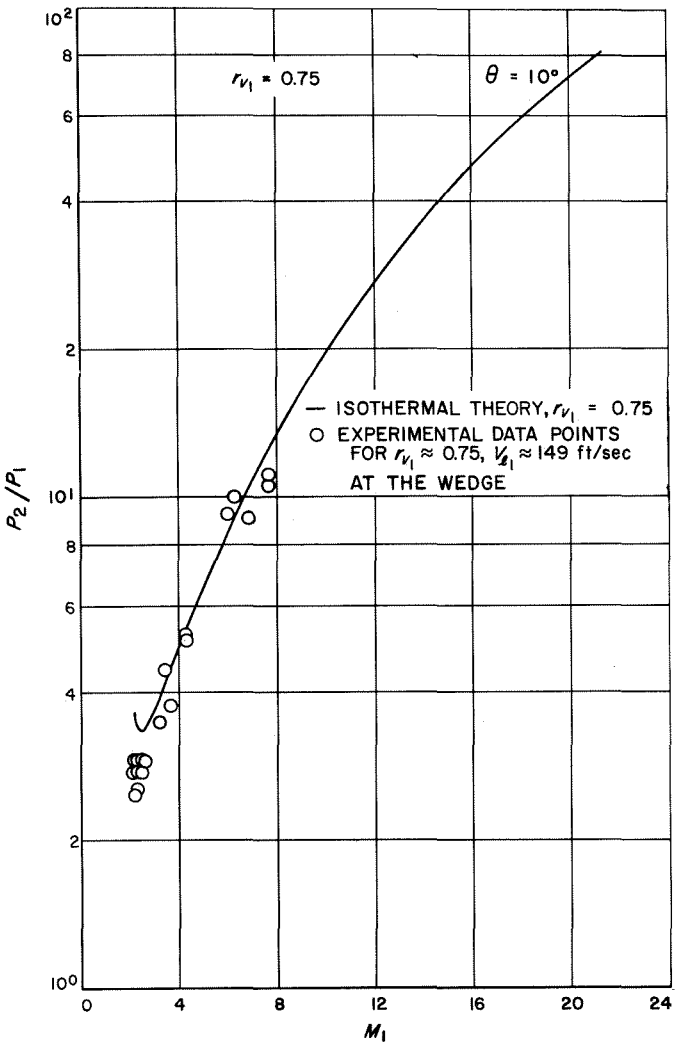

Fig. V-81. Oblique shock pressure ratio as a function of Mach number for a 10° deflection wedge at a constant velocity (V_1 = 149 ft/sec)

the vicinity behind the shock front. A complete void exists behind the wedge up to nearly $M_1 = 4.0$. At higher liquid velocities, the pressure is sufficiently high behind the shock to turn the flow more quickly and partially close in the void area.

At Mach numbers higher than 4.0 created by lowering the test section pressure below atmospheric (14.2 psia), the voids behind the double wedge are clearly evident. There are no expansion-type shock structures evident in the two-phase flow that are capable of turning the flow about a sharp corner. Expansion flow appears dependent upon pressure and the directional momentum of the flow.

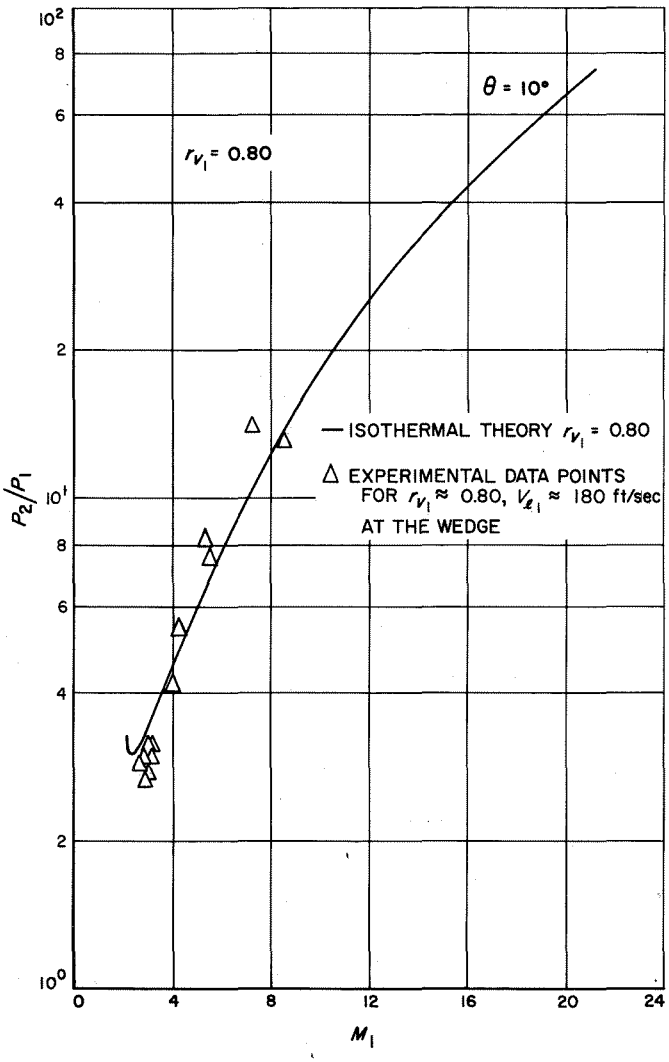

Fig. V-82. Oblique shock pressure ratio as a function of Mach number for a 10° deflection wedge at a constant velocity (V_1 = 180 ft/sec)

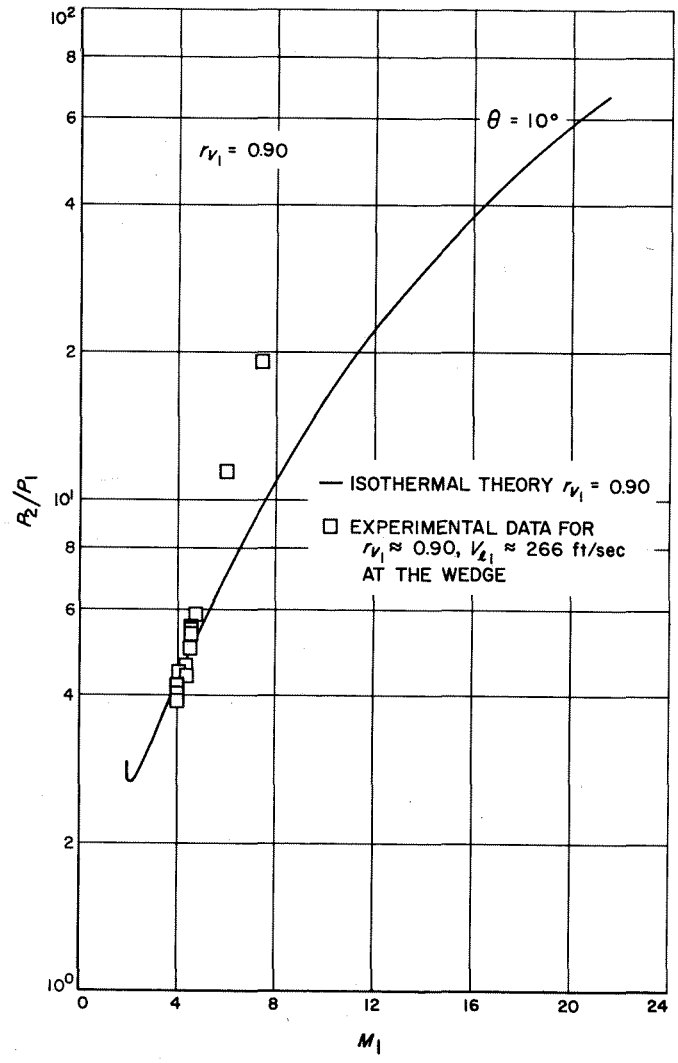

Fig. V-83. Oblique shock pressure ratio as a function of Mach number for a 10° deflection wedge at a constant velocity (V_1 = 266 ft/sec)

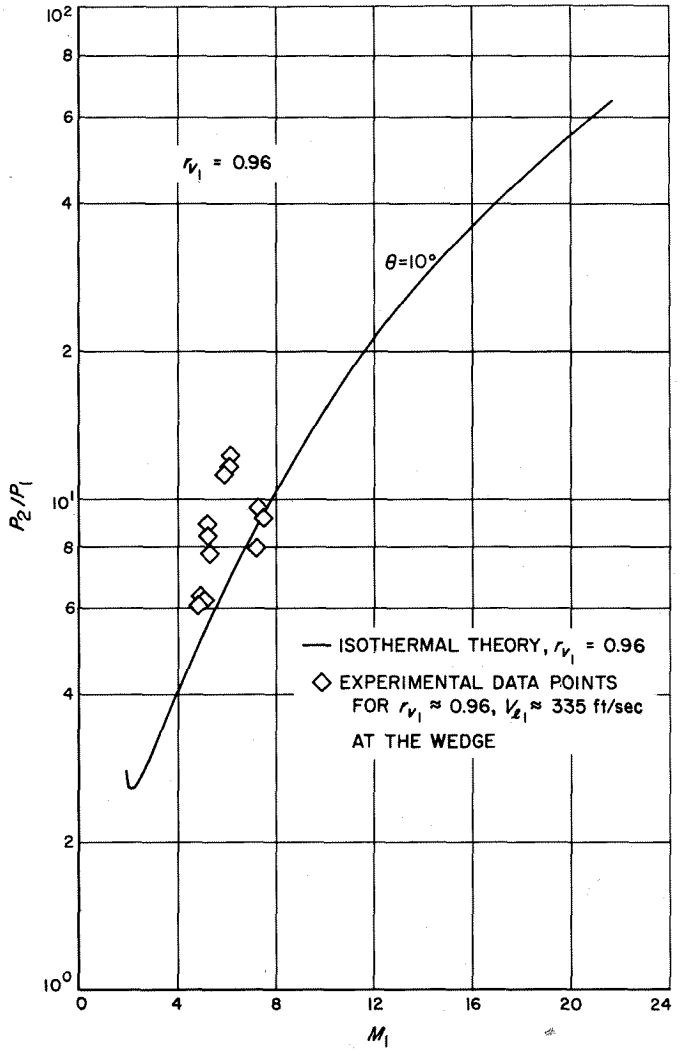

Fig. V-84. Oblique shock pressure ratio as a function of Mach number for a 10° deflection wedge at *a constant* velocity ($V_1 = 335$ ft/sec)

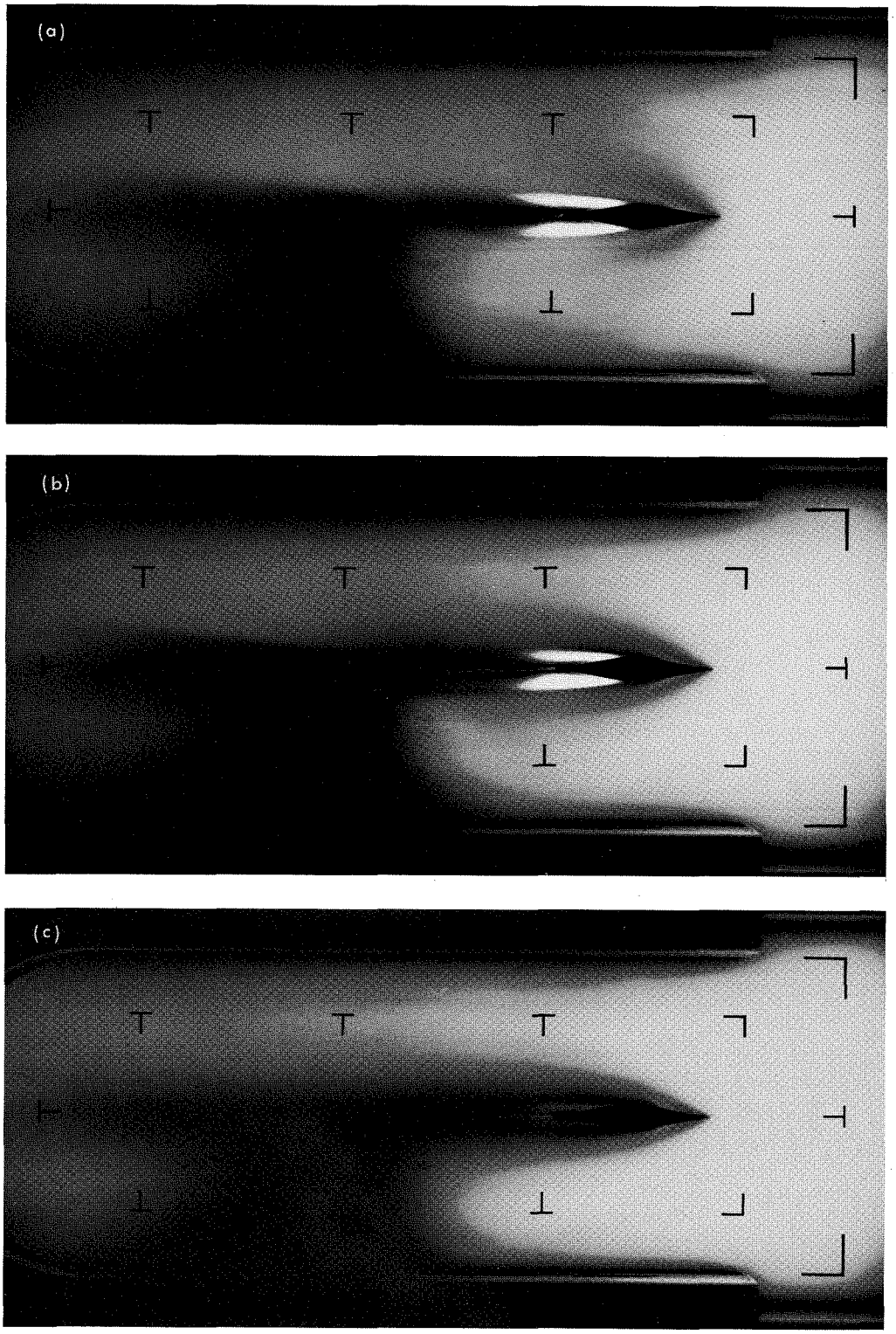

Fig. V-85. Supersonic flow over a 10° deflection wedge at constant pressure ($P_1 = 14.2$ psia), and variable volume ratio ($r_{v_1} = 0.75$ to 0.96), [(a) $V_1 = 151.6$ ft/sec, $M_1 = 2.40$, (b) $V_1 = 196.5$ ft/sec, $M_1 = 3.08$, (c) $V_1 = 258$ ft/sec, $M_1 = 4.00$, (d) $V_1 = 297$ ft/sec, $M_1 = 4.45$, (e) $V_1 = 335$ ft/sec, $M_1 = 4.95$]

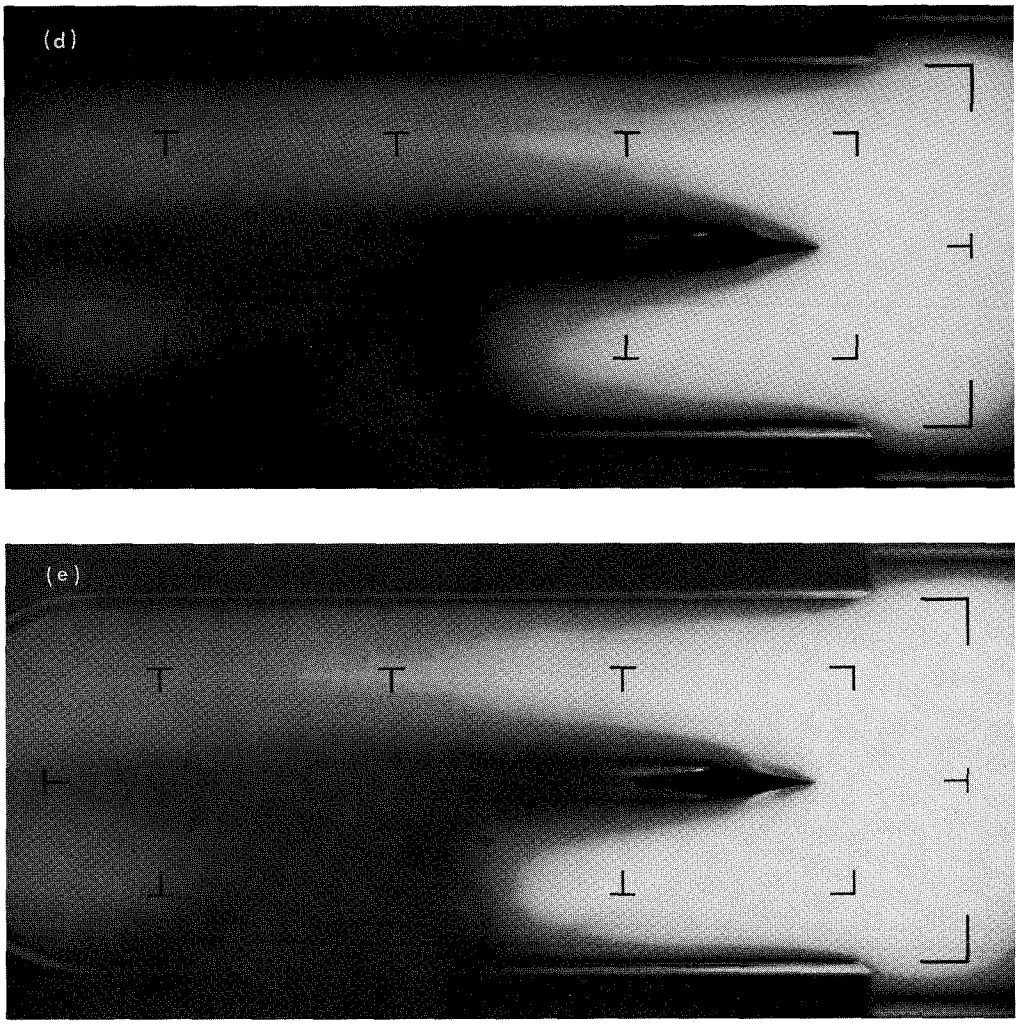

Fig. V-85 (contd)

Figure (V-86) shows an increasing Mach number sequence at a constant liquid velocity of $V_{l_1} = 149$ ft/sec, and an $r_{v_1} = 0.75$ over a Mach number range of $2.30 \leqq M_1 \leqq 8.30$. In this sequence, the shock wave created by the rubber bumper at the edge of the wedge is clearly evident. In pictures (a), (b), and (c) of Fig. V-86, flow can be seen about the leading edge of the bumper. In pictures (d) and (e), the bumper flow or shock conflicts with the previously continuous slope of the oblique shock from the leading edge of the wedge, and bends it outward about half of the way back to the wedge surface. In pictures (f), (g), and (h), the oblique shock from the leading edge of the wedge is actually below the outer shock wave. This has been confirmed by a careful analysis of motion pictures of a similar Mach number sequence and an analysis of ½-μsec pictures at similar flow conditions.

Figure V-87 shows an increasing Mach number sequence at a constant V_{l_1} of 180 ft/sec, and an r_{v_1} of 0.800 over a range of $2.80 \leqq M_1 \leqq 9.50$. A conflict with the shock phenomena from the rubber bumper first appears in picture (c) of Fig. V-87, and continues through picture (g). The actual oblique shock from the wedge's leading edge is completely obscured in picture (g), and its location was determined by visual observation and comparison with motion pictures of a similar Mach number sequence.

Figure V-88 shows an increasing Mach number sequence at a constant V_{l_1} of 266 ft/sec, and an r_{v_1} of 0.90 over a range of $4.10 \leqq M_1 \leqq 13.3$. In pictures (a) and (b), the oblique shocks from the leading edge of the wedge are weak but visible because the infrared pictures were very slightly underexposed.

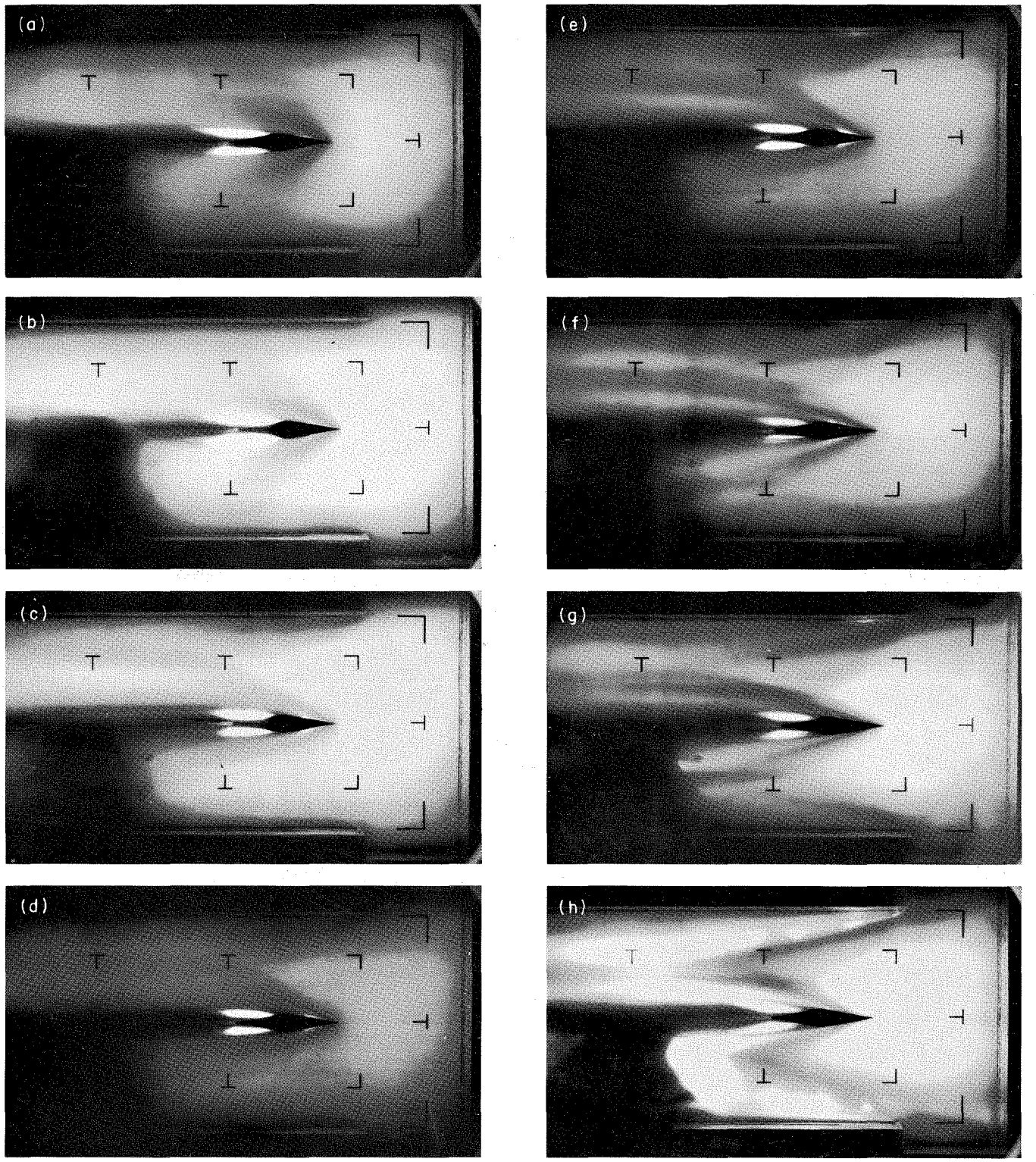

Fig. V-86. Infrared photographs of supersonic flow over a 10° deflection wedge at constant velocity ($V = 149$ ft/sec), constant volume ratio ($r_{v_1} = 0.750$), and variable pressure [(a)$M_1 = 2.30$, (b) $M_1 = 2.50$, (c) $M_1 = 3.20$, (d) $M_1 = 4.30$, (e) $M_1 = 6.00$, (f) $M_1 = 7.00$, (g) $M_1 = 7.80$, (h) $M_1 = 8.30$]

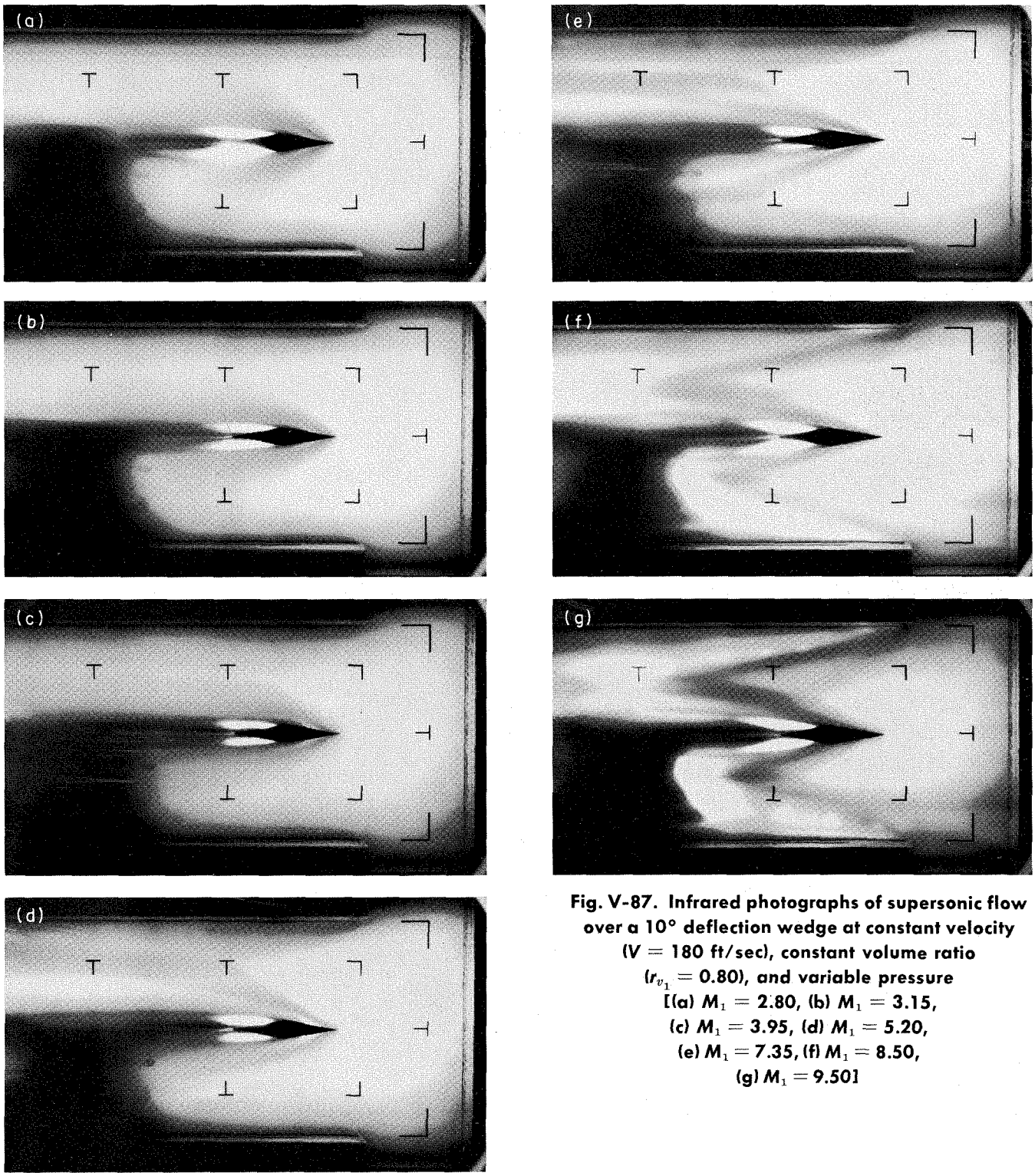

Fig. V-87. Infrared photographs of supersonic flow over a 10° deflection wedge at constant velocity (V = 180 ft/sec), constant volume ratio (r_{v_1} = 0.80), and variable pressure [(a) M_1 = 2.80, (b) M_1 = 3.15, (c) M_1 = 3.95, (d) M_1 = 5.20, (e) M_1 = 7.35, (f) M_1 = 8.50, (g) M_1 = 9.50]

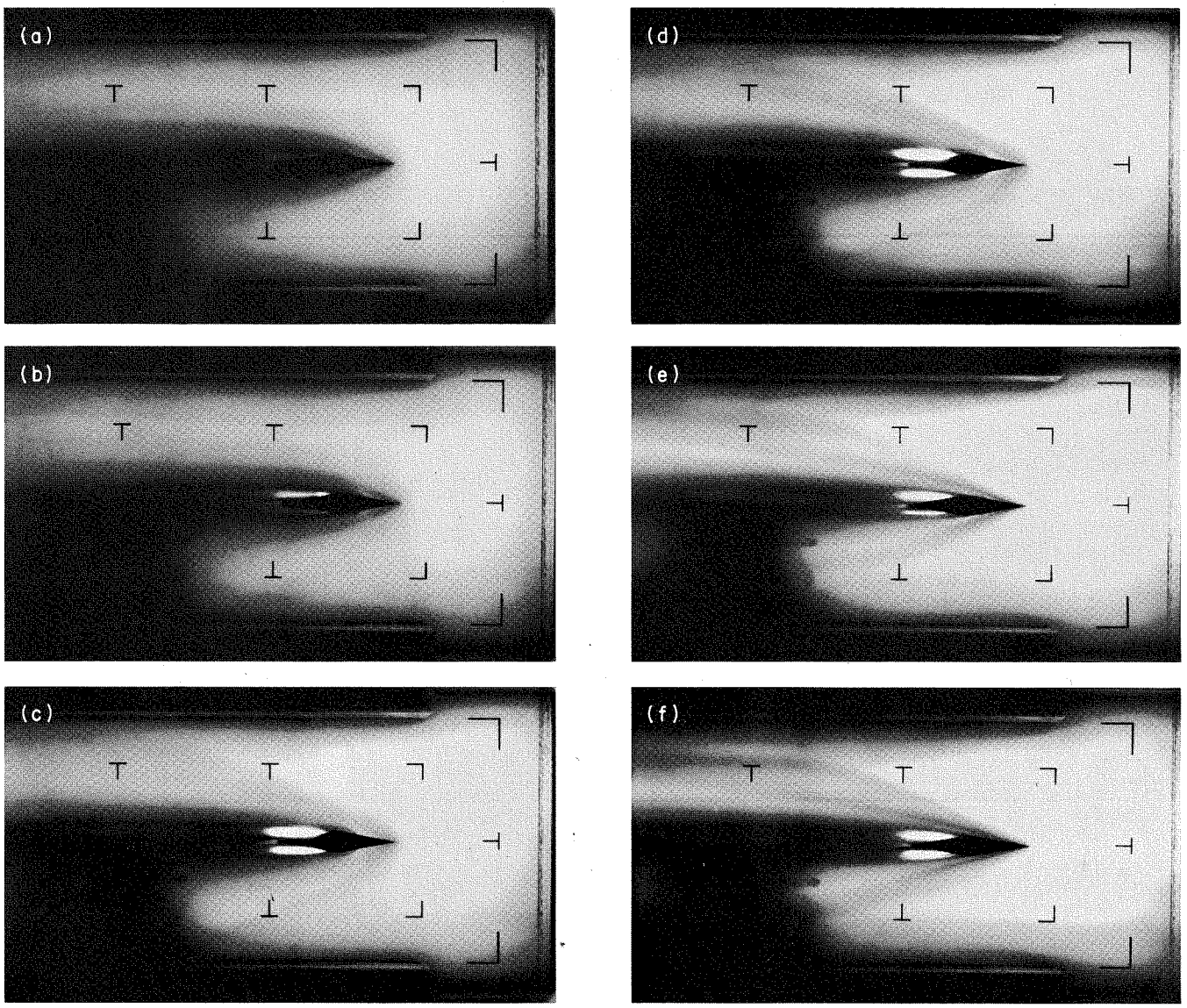

Fig. V-88. Infrared photographs of supersonic flow over a 10° deflection wedge at constant velocity (V_1 = 266 ft/sec), constant volume ratio (r_{v_1} = 0.90), and variable pressure [(a) M_1 = 4.10, (b) M_1 = 4.70, (c) M_1 = 6.00, (d) M_1 = 7.40, (e) M_1 = 11.8, (f) M_1 = 13.0]

Figure V-89 shows an increasing Mach number sequence at a constant V_{l_1} of 335 ft/sec, and an r_{v_1} of 0.96 over a range of $5.90 \leq M_1 \leq 10.0$.

Figure V-90 represents an increasing Mach number sequence at a constant pressure (P_1 = 14.2 psia), each taken at an exposure of ½-μsec. The fine structure of the flow near the wall is discernible. The incoming flow is characterized by linear chains of gas voids that are distributed more uniformly upon passing through the shock front. As previously stated, this change in distribution is the key to the ability of the shock front to sustain its characteristic pressure rise through the relative phase drag. The light variations along the upper surface of the tunnel are not due to the flow, but to shadows of the static tap fittings.

Pictures (a) through (c) of Fig. V-91 show an increasing Mach number sequence at a constant V_{l_1} of 335 ft/sec.

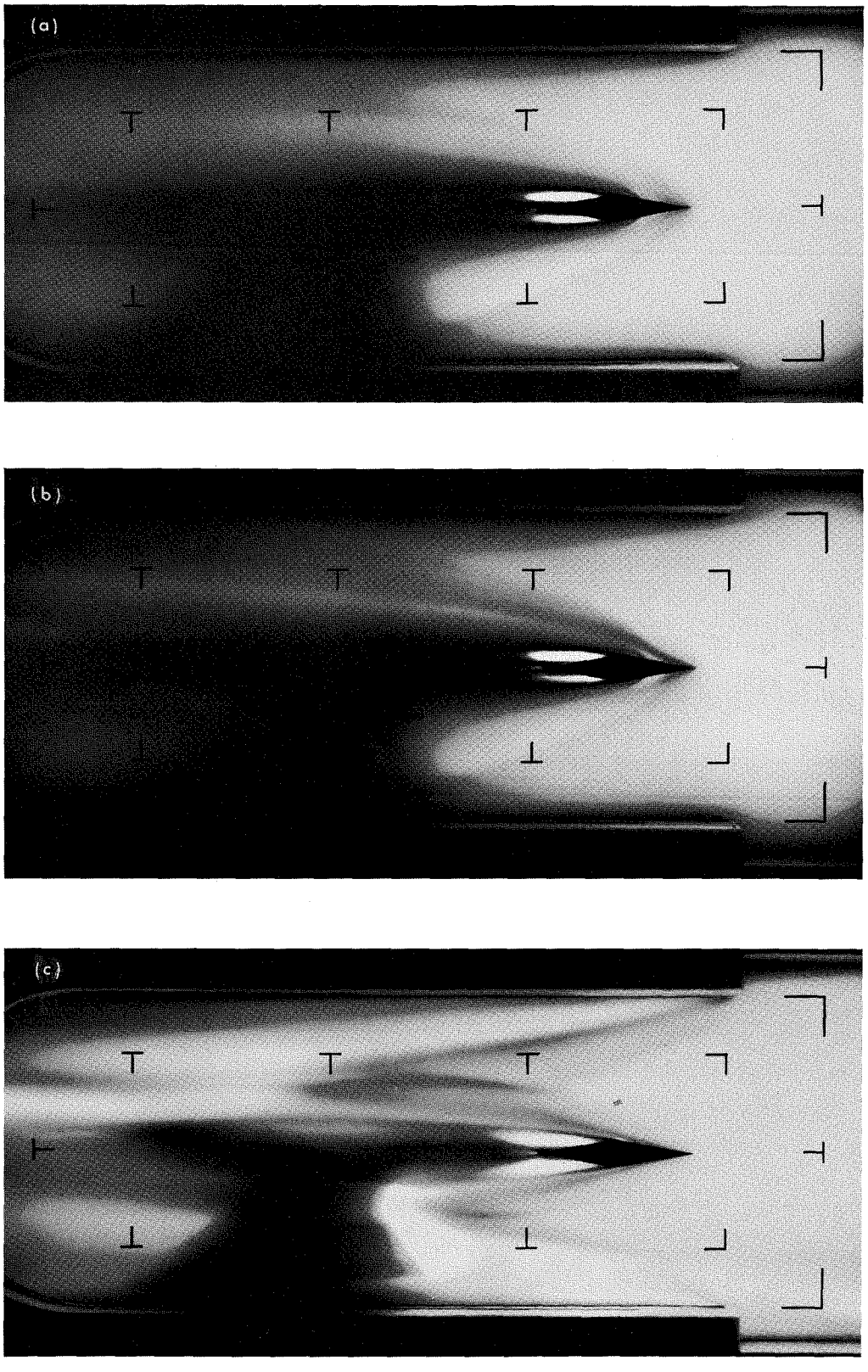

Fig. V-89. Supersonic flow over a 10° deflection wedge at constant velocity ($V_1 = 335$ ft/sec), constant volume ratio ($r_{v_1} = 0.96$), and variable pressure [(a) $M_1 = 5.90$, (b) $M_1 = 7.40$, (c) $M_1 = 8.51$]

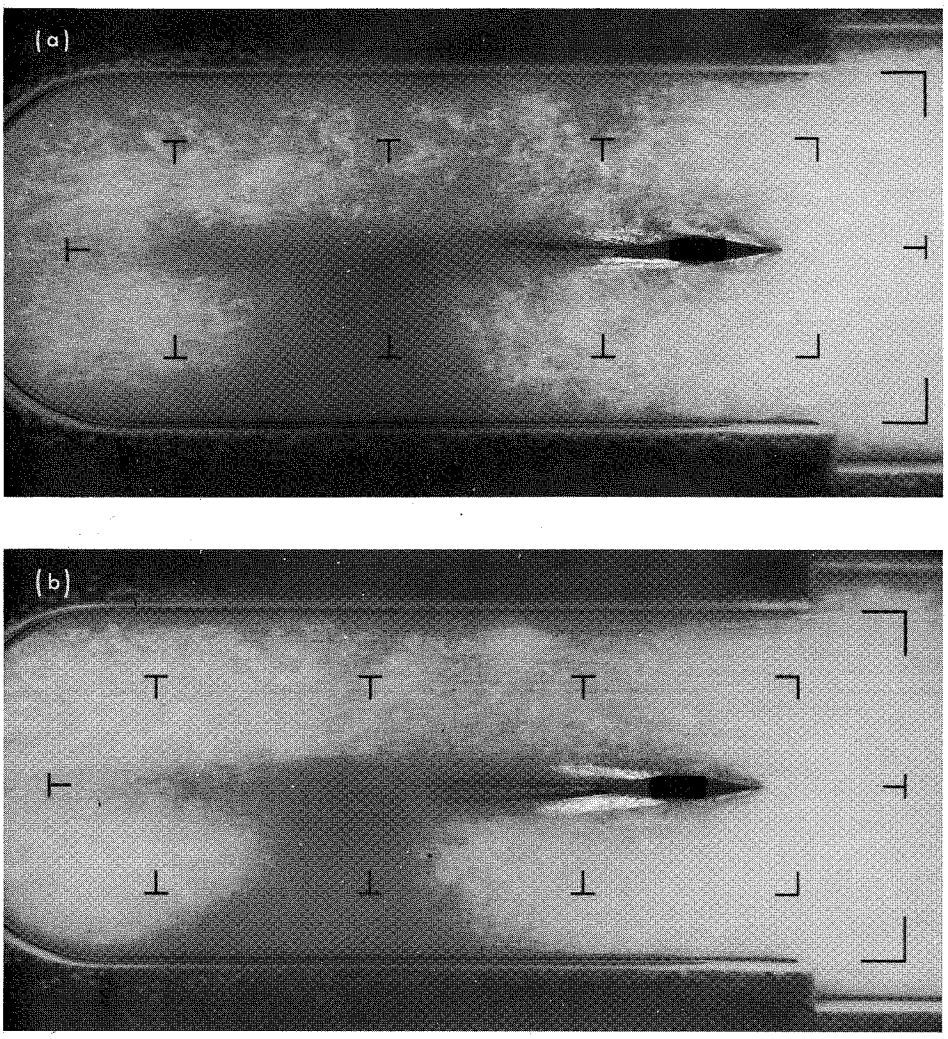

Fig. V-90. One-half-μsec exposure of supersonic flow over a 10° deflection wedge at constant pressure ($P_1 = 14.2$ psia), variable volume ratio ($r_{v_1} = 0.75$ to 0.96), and variable velocity ($V_1 = 147$ to 335 ft/sec) [(a) $M_1 = 2.25$, (b) $M_1 = 2.68$, (c) $M_1 = 4.00$, (d) $M_1 = 4.60$, (e) $M_1 = 5.20$]

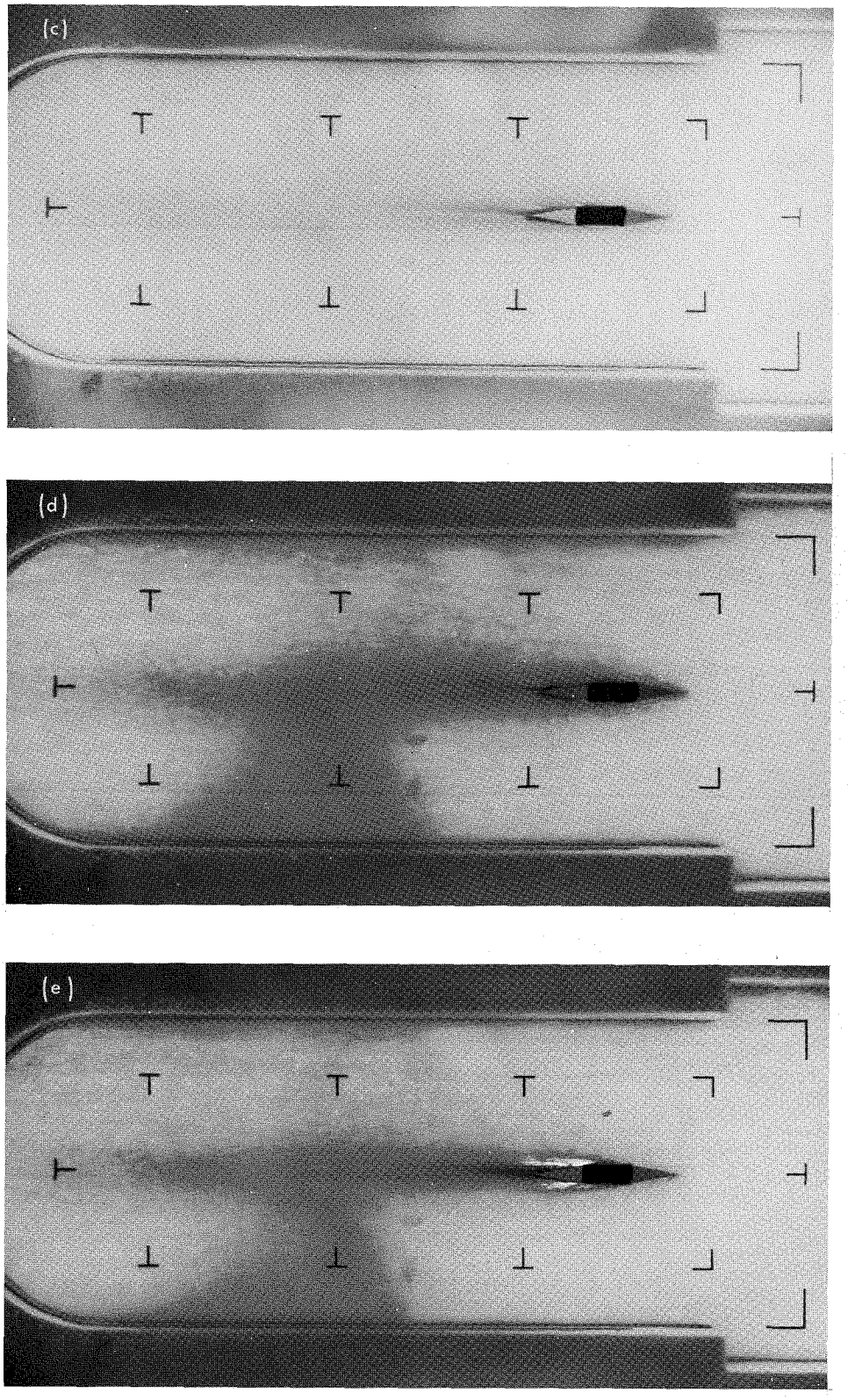

Fig. V-90 (contd)

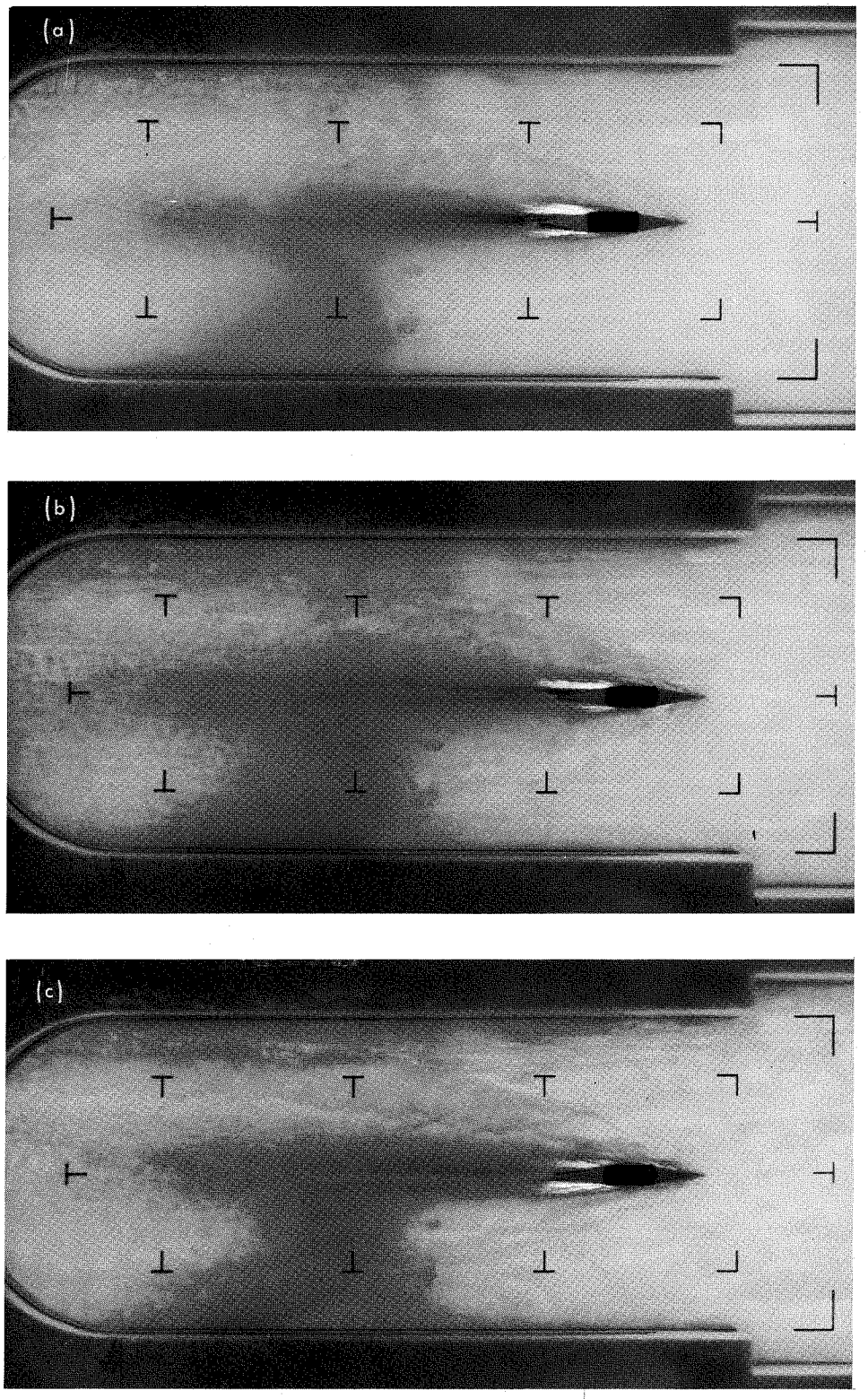

Fig. V-91. One-half-μsec exposure of supersonic flow over a 10° deflection wedge at constant velocity ($V_1 = 335$ ft/sec), constant volume ratio ($r_{v_1} = 0.96$), and variable pressure (P_1) [(a) $M_1 = 7.40$, (b) $M_1 = 10.30$, (c) $M_1 = 14.90$, (d) $M_1 = 16.1$]

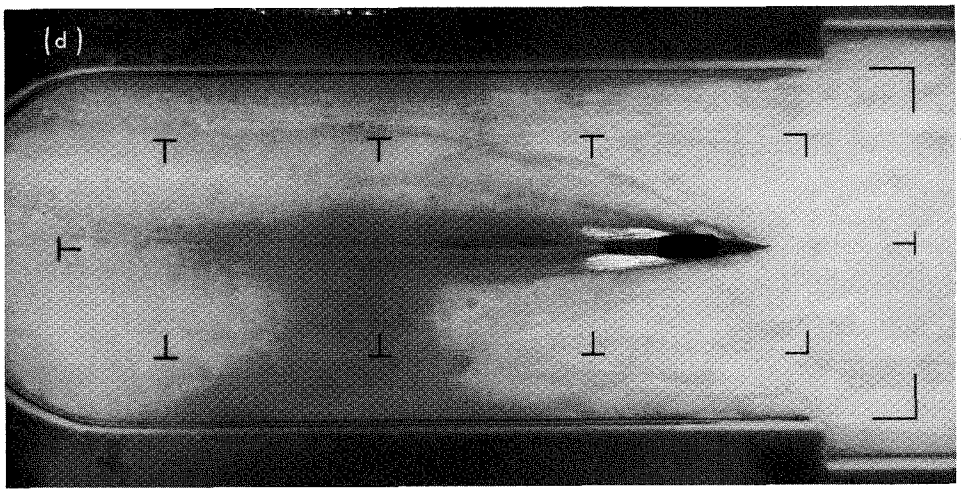

Fig. V-91 (contd)

Picture (d) clearly shows the interference to the latter sections of the upper and lower oblique shocks caused by the unattached shock from the leading edge of the rubber bumper.

Figures V-92 and V-93 are restricted views of the test section at Mach numbers 2.25 and 4.00, respectively, magnified fivefold. Bubbles of 0.002-in. diameter are visible in the individual chains, but the diameters lie more generally in the range of 0.005 to 0.010 in. The upstream bubbles are elongated in the direction of flow, effectively reducing their coefficient of drag. A considerable number of liquid voids can be seen leading the shock area. These voids occur just prior to attachment.

3. The 20° Deflection Wedge

With reference to Fig. V-2, the maximum deflection angle for oblique shock attachment in a flow having a maximum volume ratio of 0.96 is approximately 18.8°. At a Mach number of 5.0, this value is reduced to 17.2°. A twenty-degree wedge constructed for, and subjected to the same range of Mach numbers as wedges of lesser deflection angles was used to verify, according to the isothermal theory, that the shock was unattached at the lower Mach numbers, to determine if attachment occurred at any higher Mach number, and, finally, the form of an unattached shock wave.

Figure V-94 shows an increasing Mach number series at a constant V_{l_1} of 298 ft/sec, and an r_{v_1} of 0.9 over a range of $4.0 \leq M_1 \leq 12.5$. The flow must approach a Mach number of at least 4.0 before the previously normal shock in the test section moves downstream to the leading edge of the wedge and folds back in the manner of an oblique shock as shown in picture (a) of Fig. V-94. Figure V-95 shows a flow at nearly the same Mach number (4.0) taken at an exposure of ½ μsec; the shock wave appears close to attachment, yet there is obvious rounding in front of the leading edge. To investigate further the area adjacent to and in front of the leading edge, an isodensity analysis[3] was made of negatives of the ½-μsec exposure in the range of Mach 4 to 5. Tracings from this analysis are shown in pictures (a) and (b) of Fig. V-96. Regions of distinct density variation associated with the shock phenomena are evident well ahead of the leading edge of the wedge, particularly in picture (b). This confirms that the shock phenomena is not attached to the leading edge.

Measurement of the angle of the leading shock curve near Mach 4.0 from the various types of photographs indicates basic shock angle (β) of 53 to 57° in the initial relatively straight portion of the wave. With reference to Figs. V-2 and V-10, the limiting β for the 18° wedge at $M_1 = 4.0$ is 57°. Thus the shock phenomena is near attachment and near the proper β angle, but has not attached as predicted in Fig. V-2, which was plotted by the isothermal theory.

[3]Isodensity analysis courtesy of Beckman and Whitley, Mountain View, California.

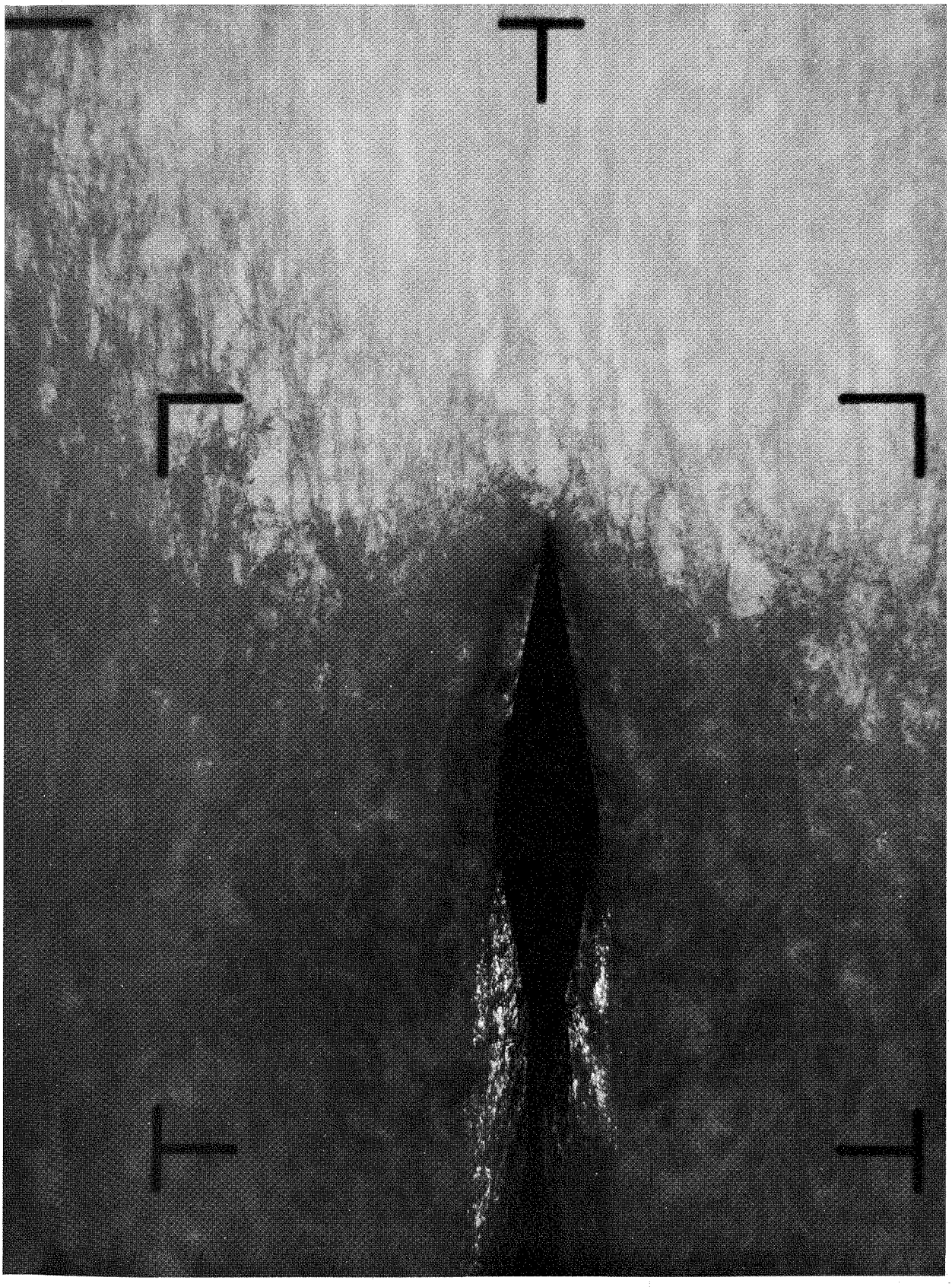

Fig. V-92. One-half-μsec exposure of supersonic flow over a 10° deflection wedge, enlarged, at $V_1 = 147$ ft/sec, $r_{v_1} = 0.75$, and $M_1 = 2.25$

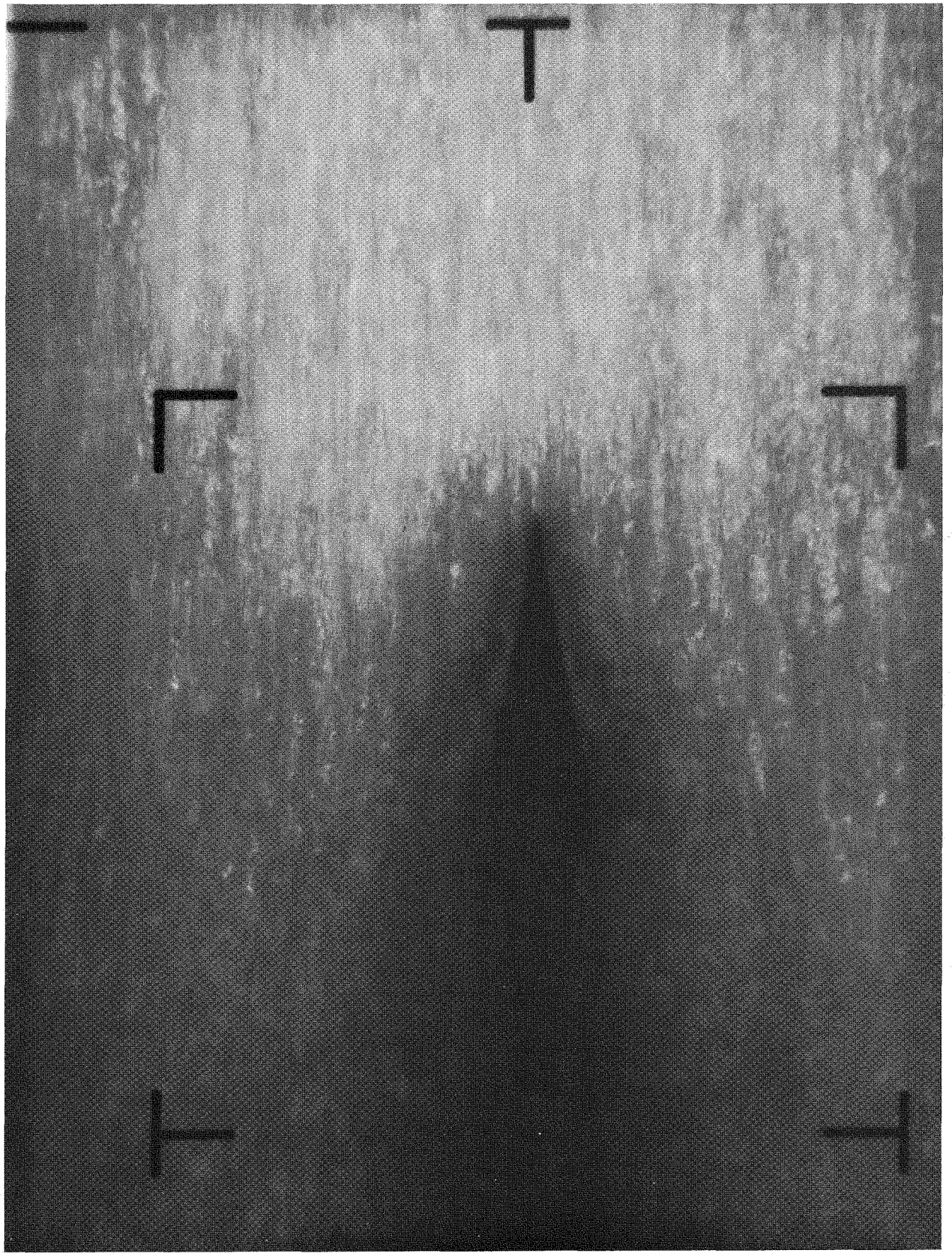

Fig. V-93. One-half-μsec exposure of supersonic flow over a 10° deflection wedge, enlarged, at $V_1 = 259$ ft/sec, $r_{v_1} = 0.89$, and $M_1 = 4.00$

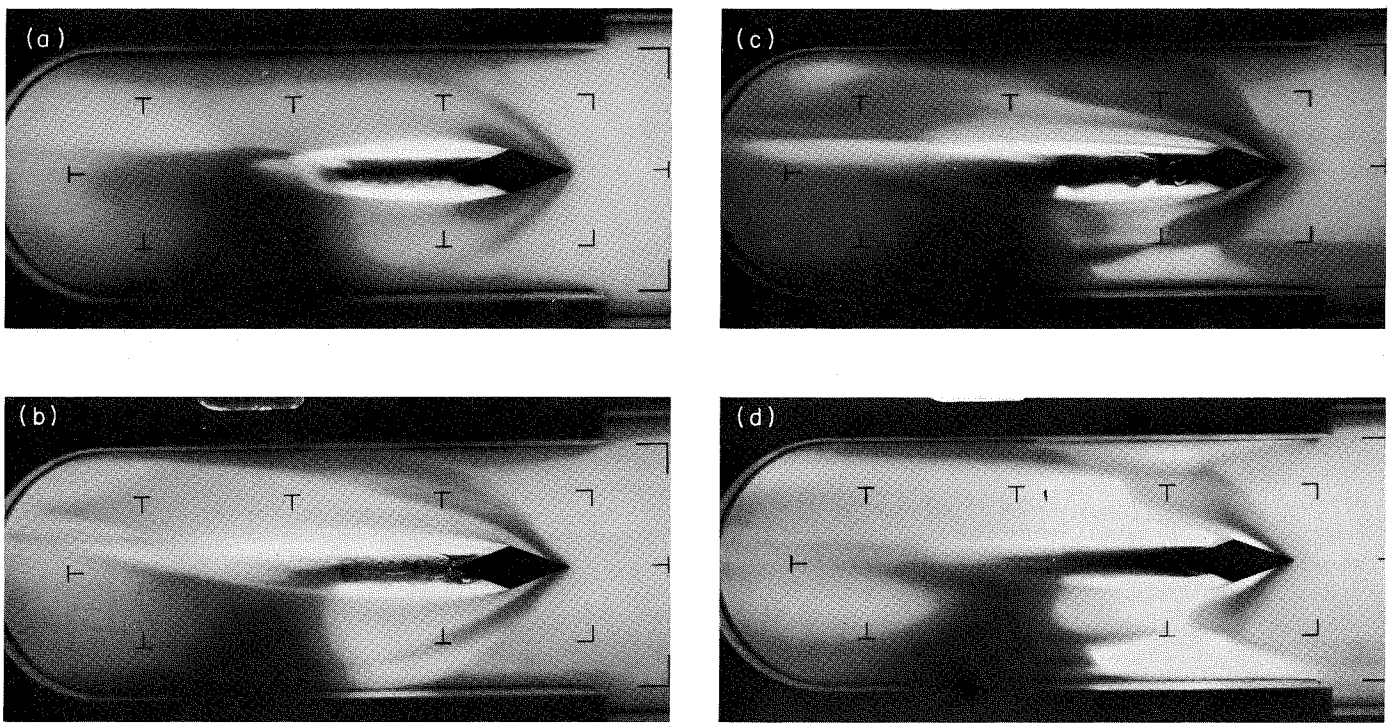

Fig. V-94. Supersonic flow over a 20° deflection wedge at a constant mixture velocity ($V_1 = 298$ ft/sec), constant volume ratio ($r_{v_1} = 0.9$), and variable pressure [(a) $M_1 = 4.0$, (b) $M_1 = 9.30$, (c) $M_1 = 11.3$, (d) $M_1 = 12.5$]

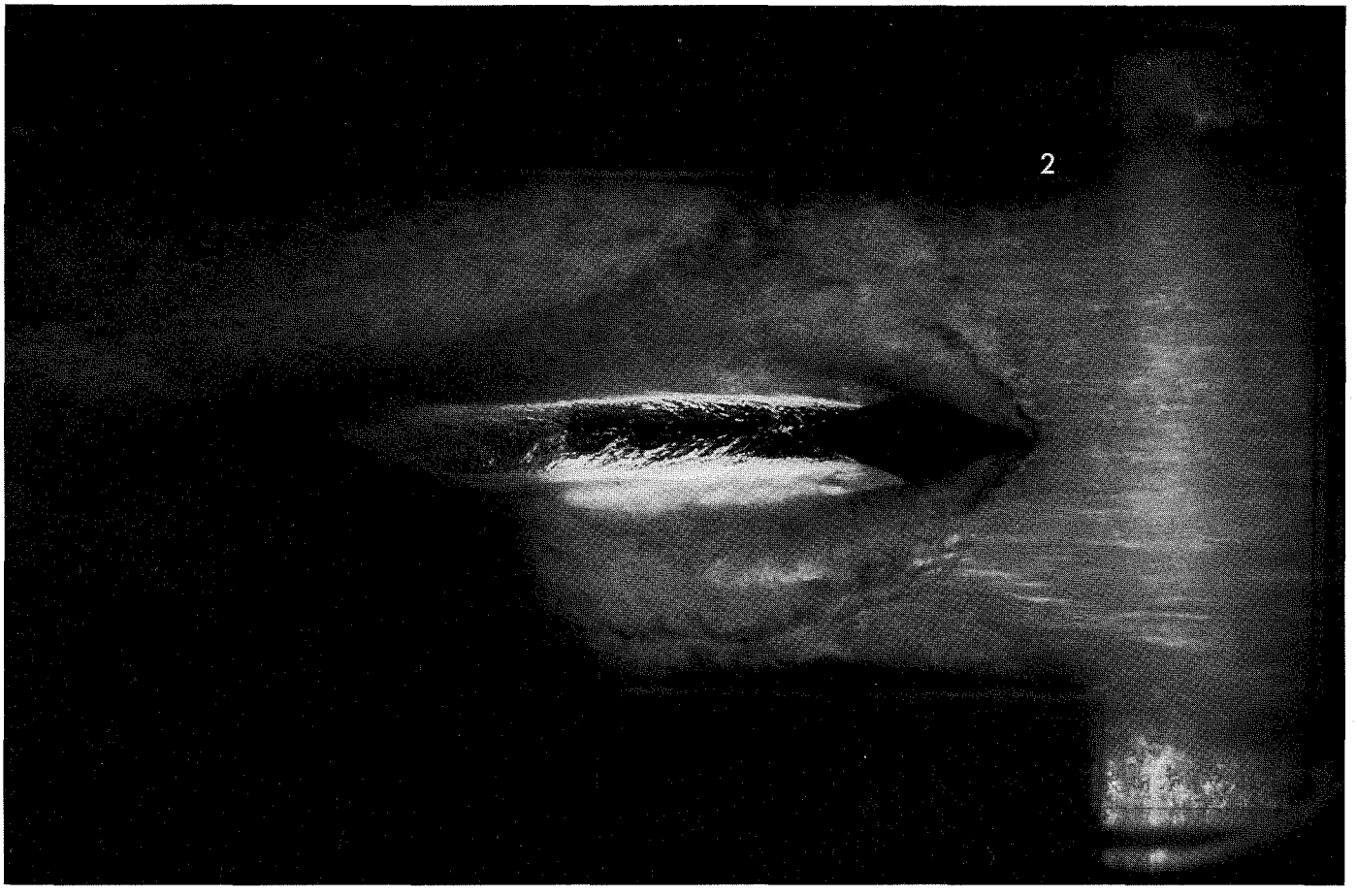

Fig. V-95. One-half-μsec exposure of supersonic flow over a 20° deflection wedge at a Mach number ($M_1 = 4.0$)

The form of the shock at higher Mach numbers, the final question answered by the 20° wedge, is shown in pictures (b), (c), and (d) of Fig. V-94. At higher Mach numbers, the shock front tends to approach the leading surfaces of the wedge just behind the leading edge, but β is relatively unaffected by the higher Mach numbers, as predicted by the isothermal theory.

Figure V-97 shows a tunnel-starting sequence for the 20° wedge at a ½-μsec exposure. In picture (a) where $M_1 = 0.8$, a pressure gradient of strength sufficient to drive the bubbles outward has developed near the wedge. At picture (c), traces of the unattached shock in the form of change in the bubbles' direction can be seen, but, as the flow reaches a Mach number of 1.4 in picture (d), the inlet becomes choked, and a normal shock coincident with the leading edges of the upper and lower boundary layer knives is evident. The shock is strengthened as the Mach number increases to 2.5, but remains at the knife edges as shown in picture (e). In picture (f) of Fig. V-97, the liquid velocity is increased to over 100 ft/sec with a pressure increase sufficient to keep the Mach number at 2.5. No significant change occurs in the form or position of the essentially normal shock wave as long as the effective Mach number remains constant.

As the Mach number reaches the 3.5 value shown in picture (g), the normal shock moves back to the vicinity of the wedge's leading edge. The Mach number has reached 4.6 by picture (h), and the shock wave has assumed the near but detached form shown in picture (a) of Fig. V-94.

4. Dynafax Analysis of Double-Wedge Flows

Dynafax sequences of approximately 133 frames per sequence at 26,000 frames/sec were made for the majority of flow conditions previously described for the 4°, 10° and 20° deflection wedges. Slow-projected (3 to 8 frames/sec)

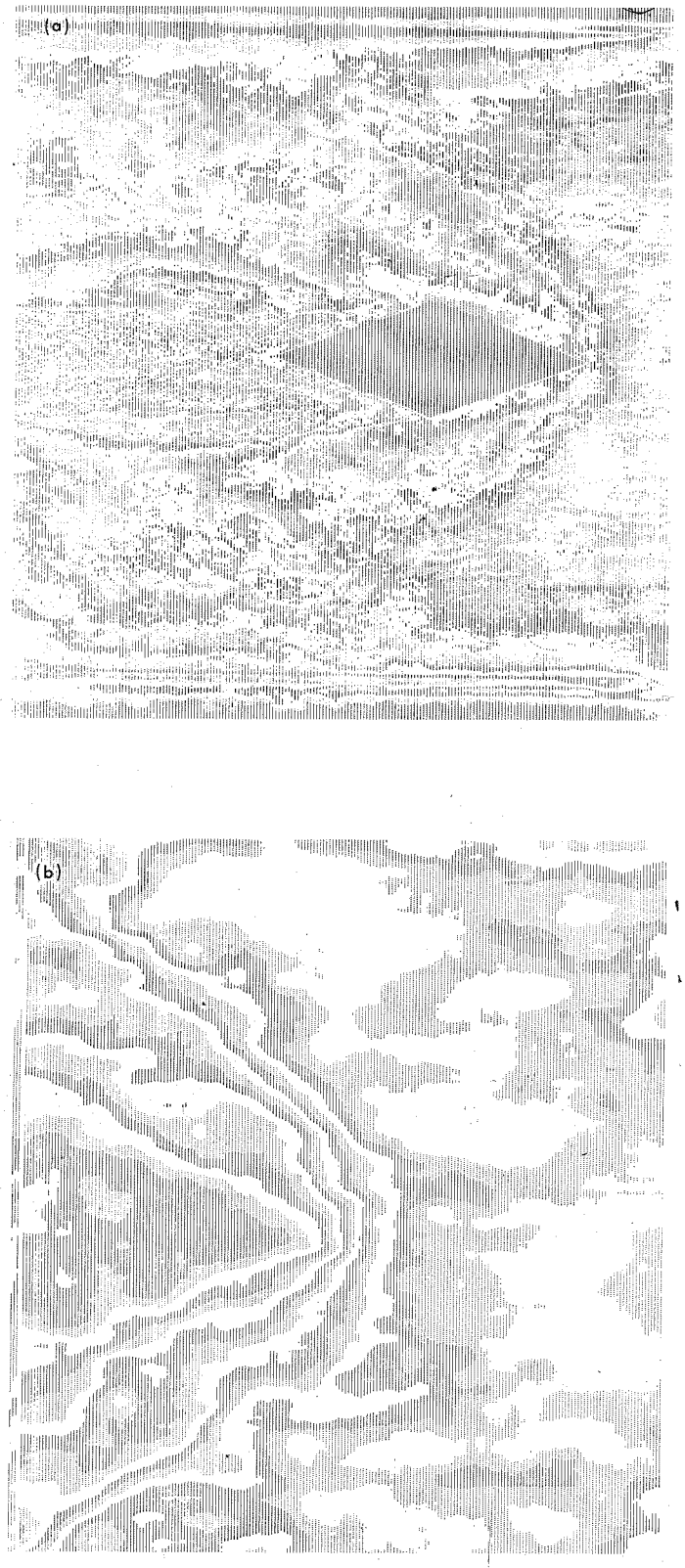

Fig. V-96. Isodensity tracings made from the negatives of supersonic flow over a 20° deflection wedge at $M_1 = 4.0$; ½-μsec exposure [(a) tracing of 4 × 5 negative; (b) enlargement of a Dynafax frame]

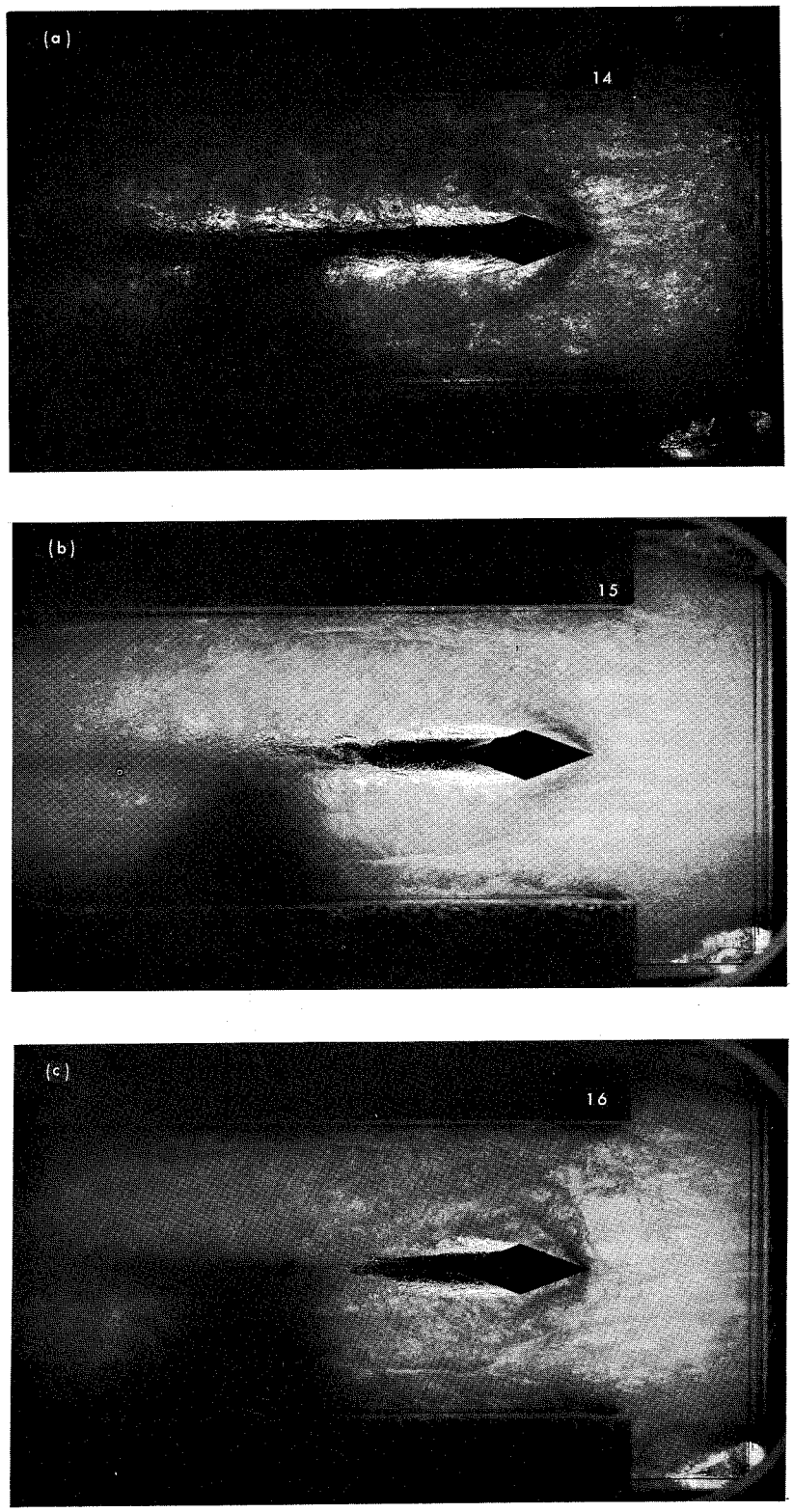

Fig. V-97. Tunnel starting sequence of flow over a 20° deflection wedge; ½-μsec exposure [(a) $V_1 = 50$ ft/sec, $M_1 = 0.8$, (b) $V_1 = 75$ ft/sec, $M_1 = 1.1$, (c) $V_1 = 100$ ft/sec, $M_1 = 1.2$, (d) $V_1 = 125$ ft/sec, $M_1 = 1.4$, (e) $V_1 = 200$ ft/sec, $M_1 = 2.5$, (f) $V_1 = 318$ ft/sec, $M_1 = 2.5$, (g) $V_1 = 259$ ft/sec, $M_1 = 3.5$, (h) $V_1 = 318$ ft/sec, $M_1 = 4.6$]

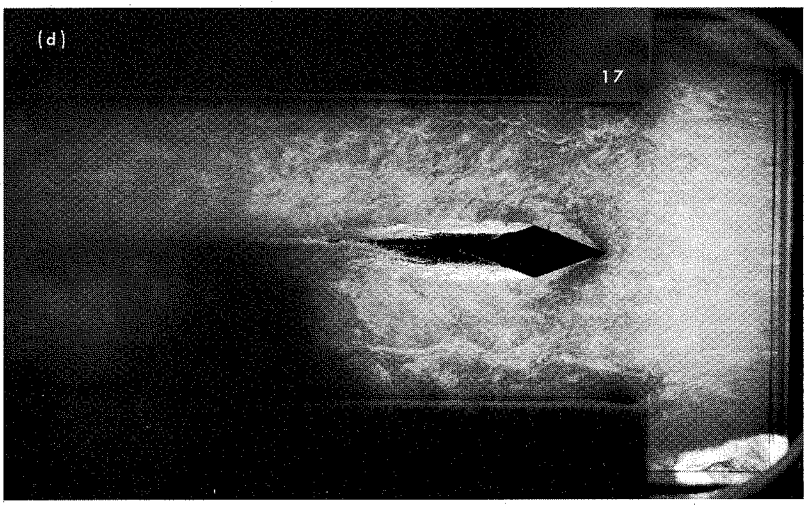

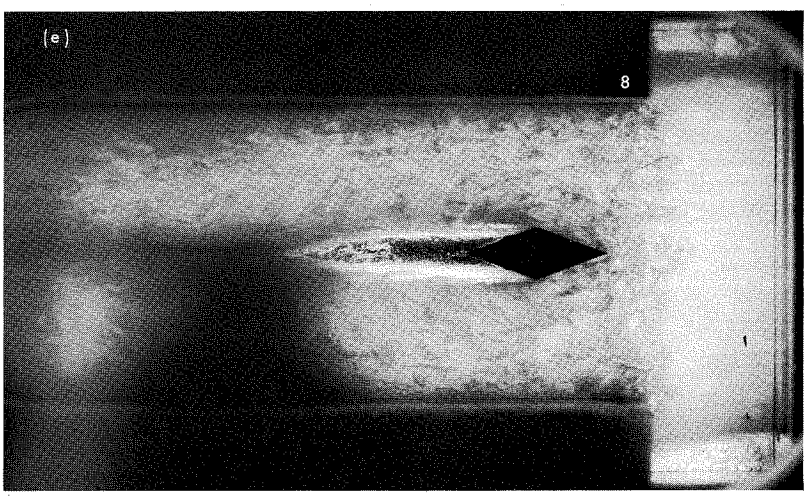

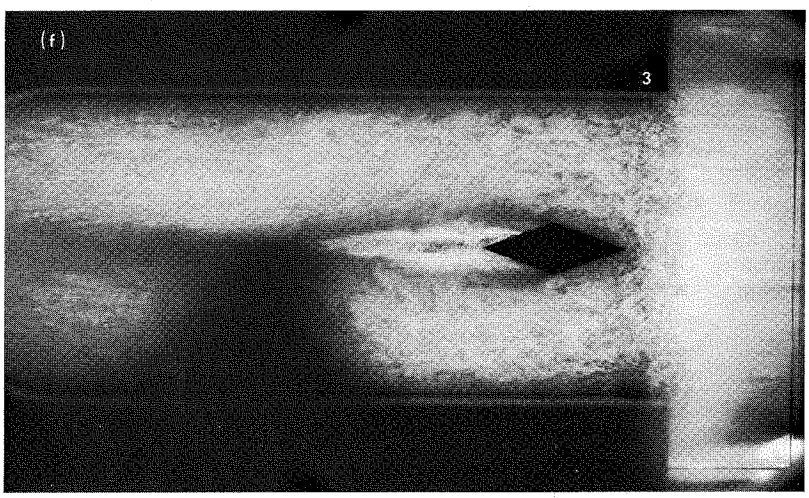

Fig. V-97 (contd)

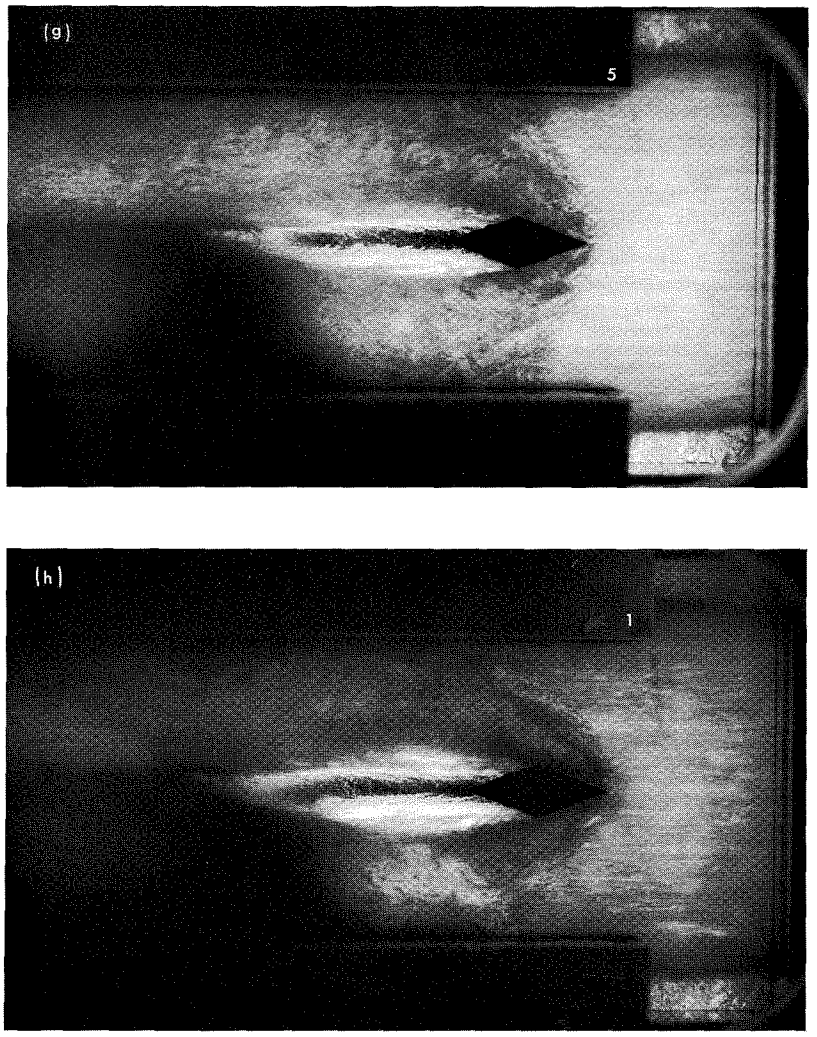

Fig. V-97 (contd)

motion analysis of these sequences was intended to determine the direction and velocity of the two-phase flow in the various positions of the test section both upstream and downstream of any shock phenomena. Six frames from a sequence of flow about a 10° wedge are shown in Fig. V-98.

Because of the original exposure time of 2.5 μsec/frame that reduced definition from that of the ½-μsec still frames, the twenty-fold magnification, and the rephotographing required to place the Dynafax frames in sequence, the quality of the individual prints was far less than that of the ½-μsec exposures. The dark strata of bubbles and the lighter regions of liquid, however, could be followed through the shock structure.

Directional movement through the shock structure was both similar and different from that generally attributed to a single-phase gaseous flow. Upon entering the shock region, the upstream two-phase mixture was observed to turn toward the oblique shock onto a path generally parallel with the deflection angle of the wedge surface. With this condition, the similarity with single-phase flow ends. Superimposed upon the general flow was the relative movement of some of the connected gas-bubble strata under the influence of the pressure gradients encountered in the shock structure.

Gas bubble movement appears to begin at the leading edge of the wedge and appears to move outward along the leading edge of the shock wave, as shown in Fig. V-99. Between the leading edge of the shock and the wedge surface there is a bubble movement generally along rays from the leading edge of the wedge. Apparently, a portion of the gas, that which is in the configuration having the lowest C_d value, is deflected outward along the rays, and

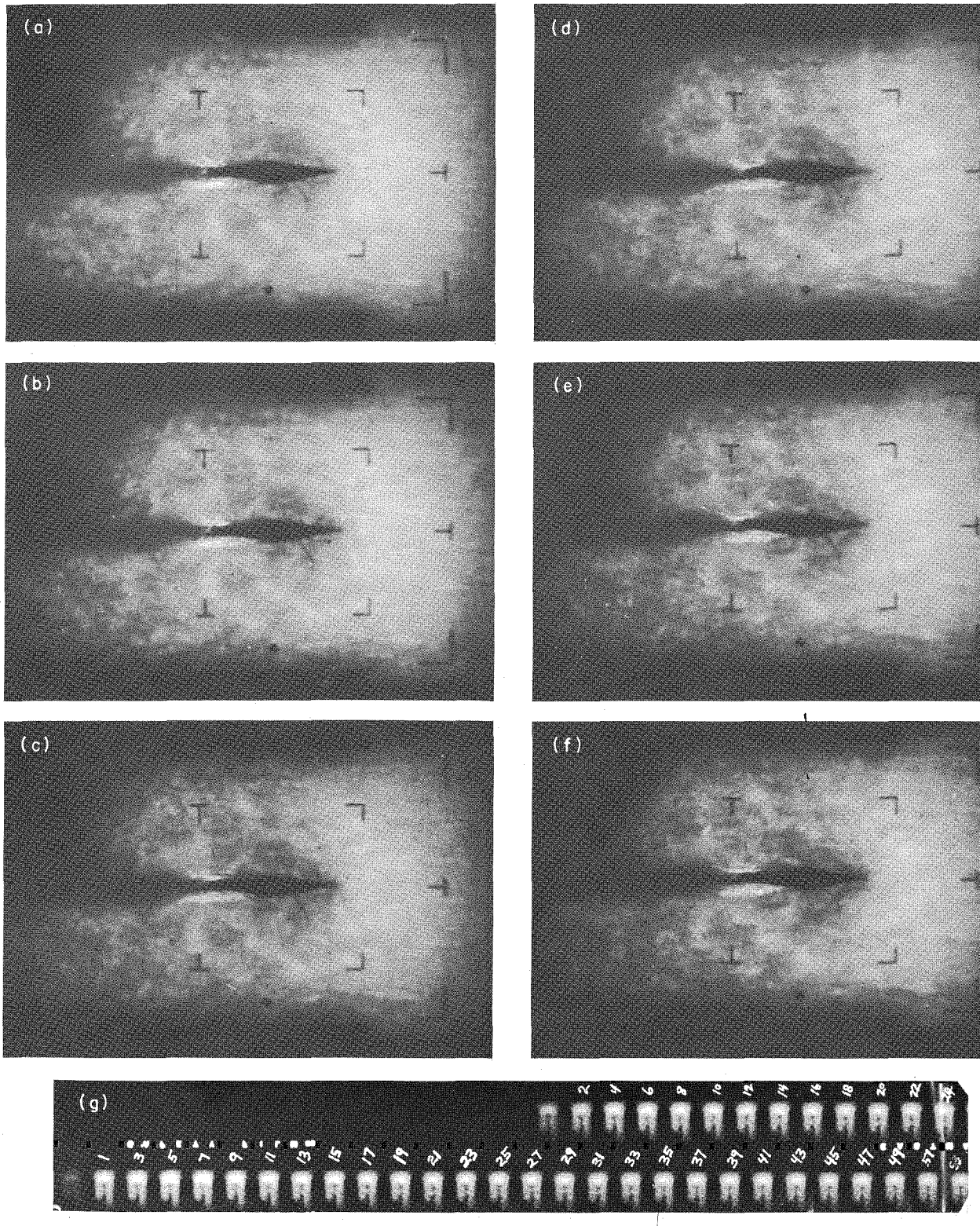

Fig. V-98. Frames from Dynafax sequence (listed alphabetically in the sequence taken) of supersonic flow over a 10° deflection wedge at a frame rate of 25,000 frames/sec, 2.5-μsec exposure per frame; $V_1 = 150$ ft/sec. Frame (g) is a typical portion of a Dynafax negative

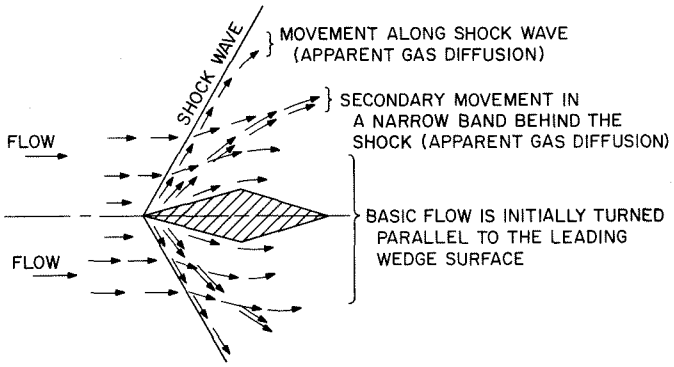

Fig. V-99. Schematic of supersonic flow patterns over a double wedge

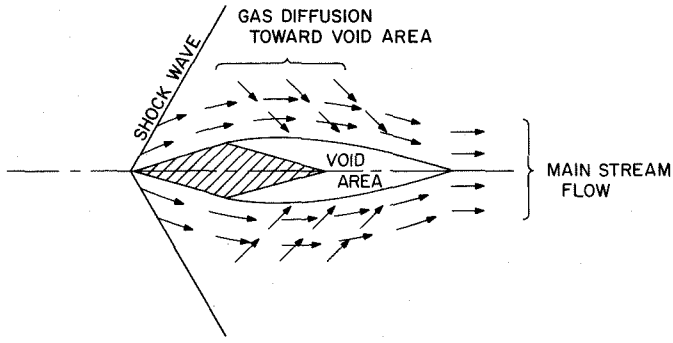

Fig. V-100. Schematic of supersonic flow patterns over a double wedge showing gas diffusion directions

the remaining mixture moves more or less parallel to the deflection surface. The superimposed gas flow appears to be continuous, but in reality moves under the influence of the pressure gradient according to the C_d value of its local configuration, which changes because of the turbulence. Gas which initially began moving along the oblique shock, for instance, will be deflected into the general flow and be replaced by gas entering the shock structure in a low C_d configuration with respect to the slight pressure gradient parallel with the shock. The result is partial separation of the phases as the mixture passes through the oblique shock: the liquid tends to remain near the wedges, and the gas tends to diffuse outward toward the regions farthest from the leading wedge surface.

As the flow passes the wedge apex, a transverse, negative pressure gradient not only tends to bend the flow toward the symmetrical void area behind the wedge, but tends to diffuse gas through the flow toward the void (Fig. V-100).

The appearance of a reflected shock structure downstream of the wedge continues to create regions of varying volume ratio due to pressure gradients associated with the original shock structure and the nonisotropic and time-dependent C_d of the gas structure.

Suitable instrumentation that could determine the local volume ratio in regions behind the oblique shock was unknown at the time of the test.

The gas-phase migration constitutes a portion of the overall relaxation process and consideration of proximity to the deflecting surface. True downstream conditions are difficult to obtain for the oblique shock wave, particularly in view of the lateral nonuniform void fraction distribution caused by the gas migration. The generally close agreement of the isothermal oblique shock theory with the measurements of shock angle (β) and pressure ratio (P_2/P_1) made in the various test series gives substantial credibility to this theory for representation of the basic nature of the two-phase oblique shock. Any further accuracy and definition, particularly in the initial stage of development of an oblique shock wave, would necessarily require consideration of the interphase movements and relaxation processes along with their proximity to the deflecting surface, which would result in a considerable increase in the complexity of the governing system of equations.

Nomenclature

c velocity of sound in mixture (ft/sec)

M Mach number

P static pressure (lb_f/ft^2)

r_m gas-to-liquid mass ratio (static)

r_v gas-to-liquid volume ratio (static)

u X component of mixture velocity (ft/sec)

$\bar{u}$ component of mixture velocity normal to the shock wave (ft/sec)

u' component of mixture velocity parallel to inclined plane (ft/sec)

V component of velocity (ft/sec)

β angle of shock wave with the horizontal (deg)

θ angle of inclined plane with the horizontal (deg)

ρ mixture density ($slugs/ft^3$)

ρ_l density, liquid phase ($slugs/ft^3$)

Subscripts

1 upstream of oblique shock

2 downstream of oblique shock

VI. Stagnation Pressure Recovery

The velocity of a two-phase mixture or, in particular, the velocity of either phase separately is difficult to measure. In single-phase media, the total head probe or pitot-static probe in which the dynamic pressure is measured can be related to the velocity of flow. For subsonic single-phase flow, compressibility effects can be compensated in the measurement of dynamic pressure at higher velocities. The presence of a normal shock with a subsequent isentropic stagnation of flow at the probe tip in supersonic single-phase flow can be correlated to the measured pressure from which, in turn, velocity can be determined.

In two-phase flows, the total head probe is sensitive to the velocities of component phases, and the void ratios of the phases. If neither the void ratio nor velocities are known, the total head probe is of little use in two-phase flow. If at least the void ratio is known, the problem of how well the measured stagnation pressure recovery can be correlated to the characteristic phase velocities of the flow still remains.

A. Fundamentals

1. Isentropic Stagnation Pressure Recovery

First, the relationship for isentropic pressure recovery will be developed. If a mixture can decelerate over a finite distance with a change in cross-sectional area, the restriction of Eq. (IV-1) does not apply and the momentum equation at each point is

$$\rho V dV = -dP \tag{VI-1}$$

The expression VdV can be replaced by $dV^2/2$ and, substituting for mixture density from Eq. (I-3), the equation becomes

$$dV^2 = -\frac{2(1+r_v)}{\rho_l(1+r_m)}dP \tag{VI-2}$$

Integrating the left side for a velocity change over a pressure rise from P_1 to P_2 gives:

$$V^2\Big|_{V_1}^{V_2} = -2\int_{P_1}^{P_2}\frac{1}{\rho_l}\frac{(1+r_v)}{(1+r_m)}dP \tag{VI-3}$$

For pressure less than 1000 psi, $\rho_l \sim$constant; r_m will be a constant for nonstratified steady flow conditions:

$$V_1^2 - V_2^2 = \frac{2}{\rho_l(1+r_{m_1})}\int_{P_1}^{P_2}(1+r_v)\,dP \tag{VI-4}$$

From the isothermal equation of state, Eq. (I-4), $r_v P =$ constant that can be chosen as $r_{v_1} P_1$:

$$V_1^2 - V_2^2 = \frac{2}{\rho_l (1 + r_{m_1})} \int_{P_1}^{P_2} \left(dP + r_{v_1} P_1 \frac{dP}{P} \right) \qquad \text{(VI-5)}$$

Integrating the right side of Eq. (VI-5),

$$V_1^2 - V_2^2 = \frac{2}{\rho_l (1 + r_{m_1})} \left[P_2 - P_1 + r_{v_1} P_1 \ln \left(\frac{P_2}{P_1} \right) \right] \qquad \text{(VI-6)}$$

Rearranging Eq. (VI-6),

$$P_2 = P_1 + \frac{1}{2} \rho_l (1 + r_{m_1}) (V_1^2 - V_2^2) - r_{v_1} P_1 \ln \left(\frac{P_2}{P_1} \right) \qquad \text{(VI-7)}$$

which represents the stagnation pressure recovery possible in shock-free isentropic flow. To distinguish this pressure from the downstream pressure of normal shock flow, stagnation pressure recovery will be designated P_3.

2. Normal Shock Plus Isentropic Stagnation Pressure Recovery

The introduction of a blunt probe tip into supersonic two-phase flow should create an unattached shock ahead of the probe, followed by an isentropic deceleration of the mixture to zero movement at the probe entrance (Fig. VI-1).

The section of the unattached shock directly ahead of the probe on the center line can be considered a normal shock, and, from isothermal normal shock theory, the pressure rise across the shock is given by Eq. (IV-19):

$$P_2 = \rho_l V_1^2 r_{v_1} \frac{(1 + r_{m_1})}{(1 + r_{v_1})^2}$$

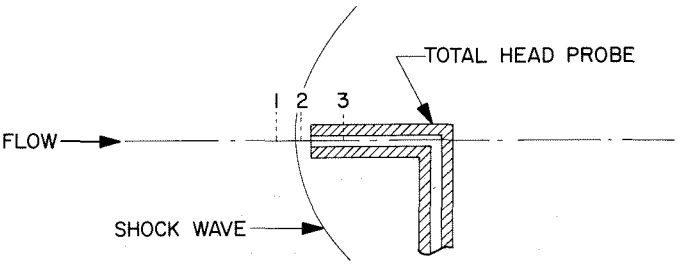

Fig. VI-1. Schematic of shock wave in front of pressure probe body

The isentropic slowdown begins at point 2, Fig. VI-1; the pressure at the probe tip is the sum of the pressure rise across the shock, and the isentropic stagnation pressure recovery. Substituting the normal shock pressure for P_1 in Eq. (VI-7), and writing the final pressure in terms of P_4 to distinguish it from the static and all-isentropic pressure recovery,

$$P_4 = \rho_l V_1^2 r_{v_1} \frac{(1 + r_{m_1})}{(1 + r_{v_1})^2} + \frac{1}{2} \rho_l (1 + r_{m_1}) (V_1^2 - V_2^2) - \rho_l V_1^2 r_{v_1}{}^2 \frac{(1 + r_{m_1})}{(1 + r_{v_1})^2} \ln \left[\frac{P_4 (1 + r_{v_1})^2}{\rho_l V_1^2 r_{v_1} (1 + r_{m_1})} \right] \qquad \text{(VI-8)}$$

The contention that a detached shock should appear ahead of the probe inlet is well confirmed in Fig. II-24. The total head probe, positioned such that the probe body protrudes completely through a normal shock in the duct, has a detached shock just upstream of the tip inlet. However, from analysis of the shock pressure profiles of Section IV, the distance required for the completion of the relaxation processes in a normal shock is many times the distance between the shock leading edge and the probe inlet. Consequently, the probe is not sampling the isentropically stagnated downstream flow, but a partially compressed stagnated flow. Therefore, neither approach is completely valid for a supersonic stagnation pressure recovery probe. This will become more apparent in the discussion that follows.

B. Results

Total head probe surveys were made both ahead of and behind normal shocks over the full range of flow conditions used in the supersonic two-phase tunnel. For each data point shown in the figures referenced below, between two hundred and three hundred cross-sectional points were surveyed in the flow, and averaged to give an accurate representation of the core flow for those conditions of P_1, V_1, r_m, and r_{v_1} selected. The qualities of the upstream

flow were well-known, allowing easy calculation of the isothermal stagnation pressure recoveries according to Eqs. (VI-7) and (VI-8).

The measured stagnation pressure in free flow is shown in Figs. VI-2 and VI-3 as a function of upstream liquid velocity V_{l_1}. In Fig. (VI-2), the theoretical isentropic stagnation pressure recovery relationship for the given data point conditions is plotted for comparison. The measured stagnation pressure recoveries closely follow the isentropic theory up to a liquid velocity of about 270 ft/sec, and fall away to 10% lower than the theoretical values at a velocity of 335 ft/sec.

In comparison with the normal shock plus isentropic stagnation pressure recovery plotted in Fig. VI-3, the measured values are generally in excess of the theory by about 9%. Fig. VI-3 is, in addition, a plot of the measured values of stagnation pressure downstream of a normal shock. These values are about 4% above the theory at velocities up to 200 ft/sec, and, at the highest velocity of 335 ft/sec, approach to within a few percent of the theoretical value.

It would seem clear, then, that stagnation pressure recoveries sampled downstream of the shock structure at a distance sufficient for completion of the relaxation processes would represent isentropic stagnation in subsonic flow in accordance with Eq. (VI-7). The fact that the

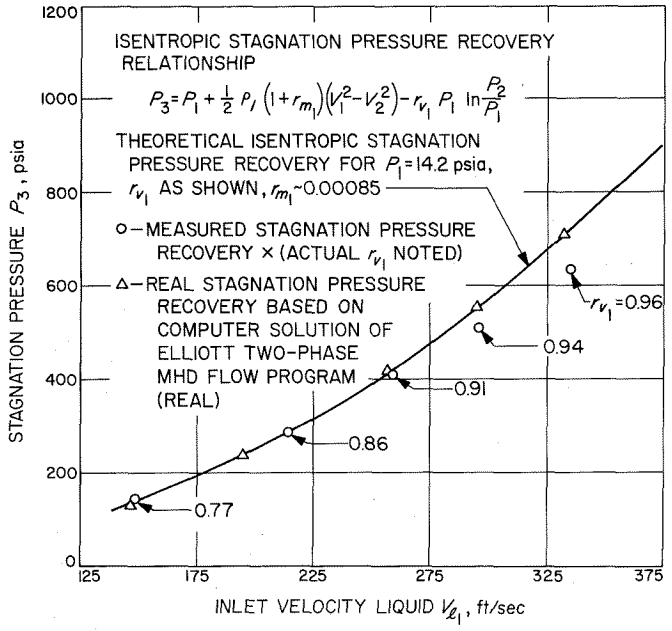

Fig. VI-2. Stagnation pressure as a function of liquid velocity at actual tunnel volume ratio

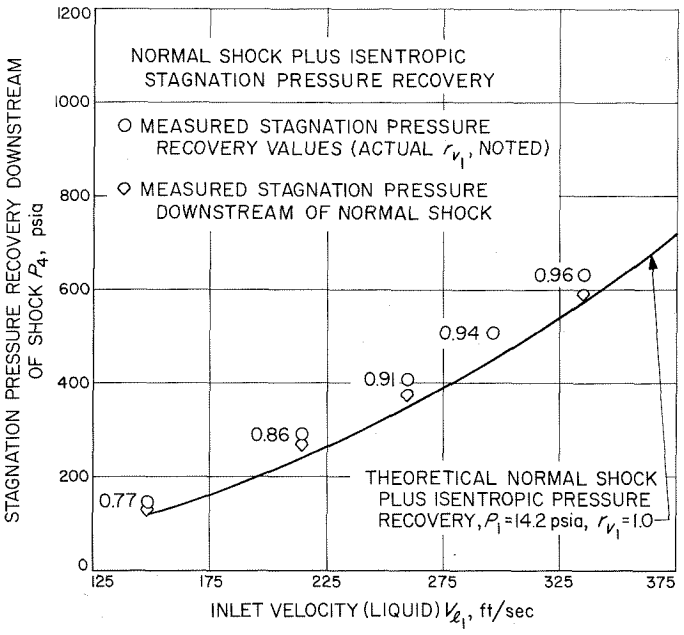

Fig. VI-3. Stagnation pressure measured downstream from a normal shock as a function of the upstream liquid velocity

supersonic flow stagnation pressure recovery measured by the probe is closely approximated by Eq. (VI-7) for a substantial range of mixture velocities suggests a possible decrease in local volume ratio directly ahead of the probe inlet. From the results of the studies of oblique shock, gas-phase migration was found along nonnormal shock geometrics; this could account for the r_v decrease along the center line of the shock symmetry. At velocities above 270 ft/sec, increasing entropy losses along with a relative increase in r_v along the center line most probably contribute to the downward pressure transition from the isentropic curve toward the normal shock plus isentropic stagnation curve.

Figure VI-4 shows the measured stagnation pressure as a function of upstream static pressure for values of liquid velocity. It should be noted that the pressures shown for the highest velocities are slightly in excess of the more accurate values in Fig. VI-2. The curvature of each theoretical curve, however, is surprisingly well duplicated by the data; this further confirms the applicability of Eq. (VI-7) for the lower velocity ranges.

The behavior of Eq. (VI-7) has been investigated over a wide range of static pressures, volume ratios, and liquid velocities. The equation is presented in Figs. VI-5 through VI-18. In Figs. VI-5 and VI-6, P_3 is a function of V_{l_1} for three values of r_{v_1} and three static pressure values; the

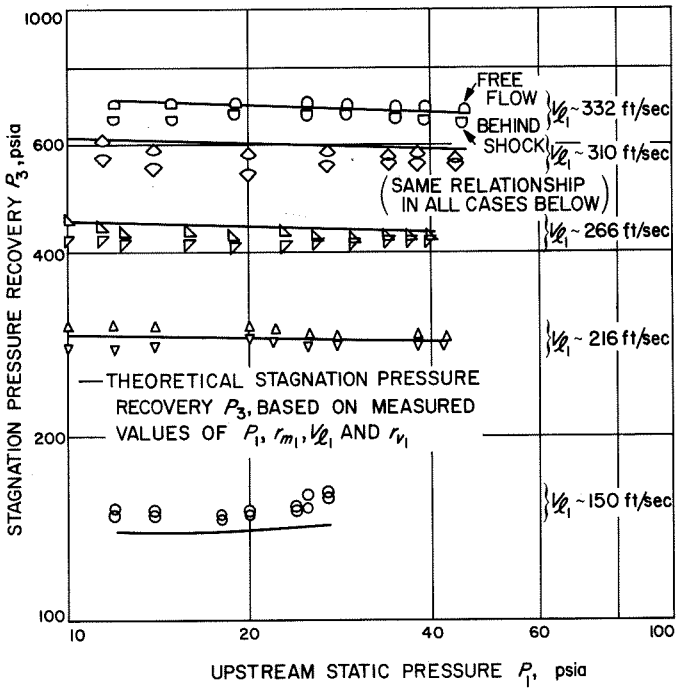

graph shows the general trends with changes in each quantity. In Fig. VI-6, reversal of the influence of stagnation pressure on liquid velocity is obvious for velocities below 200 ft/sec. Figures VI-7 through VI-9 show P_3 as a function of V_{l_1} for a range of r_{v_1} from 0.1 to 10.0; the static pressure P_1 in each figure is fixed.

For a wider range of static pressures, Figs. VI-10 through VI-12 show P_3 as a function of static pressures P_1 for parameters of V_{l_1}; each figure has a fixed value of r_{v_1} equal to 0.1, 1.0 and 10.0, respectively. Figures VI-13 through VI-18 give P_2 as a function of r_{v_1} for parameters of velocity, with each figure at a fixed value of static pressure P_1 from 4.0 to 500 psia. These graphs should be used to determine quickly the general influence of each of the variables P_1, r_{v_1}, and V_{l_1} on P_3, and to generally correlate the measured stagnation probe pressure values.

Fig. VI-4. Stagnation pressure recovery as a function of upstream static pressure for values of upstream liquid velocity

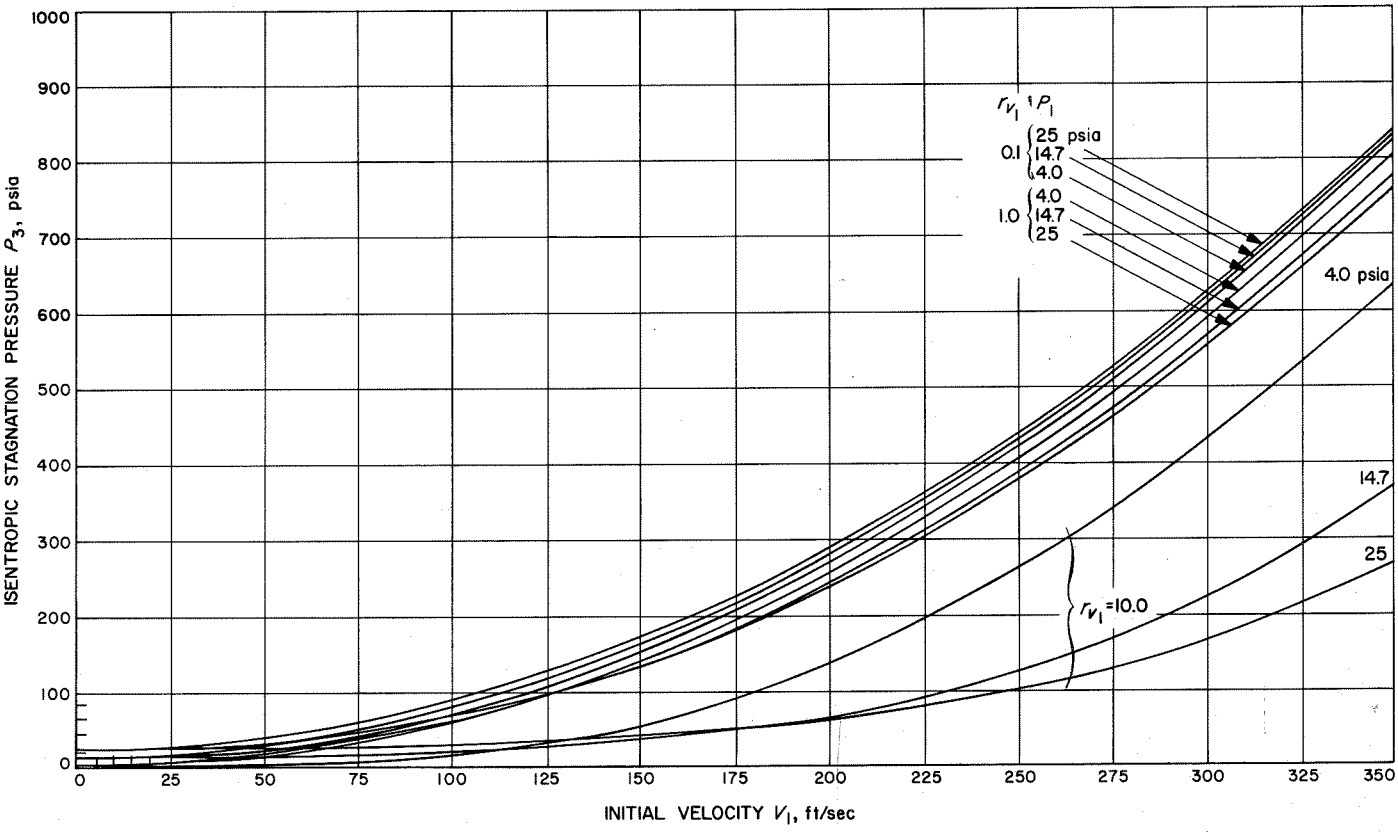

Fig. VI-5. Isentropic stagnation pressure as a function of mixture velocity for values of volume ratio and pressure

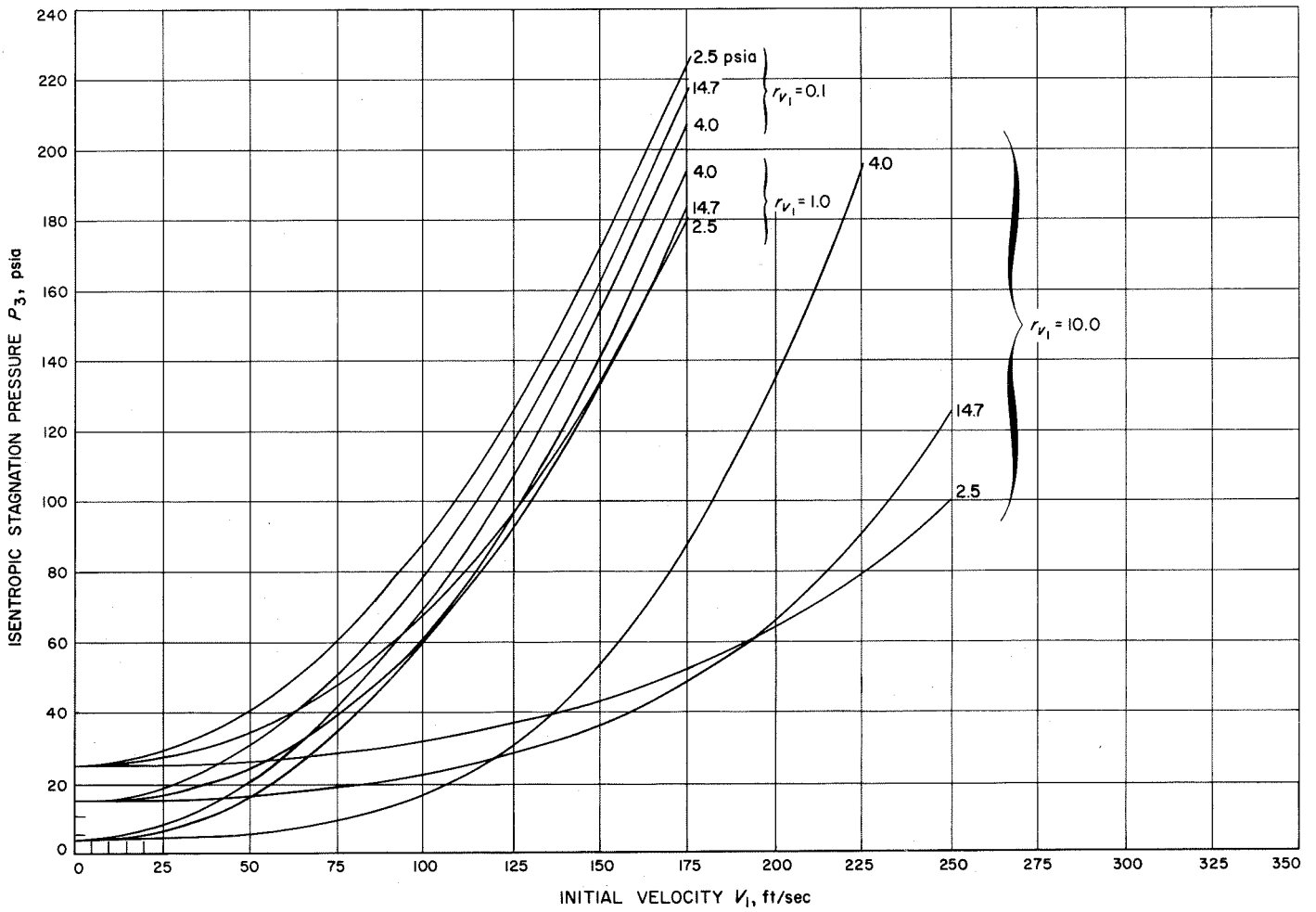

Fig. VI-6. Isentropic stagnation pressure as a function of mixture velocity for values of volume ratio and pressure, expanded scale

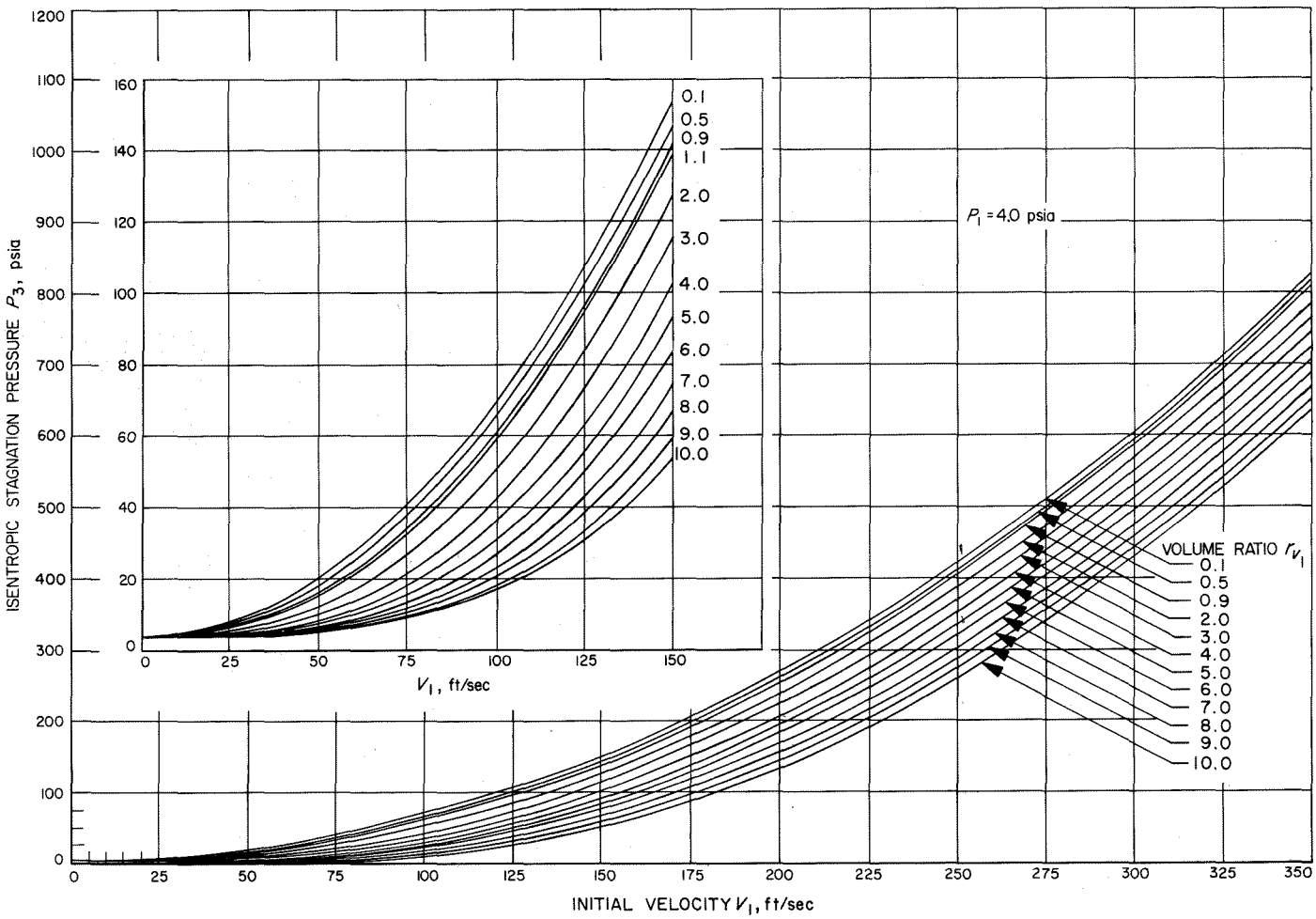

Fig. VI-7. Isentropic stagnation pressure as a function of mixture velocity for values of volume ratio (P_1 = 4.0 psia)

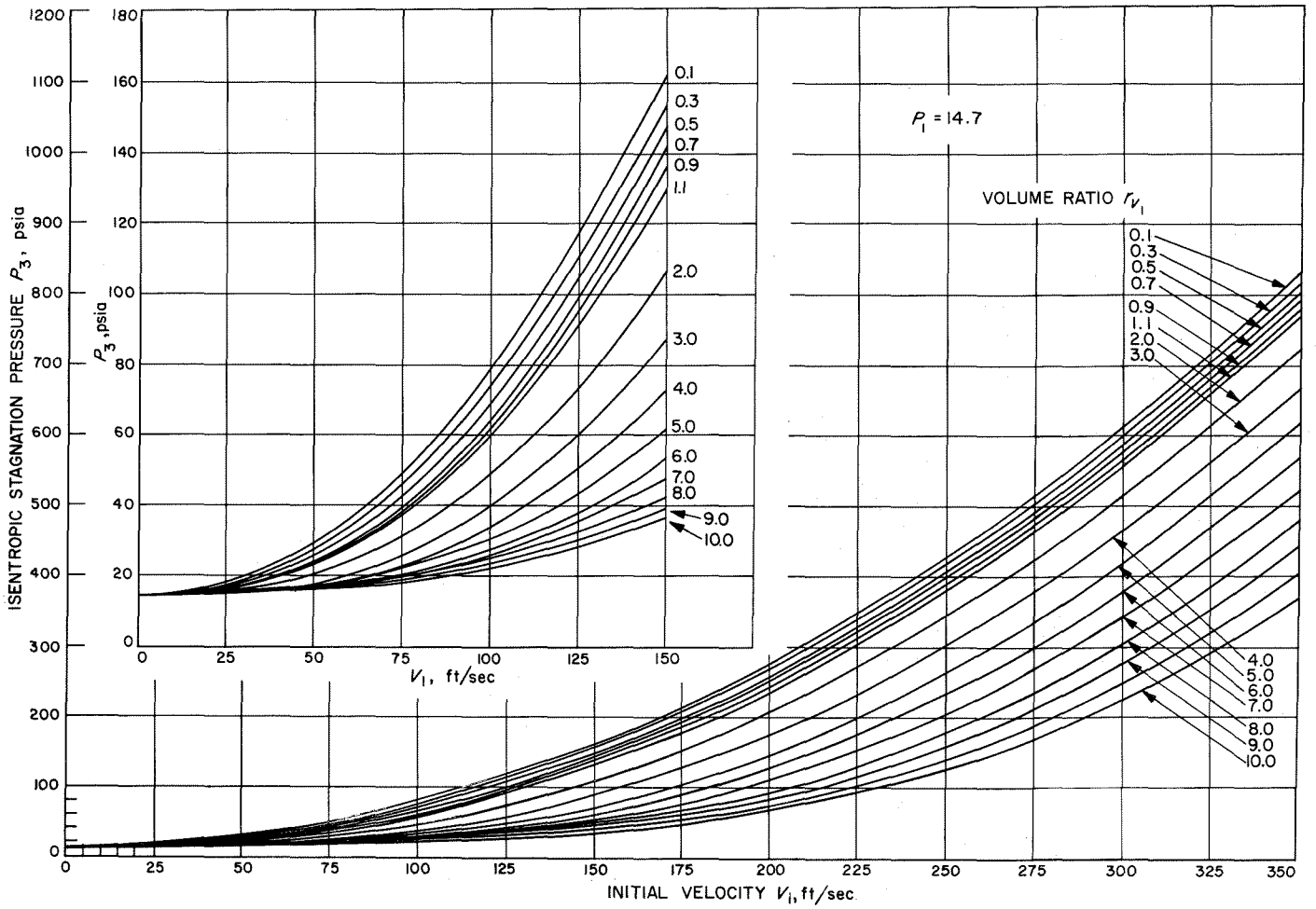

Fig. VI-8. Isentropic stagnation pressure as a function of mixture velocity for values of volume ratio (P_1 = 14.7 psia)

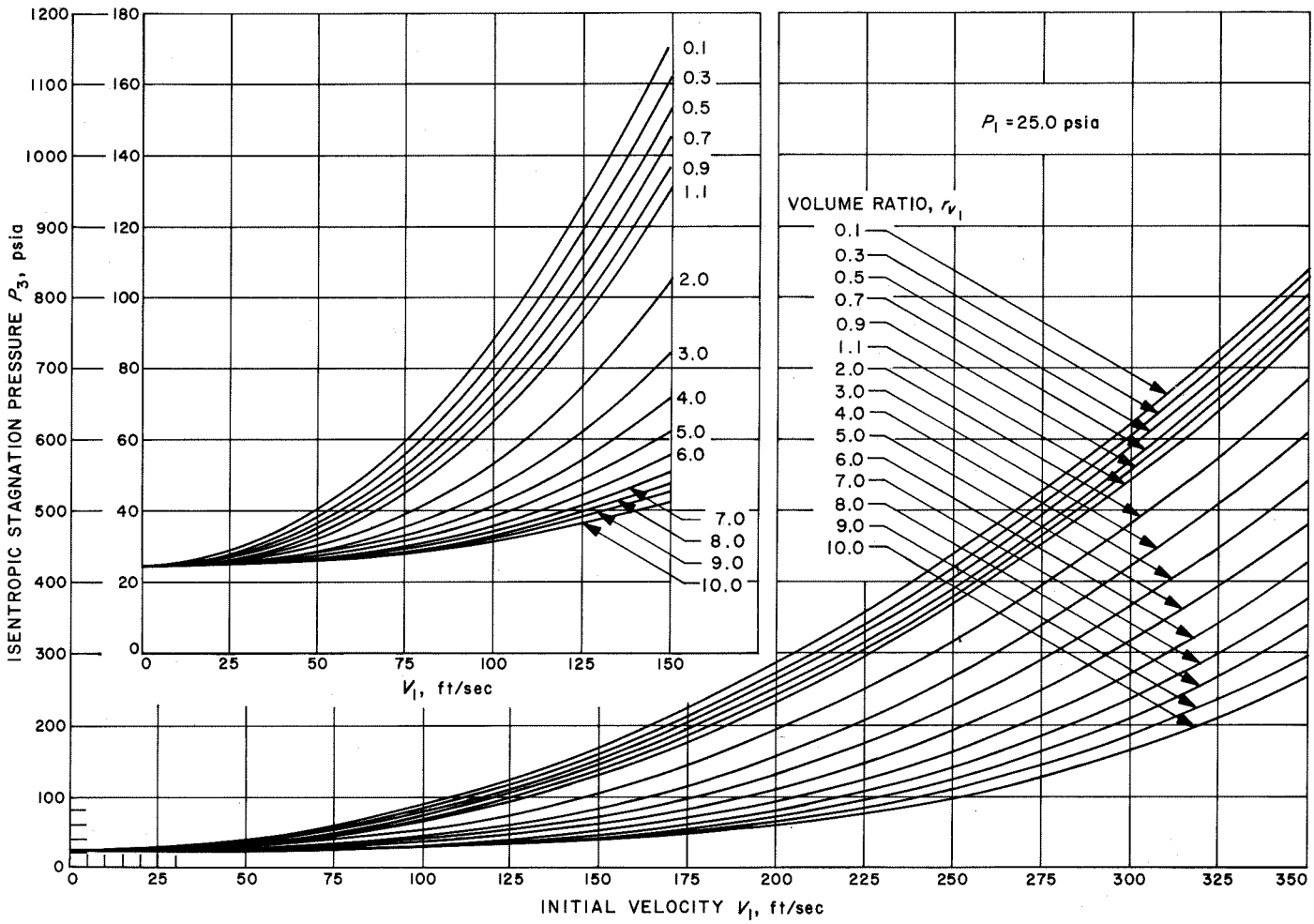

Fig. VI-9. Isentropic stagnation pressure as a function of mixture velocity for values of volume ratio ($P_1 = 25.0$ psia)

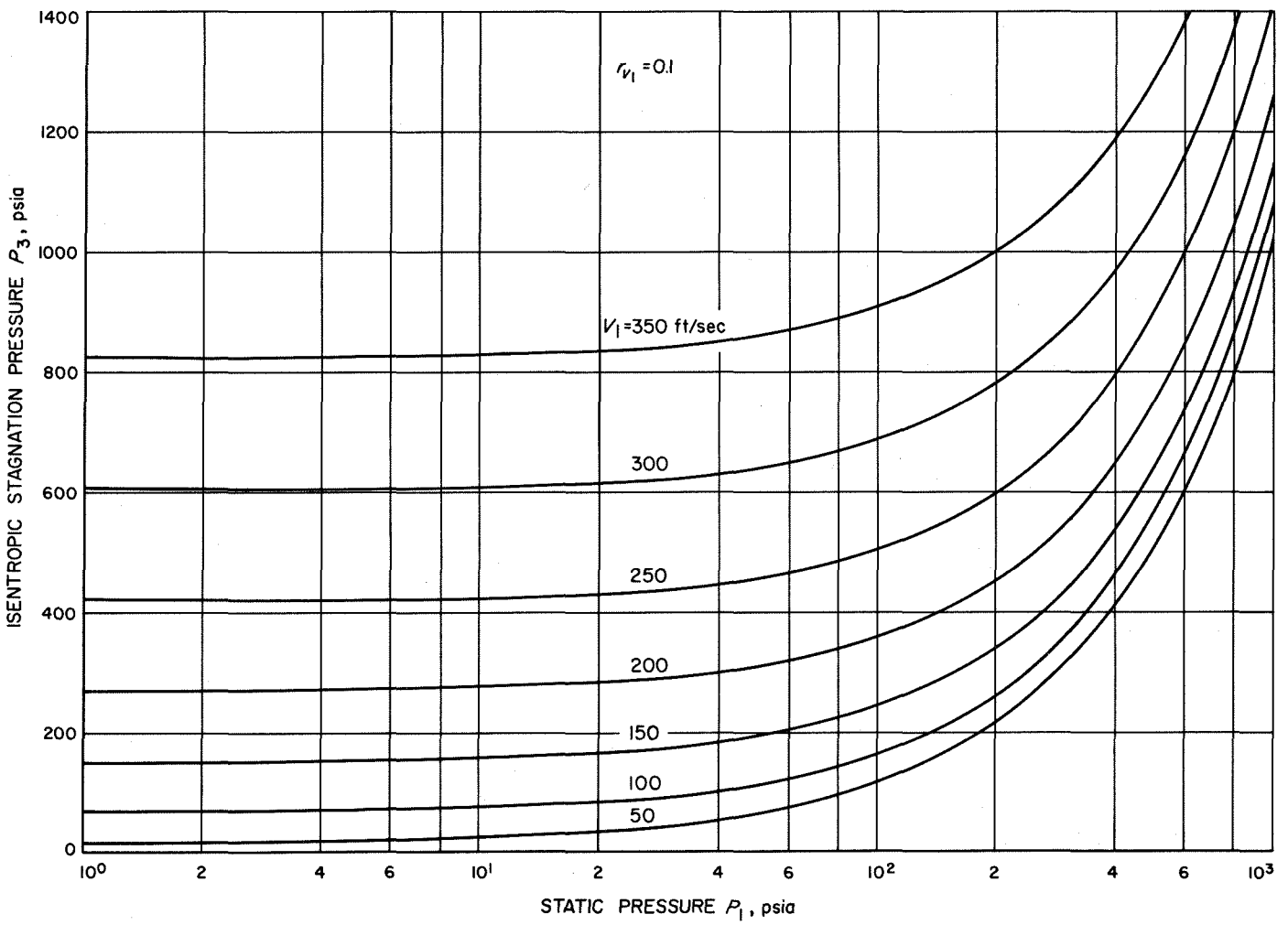

Fig. VI-10. Isentropic stagnation pressure as a function of static pressure for values of mixture velocity ($r_{v_1} = 0.1$)

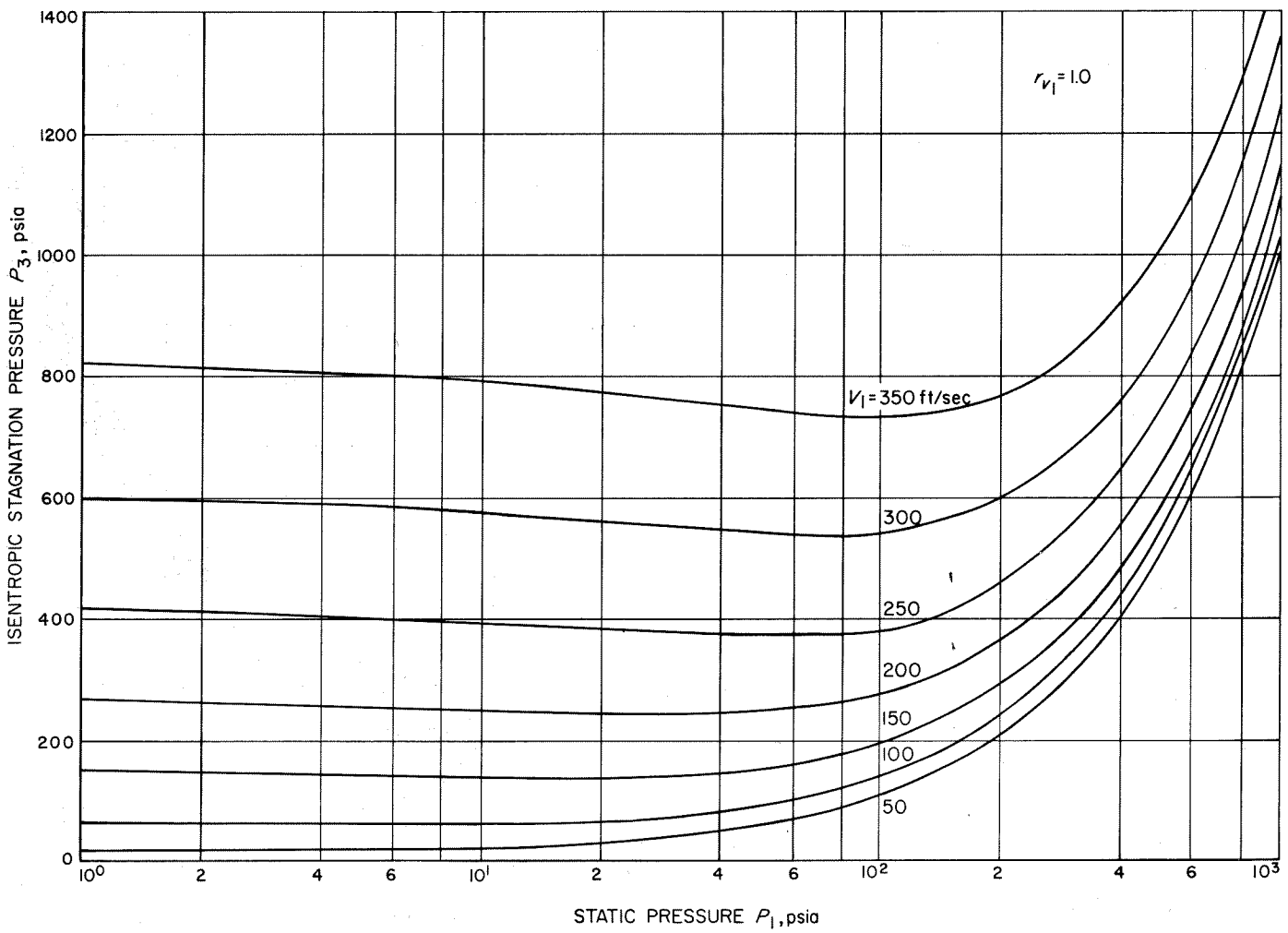

Fig. VI-11. Isentropic stagnation pressure as a function of static pressure for values of mixture velocity ($r_{v_1} = 1.0$)

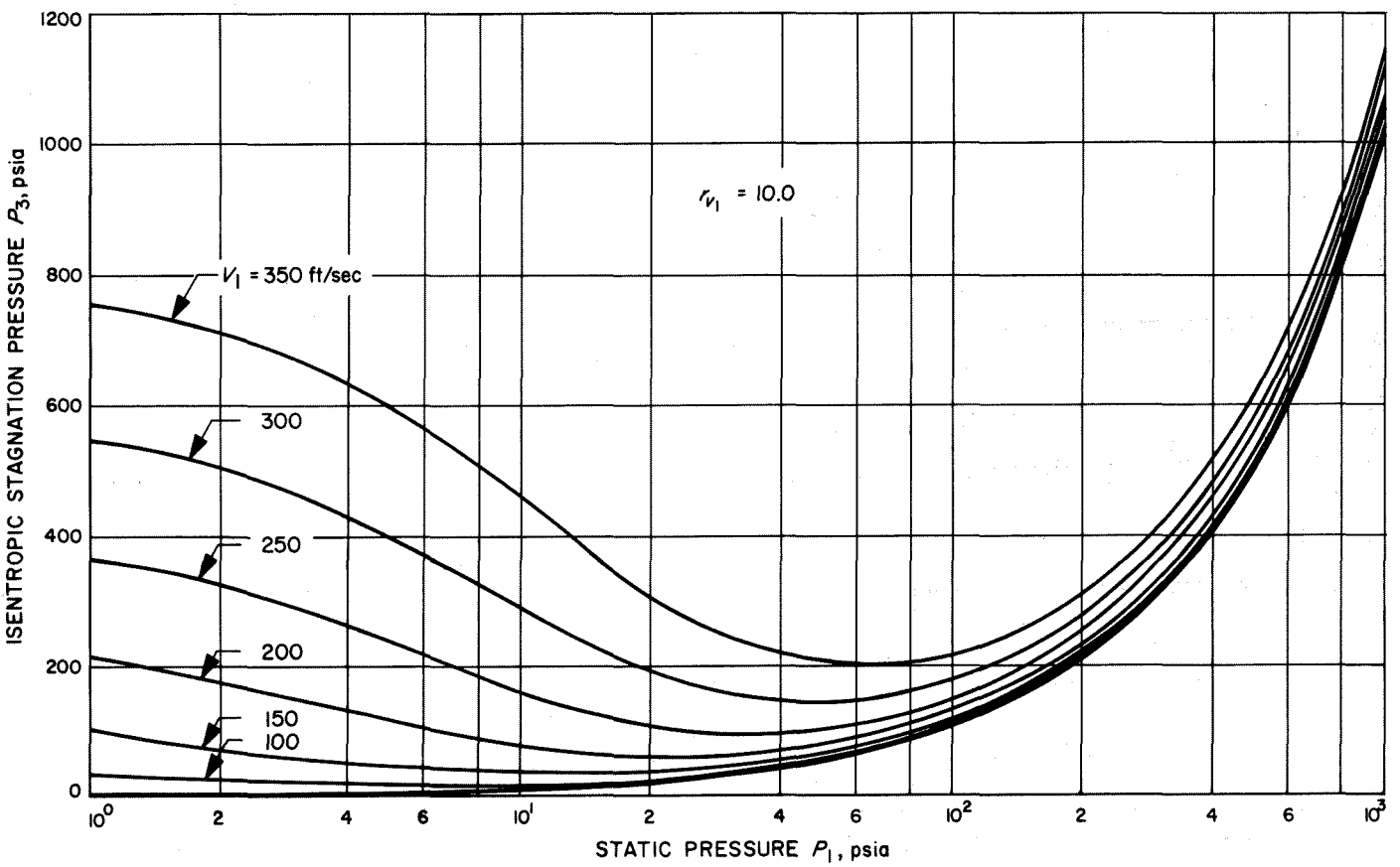

Fig. VI-12. Insentropic stagnation pressure as a function of static pressure for values of mixture velocity ($r_{v_1} = 10.0$)

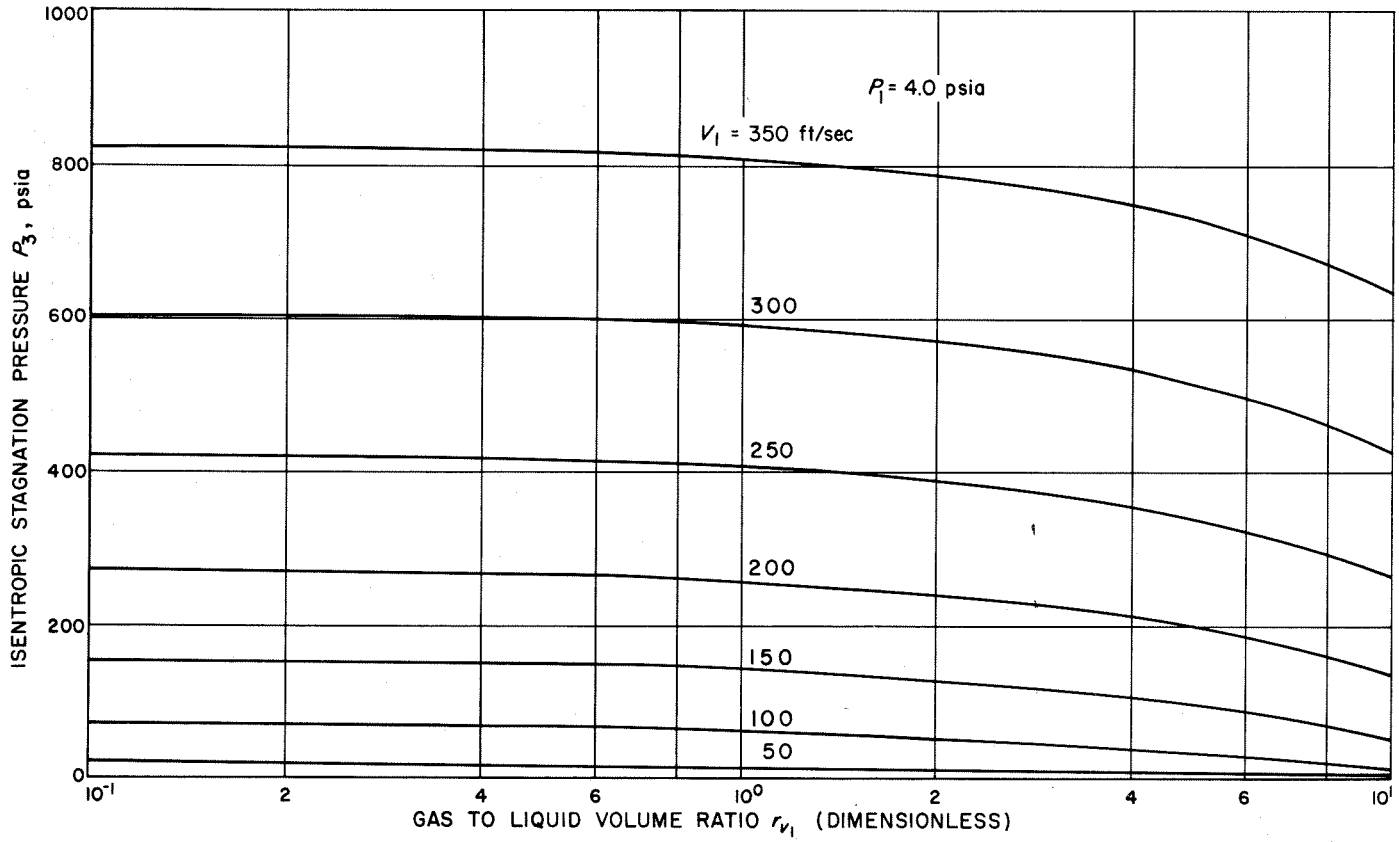

Fig. VI-13. Isentropic stagnation pressure as a function of volume ratio for values of mixture velocity (P_1 = 4.0 psia)

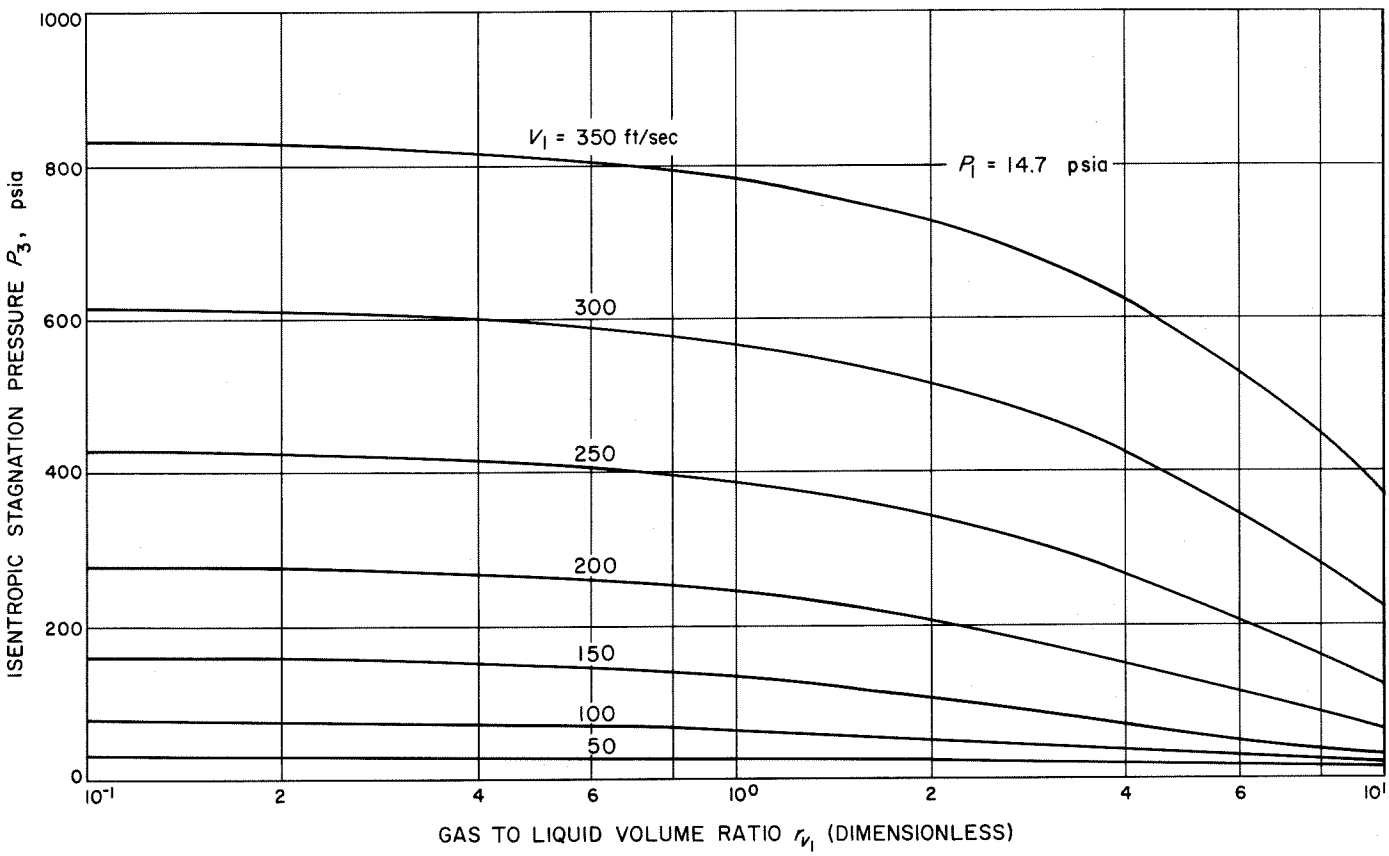

Fig. VI-14. Isentropic stagnation pressure as a function of volume ratio for values of mixture velocity (P_1 = 14.7 psia)

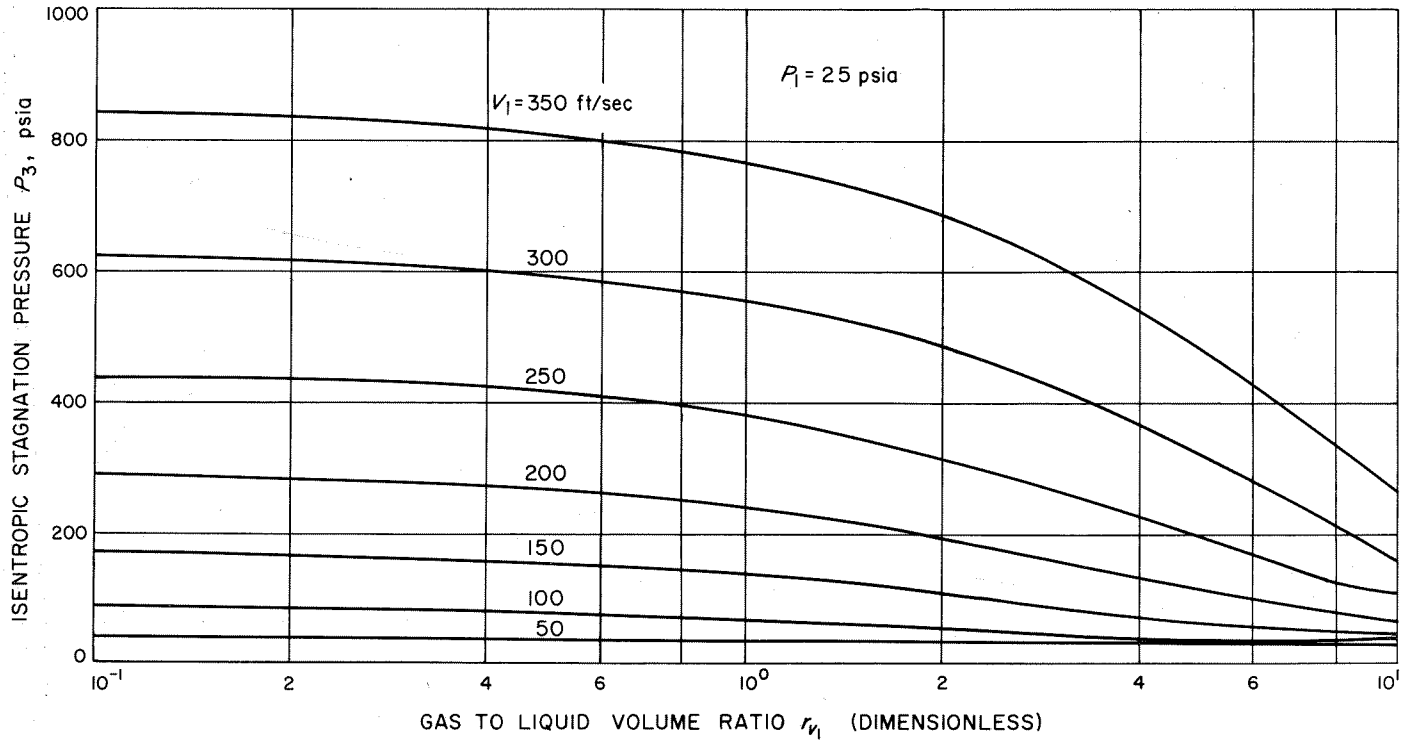

Fig. VI-15. Isentropic stagnation pressure as a function of volume ratio for values of mixture velocity (P_1 = 25 psia)

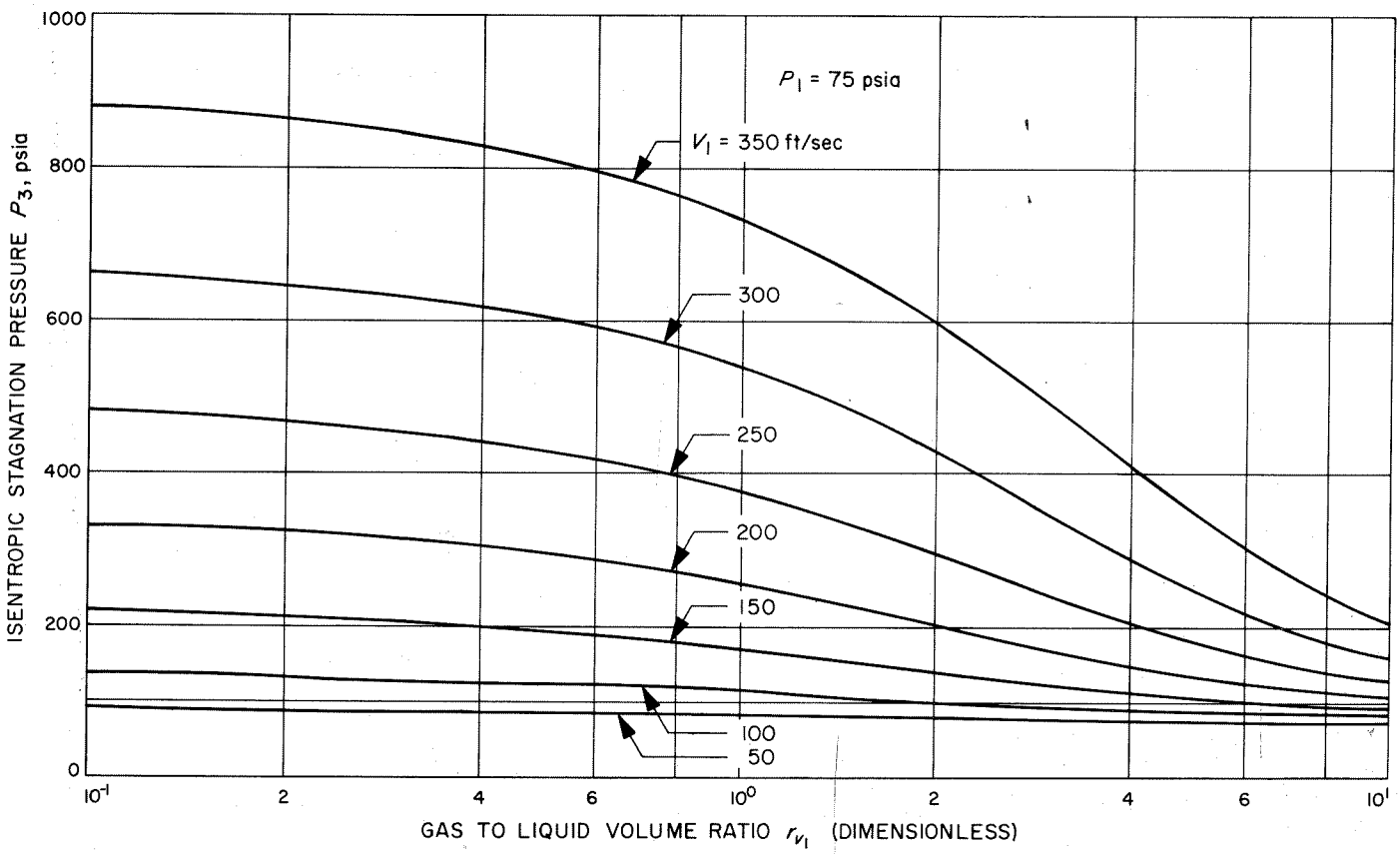

Fig. VI-16. Isentropic stagnation pressure as a function of volume ratio for values of mixture velocity (P_1 = 75.0 psia)

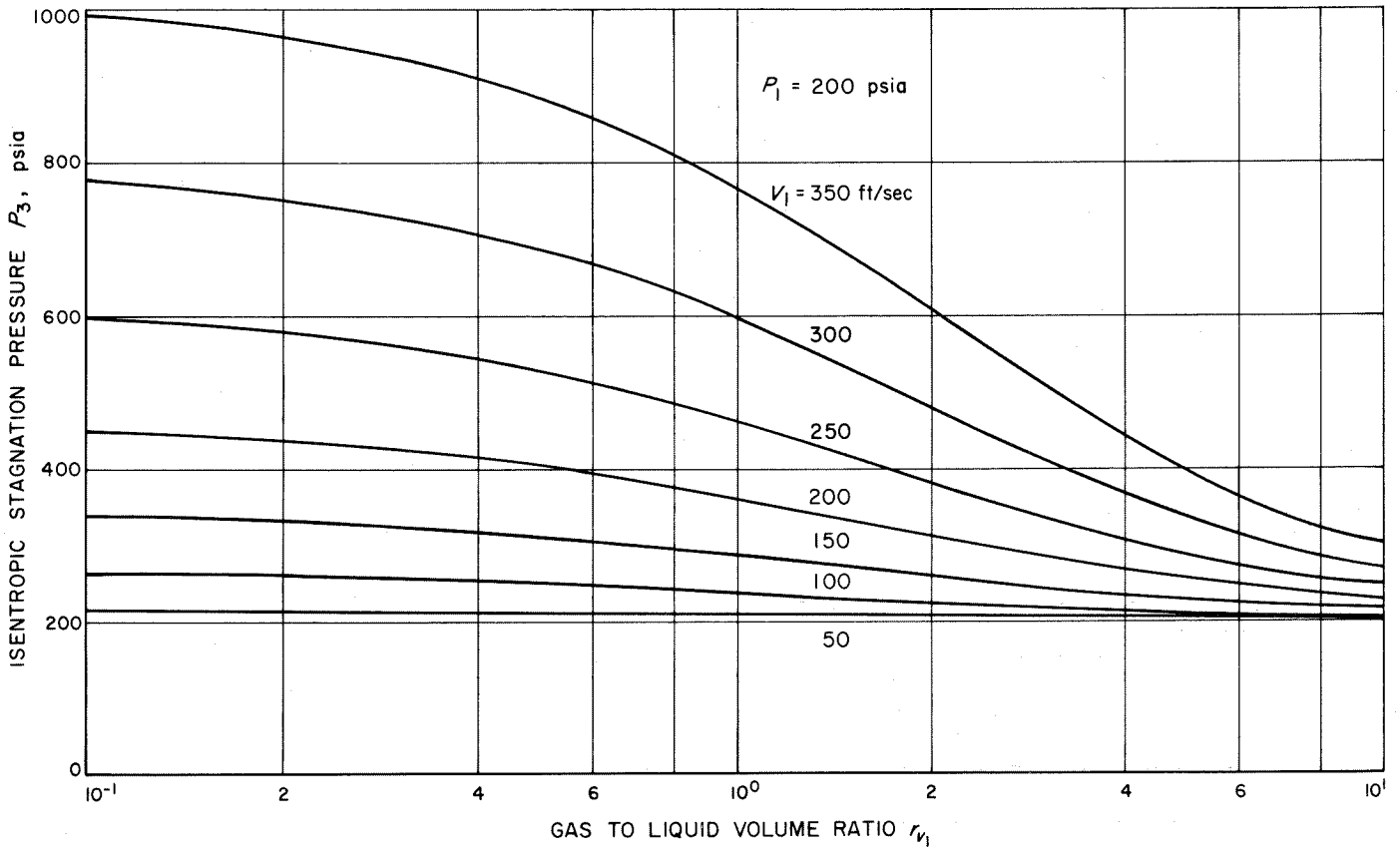

Fig. VI-17. Isentropic stagnation pressure as a function of volume ratio for values of mixture velocity (P_1 = 200 psia)

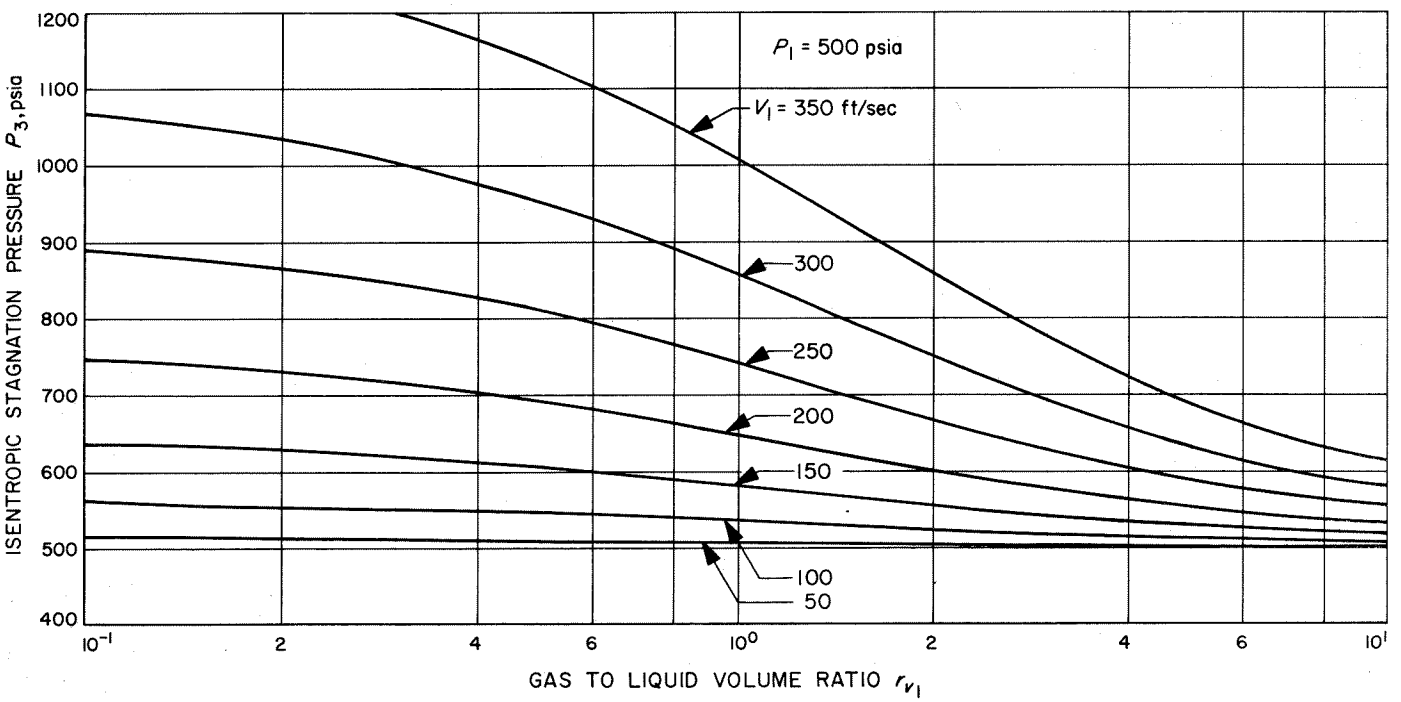

Fig. VI-18. Isentropic stagnation pressure as a function of volume ratio for values of mixture velocity (P_1 = 500 psia)

Nomenclature

P mixture pressure, static (lb_f/ft^2)

P_3 isentropic stagnation pressure, mixture (lb_f/ft^2)

P_4 normal shock plus isentropic stagnation pressure, mixture (lb_f/ft^2)

r_m gas-to-liquid mass ratio

r_v gas-to-liquid volume ratio

V mixture velocity (ft/sec^2)

ρ mixture density ($slugs/ft^3$)

ρ_l density, liquid phase ($slugs/ft^3$)

Subscripts

1 upstream of shock

2 downstream of shock

VII. Determination of Wall Shear in Two-Phase Flow

A. Fundamentals

Wall shear (τ_w), or coefficient of friction (C_f), can be determined with minimum apparatus if accurate measurements of thrust, static pressures, and nitrogen and water flow rates can be made for different known lengths of flow duct. Configurations for these tests follow, along with their mathematical justification.

1. Test Configuration A

Consider a short length of duct (Fig. VII-1) through which a two phase flow of known volume ratio is discharged. The balance of forces on the duct is

$$\mathring{m}_A V_{2A} = F_A - P_{2A} A_d \qquad \text{(VII-1)}$$

where $\mathring{m}_A$, V_A, F_A and A_d are the mass flow rate, velocity, pressure, and inner transverse duct area, respectively, at the numerical stations listed in the subscripts and in Fig. VII-1. The momentum balance between stations 1 and 2 is

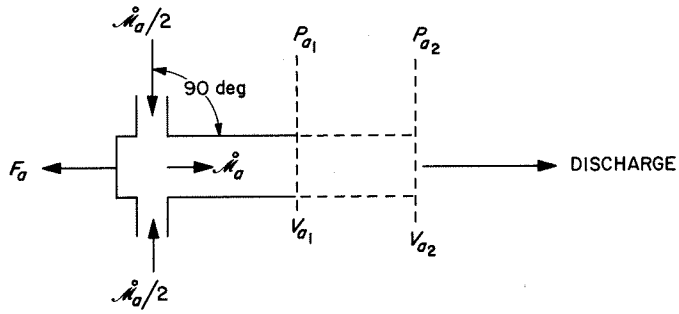

Fig. VII-1. Duct schematic

$$\mathring{m}_A (V_{A1} - V_{A2}) = (P_{A2} - P_{A1}) A_d + \tau_w A_w \qquad \text{(VII-2)}$$

in which the subscript w refers to the interior wall area.

2. Test Configuration B

If the length of duct from station 1 to station 2 is removed, Fig. VII-2 represents Test B.

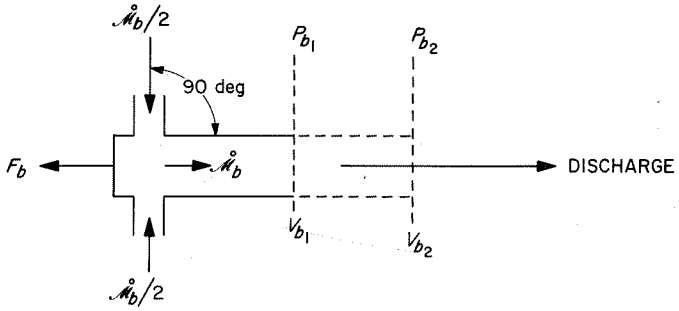

Fig. VII-2. Duct schematic with section removed

The balance of forces for Test B is

$$\dot{m}_B V_{B1} = F_B - P_{B1} A_d \qquad \text{(VII-3)}$$

If flow conditions are adjusted to

$$P_{B1} = P_{B2} \qquad \text{(VII-4)}$$

the flow rates for supersonic flow ($M_1 > 1$) in both tests should be equal:

$$\dot{m}_B = \dot{m}_A \qquad \text{(VII-5)}$$

Because the transverse area is constant, the continuity equation gives equal velocities at station 1:

$$V_{B1} = V_{A1} \qquad \text{(VII-6)}$$

Substituting Eqs. (VII-4), (VII-5), and (VII-6) into Eq. (VII-3),

$$\dot{m}_B V_{B1} = \dot{m}_A V_{A1} = F_B - P_{A1} \qquad \text{(VII-7)}$$

Substituting Eqs. (VII-1) and (VII-7) into Eq. (VII-2),

$$(F_B - P_{A1} A_d) - (F_A - P_{A2} A_d) = (P_{A2} - P_{A1}) A_d + \tau_w A_w$$

or

$$(F_B - F_A) = \tau_w A_w$$

or

$$\frac{F_B - F_A}{A_w} = \tau_w \qquad \text{(VII-8)}$$

Thus a determination of the wall shear stress can be made from an accurate measurement of the difference in thrust between the two test conditions ($F_B - F_A$) and a measurement of the internal wall area removed between tests.

3. Coefficient of Friction

The coefficient of friction can be determined from

$$\tau_w = \frac{\rho_l V^2 C_f}{2}\left(\frac{1}{1 + r_v}\right) \qquad \text{(VII-9)}$$

where $1/(1 + r_v)$ is the volume fraction occupied by the liquid. Solving for C_f,

$$C_f = \frac{2\tau_w}{\rho_l V^2}(1 + r_v)$$

Substituting for τ_w from Eq. (VII-8),

$$C_f = 2(1 + r_v)\frac{(F_B - F_A)}{\rho_l V^2 A_w} = 2(1 + r_v)\frac{(F_B - F_A)}{\dot{m}_l V} \qquad \text{(VII-10)}$$

B. Equipment

The two-phase injector described in Section II was attached to a duct 15 in. in length, and 0.75 × 1.95 in. in cross section (Figs. VII-3 and VII-4). The assembly was mounted on a thrust stand capable of determining thrust to 0.1 lb in the thrust range predicted (Fig. III-7). The injector provided homogenous two-phase flow at velocities from 146 to 330 ft/sec at atmospheric pressure. Sections of duct approximately 2 in. long were removed between thrust measurements for determination of wall shear (τ_w) in accordance with Eq. (VII-8).

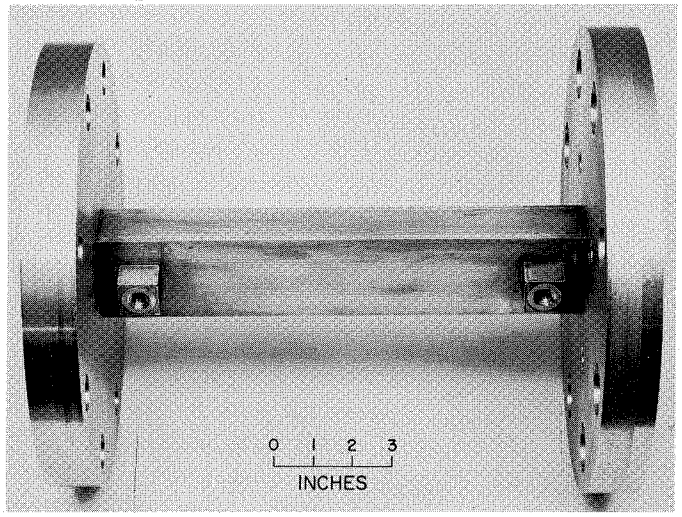

Fig. VII-3. Duct assembly used for coefficient of friction tests

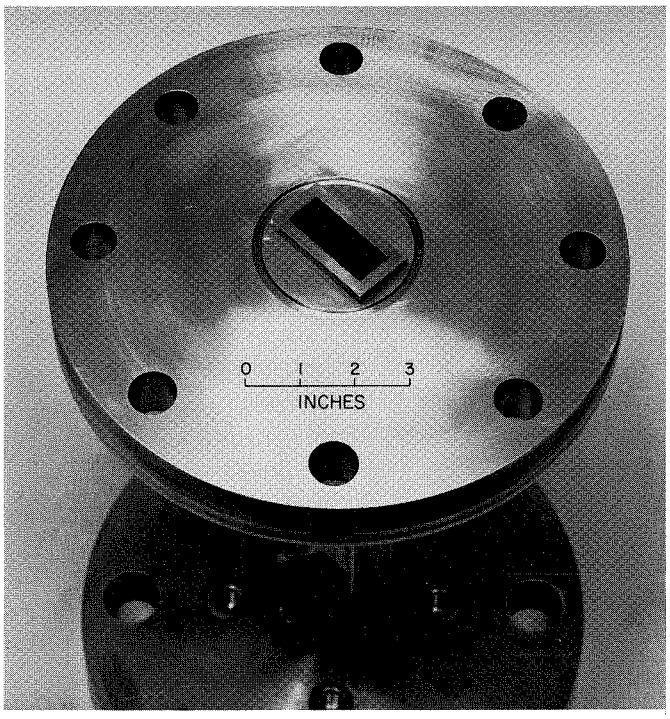

Fig. VII-4. End view of duct assembly

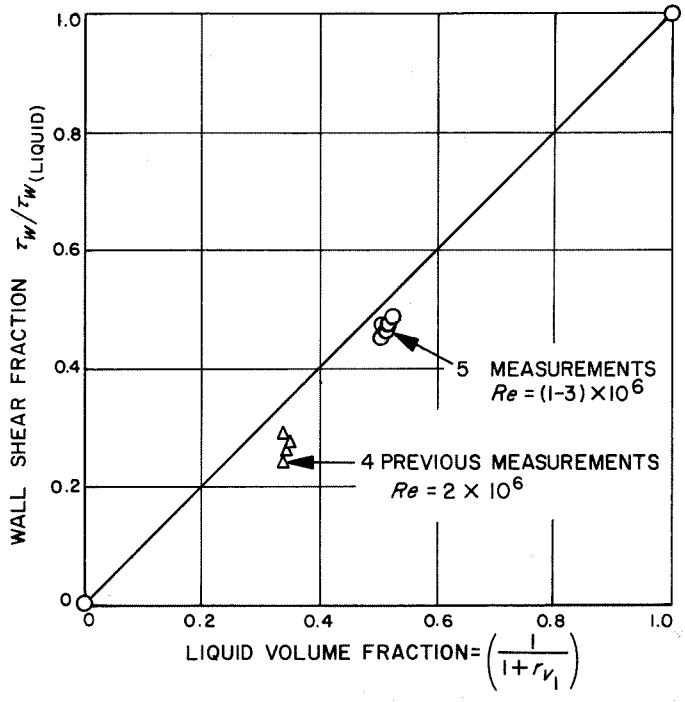

Fig. VII-5. Variation of wall shear fraction with liquid volume fraction

C. Friction Factor vs Reynolds Number

From a previous but less accurate experiment of this type, wall shear results corresponding to a liquid volume fraction of 0.35 were available.

By computing τ_{w_l} to correspond with a completely water-filled duct at the same velocity as the two-phase flow, the ratio of shear stresses τ_w/τ_{w_l} was determined for each velocity and plotted as a function of liquid volume fraction for the two groups of data. The results are shown in Fig. VII-5. Comparison with a straight line between zero (wall shear with pure gas would be 0.0013 τ_{w_l}, or negligible) and 1.0 shows that the simple relationship

$$\tau = \tau_{w_l} \times (\text{liquid volume fraction}) \qquad \text{(VII-11)}$$

can be conservatively used for predicting wall shear in high velocity homogeneous two-phase flows of this type.

Equation (VII-11) is equivalent to using the mixture density (ρ = liquid density $\times$ liquid volume fraction, ignoring gas density) of the two-phase flow and calculating the shear stress as though the mixture were a single-phase medium. If friction factors for the experiments are computed as a function of mixture density and plotted against the Reynolds number also as a function of mixture density and liquid velocity, then the results for the 0.5 volume fraction case (Fig. VII-6) fall within 10% of the Prandtl-von Kármán resistance law.

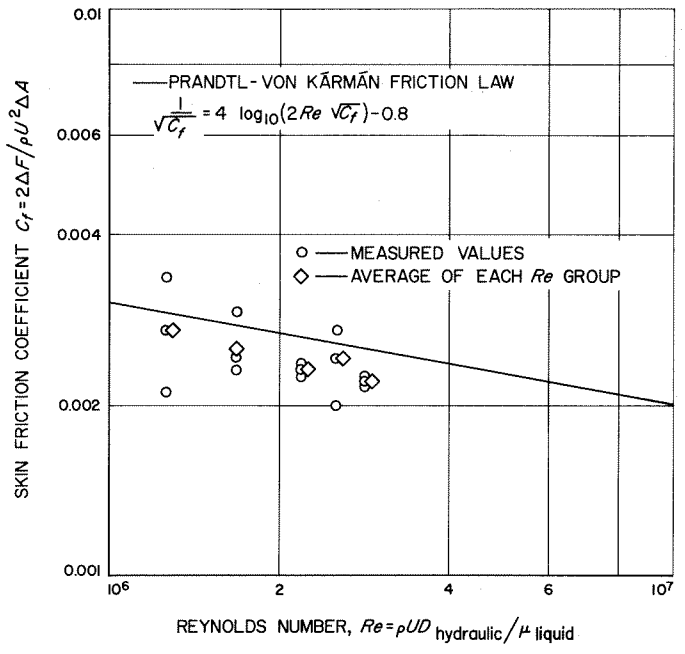

Fig. VII-6. Skin friction coefficient as a function of Reynolds number

Nomenclature

A_d cross-sectional duct area, internal (ft^2)

A_w duct wall area (ft^2)

C_f coefficient of friction

F thrust (lb_f)

$\mathring{m}$ mass flow rate, mixture (slugs/sec)

P static pressure (lb_f/ft^2)

V velocity, mixture (ft/sec)

τ_w wall shear stress, mixture (lb_f/ft^2)

τ_{w_l} wall shear stress, liquid (lb_f/ft^2)

Subscripts

A test A

B test B

VIII. Summary and Conclusions

Results from the operation of the supersonic two-phase tunnel indicate that all of the shock phenomena, including normal, oblique, and conical shocks, that are typical of single-phase supersonic gas flows can be generated in supersonic two-phase gas-liquid continuum-type flows. Shock angles, pressure ratios, volume ratios, velocity ratios, and Mach numbers can be accurately predicted by the relatively simple isothermal theory for a two-phase continuum (the two phases were selected to preclude significant condensation or dissolution of the gas phase into the liquid phase). Such inherent complexities of the interphase relationships as surface tension, dynamic bubble behavior, heat conduction, and dissolution of the gas phase into the liquid phase can be neglected for a wide range of volume ratios and shock strengths as long as the flow characteristics are determined outside of the region in which the various relaxation processes are taking place.

The supersonic two-phase tunnel is capable of providing uniform, well-defined supersonic flows at Mach numbers from 1 to nearly 100, giving it the most extended Mach number range of any such device in existence. Such uniformity results from the multitube water and gas injector that operated at a fixed area ratio for a wide range of mass-flow rates.

The boundary layer has been successfully removed with negligible influence on the core flow, allowing accurate observation of core characteristics in the tunnel test section. Unusual stability of operation without such transient flow characteristics as the water hammer effect has allowed long and continuous use of the tunnel over most of its potential range. At the highest Mach numbers, however, cavitation downstream of the shock phenomenon damaged the transparent side walls of the test section, limiting the allowable operation time under these conditions to a few minutes.

The propagation velocity of a shock wave in a two-phase liquid-gas continuum corresponds closely to the velocity predicted by the isothermal theory. Such waves have a finite structure that depends upon the gas-liquid volume ratio, isotropy of phase distribution, and wave strength.

The first visible evidence of shock structure occurs at a volume ratio of approximately 0.77 for all mixture velocities. For strong shocks, this evidence is a rapid disorientation of the chain-like bubble structure into a random pattern. Disorientation was less pronounced in the progressively weaker shocks, such as the weak oblique shocks, where their presence was evidenced primarily

by the change in direction of the bubble chains upon passing through the shock front.

Superimposed upon the oblique shock patterns were bubble migrations in the directions of negative pressure gradients. This was most evident along the leading edge of the oblique shock wave where a portion of the gas phase appeared to flow outward at significant velocities. Such migrations were noted also behind the oblique shock where negative pressure gradients existed in a direction toward the wake void at the center line behind the test wedge. These deviations of a portion of the gas phase in directions that were not parallel with the local mixture velocity obviously lead to nonuniform void fraction distributions.

The gas-phase migration in oblique shock waves is but a part of the overall consideration of wave dimension and proximity to a deflection surface. It was found from theoretical consideration of the relaxation processes that shock-wave thickness in two-phase liquid-gas mixtures is sufficiently large to encompass a portion of any deflection geometry. Therefore, in contrast to the normal shock in which upstream and downstream conditions can be separated from the shock relaxation processes, the oblique shock relaxation processes are being carried out over a portion of the initial deflection surface. This results in some curvature of the leading edge of the oblique shock as the local gas-to-liquid volume ratio is increased from the deflection point outward along the shock. Consequently, the presence of oblique shock structure can lead to variations in void fraction distribution downstream of the shock from an originally uniform upstream flow.

There was no evidence of Prandtl-Meyer-type flow around expansion corners in the supersonic two-phase flow. Although no diffuser work was done in the investigation, it is obvious that expansion without separation can occur only at very limited diffuser angles.

With a reasonably uniform two-phase liquid-gas flow possessing no time-dependent transverse stratifications other than a boundary layer, such core flow characteristics as gas velocity, liquid velocity, and volume ratio or void ratio can be determined on a thrust stand by removal of the boundary layer. The overall average characteristics for fully developed two-phase duct flows can likewise be determined on a thrust stand for a wide range of gas-to-liquid mass ratios.

Near the gas-liquid volume ratio of one-to-one, there are no simple geometric distributions of one or the other phase. The flow model changes from a typically gas-connected model at volume ratios greater than unity, to a liquid-connected model by a very minimum value of volume ratio equal to approximately 0.77. The typical interphase drag will be increased approximately a thousandfold with such a model change. Injectors such as the water-tube type used in the supersonic tunnel can create nonisotropic drag models, as was evident in the chain-like bubble formations downstream of the one-to-one area ratio injector.

Overall volume ratio and void fraction distribution for an initially uniform two-phase liquid-gas flow will continuously change in duct flow because of wall shear stress. The reduced water velocity in the developing boundary layers tends to decrease the core volume ratio and create changing void distributions within the boundary layer. A positive pressure gradient concurrent with the change in volume ratio will cause a deceleration of the gaseous phase in accordance with the interphase drag model. For a gaseous-connected model of relatively low interphase drag, relative velocities can reach a substantial fraction of the flow velocity.

The isentropic stagnation pressure recovery theory for two-phase continuum flows gives a close approximation to the stagnation pressure recovery measured by a total head probe for mixture velocities approaching 270 ft/sec. Above this velocity, the measured pressure drops below the isentropic predicted value and becomes more closely approximated by the normal shock pressure rise, which is followed by an isentropic stagnation recovery of the downstream flow. Here again, the shock thickness in which the relaxation processes are taking place is substantially greater than the distance to the probe opening. Consequently, the relaxation processes have not been completed at the stagnation position.

Results of the investigation into the coefficient of friction indicate that the wall shear stress for two-phase supersonic flow can be conservatively approximated by multiplying the liquid volume fraction of the mixture by the wall shear stress of a liquid component that flows at the same velocity as the two-phase flow. This relationship is equivalent to using the mixture density (ρ) of the two-phase flow for calculation of shear stress as though the mixture were a single-phase media.